

University of Warwick institutional repository: <http://go.warwick.ac.uk/wrap>

A Thesis Submitted for the Degree of PhD at the University of Warwick

<http://go.warwick.ac.uk/wrap/61997>

This thesis is made available online and is protected by original copyright.

Please scroll down to view the document itself.

Please refer to the repository record for this item for information to help you to cite it. Our policy information is available from the repository home page.

**The synthesis and characterisation of
single-walled carbon nanotubes and
graphene for electrochemical applications**



Thomas S. Miller

A thesis submitted for the degree of Doctor of Philosophy

Dept. of Chemistry

University of Warwick

November 2013

Table of Contents

Chapter 1: Introduction	1
1.1 The carbon nanotube	2
1.1.1 The structure of CNTs.....	2
1.2 Synthesis of carbon nanotubes	7
1.2.1 Arc discharge	7
1.2.2 Laser ablation	8
1.2.3 Catalytic Chemical vapour deposition (cCVD)	10
1.2.4 High pressure carbon monoxide (HiPco).....	13
1.2.5 Mechanism for catalytic cCVD CNT growth	14
1.3 Electrochemistry.....	15
1.3.1 Dynamic electrochemistry	15
1.3.2 Mass transport	16
1.3.3 Cyclic voltammetry (CV).....	17
1.3.4 Electrode kinetics	19
1.4 Electrochemistry using intrinsic carbon nanotube electrodes	20
1.4.1 Early work using CNTs as electrodes	20
1.4.2 Intrinsic electrochemical properties of CNTs	23
1.5 Modification of CNTs for electrochemistry	27
1.5.1 Chemical, physical and electrochemical routes	27
1.5.2 Modification with metal NPs	27
1.6 The use of CNTs for electrocatalysis	29
1.6.1 CNTs for the promotion of the oxygen reduction reaction (ORR)	29
1.6.2 CNTs for promotion of the methanol oxidation reaction (MOR)	33
1.7 Graphene	35
1.7.1 The structure of graphene.....	35
1.7.2 Graphene synthesis.....	37
1.7.3 Graphene characterisation.....	40
1.7.4 Graphene electrochemistry.....	43
1.8 Aims and objectives	44
1.9 References	47
Chapter 2: Experimental	56

2.1	SWNT catalyst preparation	57
2.1.1	2D SWNT networks	57
2.1.2	Very high density (VHD) SWNT networks.....	58
2.1.3	3D SWNT forests	58
2.2	SWNT Growth by cCVD	59
2.2.1	CVD systems.....	59
2.2.2	Generalised cCVD growth procedure	61
2.3	Graphene growth by cCVD	63
2.3.1	CVD system	63
2.3.2	Substrate preparation.....	64
2.3.3	Graphene growth by cCVD.....	65
2.3.4	Graphene transfer	67
2.4	Characterisation techniques	68
2.4.1	Optical microscopy	68
2.4.2	Field-emission scanning electron microscopy (FE-SEM)	69
2.4.3	Transmission electron microscopy (TEM)	69
2.4.4	Atomic force microscopy (AFM).....	69
2.4.5	Micro-Raman microscopy.....	69
2.4.6	X-ray photoelectron microscopy	70
2.4.7	SWNT network density calculation	70
2.5	Substrate preparation	71
2.5.1	Evaporation of gold contacts.....	71
2.6	Electrochemical measurements	72
2.6.1	Microcapillary electrochemical method (MCEM).....	72
2.6.2	Nano-scale capillary measurements	74
2.7	Carbon fibre ultramicroelectrodes (UMEs) for generation/collection ..	75
2.7.1	Fabrication.....	75
2.7.2	MCEM generation/collection experiments	76
2.8	Chemicals, reagents and materials	77
2.9	References	80
Chapter 3: SWNT and graphene: Growth and characterisation		81
3.1	Introduction	82
3.1.1	Carbon nanotubes	82
3.1.2	Graphene	83
3.2	2D SWNT networks results and discussion	84
3.2.1	Catalyst nanoparticle deposition	84

3.2.2	2D SWNT network growth and network density evaluation	87
3.2.3	Micro-Raman spectroscopy	91
3.3	3D SWNT forests results and discussion	97
3.3.1	Catalyst system	97
3.3.2	3D SWNT forest growth and characterisation	100
3.4	Graphene results and discussion.....	102
3.4.1	Growth and characterisation of SLG on Cu foils.....	102
3.4.2	Characterisation of graphene post-transfer to Si/SiO ₂	106
3.4.3	Electrochemical measurements.....	109
3.5	Conclusions	111
3.6	References	112
Chapter 4: Electrochemistry at SWNT forests: sidewalls and closed ends allow fast electron transfer.....		115
4.1	Introduction	116
4.2	Results and discussion.....	118
4.2.1	Preparation and characterisation of SWNT forest electrodes	118
4.2.2	Conductance and voltammetric analysis.....	121
4.3	Conclusions	125
4.4	References	127
Chapter 5: Electrochemical activation of pristine SWNTs: impact on oxygen reduction and other surface sensitive redox processes.....		129
5.1	Introduction	130
5.2	Electrode preparation and Electrochemical measurements.....	132
5.3	Electrochemistry of surface sensitive redox couples and the effect of anodic oxidation of SWNTs.....	133
5.4	Effect of anodic pre-treatments on oxygen reduction at SWNTs.....	138
5.5	Macroscopic SWNT forest electrodes.....	145
5.6	Conclusions	146
5.7	References	147
Chapter 6: Pt Nanoparticle Modified SSWNT network electrodes for electrocatalysis: control of the specific surface area of Pt-modified electrodes over three orders of magnitude.		150
6.1	Introduction	151
6.2	Electrodeposition of Pt NPs on SWNT networks	152
6.3	Pt deposition and NP characterisation.....	154
6.3.1	Deposition procedure	154
6.3.2	Pt deposition and NP characterisation.....	155

6.4	ORR and MOR on low density SWNT/Pt composites.....	160
6.4.1	ORR on low density SWNT/Pt composites	160
6.4.2	MOR on low density SWNT/Pt composites	165
6.5	ORR and MOR on high density SWNT/Pt composites.	167
6.5.1	ORR on high density SWNT/Pt composites	167
6.5.2	MOR on high density SWNT/Pt composites	169
6.6	Conclusions	170
6.7	References	172
Chapter 7: Generation – collection measurements within the meniscus of a microcapillary electrochemical cell using a carbon fibre ultramicroelectrode..		174
7.1	Introduction	175
7.2	Microcapillary generation-collection (G/C)	176
7.3	Proof of concept	177
7.4	Applications.....	181
7.4.1	SWNT forest	181
7.4.2	Oxygen reduction reaction mechanism	182
7.5	Conclusions	184
7.6	References	186
Chapter 8: Conclusions		187

List of Figures

Figure 1.1 – Schematic representation of the chiral vector (C_h) of SWNTs, showing the unit vectors a_1 and a_2 and the chiral angle (θ). The red line shows C_h for a zigzag (10,0) SWNT, the blue line shows C_h for a chiral (7,3) SWNT and the green line shows C_h for an armchair (5,5) SWNT.	3
Figure 1.2 – a) STM images of SWNTs of different chiralities, ¹¹ ‘no. 10, 11 and 1’ are chiral SWNT, ‘no. 7 is zigzag and ‘no. 8’ is armchair. b) aberration corrected TEM images of a zigzag (10,0) layer of a MWNT. ¹² Image 1 is a magnification of image 4.	5
Figure 1.3 – A schematic of a typical arc discharge chamber ²⁰	7
Figure 1.4 – A schematic of a typical laser ablation system ²⁵	8
Figure 1.5 – SWNT produced by laser ablation, the majority of which were claimed be zigzag (10,10) chirality from TEM and XRD measurements. ²⁶ Scale bars are 20 nm.	9
Figure 1.6 – Schematic of a typical atmospheric pressure cCVD system.	11
Figure 1.7 – a) Photograph of a ‘super long’ (2.5 mm) SWNT forest grown by water assisted cCVD ⁵⁷ ; b) FE-SEM image of the SWNT forest. ⁵⁷ c) AFM image of a 2D SWNT network. ⁶⁶	12
Figure 1.8 – Schematic of a HiPco reactor (left) and TEM image of SWNT produced using the HiPco method. ⁷²	13

Figure 1.9 – a) Schematic of ‘root’ and ‘tip’ growth mechanisms. b,c and d)TEM images of SWNT growing by ‘root’ mechanism. ⁷⁹ e)TEM image of MWNT growing by ‘tip’ mechanism. ⁸⁰	14
Figure 1.10 – Schematic of the processes that influence Faradaic processes at an electrode surface during dynamic electrochemistry, adapted from reference. ⁸² ..	16
Figure 1.11 – a) The triangular waveform of a CV. A typical CV for a reversible system at a macroelectrode (b) and a microelectrode (c). Diffusion profiles at a macroelectrode (d) and a ultramicroelectrode (e).	18
Figure 1.12 – CVs for a reversible and quasi-reversible electrochemical system. ⁸²	20
Figure 1.13 – a) MWNT and b) graphite powder abrasively modified BPPG electrodes. c) Cyclic voltammograms for the oxidation of 1 mM norepinephrine on bare BPPG and with the above modified electrodes. d) Cyclic voltammograms for the oxidation of 1 mM norepinephrine on bare BPPG and with MWNT and graphite powder drop cast electrodes. ⁹⁴	22
Figure 1.14 – a) Schematic and AFM image of single SWNT electrode. CVs for the oxidation of FcTMA^+ at different lengths of SWNT sidewall. ⁴⁷ b) SEM image of aligned SWNT and SECM image of the SWNT indicated by the arrow. Colour scale represents redox current. ⁹⁸ c) SECCM image of a 2D SWNT network and corresponding line scan, greyscale represents redox current. Finite element simulation of the current profile as a SECCM tip is scanned across a SWNT where: the whole sidewall (blue); a single defect (red); 3 defects (green); are responsible for ET, real data shown as black dots. ⁹⁷	26
Figure 1.15 – a) SEM and b) TEM images of metal free N-doped MWNT forest. c) Comparison of the linear sweep voltammetry (LSV) of a commercial Pt/C	

electrode, an undoped MWNT forest and an N-doped forest. d) Schematic of the O ₂ binding at an undoped CNT (top) and an N-doped CNT (middle), charge density at an N-doped site (bottom). ¹⁴⁵	32
Figure 1.16 – Summary of the major processes involved in the methanol oxidation reaction (MOR), adapted from Baltruschat et al. ¹⁵⁹	34
Figure 1.17 – a) STM image of single layer graphene, b) STM image of multi layer graphene. ¹⁶⁷ c) TEM image of few (2 to 4) layer graphene showing graphene edges. ¹⁶⁸ d)TEM image of single layer graphene showing grain boundary between two distinct flakes. ¹⁶⁹	36
Figure 1.18 – CVD graphene: a) SEM and b) optical image of single- (red circle), bi- (blue circle) and few-layer (green arrow) cCVD grown graphene on Si/SiO ₂ . ¹⁸³ c) Representative transfer process of graphene from metal catalyst to Si/SiO ₂ . ¹⁸² d) Transfer process for large area (35 inches diagonal length) graphene onto polymer supports e) 30 inch diagonal length (predominantly single layer) graphene sheet on polyethylene terephthalate (PET). ¹⁸⁶	38
Figure 1.19 – Graphene characterisation: a) AFM image of mechanically exfoliated graphene, SLG height is ca. 4Å. ¹⁷⁵ Optical microscopy images of graphene of on Si with a 300 nm thick oxide layer, images with white (b) and green (c) light. ¹⁹⁶ Micro-Raman spectroscopy of graphene 1 to 4 layers thick (d) with a magnification of the 2D region (e) showing the peak splitting due to layer stacking. ¹⁹⁷	41
Figure 2.1 - Schematic and pictures of the cCVD systems used to grow SWNT (not to scale).....	60

Figure 2.2 - Graphical representation of a generic cCVD growth scheme, t1-5 represent process times, G1-5 represent process gas mixtures, T1 and 2 represent process temperatures. (not to scale). See Table 2.1 for T, t and G values.	62
Figure 2.3 – a) & b) low pressure cold wall CVD system, c) NanoCVD 8G commercial CVD system	64
Figure 2.4 – cCVD growth regime for graphene growth on Cu foil.....	66
Figure 2.5 – A schematic of the processes required to transfer graphene.....	68
Figure 2.6 – Summary of the SWNT network density calculation process, from a) FE-SEM image, b) colour inversion and c) density calculation.	71
Figure 2.7 – Schematic of masking and evaporation of gold onto SWNT networks and forests.....	72
Figure 2.8 – Generalised schematic for a microcapillary electrochemical method (MCEM) measurement. Not to scale.	74
Figure 2.9 – Schematic of a carbon fibre UME. Not to scale.	76
Figure 2.10 – Schematic of the microcapillary based generation/collection set up. Not to scale.....	77
Figure 3.1 – Different catalytic NP systems used for 2D network growth of SWNT (all on Si/SiO ₂). a) as deposited sputtered Co, b) Co NP formed by heating (a) to 850 °C under H ₂ flow, c) histogram showing the height distribution of Co NPs, d) as deposited ferritin (1:150, ferritin:water), e) resultant Fe NPs after exposing (d) to an oxygen plasma, f) resultant Fe NPs after deposition and exposure to an oxygen plasma of 1:500 (ferritin:water) g) histogram showing the height distribution of ferritin particles (as deposited), h) histogram showing the height distribution of Fe NPs (after oxygen plasma).	85

Figure 3.2 – 2D SWNT networks: AFM (a) and FE-SEM (c) of low density ($2 \mu\text{m}_{\text{SWNT}} \mu\text{m}^{-2}$) SWNT network grown using catalyst deposited from 1:500 ferritin:water. AFM (b) and FE-SEM (d) of high density ($5 \mu\text{m}_{\text{SWNT}} \mu\text{m}^{-2}$) SWNT network grown using catalyst deposited from 1:150 ferritin:water.	88
Figure 3.3 - 2D VHD SWNT networks: FE-SEM (a) and AFM (b & c) of a very high density SWNT network.....	91
Figure 3.4 – Typical Micro-Raman spectroscopy (laser wavelength 514 nm) of metallic (all red lines) and VHD (all black lines) SWNT networks. a) Full range survey with the RBM, G, D and G' peaks labelled. b) and c) magnification of the D and G peaks. d) and e) magnification of the RBM region.	93
Figure 3.5 – a) Histogram showing the distribution in diameter of SWNT grown from Fe NPs by cCVD. b) AFM image of SWNT network, black arrow indicates SWNT bundle, blue arrow indicates the SWNT bundle splitting into individual SWNT, height scale +/- 7.5 nm. c) Line trace showing SWNT bundle (black line) and individual SWNT (blue line).....	96
Figure 3.6 – SWNT forest catalyst system a) as deposited Al b) Al after exposure to oxygen plasma 2 mins c) Al/Al ₂ O ₃ with sputtered Co d) Forest catalyst after heating (with no source of carbon).....	98
Figure 3.7 – XPS spectra of the SWNT growth catalyst system. a) Al 2p region b) Co 2p region.	99
Figure 3.8 – a) photograph of SWNT forest with two gold bands evaporated onto the surface b) FE-SEM image of SWNT forest c) micro-Raman spectrum (laser wavelength 514 nm) of SWNT forest, inset shows the RBM region in more detail.....	101

Figure 3.9 – AFM image of a Cu foil post graphene growth according to scheme described in section 2.3.3.	103
Figure 3.10 – Micro-Raman spectra (laser wavelength 514 nm) on copper: a) and b) single layer graphene, c) multi-layer graphene and d) bare copper. The bare copper sample was exposed for an increased number of cycles to demonstrate that no weak sp^2 carbon peaks were present.	105
Figure 3.11 – Typical micro-Raman spectra (laser wavelength 514 nm) of SLG on Si/SiO ₂	106
Figure 3.12 – Optical microscope images at a) 200× and b) 500× magnification, FE-SEM images (c and d) and AFM images (e and f) of SLG on Si with 300 nm SiO ₂	108
Figure 3.13 – CVs for the oxidation of 0.5 mM FcTMA ⁺ in 50 mM KCl, 50 mV s ⁻¹ performed at two different areas of a SLG connected as an electrode.....	110
Figure 4.1 - (a) FE-SEM image of a SWNT forest. (b) Typical TEM image of a SWNT extracted from a forest.	118
Figure 4.2 - Micro-Raman spectra of an intact SWNT forest focusing on the sidewalls and tube ends.....	119
Figure 4.3 - a) XPS spectra of bare catalyst substrate (red line) and SWNT forest surface (black line). The inset shows the spectral range corresponding to Co 2p _{3/2} for both SWNT forest (black line) and catalyst (red line) surfaces. b) Typical TEM image of SWNT ends.....	120
Figure 4.4 - a) Digital photograph and schematic (not to scale) of the pipet in contact with the forest sidewalls, for voltammetric and conductance analysis. b) Current-voltage curves (forward and reverse) recorded on the closed ends (blue)	

and sidewalls (red), with a pipet of inner diameter 400 nm, containing 50 mM KCl, at 100 mV s ⁻¹	122
Figure 4.5 - Typical CVs of 5 mM Ru(NH ₃) ₆ ³⁺ reduction in 50 mM KCl at a scan rate of 100 mV s ⁻¹ . Red lines indicate forest sidewalls, blue lines, forest closed ends.	124
Figure 4.6 –Typical CVs of 2 mM FcTMA ⁺²⁺ oxidation in 50 mM KCl at a scan rate of 100 mV s ⁻¹ . Red lines indicate forest sidewalls, blue lines, the forest closed ends.	124
Figure 5.1 - (a) FE-SEM image of a typical SWNT forest. (b) Schematic of the micro-capillary set up used for voltammetric experiments.....	132
Figure 5.2 - Typical CVs for the oxidation of 1 mM Fe ²⁺ (50 mV s ⁻¹) in 50 mM HClO ₄ performed on the top surface of an SWNT forest. Capillary inner diameter was 50 μm. The CVs were scanned from -0.2 V to +0.87 V (red dotted line) and -0.2 V to +0.95 V (blue line).....	134
Figure 5.3 - a) CVs for the oxidation of 1 mM Fe(CN) ₆ ⁴⁻ in 50 mM KCl (50 mV s ⁻¹) on SWNT forests: black dotted line shows the response with no AP; blue line after AP at +1 V for 2 s. b) CVs for the oxidation of 1 mM FcTMA ⁺ in 50 mM KCl (50 mV s ⁻¹) on SWNT forests: red line shows response before AP; black line after AP at 1 V for 2 s.....	137
Figure 5.4 - a) CV showing the response of a SWNT forest electrode to ORR in 100 mM KCl. CV is scanned from 0 V to -1.3 V and then back to +1.5 V. Cathodic segment of first scan (red line), anodic segment of first scan and full second scan (black line). b) CV response of the SWNT forest electrode in 100 mM KCl, starting at 0 V to +1.4 V then to -1 V (100 mV s ⁻¹). Dashed line (de-aerated solution), solid line (aerated).	140

Figure 5.5 - Micro-Raman spectra of adjacent spots on a SWNT forest. Red line as grown forest, blue line, electrochemically cycled forest; the electrode potential was scanned 10 times from 0 V to +1.3 V, and then back to -1.0 V (100 mV s ⁻¹).	141
Figure 5.6 - CVs showing the ORR response on the SWNT forest in 100 mM KCl (0.1 V s ⁻¹) scanned first from 0 V to different positive potentials: a) + 1.1 V (black); b) +1.2V (pink); c) +1.25 V (red); d) +1.3 V (green); e) +1.35 V (blue) and then to -0.6 V. f) The capacitive current measured prior to each CV, used to assess the wetted electrode area (1 V s ⁻¹), colour coded to the CVs in a-e. g) Comparison of mean G/D values measured from micro-Raman spectra taken at an untreated SWNT forest (5 areas) and at areas anodically pre-treated at different scan ranges. Error bars show plus/minus one standard deviation.	143
Figure 5.7 - a) ORR CV rtesponse of a SWNT forest macroelectrode in 100 mM KCl cycled from 0 V to +1.3 V and back to -1.0 V at 0.1 V s ⁻¹ . Inset shows an optical photograph of the SWNT forest macroelectrode, dashed line indicates proportion of submerged electrode.	145
Figure 6.1 - a) FE-SEM image of a typical SWNT network above the metallic percolation threshold. b) AFM image of a typical SWNT network c) Schematic of Pt NP electrodeposition using the microcapillary. d) Schematic of the set up used to measure ORR and MOR.	153
Figure 6.2 - a) CVs for the deposition of Pt NPs, 5 mM K ₂ PtCl ₆ , one hundred voltammetric cycles at 50 mV s ⁻¹ . The first and the last voltammetric cycles are shown in red and green and shown in an inset for clarity. b) Plot of charge transferred during hydrogen desorption vs. deposition cycle number.	156

Figure 6.3 - (a) FE-SEM and (b) AFM images of electrodeposited NPs and (c) Histogram analysis of Pt NP heights extracted from AFM images of three repeats of each of Pt deposition regime: (i) 1 deposition cycle; (ii) 10 deposition cycles and (iii) 25 deposition cycles.	157
Figure 6.4 - CVs of electrodeposited Pt NPs in de-aerated 0.5 M H ₂ SO ₄ , (50 mV s ⁻¹) prepared by: a) 1 deposition cycle; b) 10 deposition cycles; c) 25 deposition cycles. d) Plot of specific surface area as a function of the number of deposition cycles, calculated from the charge passed in the H _{UPD} region (left axis) and the percentage of the geometric surface area with respect to the area of the droplet on the SWNT network during electrodeposition (right axis).....	159
Figure 6.5 - a) Linear sweep voltammograms for ORR (0.5 M H ₂ SO ₄ , 100 mV s ⁻¹) on Pt NP deposited with 1, 10 and 25 cycles. b) Magnification of the LSV for the ORR on Pt NP deposited with 1 cycle. c) Mass-transport corrected Tafel plot for the high overpotential region of the ORR LSV on Pt NP deposited with 1 cycle, red dotted line has a slope of – 275 mV dec ⁻¹ . d) Plot of ORR current measured at 0.35 V (chosen as it was close to limiting but before there was a contribution from hydrogen adsorption) vs. number of Pt deposition cycles. ...	161
Figure 6.6 - a) CVs for the MOR (0.5 M methanol in 0.5 M H ₂ SO ₄ , 100 mV s ⁻¹) on Pt NP deposited for 1, 10 and 25 cycles. The anodic sweep is shown with a solid line; the cathodic sweep is shown by dotted line. b) Plot of MOR peak current vs. specific Pt surface area.	166
Figure 6.7 - FE-SEM (a and b) and AFM (c) images of electrodeposited NPs (from 5 mM K ₂ PtCl ₆) after: (i) 50 deposition cycle; (ii) 75 deposition cycles and (iii) 100 deposition cycles.	167

Figure 6.8 - a) LSVs starting at 1.3 V and extending to – 0.1 V (aerated 0.5 M H ₂ SO ₄ , 100 mV s ⁻¹) at Pt electrodeposits (from 5 mM PtCl ₆ ²⁻) for different numbers of deposition cycles, b) CVs for the MOR (0.5 M methanol in 0.5 M H ₂ SO ₄ , 100 mV s ⁻¹) performed on Pt NP deposited from 5 mM PtCl ₆ ²⁻ for different numbers of cycles (start and end potential 0V, scanning to 1.3 V).....	169
Figure 7.1 - a) CV for the oxidation of 0.25 mM FcTMA ⁺²⁺ in 50 mM KCl (25 mV s ⁻¹) at a carbon fibre UME. b) Schematic of the MCEM G/C set up. c) Optical photograph of carbon fibre UME in the capillary meniscus. d) Large scale view of MCEM G/C on a glassy carbon electrode.	177
Figure 7.2 - FE-SEM images of a polyoxyphenylene coated carbon fibre which has been cut to form a UME.	178
Figure 7.3 - G/C CVs of 0.5 mM FcTMA ⁺²⁺ in 50 mM KCl, 25 mVs ⁻¹ , performed on a SWNT network: a) generation; b) collection with UME held at 0 V. c) generation; d) collection with UME held at 0.4 V.	180
Figure 7.4 - G/C CVs of 0.5 mM FcTMA ⁺²⁺ in 50 mM KCl, 50 mVs ⁻¹ , performed on a SWNT forest. Generation is shown in the main figure body, collection inset, with UME held at 0 V.....	182
Figure 7.5 - a) CV in 0.5 M H ₂ SO ₄ , 25 mVs ⁻¹ , on a Pt NP decorated SWNT network. b) Collector response at Pt coated UME held at 0.9 V. a) CV in 0.5 M H ₂ SO ₄ , 25 mVs ⁻¹ , on a glassy carbon electrode. b) Collector response at Pt coated UME held at 0.9 V.	183

List of Tables

Table 1.1 – Summary of the various pathways for the ORR. ¹³⁴	30
Table 2.1 – CVD growth conditions for different SWNT structures	63
Table 2.2 – List of materials and chemicals used in this work	79

Acknowledgements

There are a number of people I would like to thank for the help and support they have given me. To start, I would like to thank both of my supervisors, Professor Julie Macpherson and Professor Pat Unwin. Their incredible insight, guidance and kindness have been overwhelming, they are truly an inspiration.

I would also like to thank all of those of the Warwick electrochemistry and interfaces group, past and present, for their help and solidarity. In particular I would like to mention Dr Jon Edgeworth, Dr Aleix Güell and Dr Stanley Lai for the knowledge and skills they have passed on to me.

Special thanks should go to all of the doctors at the London chest hospital and Dr W. Drake, who fixed me when I was broken and without whom this work would have been cut short.

Finally, I would like to thank my parents, family and friends for their support and understanding over the past few years. Particular thanks should go to Katharine Young, who has had to be the most understanding of all, she has been fantastic.

Declarations

The work described in this thesis has not been submitted for a degree at any other university. This is entirely my own work except for the following contributions:

Chapter 2: Aluminium was sputtered by Dr David Burt at the University of Glasgow.

Chapter 3: Electrochemical measurements were performed by Dr Aleix Güell and Dr Neil Ebejer.

Publications

Parts of this thesis have been published in the following articles:

T. S. Miller, N. Ebejer, A. G. Güell, J. V. Macpherson, and P. R. Unwin, Electrochemistry at carbon nanotube forests: sidewalls and closed ends allow fast electron transfer, *Chem. Commun.*, **2012**, 48, 7435-7437. Cover article and highlighted in the RSC Chemistry world magazine.

T. S. Miller, J. V. Macpherson, and P. R. Unwin Electrochemical activation of pristine single walled carbon nanotubes: impact on oxygen reduction and other surface sensitive redox processes. *Phys. Chem. Chem. Phys.* Accepted for publication. **DOI:** 10.1039/C3CP53717J

Two further publications based on this thesis are currently in preparation.

Work to which I have contributed, but is not featured in this thesis has been published in the following articles:

S. E. F. Kleijn, S. C. S. Lai, T. S. Miller, A. Yanson, M. T. M. Koper, and P. R. Unwin, Landing and Catalytic Characterization of Individual Nanoparticles on Electrode Surfaces, *J. Am. Chem. Soc.*, **2012**, 134 (45), 18558–18561.

D. Wakerley, A. G. Güell, L. A. Hutton, T. S. Miller, A. J. Bard, and J. V. Macpherson, Boron doped diamond ultramicroelectrodes: a generic platform for sensing single nanoparticle electrocatalytic collisions, *Chem. Comm.*, **2013** 49, 5657–5659.

Anisha N. Patel, Sze-yin Tan, Thomas S. Miller, Julie V. Macpherson, and Patrick R. Unwin, Comparison and Reappraisal of Carbon Electrodes for the Voltammetric Detection of Dopamine, *Anal. Chem.*, **2013**, 'Just accepted' at time of print.

Abstract

In recent years sp^2 carbon materials, including single-walled carbon nanotubes (SWNT) and graphene have attracted significant attention, especially in the field of electrochemistry. However there is a marked disparity of opinion concerning the fundamental inherent electron transfer (ET) properties of these materials, largely due to complications regarding their synthesis, characterisation and the methods utilised to measure their electrochemical characteristics. As shown in this thesis, catalysed chemical vapour deposition (cCVD) allows the growth of very high quality SWNT directly onto insulating substrates and so it is considered by many to be the ideal method to produce SWNT for fundamental studies and applications. However, graphene must be transferred post cCVD growth to insulating substrates, as it grows on metal foil catalysts and this process is currently associated with issues with contamination and mechanical damage.

In this thesis SWNTs with both 2D and 3D geometries are investigated using micro- or nano- scale capillary electrochemical methods. By using outer sphere redox mediators and by isolating the SWNT sidewalls and end-caps it is shown that ET at SWNTs is both fast and occurs on both pristine sidewalls and closed ends. This opposes the commonly held view that ET only happens at open ends and defects. Then, it is shown that functionality can be introduced into pristine SWNTs either by platinum nanoparticle (NP) electrodeposition or anodic pre-treatment. These activated SWNTs are shown to display improved ET to a range of complex and inner sphere redox reactions, including becoming electrocatalytic for the oxygen reduction reaction (ORR) and the methanol oxidation reaction (MOR).

Also in this thesis a method of performing generation/collection (G/C) electrochemical measurements within the meniscus of a microcapillary is demonstrated. This system is shown to be effective at both investigating processes on complex electrode surfaces and at investigating the mechanistic aspects of the ORR.

List of abbreviations

2D	Two dimensional
3D	Three dimensional
AFM	Atomic force microscopy
AP	Anodic polarisation
BLG	Bi-layer graphene
BPPG	Basal plane pyrolytic graphite
cCVD	Catalysed chemical vapour deposition
CNT	Carbon nanotube
CV	Cyclic voltammetry/Cyclic voltammogram
CVD	Chemical vapour deposition
DI	Deionised
DMFC	Direct methanol fuel cell
EPPG	Edge plane pyrolytic graphite
ET	Electron transfer
FE-SEM	Field-emission scanning electron microscopy
FLG	Few-layer graphene
G/C	Generation/collection
GC	Glassy carbon
HER	Hydrogen evolution reaction
HET	Heterogeneous electron transfer
HOPG	Highly oriented pyrolytic graphite

LSV	Linear sweep voltammetry/linear sweep voltammogram
MCEM	Microcapillary electrochemical method
MFC	Mass flow controller
MOR	Methanol oxidation reaction
mSWNT	Metallic single walled carbon nanotube
MWNT	Multi-walled carbon nanotube
NP	Nanoparticle
ORR	Oxygen reduction reaction
PECVD	Plasma enhanced chemical vapour deposition
PMMA	Poly(methyl methacrylate)
QRCE	Quasi reference counter electrode
RBM	Radial breathing mode
RDE	Rotating disk electrode
RE	Reference electrode
RT	Room temperature
sccm	Standard cubic centimetres per minute
SECCM	Scanning electrochemical cell microscopy
SECM	Scanning electrochemical microscopy
SHE	Standard hydrogen electrode
SLG	Single-layer graphene
sSWNT	Semiconducting single walled carbon nanotube
STM	Scanning tunnelling microscopy
SWNT	Single walled carbon nanotube
TEM	Transmission electron microscopy
UME	Ultramicroelectrode

VHD	Very high density
VLS	Vapour-liquid-solid
WE	Working electrode
XPS	X-ray photoelectron spectroscopy

List of symbols

$[O]_{\infty}$	Bulk concentration of oxygen
a	Graphene sheet lattice constant
a_1, a_2	Graphene sheet unit vectors
$A_{electrode}$	Electrode area
C	Capacitence
C	Concentration
C_{bulk}	Bulk concentration
C_h	Chiral vector
D	Diffusion coefficient
d_{SWNT}	Single walled carbon nanotube diameter
$E^{0'}$	Formal potential
F	Faraday constant
G	Gas mixture
i_{cap}	Capacitative current
i_p	Peak current
j	Current density
j_k	Kinetic current density
j_{lim}	Mass transport limited current density
k_0	Standard rate constant
k_t	Mass transfer coefficient
L	SWNT circumferential length

n	Number of electrons
n, m	SWNT structural indices
R	Universal gas constant
R_c	Capillary radius
T	Temperature
t	Time
α	proportionality constant
$\Delta E_{3/4}-E_{1/4}$	Interquartile separation
ΔE_p	Difference in peak potential (CV)
η	Overpotential
θ	Chiral angle
ρ	Length of SWNT per unit area
ρ_{th}	Percolation threshold
$\rho_{th}^{metallic}$	Percolation threshold for metallic network behaviour
$\rho_{th}^{semiconducting}$	Percolation threshold for semiconducting network behaviour
v	Scan rate
ω_{RBM}	Radial breathing mode frequency

1

Introduction

This thesis concerns the growth, characterisation and development of both single-walled carbon nanotubes (SWNT) in a variety of geometries, and graphene, for electrochemical applications. This introduction is a review of the current state of work relevant to this topic.

1.1 The carbon nanotube

The first report of carbon nanotubes (CNT) is commonly accepted to have been made in 1991 by Iijima.¹ This work reported the presence of multi-walled carbon nanotubes (MWNT) (although they were termed ‘graphitic’ carbon needles) in the soot like material produced when arc-discharge was performed on a carbon electrode. The same author later adapted the synthesis process to include catalytic iron particles, allowing the formation of single-walled carbon nanotubes (SWNT).² CNTs have to-date been utilised in a wide variety of applications ranging from medicine³ to transistors⁴ (and hundreds of others)⁵ and are considered to be a material with significant promise.⁶

1.1.1 The structure of CNTs

A CNT can, in its simplest form, be considered to be a single sheet of sp^2 carbon atoms, commonly known as graphene, rolled up to form a cylinder with a diameter as small as 7 \AA ⁷ and a length commonly on the scale of microns (and often millimetres, even centimetres).⁸ If the CNT consists of a single graphene sheet, it is a SWNT, with diameters typically in the range 1 to 3 nm. If multiple concentric sheets are present the tube is a MWNT and will have a diameter above 2 nm and regularly greater than 20 nm.⁸

The basic structure of a CNT is defined by its unique ‘rolling vector’, more commonly known as chiral vector (C_h). This defines the points at which two carbon atoms in the graphene lattice are ‘joined’ (i.e. the two C atoms in the theoretical graphene sheet are actually at a crystallographically identical lattice point in the CNT) to form the tube. C_h is defined as a pair of indices (n, m) that

represent the number of unit vectors (\mathbf{a}_1 and \mathbf{a}_2) in the lattice, within vector C_h . It is therefore possible to write:

$$C_h = n\mathbf{a}_1 + m\mathbf{a}_2 \quad (1.1)$$

Due to hexagonal symmetry effects, the chiral angle (θ) must be greater than (or equal to) 0° and no greater than 30° , therefore $n \geq m$. These concepts are shown in Figure 1.1.

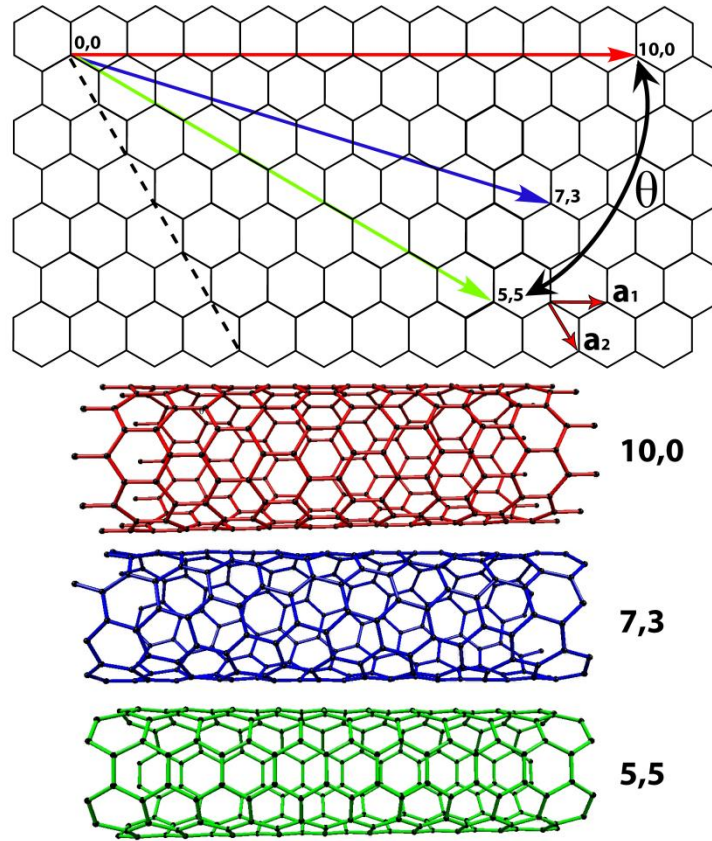


Figure 1.1 – Schematic representation of the chiral vector (C_h) of SWNTs, showing the unit vectors \mathbf{a}_1 and \mathbf{a}_2 and the chiral angle (θ). The red line shows C_h for a zigzag (10,0) SWNT, the blue line shows C_h for a chiral (7,3) SWNT and the green line shows C_h for an armchair (5,5) SWNT.

The three SWNT shown in Figure 1.1 show the three different chiralities of SWNT, which can be distinguished from each other by looking at the shape at the end of the open carbon nanotube. The achiral nanotube structures (i.e. one

where the mirror image has the same structure) are zigzag (red SWNT) and armchair (green SWNT) and have C_h of $(n, m=0)$ and $(n,m=n)$ respectively. A SWNT with any other C_h is chiral, an example of which is shown by the blue SWNT. From the chiral indices (n,m) , it is possible to calculate the circumference of a SWNT, using equation (1.2)

$$L = |C_h| = a\sqrt{n^2 + m^2 + nm} \quad (1.2)$$

where L is the circumferential length, n and m are the chiral indices and a is the lattice constant for graphene ($a=2.49 \text{ \AA}$). From this the diameter of a SWNT (d_{SWNT}) can be calculated from equation (1.3)

$$d_{SWNT} = \frac{L}{\pi} \quad (1.3)$$

therefore the (10,0), (7,3) and (5,5) SWNTs shown in Figure 1.1 have diameters of 7.92 \AA , 7.04 \AA and 6.86 \AA respectively. Although there are theoretically lots of ways a SWNT can be orientated, in reality energetic and structural constraints limit the range of possibilities.

The atomic structure of CNTs has been confirmed through studies initially utilising scanning tunnelling microscopy (STM)⁹⁻¹¹ and later aberration corrected transmission electron microscopy (TEM).¹² From the STM images in Figure 1.2 (a) Dekker *et al*¹¹ visualised the atomic structure of multiple SWNTs and identified their chirality by measuring the chiral angle of each. For example they identified the uppermost SWNT in Figure 1.2(a) as a chiral tube with chiral indices of (11,7), they also showed armchair and zigzag SWNT.

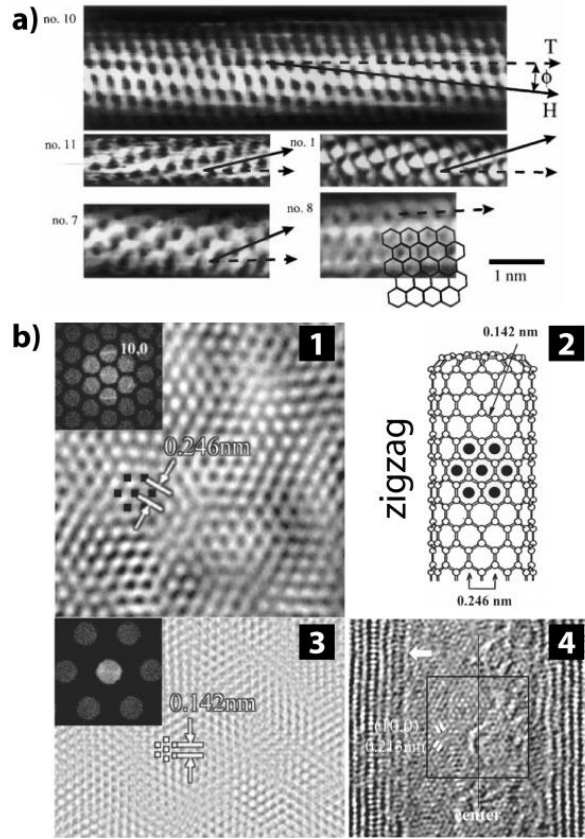


Figure 1.2 – a) STM images of SWNTs of different chiralities,¹¹ ‘no. 10, 11 and 1’ are chiral SWNT, ‘no. 7 is zigzag and ‘no. 8’ is armchair. b) aberration corrected TEM images of a zigzag (10,0) layer of a MWNT.¹² Image 1 is a magnification of image 4.

Figure 1.2(b) shows TEM images, collected by Pan *et al.*,¹² clearly showing the atomic structure of a MWNT, Figure 1.2 (b). The chirality of one of its layers was identified as an achiral zigzag tube, with indices of (10, 0) (the same as the red SWNT in Figure 1.1).

It is well-known that practically the atomic structure of CNTs is never completely pristine and ‘defects’ are present.^{13, 14} The concentration of these defects depends on the method of synthesis. The inclusion of five- or seven-membered rings into the structure can cause kinks in the CNT and is common at the ends of the CNT due to the formation of end-caps.⁷ If CNT are exposed to

harsh purification procedures it is also often common to have sp^3 hybridised sites and oxygen terminated, open tube ends.¹⁵

The electronic properties of SWNT are a direct consequence of their atomic structure and chirality. Like with the atomic structure, the electronic structure of SWNT can be initially considered in terms of a graphene sheet, where carbon atoms are sp^2 hybridised and form σ bonds with the neighbouring atoms, with the fourth valence electron occupying a delocalised network of π bonds formed from the unhybridised $2p_z$ orbital. The properties of this π bonded network dominate the conduction properties of the graphene sheet as they are close to the Fermi level.

Graphene, due to the valence and conduction bands meeting at specific points of its Brillouin zone, is a semi-metal (or zero band gap semiconductor) and is therefore always conductive, however, as the curvature of a SWNT slightly disrupts the symmetry of the graphene sheet this is not always the case with SWNT. Calculations,¹⁶ which have been corroborated through experimental measurements,^{10, 11} have shown that in fact only one third of SWNTs display metallic behaviour (mSWNT), with the other two thirds semiconducting (sSWNT). As the electronic structure of SWNTs is directly linked to the individual SWNTs chirality, it is unsurprising that the conduction properties of SWNTs can also be differentiated by chirality. Arm-chair SWNT ($n,m=n$) always display metallic conduction properties. Otherwise, if equation (1.4) holds

$$\text{integer} = \frac{(n-m)}{3} \quad (1.4)$$

the SWNT will be metallic, all others are sSWNT.

For MWNTs the principles discussed above hold for each layer of tubes, however, when the MWNT consists of more than three layers it is unlikely the tube will exhibit semiconducting properties, as only a single layer needs to be conductive to render the whole MWNT so.

1.2 Synthesis of carbon nanotubes

CNT can be synthesised by a variety of methods, however the most commonly utilised are arc discharge, laser ablation, catalytic chemical vapour deposition (cCVD) and the high pressure carbon monoxide (HiPco) floating catalyst method.

1.2.1 Arc discharge

Arc discharge is arguably the simplest method for production of CNTs and is the method which was utilised to produce the first MWNTs and SWNTs.^{1,2} CNTs are produced when an arc is ignited between two graphite electrodes, usually in an argon atmosphere, by the application of a high voltage (20 - 25 V) causing a current up to 120 A, which results in temperatures in excess of 3000 °C.¹⁷⁻¹⁹

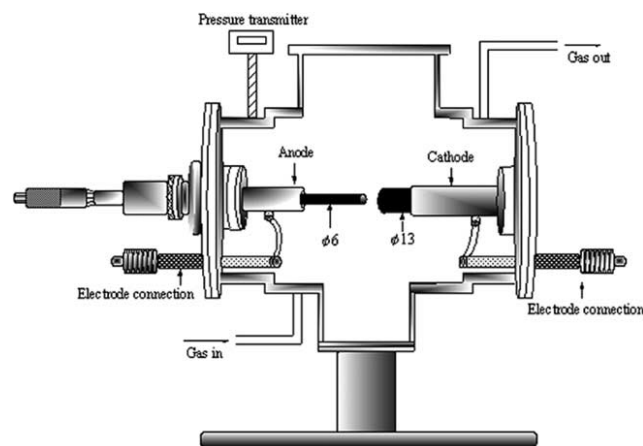


Figure 1.3 – A schematic of a typical arc discharge chamber.²⁰

The arc acts to vaporise the carbon from the anode, which then condenses and cools on the cathode, forming a mix of amorphous carbon, other fullerenes and MWNT.²¹ To synthesise SWNTs using arc discharge, the anode must be implanted with transition metals such as Co, Ni and Fe which act as catalysts,² however, this leads to contamination of the SWNT with metal nanoparticles (NPs), with a weight ratio of NPs to carbon of 2:1 being common.²²

1.2.2 Laser ablation

Laser ablation is similar to arc discharge in a variety of ways, including the vaporisation of a carbon target to produce CNTs, only producing MWNT if the target is pure carbon²³ and producing SWNTs if the carbon target is implanted with transition metal catalysts.²⁴ However, with this technique a pulsed laser vaporises the target and a stream of inert gas causes the carbon to deposit downstream on a cooled collector.

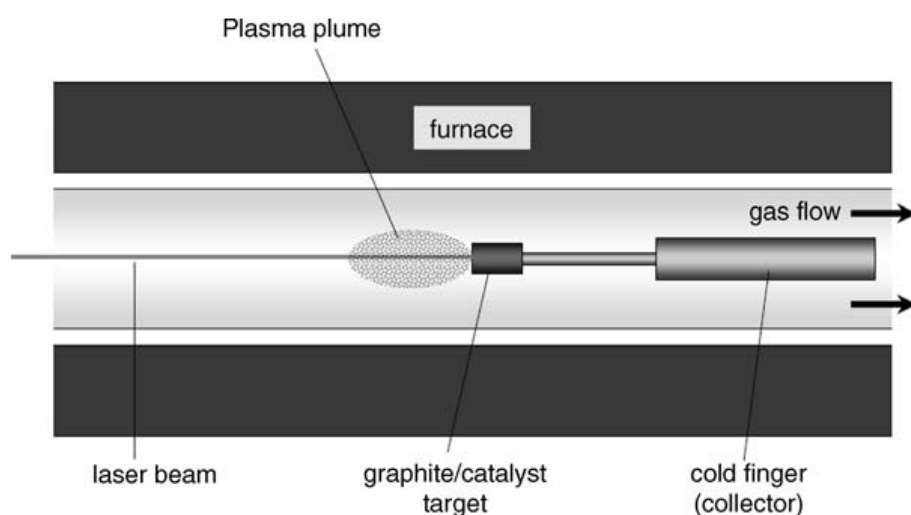


Figure 1.4 – A schematic of a typical laser ablation system.²⁵

This technique has been shown to produce SWNTs with a very consistent diameter,²⁶ which is very unusual for the synthesis of CNTs. The SWNTs in

Figure 1.5 were produced by laser ablation and the authors argue the majority of them were (10,10) zigzag, based on XRD and TEM measurements. This fine control is attributed by the authors to a different SWNT initiation mechanism where metal atoms adsorb onto the edge of a forming fullerene edge and ‘scoot’ around forming a SWNT. They claim this mechanism leads to a rearrangement of the structure over a short timescale, under these specific growth conditions, which forms an energetically preferable SWNT, i.e. (10, 10). Only later in this mechanism does a NP form.²⁶

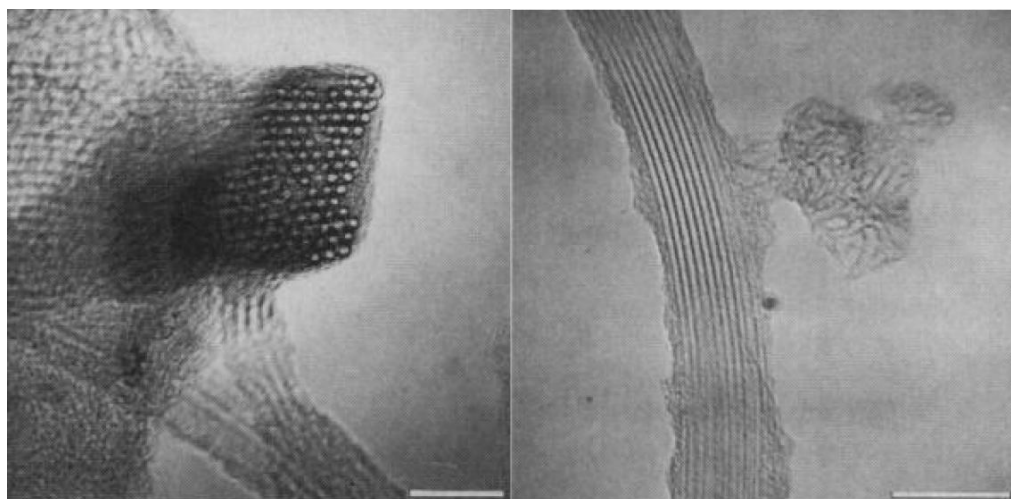


Figure 1.5 – SWNT produced by laser ablation, the majority of which were claimed be zigzag (10,10) chirality from TEM and XRD measurements.²⁶ Scale bars are 20 nm.

Although control of the d_{SWNT} is useful, the CNTs synthesised using laser ablation, as with arc discharge, are produced in a ‘soot’ of amorphous carbon and other fullerenes.²⁷ The CNTs account for a larger proportion of the material created using laser ablation (70-90 %), however, there is significant contamination from the metal NP catalysts.

Because of this contamination it is necessary to purify the CNTs grown by both techniques, to remove amorphous material, other fullerenes and catalytic

metals. Traditional purification techniques such as centrifugation and filtering are ineffective at removing these contaminants,⁷ so the development of aggressive cleaning procedures has been necessary to obtain clean CNTs. The most commonly used involve the use of strong oxidising agents, most often concentrated acids.^{22, 27-30} A generalised procedure involves mechanical grinding the as-grown CNT, mixing with concentrated acid (often a mixture of different acids e.g. $\text{H}_2\text{SO}_4/\text{HNO}_3$),³⁰ which is then refluxed for up to 24 hours and often sonicated. The CNTs are then washed with water and dried. This results in CNTs that are free from metal NPs and amorphous material.

Exposing CNTs to these harsh environments does have an effect on the structure and chemical nature of the tube. Post-cleaning, there is a significant reduction in the length of the CNTs and the end caps are opened.^{22, 30, 31} Defects are also introduced into the pristine sidewalls.¹⁵ Cleaning also acts to functionalise the CNT, introducing oxygen containing functional groups onto the surface, commonly hydroxyl groups,^{22, 30} ketones^{22, 32} and carboxylic acids,³³ which also acts to make the CNTs less hydrophobic.²²

1.2.3 Catalytic Chemical vapour deposition (cCVD)

There are many different variations on cCVD, however, the most often used is thermal cCVD.³⁴ With this technique, catalytic metal NPs, most commonly Fe,^{33, 35-37} Ni^{38, 39} and Co,^{33, 40, 41} are supported on a substrate and inserted into a quartz tube, which runs through a high temperature oven (hot wall). The substrate is heated to the temperature required for growth, generally 800 – 1000 °C, and a gaseous carbon feedstock is flowed through the chamber usually with H_2 and an inert carrier gas e.g. argon. After the growth time has

elapsed the chamber is allowed to cool and the substrates are removed. A schematic of a hot wall cCVD chamber is shown in Figure 1.6.

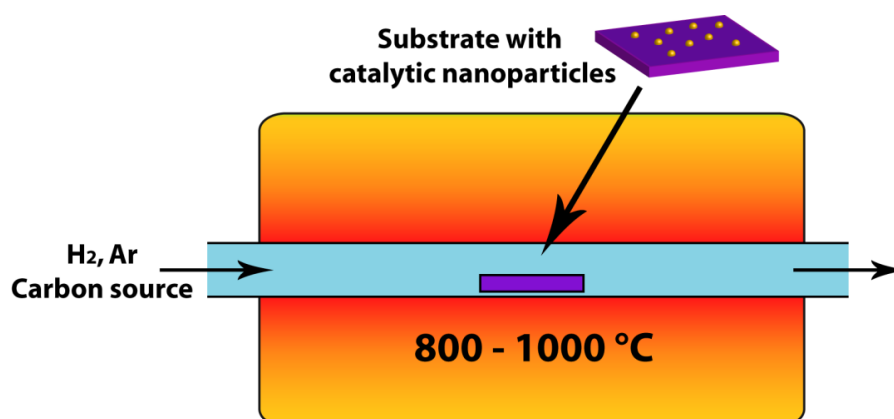


Figure 1.6 – Schematic of a typical atmospheric pressure cCVD system.

cCVD was originally utilised to grow carbon fibres and filaments,^{42, 43} and only later was it developed to grow firstly MWNT^{33, 44} and then SWNT.^{45, 46} Since then there have been many more reports of cCVD growth of CNT, utilising many different growth schemes.

As CNTs grown by cCVD are usually attached to a substrate material (e.g. Si/SiO₂ or quartz) it is possible to grow them in a variety of geometries by adapting the growth conditions or catalyst system. These geometries range from isolated CNTs,^{47, 48} arrays of CNTs aligned parallel to the substrate,⁴⁹⁻⁵¹ random 2D networks of interconnected CNT⁵²⁻⁵⁴ and 3D, super high density, vertically aligned CNT forests.⁵⁵⁻⁵⁷ It is also possible to pattern growth to specific locations and shapes.^{58, 59}

Random 2D networks (Figure 1.7 (c)) are simply grown from NPs that are randomly oriented onto the substrate, which can be deposited by either solution based methods^{60, 61} or more commonly by deposition of thin transition metal films^{54, 62} which form NP on heating. However, the growth of vertically

aligned 3D CNTs (Figure 1.7 (b, c)) often requires the use of a catalyst support material, commonly Al_2O_3 ,^{55, 57} which is reported to act as a barrier to diffusion keeping the catalytic NPs active and promoting CNT growth by preventing NPs from agglomerating.^{55, 63, 64} Other effects, such as surface reactivity and wettability of the support material, have also been shown to have an effect.⁶⁵ The use of ‘advanced’ cCVD techniques such as plasma enhanced cCVD (PECVD) or water assisted cCVD has allowed the growth of super-long (mm tall) CNTs.⁵⁷

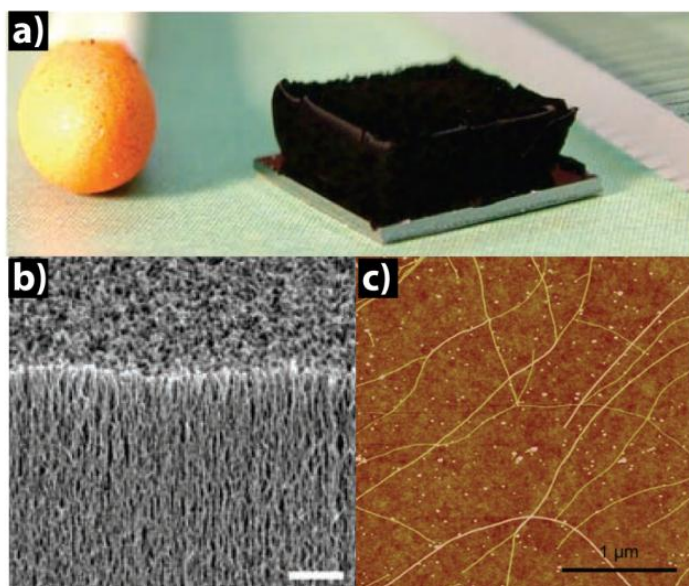


Figure 1.7 – a) Photograph of a ‘super long’ (2.5 mm) SWNT forest grown by water assisted cCVD⁵⁷; b) FE-SEM image of the SWNT forest.⁵⁷ c) AFM image of a 2D SWNT network.⁶⁶

One of the major advantages to using cCVD is that by tuning the growth parameters it is possible to create CNTs (most commonly SWNTs) which are clean (little or no amorphous carbon) and with low defect densities.^{8, 48, 66-69} The defect spacing (i.e. distance between defects) in SWNT grown by cCVD has been found to be as high as 4 μm .⁷⁰ The required NP density to grow 2D SWNT networks, arrays or isolated CNTs is also usually low when compared to ~ 60 %

by weight for arc discharge post synthesis,²² as can be seen in Figure 1.7(c). Although not all NPs grow a CNT, those remaining on the insulating surface, in the vast majority, remain isolated from the network.^{52, 66, 69} These factors mean that CNTs produced by cCVD can often be utilised for applications in their pristine state, without purification, therefore no shortening, opening or defect creation.

1.2.4 High pressure carbon monoxide (HiPco)

One notable variant of cCVD for SWNT growth is the HiPco floating catalyst method. This process utilises the principles of CVD, i.e. the high temperature (900 – 1100 °C) decomposition of carbon gas (CO) over catalyst NPs, but in HiPco the NPs are not anchored to a surface but are formed in the gas phase by the thermal decomposition of $\text{Fe}(\text{CO})_5$.^{71, 72} A schematic of a HiPco reaction chamber is shown in Figure 1.8.

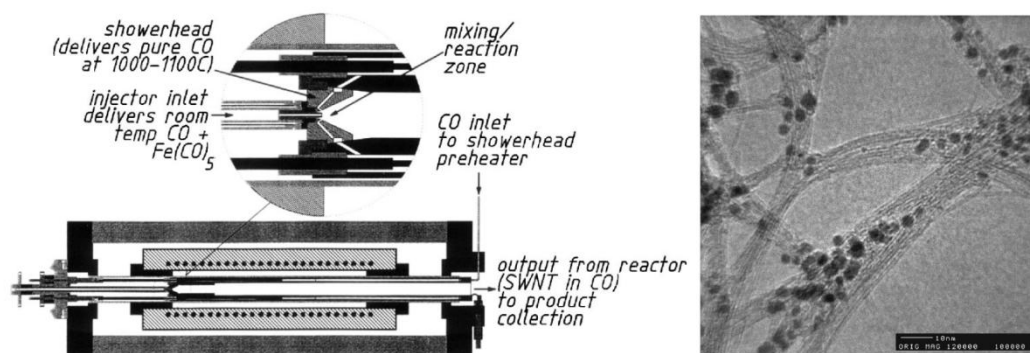


Figure 1.8 – Schematic of a HiPco reactor (left) and TEM image of SWNT produced using the HiPco method.⁷²

This method has been shown to be very effective for the production of large quantities of SWNT (~ 10 g/day)⁷² due to the high throughput of the starting materials. As shown in the TEM image in Figure 1.8 the SWNT

produced are largely free from amorphous carbon, however, a downside to this method is that large quantities of metal catalyst particles are also mixed with the SWNT (up to 30 % by weight³⁴), meaning cleaning is still essential.

1.2.5 Mechanism for catalytic cCVD CNT growth

The cCVD CNT growth process begins with the diffusion of the growth precursor to the surface, then the active species adsorbs onto the particle surface and the reactions leading to CNT growth occur after which the by-products desorb and diffuse away.³⁴ During growth the catalytic NP is in a semi-molten state, despite the melting point (m.p.) of the bulk metal (e.g. Fe m.p. 1583 °C⁷³) being significantly higher than the growth temperature (e.g. 850 °C), due to the significant surface area to volume ratio of the NP.⁷⁴ As the carbon feedstock decomposes on the NP surface the carbon that is released is able to dissolve into it. When the NP is saturated, carbon begins to precipitate out forming a CNT. The NP is either forced from the surface and stays in the end of the CNT, known as tip growth, or remains on the surface forcing the CNT from it, known as root growth (Figure 1.9). The whole process is widely known as the vapour, liquid, solid (VLS) model⁷⁵ and has been observed in in-situ TEM studies.⁷⁶⁻⁷⁸

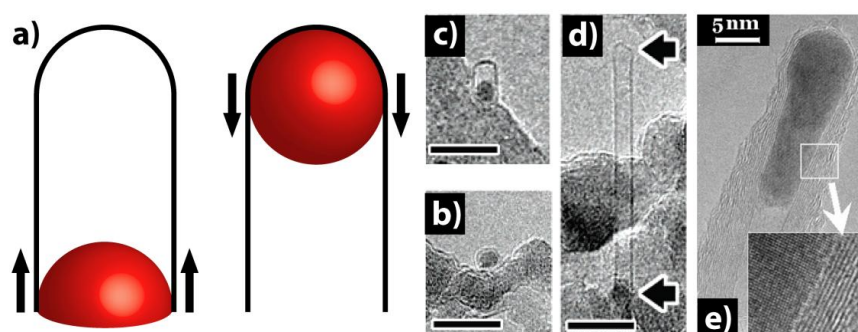


Figure 1.9 – a) Schematic of ‘root’ and ‘tip’ growth mechanisms. b,c and d) TEM images of SWNT growing by ‘root’ mechanism.⁷⁹ e) TEM image of MWNT growing by ‘tip’ mechanism.⁸⁰

It has been shown that MWNTs primarily proceed by the tip growth mechanism whilst SWNTs are more prone to root growth.⁸⁰ It has also been shown that with the same catalyst system there is a transition point between these two processes, which depends on both the strength of interaction of the metal NP to the surface and the interaction between the metal NP and the forming carbon structure.⁸⁰

1.3 Electrochemistry

1.3.1 Dynamic electrochemistry

Dynamic electrochemistry concerns the processes that occur at an electrode/solution interface under non equilibrium conditions.^{81, 82} In a typical experiment a potential is applied to a working electrode (WE) with respect to a reference electrode (RE), which drives the oxidation or reduction of the chosen electroactive mediator in a solution containing excess supporting electrolyte. The rate of these (Faradaic) processes, and therefore current magnitude, is influenced by a range of factors including the potential that is applied, electron transfer kinetics and mass transport of species to/from the electrode, summarised in Figure 1.10.⁸² The electrode is also subject to non-Faradaic processes, where no charge is transferred across the interface, but current flows due to changes in the electrode/electrolyte interface.^{81, 82} Capacitance is an example of a non-Faradaic process. Under certain experimental conditions a third electrode is introduced into the system, namely the counter electrode (CE). This is necessary when the system has a significant contribution from ‘ohmic drop’, which is an effect caused by the passing of large currents or the presence of high solution

resistance.⁸¹ However, as the majority of studies in this thesis produce $< 1 \mu\text{A}$ the contribution from ohmic drop can be considered negligible,⁸¹ therefore justifying the use of two electrode cells.

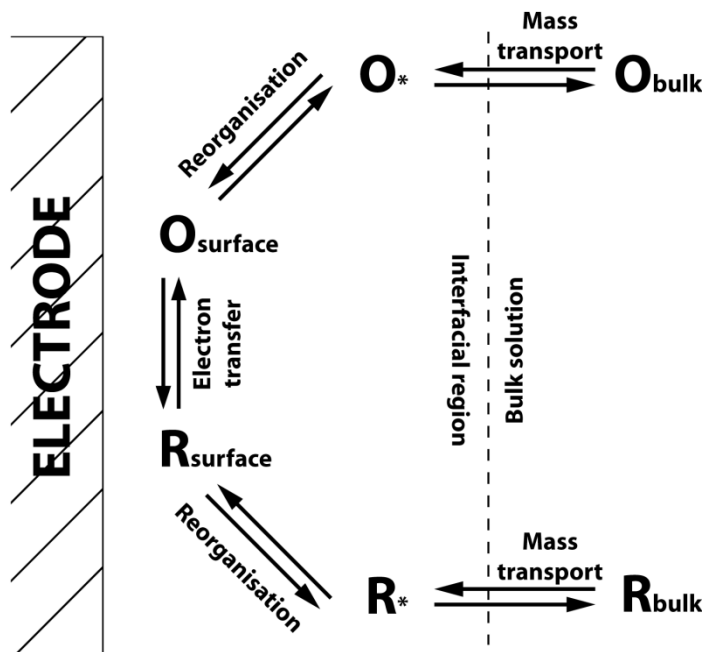


Figure 1.10 – Schematic of the processes that influence Faradaic processes at an electrode surface during dynamic electrochemistry, adapted from reference.⁸²

1.3.2 Mass transport

Mass transport is the movement of species to an electrode surface, and can occur by diffusion, convection and migration.^{81, 82} Diffusion is the movement of species down a concentration gradient. When a redox process is performed at an electrode the species being turned over (oxidised or reduced) becomes depleted at the electrode, creating a concentration gradient from the electrode surface to bulk solution. This means that during a dynamic electrochemical process diffusion is always present. Fick's Law describes the diffusional flux (J), which in one dimension is given by:

$$J = -D \frac{\partial C}{\partial x} \quad (1.5)$$

D is the diffusion coefficient ($\text{cm}^2 \text{s}^{-1}$), C is the concentration (mol cm^{-3}).⁸¹

Convection is caused by a physical action on the solution e.g. stirring, which increases flux to the electrode. It can also be introduced if there are temperature gradients in the solution being used. Convection is often deliberately introduced into electrochemical experiments e.g. rotating disk electrode (RDE).⁸¹ The effects of convection are negated simply by keeping solutions at a constant temperature and still (i.e. no vibrations).

Migration is caused by the movement of charged species in a solution according to a potential gradient.^{81, 82} However, when an inert salt (e.g. KCl) is introduced in excess into the solution of interest, the potential field effects are essentially shielded, meaning migration effects can be disregarded.^{81, 82} In all the experiments described in this thesis excess electrolyte was employed and the solution held under constant temperature, hence mass transport by diffusion is the only mass transport mechanism for consideration.

1.3.3 Cyclic voltammetry (CV)

Potential sweep electrochemical techniques, including cyclic voltammetry (CV), are very commonly used to study electrode processes.⁸² In CV the potential applied to an electrode is swept from an initial potential to a second potential before it is swept back to the initial potential, at a constant sweep rate (Figure 1.11).^{81, 82} From the Faradaic current recorded at the electrode, during this sweep, information regarding the electron transfer (ET) process of interest can be extracted.

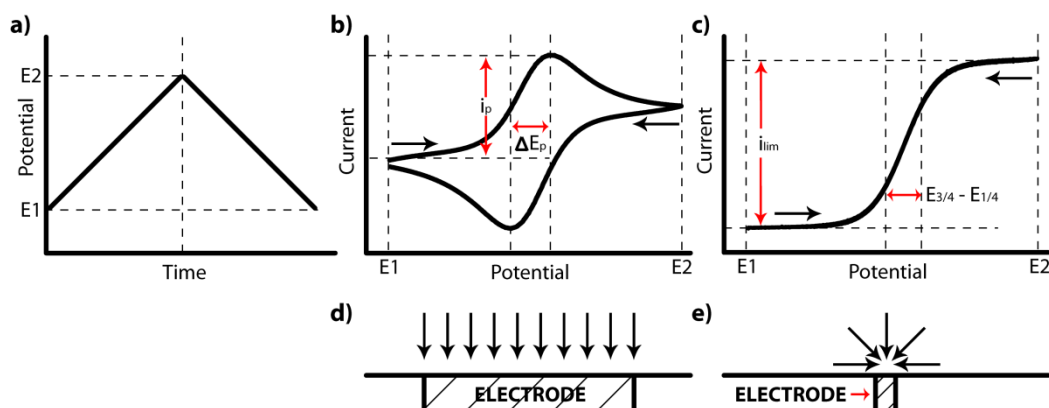


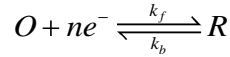
Figure 1.11 – a) The triangular waveform of a CV. A typical CV for a reversible system at a macroelectrode (b) and a microelectrode (c). Diffusion profiles at a macroelectrode (d) and a ultramicroelectrode (e).

At the starting potential of a CV (E_1 , Figure 1.11 b,c) no Faradaic process occurs, however as the potential becomes sufficient to drive the redox process at the surface a current begins to flow, increasing as the potential is increased. The form of the CV is heavily dependent on the electrode geometry and the rate of ET compared to the rate of diffusion. A large planar macroelectrode has a linear diffusion profile (Figure 1.11, d), meaning diffusion is dominated by movement of species perpendicular to the surface.^{81, 82} As the rate of turnover of species at a macroelectrode increases, *i.e.* the overpotential (η) increases, (Butler Volmer kinetics, see 1.3.4) with increased potential, the current increases, up to a point when the diffusion can no longer keep up with the rate of electron transfer and a peak is observed in the CV response (Figure 1.11, b). Under diffusion-controlled conditions the CV has certain characteristics including a peak current (i_p) proportional to scanrate^{1/2} ($v^{1/2}$), a peak potential independent of v , an i_p of the same magnitude on the forward and reverse scans and the peak to peak potential separation (ΔE_p) is $59/n$ mV (n , number of electrons transferred).⁸¹ These characteristics mean that the rate of diffusion limits the reaction, as the rate of ET

is very fast and the system can be described as *reversible*.⁸² In contrast, at an ultramicroelectrode (UME), an electrode with a dimension on the μm scale, the diffusion profile is hemispherical in shape, with a significant radial component (Figure 1.11, e), resulting in a significantly higher diffusion flux than that seen at a macroelectrode. This means the current in a CV does not fall but instead maintains a steady-state at sufficient η (Figure 1.11, c).⁸¹

1.3.4 Electrode kinetics

In a reversible system the standard rate constant for the process (k_0) is much higher than the mass transfer coefficient (k_t). When k_0 is smaller than k_t the electrochemical system is said to become *quasi-reversible*. k_0 can be described using Butler-Volmer kinetics,



$$k_f = k_0 \exp \left[\frac{-\alpha n F (E - E^{0'})}{RT} \right] \quad (1.6)$$

$$k_b = k_0 \exp \left[\frac{(1 - \alpha) n F (E - E^{0'})}{RT} \right] \quad (1.7)$$

where k_f and k_b are the rates of the forwards and backwards reactions respectively, α is the transfer coefficient, n is the number of electrons involved, F is the Faraday constant, $(E - E^{0'})$ is the overpotential, R is the universal gas constant and T is temperature.⁸¹

For a macroelectrode CV under kinetic control the CV becomes more drawn out, compared to the reversible case, as k_0 decreases. A comparison of a reversible and a quasi-reversible CV is shown in Figure 1.12.⁸² If k_0 is much slower than k_t a higher overpotential is necessary to drive the electrochemical

process resulting in an increased ΔE_p . If the process is defined as *irreversible* no peak will appear on the reverse scan.

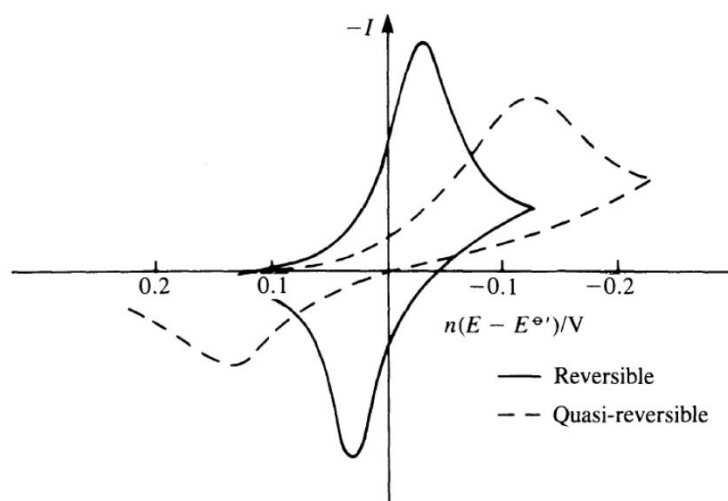


Figure 1.12 – CVs for a reversible and quasi-reversible electrochemical system.⁸²

1.4 Electrochemistry using intrinsic carbon nanotube electrodes

1.4.1 Early work using CNTs as electrodes

The earliest attempt to utilise CNTs as an electrode for electrochemistry was performed by Britto *et al.*⁸³ who mixed unpurified MWNTs, produced by arc discharge, with a binding material and packed them into a glass tube to form an electrode. This was used to investigate the oxidation of dopamine using voltammetry, which showed essentially reversible behaviour, significantly better than at other carbon electrodes. Other reports using similar electrodes,⁸⁴ or those produced from bundles⁸⁵ of, or single,⁸⁶ MWNTs produced by arc discharge, also demonstrated ideal voltammetric behaviour. However, the electrodes in these studies were either largely uncharacterised or found to contain such high levels

of amorphous material that no real understanding of the intrinsic electrochemical properties of the CNT could be gleaned.

The majority of early reports into CNT electrochemistry rely on the use of other electrodes, Pt, Au, glassy carbon (GC), which have been modified with CNTs. Electrodes of this type were first introduced by *Liu et al.*⁸⁷ who modified Au and Pt with purified SWNTs by drop casting. However, the use of a CNT modified GC electrode by *Wang et al.*⁸⁸ for the detection of NADH is often credited as the point at which the interest in CNTs for electroanalysis began to gain momentum.¹⁴ In this work it is shown that modification reduces the overpotential necessary for NADH oxidation and eliminates the effects of electrode fouling. Since this report there have been many notable reports claiming similar benefits.⁸⁹⁻⁹³

However, work in which basal plane pyrolytic graphite (BPPG) was modified with MWNTs by either abrasive attachment (rubbing into the electrode surface) or drop casting and compared with graphite powder, challenged the idea that the CNTs unique structure is responsible for the reported benefits.⁹⁴ It was shown that for the oxidation of norepinephrine, epinephrine and NADH there was little difference between the graphite and MWNT electrodes, although both showed a considerable improvement over bare BPPG (Figure 1.13).

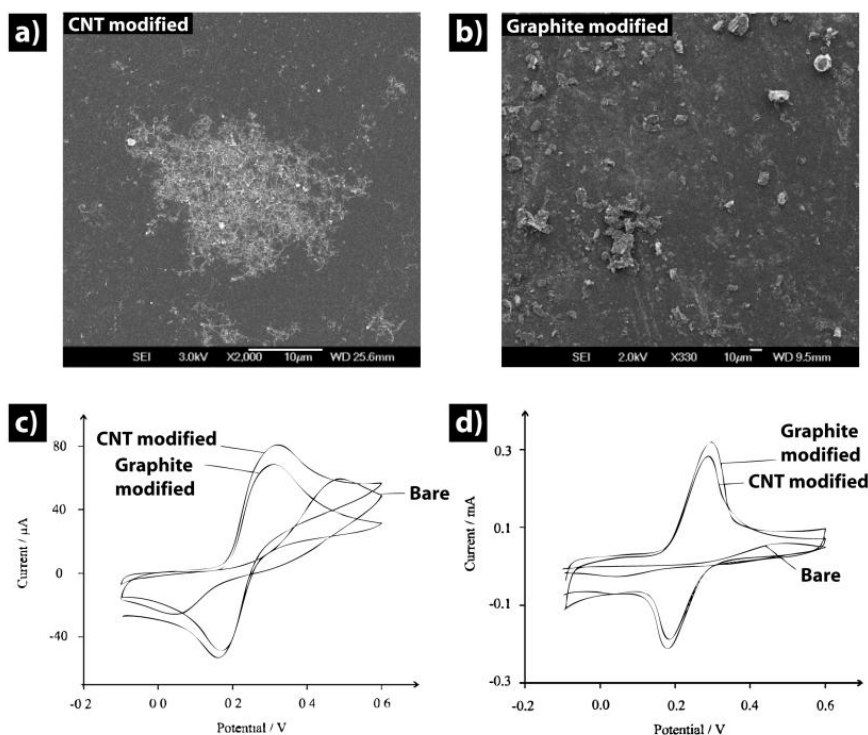


Figure 1.13 – a) MWNT and b) graphite powder abrasively modified BPPG electrodes. c) Cyclic voltammograms for the oxidation of 1 mM norepinephrine on bare BPPG and with the above modified electrodes. d) Cyclic voltammograms for the oxidation of 1 mM norepinephrine on bare BPPG and with MWNT and graphite powder drop cast electrodes.⁹⁴

In a subsequent publication the same authors compared MWNTs to both BPPG and edge plane pyrolytic graphite (EPPG) and found that EPPG and MWNT behave identically for epinephrine oxidation, whilst BPPG shows slow electrode kinetics.⁹⁵ From this they concluded that edge plane like sites in CNT (open ends and defects) are solely responsible for any electrocatalytic behaviour. This postulate has since been extended to suggest that any intrinsic electrochemical activity of CNTs is also purely due to defects and open ends and the pristine CNT sidewall can only exhibit slow ET. However, this description is considered unsatisfactory by many.^{47, 52, 96-98}

1.4.2 Intrinsic electrochemical properties of CNTs

The debate that has arisen around the inherent electroactivity of CNTs is also further complicated by the fact that the manner in which the CNTs have been grown (and in some cases purified) will play a role on the resulting electrochemical response. For example, those CNTs which have undergone harsh purification will have a very different surface structure to those which haven't. Also, some studies use CNTs dispersed on other electrodes, while others use CNTs on an insulating support. Furthermore, electrochemical studies often utilise non-ideal redox couples⁹⁹⁻¹⁰¹ (e.g. $\text{Fe}(\text{CN})_6^{4-/3-}$) which can complicate results due to issues such as surface blocking associated with the redox couple.¹⁰² Finally, MWNT electrochemical behaviour is often assumed to be analogous to SWNTs,^{100, 103} even though the SWNT is an electrode where the entire electrode is a surface, unlike the MWNT which contains an inner core. These issues may be a major contributing factor to the inconsistent reports of CNT electroactivity.

The presence of metal NPs in some CNT electrodes is responsible for one debate over the observed electrocatalytic activity of CNTs towards some redox processes,¹⁰⁴⁻¹⁰⁷ however the intrinsic ET properties of CNTs are also hotly debated. Many reports into the intrinsic electrochemical activity of CNTs focus on 'defects' as the sites of ET.^{95, 101, 108, 109} This analogy stems from earlier work on highly oriented pyrolytic graphite (HOPG) where ET was thought to occur much faster at edge plane sites^{110, 111} than at the basal surface (although this view has also been challenged^{102, 112}). In an early investigation *Li et al.*⁹⁹ used the voltammetric response of the $\text{Fe}(\text{CN})_6^{3-/4-}$ couple to investigate three different CNT electrodes, SWNT 'paper' (bundles of acid-purified SWNT collected onto

paper through filtration), MWNT towers and MWNT towers that had been heat treated to remove amorphous material. These electrodes displayed ΔE_p of 96 mV, 170 mV and 230 mV respectively, demonstrating that that the SWNT paper had the most ideal response. The authors suggest that removing amorphous carbon causes ΔE_p for the towers to get larger, and that the SWNT paper shows the best response due to edge plane like sites being introduced during SWNT purification.

There have been multiple other reports where it is claimed that graphitic like edge plane type sites are responsible for ET in CNT. *Gooding et al.* showed shortened and open ended SWNT that were vertically aligned by self assembly displayed faster ET for $\text{Fe}(\text{CN})_6^{4-}$ oxidation (ΔE_p 59 mV) when compared to gold electrodes modified with randomly oriented SWNT treated in the same way (ΔE_p 99 mV). This was reportedly due to an increased concentration of available end groups (defects).¹⁰⁰ *Wildgoose et al.* showed that ET at MWNTs that had been acid purified, to introduce defects and functionalise the CNT, was improved after the functional groups were removed by annealing, leaving unfunctionalised defects. ET was then made less facile by ‘super annealing’ the CNT which it was claimed healed defects therefore reducing active sites. However, micro-Raman spectra of these samples still had a notable, although reduced, ‘D peak’ which indicates the presence of sp^3 carbon and is indicative of defects.¹¹³ It is common to all these studies that little attempt was made to separate the response of the defects from that of the pristine CNT. The conclusion that ET is driven by defects was driven by analysis of the voltammetry alone.

The most convincing evidence that electrochemistry at SWNT electrodes is not solely driven by defects and open ends comes from studies of individual SWNT on insulating substrates. This resolution has been achieved either by the

isolation of SWNT onto a surface through low density or aligned growth^{47, 98} or through the use of nano-scale scanning electrochemical methods.⁹⁷ The work of *Dekker et al.*⁴⁷ demonstrated that the isolated sidewalls of SWNT, i.e. no tube ends exposed to solution, are extremely active for ET, displaying steady state voltammetric currents proportional to the length of SWNT sidewall exposed (Figure 1.14 (a)). The same high ET activity was found when individual SWNT were investigated using scanning electrochemical microscopy (SECM), where a ultramicroelectrode (UME) was scanned at a constant height above a surface, measuring the redox activity at different points. An SEM image and the corresponding plot of electrochemical activity of a single SWNT is displayed in Figure 1.14 (b) and shows that there is consistent electrochemical activity along a 40 μm length of the SWNT sidewall, suggesting that the activity is not driven at point defects.⁹⁸

*Güell et al.*⁹⁷ also utilised scanned electrochemical methodology using the double barrelled scanned capillary technique, scanning electrochemical cell microscopy (SECCM) which has a meniscus contact area ca. 250 nm, to investigate ET at well characterised 2D SWNT network electrodes. Again ET was shown to be facile across the whole SWNT sidewall, and at closed ends. This was supported by finite element simulations which estimated the current profile as the meniscus was scanned across a SWNT, these showed that the experimental current profile could not be explained even through a high density of point defects. There have also been many other reports that now suggest that the pristine sidewalls of SWNT are electrochemically active.^{52, 96, 114, 115}

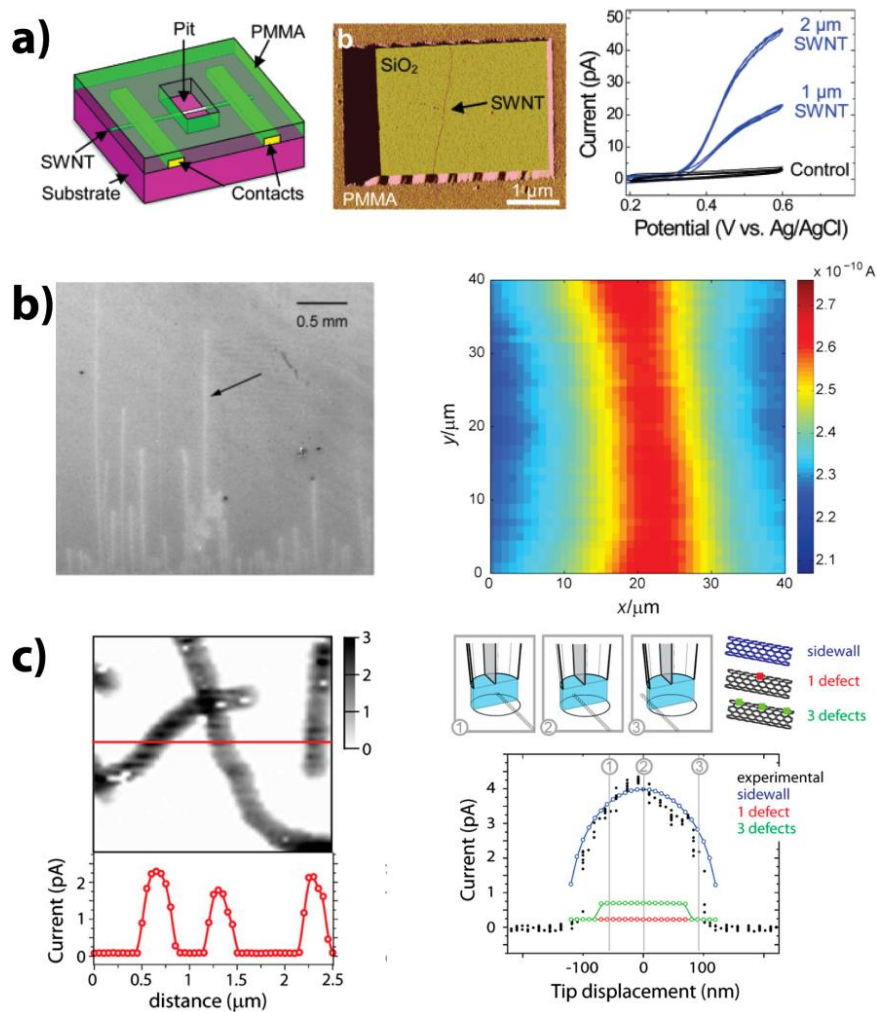


Figure 1.14 – a) Schematic and AFM image of single SWNT electrode. CVs for the oxidation of FcTMA^+ at different lengths of SWNT sidewall.⁴⁷ b) SEM image of aligned SWNT and SECM image of the SWNT indicated by the arrow. Colour scale represents redox current.⁹⁸ c) SECCM image of a 2D SWNT network and corresponding line scan, greyscale represents redox current. Finite element simulation of the current profile as a SECCM tip is scanned across a SWNT where: the whole sidewall (blue); a single defect (red); 3 defects (green); are responsible for ET, real data shown as black dots.⁹⁷

1.5 Modification of CNTs for electrochemistry

1.5.1 Chemical, physical and electrochemical routes

During purification procedures, modification of the surface is often an uncontrolled process, however through controlled chemical and electrochemical treatments it is possible to deliberately modify (or functionalise) the CNT surface in order to promote certain electrochemical reactions. It is well-known that many redox processes need to bind to a surface in order for efficient ET to occur; such ET processes are referred to as ‘inner sphere’ processes.⁸¹ $\pi - \pi^*$ interactions will be promoted on the pristine sp^2 surface but for many inner sphere couples these are not sufficient. Functional groups can be introduced onto the surface in a variety of ways, such as by controlled acid treatments,¹⁵ exposure to an oxygen plasma¹⁵ or electrochemical oxidation at high positive potentials.^{116, 117} These are common literature methods to introduce oxygen containing groups, known to promote many inner sphere reactions.¹¹⁸ Functionalisation using these methods has been shown to promote the oxidation of dopamine,¹⁵ NADH^{116, 117}, hydrazine¹¹⁶ and ascorbic acid.¹¹⁷

1.5.2 Modification with metal NPs

The modification of CNT structures with metal NPs is another well-explored research area.¹¹⁹ NPs have been deposited by chemical (e.g. reduction of metal salts^{120, 121}), physical (e.g. dispersal of pre-formed NPs¹²²) and electrochemical (e.g. electrodeposition from metal salts¹²³⁻¹²⁵) methods onto a variety of CNT structures, including 2D networks,^{123, 125, 126} single SWNTs^{70, 114, 124} and CNTs deposited by drop casting.^{121, 127} Although the preparation of CNT-

NP composite materials by chemical and physical methods is as attractive synthesis route, with this methodology there is little control over the NP distribution through the CNT structure (i.e. NPs can easily cluster together, reducing activity). Also the NPs pre-synthesised then immobilised on the CNTs are often functionalised with stabilising ligands from synthesis¹²⁸ which can adversely affect ET if not chosen carefully.¹²⁹

Electrodeposition is a powerful technique for the synthesis of NPs as it allows control over both the nucleation and subsequent growth of NPs of many metals,^{70, 123} including Pt,^{123, 125, 130} Pd,^{125, 130, 131} Ag^{15, 52, 123} and Au.^{126, 130, 132} Through variation of the deposition overpotential and time (or number of deposition cycles when depositing by CV) it is possible to control the size and distribution of NPs. This effect was shown by *Dekker et al.*¹³⁰ who controlled the size and distribution of Au, Pt and Pd NPs on SWNT by controlling the deposition potential, time and metal salt concentration. This allowed them to grow structures ranging from isolated NP to nanowires. By using a very low deposition overpotential (< 70 mV) *Collins et al.*⁷⁰ were able to selectively electrodeposit Ni at defects along the sidewalls of SWNT, whereas when higher overpotentials were employed non-selective deposition along the entire sidewall occurred.

Despite the control gained through electrodeposition, the understanding of the nucleation and growth of NPs on CNTs is still rather limited. As described above, it has been shown that NPs preferentially nucleate at defect sites at low overpotentials,⁷⁰ but a small increase in overpotential overcomes this preference. The nature of the metal being deposited,¹²⁵ the nature of the diffusional

overlap,¹²⁶ potential drop effects¹²³ and driving potential^{70, 126} have all shown to affect electrodeposition.

1.6 The use of CNTs for electrocatalysis

1.6.1 CNTs for the promotion of the oxygen reduction reaction (ORR)

The electrocatalytic reduction of oxygen is of vital importance for research into ‘clean energy’ as the oxygen reduction reaction (ORR) occurs at the cathode of most common fuel cells. Unfortunately, the kinetics of the ORR are usually slow, meaning a catalyst material is required to make fuel cells effective. Traditional ORR catalysts are based on Pt,¹³³ but these are expensive, meaning there has been a significant drive to find more viable alternatives.

The ORR itself is a complicated process involving the transfer of 4-electrons and the reaction has many intermediates. The nature of the reduction also depends heavily on the pH of the electrolyte and can occur by either a direct 4e⁻ transfer or two subsequent 2e⁻ transfer steps. The different routes are summarised in Table 1.1.

Electrolyte	Oxygen reduction reaction	E ₀ vs. NHE (V)
Acidic	$O_2 + 4H^+ + 4e^- \rightarrow 2H_2O$	1.23
	$O_2 + 2H^+ + 2e^- \rightarrow H_2O_2$	0.70
	Followed by either:	
	a) $H_2O_2 + 2H^+ + 2e^- \rightarrow 2H_2O$ b) $2H_2O_2 \rightarrow 2H_2O + O_2$	1.77
Alkaline	$O_2 + 2H_2O + 4e^- \rightarrow 4OH^-$	0.40
	$O_2 + H_2O + 2e^- \rightarrow HO_2^- + OH^-$	-0.065
	Followed by either:	
	a) $HO_2^- + H_2O + 2e^- \rightarrow 3OH^-$ b) $2HO_2^- \rightarrow 2OH^- + O_2$	0.867

Table 1.1 – Summary of the various pathways for the ORR.¹³⁴

CNTs have been utilised extensively in fuel cell catalyst research and have been investigated as both a novel support material for traditional ORR catalysts (commonly Pt NPs) and as a potential replacement for traditional metal catalysts entirely.

Bulk Pt ORR catalysts are not viable for commercial application in fuel cells primarily due to their incredible cost, which has led to the development of catalysts based on Pt NPs supported on a cheaper electrode material, most commonly carbon.¹³⁵ These electrode materials are effective, but are prone to time-dependant drift¹³⁶ and deactivation through poisoning¹³⁷ which can severely reduce efficiency. They also require high catalyst loadings ($0.8 - 8 \text{ mg}_{Pt} \text{ cm}^{-2}$).¹³⁸

The electrical conductivity, corrosion-resistance and very high specific surface area of CNTs make them an interesting catalytic Pt support material.¹³⁸ There have been multiple reports demonstrating the benefits of CNT supports over other carbon alternatives for the ORR,^{122, 128, 139-142} boasting lower ORR onset potentials, increased stability and higher catalytic activity. These improvements have largely been attributed to the beneficial structure of the CNT supports used for compositing with Pt and Pt alloys, increasing catalytic activity. For example *Kamat et al.*¹²² attributed the increased rate constant for ORR at Pt/SWNT electrodes, over commercial Pt/C electrodes, to the porosity of the SWNT structure, which allowed increased diffusion and facilitated an increased interaction with the Pt NPs. As these composite materials only utilise the Pt at relatively high loadings for catalysis, they usually proceed via the 4-electron reduction route as at high loadings the diffusion fields of individual NPs overlap meaning it is less likely for intermediates to escape into the bulk.¹²⁹

Although the use of CNTs as ORR catalyst supports is interesting as it reduces the amount of Pt required for effective catalysis, it would be of greater benefit to produce an ORR catalyst that does not require any expensive materials and is made from readily available elements, e.g. carbon. Pristine sp^2 carbon materials, including CNTs, are poor catalysts for the ORR as the lack of functional groups does not encourage adsorption and fast ET.¹⁴³ The most common method used to activate CNTs towards the ORR is to dope them with electron density withdrawing dopants, usually nitrogen. It was initially suggested that the introduction of NH_3 into the CVD synthesis of MWNT forests created FeN_2-C and/or FeN_4-C sites by combination with Fe catalyst NPs, which catalysed the ORR.¹⁴⁴ However, it was then demonstrated that the ORR was

catalysed at nitrogen doped MWNT forests where all metal residues had been removed Figure 1.15.¹⁴⁵

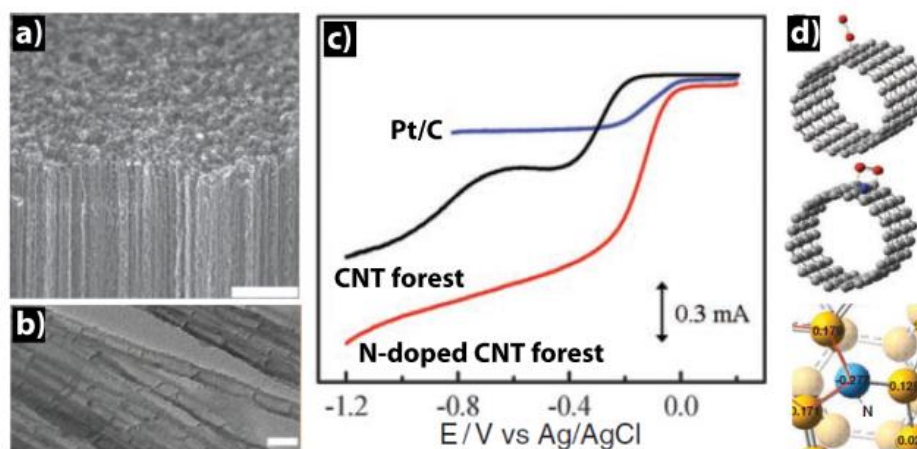


Figure 1.15 – a) SEM and b) TEM images of metal free N-doped MWNT forest. c) Comparison of the linear sweep voltammetry (LSV) of a commercial Pt/C electrode, an undoped MWNT forest and an N-doped forest. d) Schematic of the O_2 binding at an undoped CNT (top) and an N-doped CNT (middle), charge density at an N-doped site (bottom).¹⁴⁵

It was shown by Dai *et al.*¹⁴⁵ that metal free N-doped MWNTs acted as very efficient catalysts for the direct 4-electron ORR, performing better than a commercial Pt/carbon electrode, with lower onset overpotential and increased current density. The catalytic activity of this structure was attributed to the electron withdrawing nature of the N-dopants, which caused the adjacent carbon atoms to display a higher positive charge density. It was claimed this effect changed the mode of adsorption for O_2 , which weakened the O-O bond. The undoped MWNT forests in this study were also shown to catalyse the two step, 2-electron ORR, as usual for ordinary carbon electrodes.¹³⁴ However, as pristine sp^2 materials are not usually good ORR catalysts¹⁴⁶ this is likely due to high defect density or contamination from amorphous material. Since this report there

has been intense interest in doping CNT and other carbon materials for ORR catalysis.¹⁴⁷⁻¹⁵³

The creation of ORR active sites through the withdrawal of electron density has also been displayed by intermolecular charge transfer from CNTs to certain electrolytes.¹⁵⁴ By adsorbing electron-withdrawing molecules, for example poly(di-allyldimethylammonium chloride),¹⁵⁴ onto CNT forests it was shown that metal free ORR catalysis was promoted, creating a material that performed comparably (although slightly less effectively) to a commercial Pt/C catalyst and significantly better than untreated CNTs.

Although much work has been done to investigate ORR catalysis using modified CNTs, reports concerning the intrinsic ORR catalysis capabilities of undoped CNTs have utilised low quality or acid cleaned CNTs with high defect densities.¹⁵⁵⁻¹⁵⁸ This has meant the activation of CNTs towards the ORR in a controlled way has not been satisfactorily investigated. It has been shown that the presence of oxygen functionalities on CNTs promotes ORR catalysis¹⁵⁵ however, the use of glassy carbon support electrodes and highly defected CNTs complicated analysis.

1.6.2 CNTs for promotion of the methanol oxidation reaction (MOR)

Like the ORR, understanding of the methanol oxidation reaction (MOR) is vitally important for fuel cell research.¹³⁵ The MOR is a complicated inner sphere reaction with multiple possible pathways¹⁵⁹ (Figure 1.16) which should occur thermodynamically at low potentials (0.016 V vs. SHE¹⁶⁰), however does not occur experimentally on a Pt electrode until much higher potentials are

applied (ca. 0.5 V vs. SHE), as the oxidation kinetics are very slow.¹⁶⁰ The MOR can proceed by two pathways, one with formaldehyde and formic acid intermediates and one with adsorbed CO as an intermediate. As the oxidation of CO to CO₂ requires high overpotentials the formic acid route is generally favoured (direct pathway) and CO_{ads} is considered to be a poison to catalytic activity.^{160, 161}

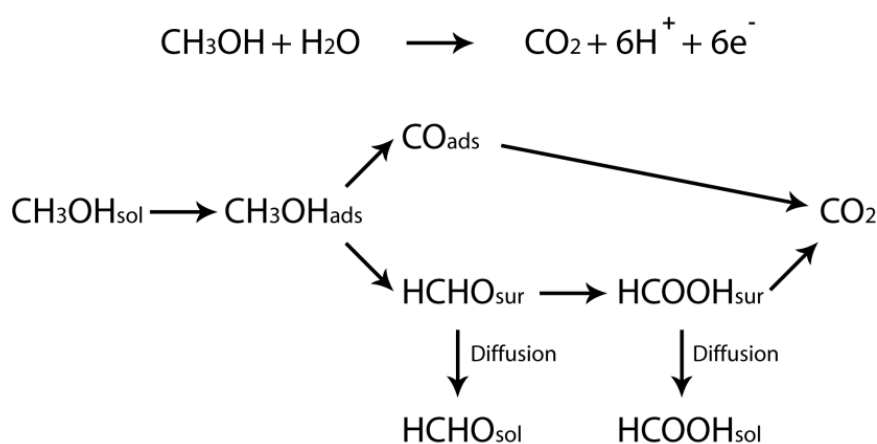


Figure 1.16 – Summary of the major processes involved in the methanol oxidation reaction (MOR), adapted from Baltruschat *et al.*¹⁵⁹

Pristine CNTs are ineffective as MOR catalysts as the reaction requires adsorption sites for the many reaction intermediates, which are not supplied by the sp² structure. As with the ORR, the MOR is traditionally catalysed by precious metal catalysts (most commonly Pt), supported on cheaper electrode materials, meaning CNT supports have been investigated as supports for similar reasons as for Pt ORR catalysts (conductivity, corrosion-resistance, high specific surface area). Unfortunately, as the MOR creates its own catalyst poison, the catalysts used are more susceptible to poisoning than ORR catalysts.¹³⁵

CNT supported Pt MOR catalysts have demonstrated significant enhancement of Pt catalytic activity.^{140,162-166} Vertically aligned MWNT synthesised CVD and

implanted with Pt NPs via chemical synthesis were shown by *Fisher et al.*¹⁶² to have a current density 20 times greater than a bulk Pt catalyst for the MOR, demonstrating significant enhancement of electrocatalytic activity. SWNT supported Pt NPs have also been shown to enhance activity (10 times higher than when the same amount of Pt is deposited on a planar electrode) towards the MOR¹⁴⁰ reducing the necessary overpotential by 200 mV. The enhanced MOR capacity was attributed to an inhibition of CO poisoning. Analogously to the use of CNTs as ORR catalysts, it has also been suggested that nitrogen-doped CNTs act as superior Pt NP supports for the MOR¹⁶⁵ demonstrating a reduced overpotential and 10 times the catalytic activity of a commercial Pt electrode. The authors claim the nitrogen containing groups decrease the electron density of the Pt, promoting MOR catalysis, however, no comparison is made to undoped CNTs.

1.7 Graphene

1.7.1 The structure of graphene

The physical structure of single layer graphene (SLG) consists of a one atom thin sheet of carbon atoms bonded in a sp^2 lattice, making it a truly two-dimensional material. The atomic structure has been confirmed by both STM¹⁶⁷ and high resolution TEM^{168, 169} (Figure 1.17). Bi-layer graphene (BLG) and few-layer graphene (< 10 graphene sheets) are also commonly referred to as graphene materials.¹⁷⁰ As with CNTs, the pristine graphene structure can be interrupted by the presence of defects, especially at the boundaries between graphene grains,

where hexagon or pentagon rings (Figure 1.17 (d)), vacancies, functional groups and adsorbed impurities can be incorporated.¹⁷¹

The electronic structure of SLG had been considered as the theoretical starting point for the electronic structure of CNTs, consisting of a σ bonded lattice with a delocalised network of electrons formed by the carbon π bonds. However, unlike the electronic structure of CNTs there is no interruption of lattice symmetry (due to curving of the sheet) meaning SLG acts as a semi-metal (or zero band gap semiconductor).¹⁷²

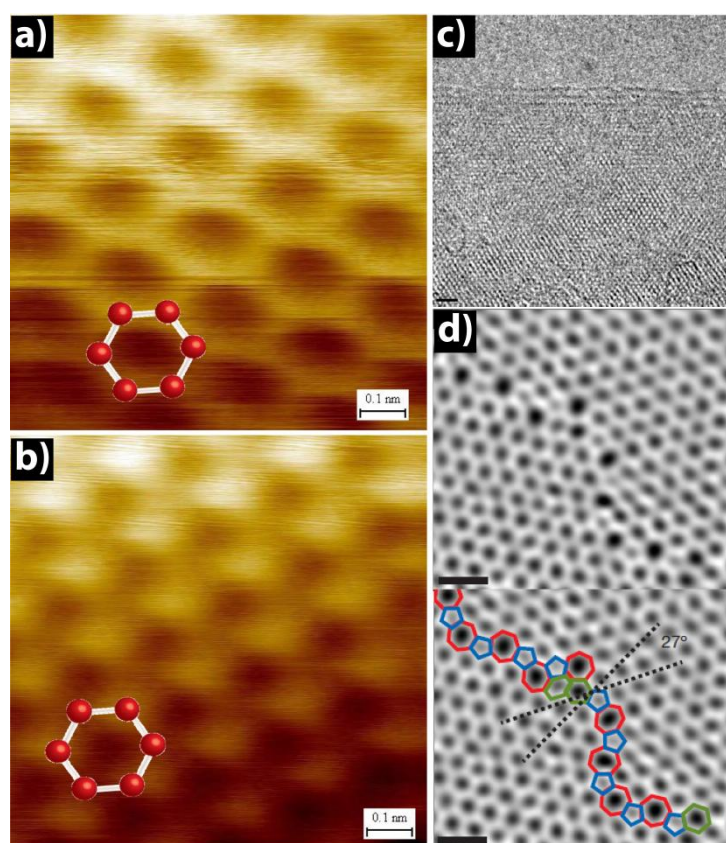


Figure 1.17 – a) STM image of single layer graphene, b) STM image of multi layer graphene.¹⁶⁷
c) TEM image of few (2 to 4) layer graphene showing graphene edges.¹⁶⁸ d) TEM image of single layer graphene showing grain boundary between two distinct flakes.¹⁶⁹

1.7.2 Graphene synthesis

There are three primary routes to the synthesis of graphene, namely mechanical exfoliation, chemical exfoliation methods and cCVD (including epitaxial growth).¹⁷³ Mechanical cleavage is the most widely known method of graphene preparation due to the enormous attention given to the isolation of free standing graphene by *Geim* and *Novoselov*.^{174, 175} This methodology incorporates a series of techniques that are simple in concept and have been shown to produce high quality graphene.¹⁷⁶ Examples of mechanical exfoliation methods include the repeated peeling of graphite with adhesive tape until a single graphene sheet remains¹⁷⁴ or the rubbing of graphite against a hard surface.¹⁷⁵ However, as these methods struggle to produce areas over 500 μm^2 and certainly not on the cm scale, their use is realistically limited to research only.

Although several chemical exfoliation routes for graphene production have been shown, by far the most common is the use of graphene from graphite oxide.¹⁷³ This is a complex multi stage process which begins with the oxidation of graphite with strong oxidants, which significantly disrupts the sp^2 lattice introducing a range of functional groups, rendering the individual graphene oxide sheets hydrophilic. Sonication in water fully exfoliates the graphite oxide, leaving a suspension of graphene oxide sheets. Due to the level of lattice disruption, graphite oxide is insulating, however chemical reduction restores conductivity to the graphene.¹⁷³ This method provides an effective means to create bulk quantities of graphene but unfortunately the graphene produced is not pristine and, despite reduction, is functionalised with oxygen containing functional groups.^{177, 178}

The use of cCVD using bulk metal catalysts (evaporated layers or foils) allows the growth of large areas of pristine graphene with a low defect density. Early reports utilised polycrystalline Ni catalysts,¹⁷⁹⁻¹⁸¹ but the graphene produced consisted of small grains with multi layers at the grain boundaries.¹⁸¹ This is in part because Ni catalyses graphene growth by an absorption-precipitation mechanism, where carbon absorbs into the bulk Ni and precipitates out on cooling.¹⁸² With this mode of growth it is difficult to control layer thickness, often resulting in multi-layered structures.^{180, 181} By using Cu foil as a catalyst *Ruoff et al*¹⁸³ were able to synthesise large area (1 cm²) graphene which was predominantly single layer (Figure 1.18 (a, b)). These structures grew continuously across steps and grain boundaries without an increase in the number of layers. This is possible as on Cu growth occurs by a self limiting surface catalysed process. This effect was subsequently reproduced by many others.^{184,}

185

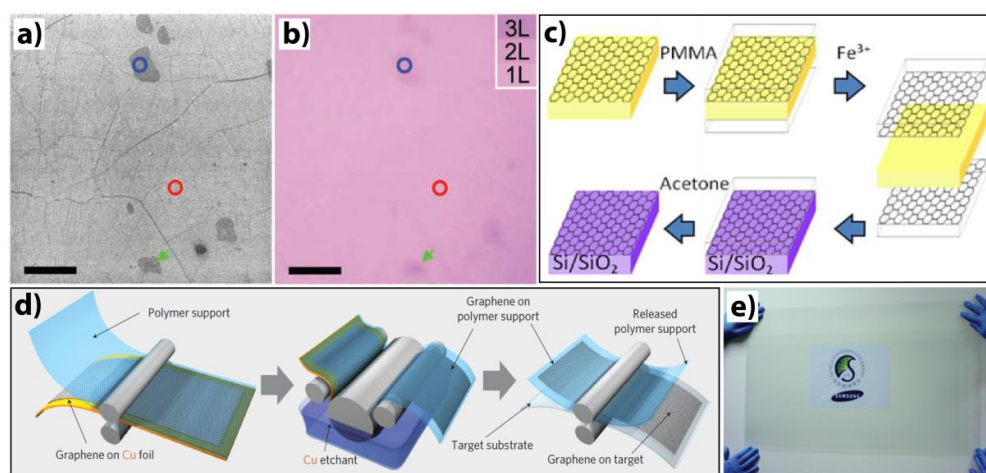


Figure 1.18 – CVD graphene: a) SEM and b) optical image of single- (red circle), bi- (blue circle) and few-layer (green arrow) cCVD grown graphene on Si/SiO₂.¹⁸³ c) Representative transfer process of graphene from metal catalyst to Si/SiO₂.¹⁸² d) Transfer process for large area (35 inches diagonal length) graphene onto polymer supports e) 30 inch diagonal length (predominantly single layer) graphene sheet on polyethylene terephthalate (PET).¹⁸⁶

Although growth of graphene on metal substrates is effective, for most applications it is necessary to have graphene on an insulating support, meaning the graphene must be transferred. This commonly involves supporting the graphene with a polymer film while the metal underlayer is dissolved, transferring the graphene/polymer onto the insulating substrate and dissolving the polymer away, a schematic of which is shown in Figure 1.18 (b).^{182, 187} Unfortunately this process can easily damage and contaminate the graphene. Transferred graphene is commonly heavily contaminated with residues left from the PMMA or other polymer supports (e.g. polycarbonate, PC) used to support it during transfer^{188, 189} despite lengthy dissolution in organic solvents. This is because strong dipole interactions between the poly(methyl methacrylate) (PMMA) and graphene surface are hard to overcome.¹⁹⁰ Furthermore dissolution, solvent rinsing¹⁸⁸ and poor interaction between the graphene and insulating substrate^{183, 189} can cause the graphene to rip and tear during the transfer process. This contamination is an especially significant problem when the graphene is to be used for electrochemical applications, including fundamental understanding, as blocked electrode surfaces and thin surface layers are known to adversely affect ET.^{118, 143, 191}

Another issue with transferred CVD graphene is that it has the tendency to ‘wrinkle’ on the surface post transfer. This has been shown to be caused by two effects, the first being that graphene contracts to a lesser extent than its metal catalyst during post CVD cooling, i.e. thermal relaxation.¹⁹² This causes the graphene to corrugate on the metal surface even before transfer. Wrinkling is also caused because graphene grows across the entire metal catalysts surface. As this surface tends to have a degree of roughness a larger area of graphene grows

than the geometric area of the catalyst. When this graphene is transferred to an insulating substrate and the supporting polymer is dissolved, the graphene folds up, causing wrinkles.¹⁹³ It has been shown previously that wrinkles formed in mechanically exfoliated SLG have lower electrical conductance than other graphene regions.¹⁹⁴ It is therefore likely that these similar wrinkles in CVD grown graphene also effect the electrical properties of graphene.

Despite these challenges, *Ahn et al.*¹⁸⁶ have developed a method for the preparation and transfer of CVD grown SLG, with a diagonal cross sectional length of 30 inches (Figure 1.18 (d and e)), onto a transparent polymer. However, this method is also considered to contaminate graphene with residues from the thermal release tape used¹⁸⁸ and introduces defects into the graphene structure.¹⁹⁵

1.7.3 Graphene characterisation

Although TEM and STM are useful techniques for the characterisation of the atomic structure of graphene, they are not trivial to perform and are therefore less useful for routine graphene characterisation. Like CNTs, graphene exhibits a unique micro-Raman spectrum and can also be studied by AFM. It has also been found that when graphene sits on Si with specific SiO₂ thickness optical microscopy can be used to differentiate between SLG, BLG and FLG (Figure 1.19).^{176, 196}

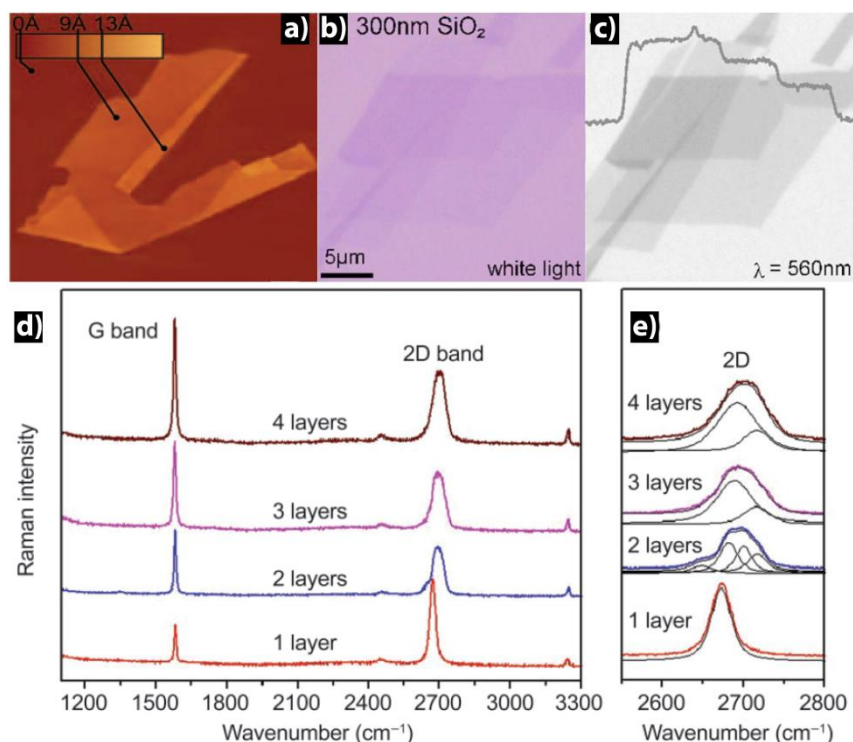


Figure 1.19 – Graphene characterisation: a) AFM image of mechanically exfoliated graphene, SLG height is ca. 4 Å.¹⁷⁵ Optical microscopy images of graphene on Si with a 300 nm thick oxide layer, images with white (b) and green (c) light.¹⁹⁶ Micro-Raman spectroscopy of graphene 1 to 4 layers thick (d) with a magnification of the 2D region (e) showing the peak splitting due to layer stacking.¹⁹⁷

The ability to resolve the difference between numbers of graphene layers by optical microscopy was vital to the initial isolation of this material, as it allowed the fast interrogation of mechanically exfoliated samples.¹⁷⁶ This is possible as graphene is optically transparent enough to allow transmission of light, resulting in a slight interference causing a layer dependent shift in colour. It is even possible to differentiate between SLG and BLG.^{174, 176, 196} This effect is heavily dependent on the thickness of oxide on the Si, for a fixed wavelength light source it was shown that a 5 % change in layer thickness (315 nm rather than the standard thickness of 300 nm) rendered SLG totally invisible.¹⁷⁴ This work was expanded to show that a combination of the oxide thickness and

wavelength of the incident light determined the graphene contrast, with green ($\lambda = 560$ nm) light producing the best contrast on Si with 300 nm oxide and blue ($\lambda = 410$ nm) light best for 200 nm thick oxides (Figure 1.19 b & c).¹⁹⁶

A micro-Raman spectrum of graphene shows the same characteristic peaks as other graphitic materials, including HOPG and CNTs. The only first order Raman process in the graphene micro-Raman spectrum is the G peak (~ 1580 cm^{-1}) caused by in-plane sp^2 lattice vibrations. Both the 2D peak (also known as G', ~ 2700 cm^{-1}) and the D peak (~ 1350 cm^{-1}) are second order Raman processes. However, the process which causes the D peak involves a lattice defect and is therefore indicative of disorder; the 2D peak is not indicative of defects and is present in pristine sp^2 structures.^{172, 198} It was quickly realised after the isolation of SLG that the shape and position of these peaks, particularly the intensity ratio of the G and 2D peaks and the breadth and position of the 2D peak, could identify the number of graphene layers.¹⁹⁸

Ferrari et al. performed micro-Raman spectroscopy on mechanically exfoliated SLG, MLG and FLG, which was characterised by TEM, and determined the difference in their spectra. They first showed there was no D peak when spectra were taken at the centre of flakes, only appearing when edges were investigated. This indicated the graphene was of very high quality and had very few defects. Furthermore, they showed that the 2D peak dramatically changes in shape and intensity with increasing number of graphene layers. In multi-layered graphene this peak is made up of multiple, less intense, peaks in the same region due to interactions between layers. SLG showed a single and sharp 2D peak, which was ca. 4 times as intense as the G peak, occurring below 2700 cm^{-1} (514 and 633 nm wavelength laser). BLG has a much broader, up-shifted (to ca. 2700

cm⁻¹) and less intense 2D peak. Above 5 graphene layers the micro-Raman spectra became difficult to distinguish from bulk graphite.¹⁹⁸ This analysis was later confirmed by others (Figure 1.19 d & e).^{172, 197}

1.7.4 Graphene electrochemistry

The use of SLG as an electrode material is still in its infancy, however, there is on-going debate over its fundamental electrochemical properties, originating from the discrepancies in interpretation of data from the of HOPG and CNTs electrochemical studies. Using both mechanically exfoliated and CVD synthesised graphene *Abruna et al.*¹⁹⁹ investigated the voltammetric response of FcMeOH. They found the current response directly scaled with electrode area and determined a k_0 of 0.5 cm s⁻¹ for the mechanically exfoliated sample by interpretation of CVs at different scan rates. This value was two orders of magnitude higher than the value they found at the basal plane of freshly cleaved bulk basal plane graphite using the same methodology. The authors attribute this increased activity to corrugations in the graphene surface, which activate the surface due to strain, although little evidence for this is shown. *Dryfe et al.*²⁰⁰ also investigated ET at mechanically exfoliated SLG and BLG, but fully insulated the edges of the samples, leaving only basal planes exposed. Using the Fe(CN)₆^{3-/4-} couple they found quasi-reversible behaviour on both SLG and BLG however they found k_0 to be higher with SLG (1.2×10^{-3} cm s⁻¹) which was twice that found for a defected multilayer graphite. They also showed that defects in the SLG did not improve the voltammetric response.

Conversely, *Banks et al.*²⁰¹ found, using voltammetry, that the electrochemistry of CVD grown graphene investigated while still on the

polycrystalline Ni surface, to be dominated by graphitic ‘islands’ on the graphene surface, i.e. multilayer structures. It is claimed that the ‘basal surface’ of these structures are relatively inert with ET only occurring at defects and edge planes. Similarly *Pumera et al.*²⁰² found CVD grown (on Ni) multilayer graphene transferred to polymer showed slow ET ($k_0 = 5.3 \times 10^{-3} \text{ cm s}^{-1}$, $\text{Ru}(\text{NH}_3)_6^{2+/3+}$), more than an order of magnitude slower than to BPPG. However, when SECCM was performed, using $\text{FcTMA}^{+/2+}$, on very similar structures transferred onto Si/SiO₂ by *Güell et al.*²⁰³ ET was shown to occur uniformly over graphene flakes, not just at edges. They did however, find that the rate of ET was slower on SLG ($k_0 \sim 0.15 \text{ cm s}^{-1}$) increasing with number of layers (4 layers $k_0 \sim 0.25 \text{ cm s}^{-1}$) and becoming essentially reversible (> 7 layers $k_0 \sim 0.55 \text{ cm s}^{-1}$).

It is clear from these early studies that consensus on the ET characteristics of graphene has not yet been reached. Studies using CVD grown graphene currently cause the greatest disagreement,²⁰¹⁻²⁰³ possibly due to problems with growth and transfer contaminating the samples. When mechanically exfoliated samples are studied relatively fast ET is found.^{199, 200}

1.8 Aims and objectives

As detailed in this introductory chapter, carbon nanomaterials have huge potential for electrochemical applications, but their eventual performance depends heavily on their careful preparation and characterisation.

Although there is increasing acceptance of the fundamental electrochemical activity of SWNTs (even at closed ends and sidewalls), the majority of reports regarding electrochemistry and electrochemical applications of SWNT are still based around the premise that CNTs are only active at defects and open ends. It

is therefore essential that experiments are performed on pristine SWNT which have been carefully synthesised and fully characterised, to first fully elucidate the inherent electrochemical activity of this material and then apply this knowledge to industrially relevant problems (e.g. catalysis). Analogously, as the ‘graphene revolution’ is still in its early stages, it is also essential that the electrochemical activity of this material is researched with the same rigorous procedures; and materials are carefully characterised in order to interpret the resulting electrochemical behaviour.

The most fundamental aim of this thesis is the synthesis by cCVD of carbon nanomaterials, namely SWNT and graphene, discussed in Chapter 3. Preparation by cCVD has many advantages over other techniques, producing high quality structures in quantities that are applicable to both research and industry with great control. The structures produced are characterised using a range of techniques including optical, electron and scanning probe microscopy, which are complemented by spectroscopic techniques meaning any electrochemical conclusions that are drawn in later work are based on an excellent understanding of the graphitic structure.

The fundamental electrochemical activity of vertically aligned SWNT forests is investigated (Chapter 4) using a nano-scale capillary technique which will allow the separation of the SWNT ends and sidewalls to be probed separately. This method negates the need for any post growth sample processing, e.g. lithography, meaning the SWNT are in the as grown pristine state. Studies in this chapter focus on the use of fast electron transfer outer sphere redox couples ($\text{Ru}(\text{NH}_3)_6^{3+/2+}$ and $\text{FcTMA}^{+/2+}$).

The next two chapters utilise the knowledge gained about the electrochemical properties of SWNT with the aim of investigating electrocatalytic reactions, specifically the ORR and MOR which are both inner sphere redox processes. In Chapter 5 the activation of SWNT forests towards the ORR and a series of other complex processes, through the systematic application of electrochemical pre-treatment at anodic potentials, is discussed. This work provides insight into the effect of defect creation, which is demonstrated using micro-Raman spectroscopy, has on mediators where the electrode surface chemistry is important. The use of structurally pristine SWNT, rather than those that have been purified, provides a significantly improved baseline over previous studies.

In Chapter 6 2D SWNT networks are used as templates for the electrodeposition of Pt NPs, which are then used as catalysts for the ORR and MOR. As Pt is an incredibly expensive catalyst material it is necessary to utilise it to its fullest, meaning no more than is absolutely necessary should be used. Through the use of microcapillary based electrodeposition the optimal Pt loading for each reaction is investigated, taking advantage of the unique properties of the SWNT network.

Finally, in Chapter 7 the microcapillary electrochemical method is adapted to allow generation/collection electrochemical measurements to be performed. By using high aspect ratio carbon fibre ultramicroelectrodes as a second working electrode, within the meniscus formed by the capillary, this work aims to demonstrate a simple, yet versatile technique for the investigation of complex surfaces and processes.

1.9 References

1. S. Iijima, *Nature*, 1991, **354**, 56-58.
2. S. Iijima and T. Ichihashi, *Nature*, 1993, **363**, 603-605.
3. E. Heister, E. W. Brunner, G. R. Dieckmann, I. Jurewicz and A. B. Dalton, *ACS Appl. Mater Interfaces*, 2013, **5**, 1870-1891.
4. S. J. Tans, A. R. M. Verschueren and C. Dekker, *Nature*, 1998, **393**, 49-52.
5. R. H. Baughman, A. A. Zakhidov and W. A. de Heer, *Science*, 2002, **297**, 787-792.
6. J. Giles, *Nature*, 2006, **441**, 265-265.
7. R. Saito, G. Dresselhaus and M. S. Dresselhaus, *Physical properties of carbon nanotubes*, Imperial College Press, London, 2004.
8. H. Dai, *Surf. Sci.*, 2002, **500**, 218-241.
9. M. Ge and K. Sattler, *Science*, 1993, **260**, 515-518.
10. T. W. Odom, J.-L. Huang, P. Kim and C. M. Lieber, *Nature*, 1998, **391**, 62-64.
11. J. W. G. Wilder, L. C. Venema, A. G. Rinzler, R. E. Smalley and C. Dekker, *Nature*, 1998, **391**, 59-62.
12. T. Nobuo, Y. Jun, K. Tomoyuki and P. Huayong, *Nanotechnology*, 2004, **15**, 1779.
13. J. C. Charlier, *Acc. Chem. Res.*, 2002, **35**, 1063-1069.
14. C. E. Banks and R. G. Compton, *Analyst*, 2006, **131**, 15-21.
15. I. Dumitrescu, N. R. Wilson and J. V. Macpherson, *J. Phys. Chem. C*, 2007, **111**, 12944-12953.
16. J. W. Mintmire and C. T. White, *Phys. Rev. Lett.*, 1998, **81**, 2506-2509.
17. T. W. Ebbesen and P. M. Ajayan, *Nature*, 1992, **358**, 220-222.
18. T. W. Ebbesen, H. Hiura, J. Fujita, Y. Ochiai, S. Matsui and K. Tanigaki, *Chem. Phys. Lett.*, 1993, **209**, 83-90.
19. S. Seraphin, D. Zhou, J. Jiao, J. C. Withers and R. Loutfy, *Carbon*, 1993, **31**, 685-689.
20. Y.-H. Wang, S.-C. Chiu, K.-M. Lin and Y.-Y. Li, *Carbon*, 2004, **42**, 2535-2541.
21. S. Iijima, *Mater. Sci. Eng. B.*, 1993, **19**, 172-180.
22. H. Hiura, T. W. Ebbesen and K. Tanigaki, *Adv. Mater.*, 1995, **7**, 275-276.
23. T. Guo, P. Nikolaev, A. G. Rinzler, D. Tomanek, D. T. Colbert and R. E. Smalley, *J. Phys. Chem-US*, 1995, **99**, 10694-10697.
24. T. Guo, P. Nikolaev, A. Thess, D. T. Colbert and R. E. Smalley, *Chem. Phys. Lett.*, 1995, **243**, 49-54.
25. D. M. Guldi and M. Nazario, *Carbon nanotubes and related structures synthesis, characterization, functionalization and applications*, WILEY-VCH Verlag GmbH & Co., Weinheim, 2010.
26. A. Thess, R. Lee, P. Nikolaev, H. Dai, P. Petit, J. Robert, C. Xu, Y. H. Lee, S. G. Kim, A. G. Rinzler, D. T. Colbert, G. E. Scuseria, D. Tománek, J. E. Fischer and R. E. Smalley, *Science*, 1996, **273**, 483-487.
27. L. A. Montoro and J. M. Rosolen, *Carbon*, 2006, **44**, 3293-3301.
28. J.-M. Moon, K. H. An, Y. H. Lee, Y. S. Park, D. J. Bae and G.-S. Park, *J. Phys. Chem. B*, 2001, **105**, 5677-5681.

29. K. R. Moonosawmy and P. Kruse, *J. Am. Chem. Soc.*, 2008, **130**, 13417-13424.
30. L. Yu, Z. Xiaobin, L. Junhang, H. Wanzhen, C. Jipeng, L. Zhiqiang, L. Ting, L. Fu, X. Guoliang, K. Xiaoxing, L. Lin and J. G. Herman, *Nanotechnology*, 2004, **15**, 1645.
31. J. Liu, A. G. Rinzler, H. Dai, J. H. Hafner, R. K. Bradley, P. J. Boul, A. Lu, T. Iverson, K. Shelimov, C. B. Huffman, F. Rodriguez-Macias, Y.-S. Shon, T. R. Lee, D. T. Colbert and R. E. Smalley, *Science*, 1998, **280**, 1253-1256.
32. A. Kuznetsova, I. Popova, J. T. Yates, M. J. Bronikowski, C. B. Huffman, J. Liu, R. E. Smalley, H. H. Hwu and J. G. Chen, *J. Am. Chem. Soc.*, 2001, **123**, 10699-10704.
33. V. Ivanov, J. B. Nagy, P. Lambin, A. Lucas, X. B. Zhang, X. F. Zhang, D. Bernaerts, G. Van Tendeloo, S. Amelinckx and J. Van Landuyt, *Chem. Phys. Lett.*, 1994, **223**, 329-335.
34. M. Meyyappan, *Carbon nanotubes Science and applications*, CRC press, USA, 2005.
35. M. Jose-Yacaman, M. Miki-Yoshida, L. Rendon and J. G. Santiesteban, *Appl. Phys. Lett.*, 1993, **62**, 657-659.
36. S. Fan, M. G. Chapline, N. R. Franklin, T. W. Tombler, A. M. Cassell and H. Dai, *Science*, 1999, **283**, 512-514.
37. Q. Fu, S. Huang and J. Liu, *J. Phys. Chem. B*, 2004, **108**, 6124-6129.
38. M. L. Terranova, V. Sessa and M. Rossi, *Chem. Vap.*, 2006, **12**, 315-325.
39. P. M. Campbell, E. S. Snow and J. P. Novak, *Appl. Phys. Lett.*, 2002, **81**, 4586-4588.
40. Y. Murakami, Y. Miyauchi, S. Chiashi and S. Maruyama, *Chem. Phys. Lett.*, 2003, **377**, 49-54.
41. S. Amelinckx, X. B. Zhang, D. Bernaerts, X. F. Zhang, V. Ivanov and J. B. Nagy, *Science*, 1994, **265**, 635-639.
42. R. T. K. Baker, M. A. Barber, P. S. Harris, F. S. Feates and R. J. Waite, *J. Catal.*, 1972, **26**, 51-62.
43. G. G. Tibbetts, *J. Cryst. Growth.*, 1984, **66**, 632-638.
44. M. Yudasaka, R. Kikuchi, T. Matsui, Y. Ohki, S. Yoshimura and E. Ota, *Appl. Phys. Lett.*, 1995, **67**, 2477-2479.
45. H. Dai, A. G. Rinzler, P. Nikolaev, A. Thess, D. T. Colbert and R. E. Smalley, *Chem. Phys. Lett.*, 1996, **260**, 471-475.
46. J. H. Hafner, M. J. Bronikowski, B. R. Azamian, P. Nikolaev, A. G. Rinzler, D. T. Colbert, K. A. Smith and R. E. Smalley, *Chem. Phys. Lett.*, 1998, **296**, 195-202.
47. I. Heller, J. Kong, H. A. Heering, K. A. Williams, S. G. Lemay and C. Dekker, *Nano Lett.*, 2004, **5**, 137-142.
48. J. Kong, H. T. Soh, A. M. Cassell, C. F. Quate and H. Dai, *Nature*, 1998, **395**, 878-881.
49. L. X. Zheng, M. J. O'Connell, S. K. Doorn, X. Z. Liao, Y. H. Zhao, E. A. Akhadow, M. A. Hoffbauer, B. J. Roop, Q. X. Jia, R. C. Dye, D. E. Peterson, S. M. Huang, J. Liu and Y. T. Zhu, *Nat. Mater.*, 2004, **3**, 673-676.
50. A. Rutkowska, D. Walker, S. Gorfman, P. A. Thomas and J. V. Macpherson, *J. Phys. Chem. C*, 2009, **113**, 17087-17096.

51. L. Ding, A. Tselev, J. Wang, D. Yuan, H. Chu, T. P. McNicholas, Y. Li and J. Liu, *Nano Lett.*, 2009, **9**, 800-805.
52. I. Dumitrescu, P. R. Unwin, N. R. Wilson and J. V. Macpherson, *Anal. Chem.*, 2008, **80**, 3598-3605.
53. I. Dumitrescu, P. R. Unwin and J. V. Macpherson, *Electrochem. Commun.*, 2009, **11**, 2081-2084.
54. I. Dumitrescu, J. P. Edgeworth, P. R. Unwin and J. V. Macpherson, *Adv. Mater.*, 2009, **21**, 3105-3109.
55. D. P. Burt, W. M. Whyte, J. M. R. Weaver, A. Glidle, J. P. Edgeworth, J. V. Macpherson and P. S. Dobson, *J. Phys. Chem. C*, 2009, **113**, 15133-15139.
56. M. Terrones, N. Grobert, J. Olivares, J. P. Zhang, H. Terrones, K. Kordatos, W. K. Hsu, J. P. Hare, P. D. Townsend, K. Prassides, A. K. Cheetham, H. W. Kroto and D. R. M. Walton, *Nature*, 1997, **388**, 52-55.
57. K. Hata, D. N. Futaba, K. Mizuno, T. Namai, M. Yumura and S. Iijima, *Science*, 2004, **306**, 1362-1364.
58. Y. Y. Wei and E. Gyula, *Nanotechnology*, 2000, **11**, 61.
59. W. D. Zhang, J. T. L. Thong, W. C. Tjiu and L. M. Gan, *Diam. Relat. Mater.*, 2002, **11**, 1638-1642.
60. C. Kocabas, M. Shim and J. A. Rogers, *J. Am. Chem. Soc.*, 2006, **128**, 4540-4541.
61. H. C. Choi, S. Kundaria, D. Wang, A. Javey, Q. Wang, M. Rolandi and H. Dai, *Nano Lett.*, 2002, **3**, 157-161.
62. A. J. Hart, A. H. Slocum and L. Royer, *Carbon*, 2006, **44**, 348-359.
63. L. Delzeit, B. Chen, A. Cassell, R. Stevens, C. Nguyen and M. Meyyappan, *Chem. Phys. Lett.*, 2001, **348**, 368-374.
64. T. de los Arcos, M. Gunnar Garnier, P. Oelhafen, D. Mathys, J. Won Seo, C. Domingo, J. Vicente Garcia-Ramos and S. Sanchez-Cortes, *Carbon*, 2004, **42**, 187-190.
65. C. Mattevi, C. T. Wirth, S. Hofmann, R. Blume, M. Cantoro, C. Ducati, C. Cepek, A. Knop-Gericke, S. Milne, C. Castellarin-Cudia, S. Dolafi, A. Goldoni, R. Schloegl and J. Robertson, *J. Phys. Chem. C*, 2008, **112**, 12207-12213.
66. J. P. Edgeworth, N. R. Wilson and J. V. Macpherson, *Small*, 2007, **3**, 860-870.
67. A. M. Cassell, J. A. Raymakers, J. Kong and H. Dai, *J. Phys. Chem. B*, 1999, **103**, 6484-6492.
68. J. Kong, A. M. Cassell and H. Dai, *Chem. Phys. Lett.*, 1998, **292**, 567-574.
69. I. Dumitrescu, P. R. Unwin and J. V. Macpherson, *Chem. Commun.*, 2009, 6886-6901.
70. Y. Fan, B. R. Goldsmith and P. G. Collins, *Nat. Mater.*, 2005, **4**, 906-911.
71. P. Nikolaev, M. J. Bronikowski, R. K. Bradley, F. Rohmund, D. T. Colbert, K. A. Smith and R. E. Smalley, *Chem. Phys. Lett.*, 1999, **313**, 91-97.
72. M. J. Bronikowski, P. A. Willis, D. T. Colbert, K. A. Smith and R. E. Smalley, *J. Vac. Sci. Technol. A*, 2001, **19**, 1800-1805.
73. *ACS Applied Materials & Interfaces*, 2013, 130306161807001.
74. W. H. Qi and M. P. Wang, *Mater. Chem. Phys.*, 2004, **88**, 280-284.

75. Y. Wu and P. Yang, *J. Am. Chem. Soc.*, 2001, **123**, 3165-3166.
76. S. Hofmann, R. Sharma, C. Ducati, G. Du, C. Mattevi, C. Cepek, M. Cantoro, S. Pisana, A. Parvez, F. Cervantes-Sodi, A. C. Ferrari, R. Dunin-Borkowski, S. Lizzit, L. Petaccia, A. Goldoni and J. Robertson, *Nano Lett.*, 2007, **7**, 602-608.
77. M. Lin, J. P. Ying Tan, C. Boothroyd, K. P. Loh, E. S. Tok and Y.-L. Foo, *Nano Lett.*, 2006, **6**, 449-452.
78. X. Feng, S. Chee, R. Sharma, K. Liu, X. Xie, Q. Li, S. Fan and K. Jiang, *Nano Res.*, 2011, **4**, 767-779.
79. H. Dai, *Acc. Chem. Res.*, 2002, **35**, 1035-1044.
80. A. Gohier, C. P. Ewels, T. M. Minea and M. A. Djouadi, *Carbon*, 2008, **46**, 1331-1338.
81. A. J. Bard and L. R. Faulkner, *Electrochemical Methods: Fundamentals and Applications, 2nd Edition*, 2nd edn., John Wiley & Sons, Inc, 2001.
82. C. M. A. Brett and A. M. O. Brett, *ELECTROCHEMISTRY Principles, Methods, and Applications*, Oxford University Press, UK, 1993.
83. P. J. Britto, K. S. V. Santhanam and P. M. Ajayan, *Bioelectroch Bioener*, 1996, **41**, 121-125.
84. P. J. Britto, K. S. V. Santhanam, A. Rubio, J. A. Alonso and P. M. Ajayan, *Adv. Mater.*, 1999, **11**, 154-157.
85. J. M. Nugent, K. S. V. Santhanam, A. Rubio and P. M. Ajayan, *Nano Lett.*, 2001, **1**, 87-91.
86. J. K. Campbell, L. Sun and R. M. Crooks, *J. Am. Chem. Soc.*, 1999, **121**, 3779-3780.
87. C. y. Liu, A. J. Bard, F. Wudl, I. Weitz and J. R. Heath, *Electrochem. Solid St.*, 1999, **2**, 577-578.
88. M. Musameh, J. Wang, A. Merkoci and Y. Lin, *Electrochem. Commun.*, 2002, **4**, 743-746.
89. N. S. Lawrence, R. P. Deo and J. Wang, *Anal. Chim. Acta*, 2004, **517**, 131-137.
90. A. Salimi, R. Hallaj and G.-R. Khayatian, *Electroanal*, 2005, **17**, 873-879.
91. S. F. Wang and Q. Xu, *Anal. Lett.*, 2005, **38**, 657-671.
92. M. Chicharro, E. Bermejo, M. Moreno, A. Sánchez, A. Zapardiel and G. Rivas, *Electroanal*, 2005, **17**, 476-482.
93. J.-S. Ye, Y. Wen, W. De Zhang, L. Ming Gan, G. Q. Xu and F.-S. Sheu, *Electrochem. Commun.*, 2004, **6**, 66-70.
94. R. R. Moore, C. E. Banks and R. G. Compton, *Anal. Chem.*, 2004, **76**, 2677-2682.
95. C. E. Banks, T. J. Davies, G. G. Wildgoose and R. G. Compton, *Chem. Commun.*, 2005, 829-841.
96. I. Dumitrescu, P. V. Dudin, J. P. Edgeworth, J. V. Macpherson and P. R. Unwin, *J. Phys. Chem. C*, 2010, **114**, 2633-2639.
97. A. G. Güell, N. Ebejer, M. E. Snowden, K. McKelvey, J. V. Macpherson and P. R. Unwin, *Proceedings of the National Academy of Sciences*, 2012.
98. J. Kim, H. Xiong, M. Hofmann, J. Kong and S. Amemiya, *Anal. Chem.*, 2010, **82**, 1605-1607.

99. J. Li, A. Cassell, L. Delzeit, J. Han and M. Meyyappan, *J. Phys. Chem. B*, 2002, **106**, 9299-9305.
100. J. Liu, A. Chou, W. Rahmat, M. N. Paddon-Row and J. J. Gooding, *Electroanal*, 2005, **17**, 38-46.
101. C. E. Banks, R. R. Moore, T. J. Davies and R. G. Compton, *Chem. Commun.*, 2004, 1804-1805.
102. A. N. Patel, M. Guille Collignon, M. A. O'Connell, W. O. Y. Hung, K. McKelvey, J. V. Macpherson and P. R. Unwin, *Journal of the American Chemical Society*, 2012, **134**, 20117-20130.
103. A. F. Holloway, K. Toghill, G. G. Wildgoose, R. G. Compton, M. A. H. Ward, G. Tobias, S. A. Llewellyn, B. n. Ballesteros, M. L. H. Green and A. Crossley, *J. Phys. Chem. C*, 2008, **112**, 10389-10397.
104. M. Pumera, *Langmuir*, 2007, **23**, 6453-6458.
105. M. Pumera and H. Iwai, *J. Phys. Chem. C*, 2009, **113**, 4401-4405.
106. E. J. E. Stuart and M. Pumera, *J. Phys. Chem. C*, 2010, **114**, 21296-21298.
107. B. Šljukić, C. E. Banks and R. G. Compton, *Nano Lett.*, 2006, **6**, 1556-1558.
108. A. Chou, T. Bocking, N. K. Singh and J. J. Gooding, *Chem. Commun.*, 2005, 842-844.
109. M. Pumera, *Chem. – Eur. J.*, 2009, **15**, 4970-4978.
110. R. J. Rice and R. L. McCreery, *Anal. Chem.*, 1989, **61**, 1637-1641.
111. K. R. Kneten and R. L. McCreery, *Anal. Chem.*, 1992, **64**, 2518-2524.
112. S. C. S. Lai, A. N. Patel, K. McKelvey and P. R. Unwin, *Angew. Chem. Int. Ed.*, 2012, **51**, 5405-5408.
113. A. Holloway, G. Wildgoose, R. Compton, L. Shao and M. H. Green, *J. Solid. State. Electrochem.*, 2008, **12**, 1337-1348.
114. P. V. Dudin, M. E. Snowden, J. V. Macpherson and P. R. Unwin, *ACS Nano*, 2011, **5**, 10017-10025.
115. P. Bertoncello, J. P. Edgeworth, J. V. Macpherson and P. R. Unwin, *J. Am. Chem. Soc.*, 2007, **129**, 10982-10983.
116. M. Musameh, N. S. Lawrence and J. Wang, *Electrochem. Commun.*, 2005, **7**, 14-18.
117. K. Gong, S. Chakrabarti and L. Dai, *Angew. Chem. Int. Ed.*, 2008, **47**, 5446-5450.
118. P. Chen, M. A. Fryling and R. L. McCreery, *Anal. Chem.*, 1995, **67**, 3115-3122.
119. G. G. Wildgoose, C. E. Banks and R. G. Compton, *Small*, 2006, **2**, 182-193.
120. D. Bera, S. C. Kuiry, M. McCutchen, S. Seal, H. Heinrich and G. C. Slane, *J. Appl. Phys.*, 2004, **96**, 5152-5157.
121. Y. Xing, *J. Phys. Chem. B*, 2004, **108**, 19255-19259.
122. A. Kongkanand, S. Kuwabata, G. Girishkumar and P. Kamat, *Langmuir*, 2006, **22**, 2392-2396.
123. T. M. Day, P. R. Unwin, N. R. Wilson and J. V. Macpherson, *J. Am. Chem. Soc.*, 2005, **127**, 10639-10647.
124. S. C. S. Lai, P. V. Dudin, J. V. Macpherson and P. R. Unwin, *J. Am. Chem. Soc.*, 2011, **133**, 10744-10747.

125. T. M. Day, P. R. Unwin and J. V. Macpherson, *Nano Lett.*, 2007, **7**, 51-57.
126. P. V. Dudin, P. R. Unwin and J. V. Macpherson, *J. Phys. Chem. C*, 2010, **114**, 13241-13248.
127. T. Matsumoto, T. Komatsu, K. Arai, T. Yamazaki, M. Kijima, H. Shimizu, Y. Takasawa and J. Nakamura, *Chem. Commun.*, 2004, 840-841.
128. N. Alexeyeva, K. Tammeveski, A. Lopez-Cudero, J. Solla-Gullón and J. M. Feliu, *Electrochim. Acta*, 2010, **55**, 794-803.
129. S. E. F. Kleijn, M. T. M. Koper, S. C. S. Lai and P. R. Unwin, *Angew. Chem. Int. Ed.*, 2013, **In Press**.
130. B. M. Quinn, C. Dekker and S. G. Lemay, *J. Am. Chem. Soc.*, 2005, **127**, 6146-6147.
131. V. R. Khalap, T. Sheps, A. A. Kane and P. G. Collins, *Nano Lett.*, 2010, **10**, 896-901.
132. D. R. Kauffman, D. C. Sorescu, D. P. Schofield, B. L. Allen, K. D. Jordan and A. Star, *Nano Lett.*, 2010, **10**, 958-963.
133. C. Song and J. Zhang, in *PEM Fuel Cell Electrocatalysts and Catalyst Layers*, ed. J. Zhang, Springer London, 2008, pp. 89-134.
134. E. Yeager, *J. Mol. Catal.*, 1986, **38**, 5-25.
135. A. S. Aricò, S. Srinivasan and V. Antonucci, *Fuel Cells*, 2001, **1**, 133-161.
136. X. Yu and S. Ye, *J. Power Sources*, 2007, **172**, 145-154.
137. M. Winter and R. J. Brodd, *Chem. Rev.*, 2004, **104**, 4245-4270.
138. L. Dai, D. W. Chang, J.-B. Baek and W. Lu, *Small*, 2012, **8**, 1130-1166.
139. G. Che, B. B. Lakshmi, E. R. Fisher and C. R. Martin, *Nature*, 1998, **393**, 346-349.
140. G. Girishkumar, K. Vinodgopal and P. V. Kamat, *J. Phys. Chem. B*, 2004, **108**, 19960-19966.
141. H.-F. Cui, J.-S. Ye, W.-D. Zhang, J. Wang and F.-S. Sheu, *J. Electroanal. Chem.*, 2005, **577**, 295-302.
142. W. Sheng, S. Woo Lee, E. J. Crumlin, S. Chen and Y. Shao-Horn, *J. Electrochem. Soc.*, 2011, **158**, B1398-B1404.
143. R. L. McCreery, *Chem. Rev.*, 2008, **108**, 2646-2687.
144. J. Yang, D.-J. Liu, N. N. Kariuki and L. X. Chen, *Chem. Commun.*, 2008, 329-331.
145. K. Gong, F. Du, Z. Xia, M. Durstock and L. Dai, *Science*, 2009, **323**, 760-764.
146. I. Morcos and E. Yeager, *Electrochim. Acta*, 1970, **15**, 953-975.
147. T. C. Nagaiah, S. Kundu, M. Bron, M. Muhler and W. Schuhmann, *Electrochem. Commun.*, 2010, **12**, 338-341.
148. D. Yu, Y. Xue and L. Dai, *J. Phys. Chem. Lett.*, 2012, **3**, 2863-2870.
149. Y. Li, W. Zhou, H. Wang, L. Xie, Y. Liang, F. Wei, J.-C. Idrobo, S. J. Pennycook and H. Dai, *Nat. Nano*, 2012, **7**, 394-400.
150. W. Xiong, F. Du, Y. Liu, A. Perez, M. Supp, T. S. Ramakrishnan, L. Dai and L. Jiang, *J. Am. Chem. Soc.*, 2010, **132**, 15839-15841.
151. D. Yu, Q. Zhang and L. Dai, *J. Am. Chem. Soc.*, 2010, **132**, 15127-15129.
152. J. Vazquez-Arenas, D. Higgins, Z. Chen, M. Fowler and Z. Chen, *J. Power Sources*, 2012, **205**, 215-221.

153. S. Kundu, T. C. Nagaiah, W. Xia, Y. Wang, S. V. Dommele, J. H. Bitter, M. Santa, G. Grundmeier, M. Bron, W. Schuhmann and M. Muhler, *J. Phys. Chem. C*, 2009, **113**, 14302-14310.
154. S. Wang, D. Yu and L. Dai, *J. Am. Chem. Soc.*, 2011, **133**, 5182-5185.
155. K. Matsubara and K. Waki, *Electrochem. Solid St.*, 2010, **13**, F7-F9.
156. N. Alexeyeva and K. Tammeveski, *Electrochem. Solid St.*, 2007, **10**, F18-F21.
157. G. Jürmann and K. Tammeveski, *J. Electroanal. Chem.*, 2006, **597**, 119-126.
158. I. Kruusenberg, N. Alexeyeva, K. Tammeveski, J. Kozlova, L. Matisen, V. Sammelselg, J. Solla-Gullón and J. M. Feliu, *Carbon*, 2011, **49**, 4031-4039.
159. H. Wang, T. Löffler and H. Baltruschat, *J. Appl. Electrochem.*, 2001, **31**, 759-765.
160. J. M. Léger, *J. Appl. Electrochem.*, 2001, **31**, 767-771.
161. S. C. S. Lai, N. P. Lebedeva, T. H. M. Housmans and M. T. M. Koper, *Top. Catal.*, 2007, **46**, 320-333.
162. G. Che, B. B. Lakshmi, C. R. Martin and E. R. Fisher, *Langmuir*, 1999, **15**, 750-758.
163. B. Rajesh, K. Ravindranathan Thampi, J. M. Bonard, N. Xanthopoulos, H. J. Mathieu and B. Viswanathan, *J. Phys. Chem. B*, 2003, **107**, 2701-2708.
164. A. N. Golikand and L. Irannejad, *Electroanal*, 2008, **20**, 1121-1127.
165. T. Maiyalagan, B. Viswanathan and U. V. Varadaraju, *Electrochem. Commun.*, 2005, **7**, 905-912.
166. H. Liu, C. Song, L. Zhang, J. Zhang, H. Wang and D. P. Wilkinson, *J. Power Sources*, 2006, **155**, 95-110.
167. E. Stolyarova, K. T. Rim, S. Ryu, J. Maultzsch, P. Kim, L. E. Brus, T. F. Heinz, M. S. Hybertsen and G. W. Flynn, *Proc. Natl. Acad. Sci. U.S.A.*, 2007, **104**, 9209-9212.
168. J. C. Meyer, A. K. Geim, M. I. Katsnelson, K. S. Novoselov, T. J. Booth and S. Roth, *Nature*, 2007, **446**, 60-63.
169. P. Y. Huang, C. S. Ruiz-Vargas, A. M. van der Zande, W. S. Whitney, M. P. Levendorf, J. W. Kevek, S. Garg, J. S. Alden, C. J. Hustedt, Y. Zhu, J. Park, P. L. McEuen and D. A. Muller, *Nature*, 2011, **469**, 389-392.
170. C. N. R. Rao, A. K. Sood, K. S. Subrahmanyam and A. Govindaraj, *Angew. Chem. Int. Ed.*, 2009, **48**, 7752-7777.
171. Y. Zhu, S. Murali, W. Cai, X. Li, J. W. Suk, J. R. Potts and R. S. Ruoff, *Adv. Mater.*, 2010, **22**, 3906-3924.
172. L. M. Malard, M. A. Pimenta, G. Dresselhaus and M. S. Dresselhaus, *Phys. Rep.*, 2009, **473**, 51-87.
173. S. Park and R. S. Ruoff, *Nat. Nano*, 2009, **4**, 217-224.
174. K. S. Novoselov, A. K. Geim, S. V. Morozov, D. Jiang, Y. Zhang, S. V. Dubonos, I. V. Grigorieva and A. A. Firsov, *Science*, 2004, **306**, 666-669.
175. K. S. Novoselov, D. Jiang, F. Schedin, T. J. Booth, V. V. Khotkevich, S. V. Morozov and A. K. Geim, *Proc. Natl. Acad. Sci. U.S.A.*, 2005, **102**, 10451-10453.
176. A. K. Geim and K. S. Novoselov, *Nat. Mater.*, 2007, **6**, 183-191.

177. S. Stankovich, D. A. Dikin, R. D. Piner, K. A. Kohlhaas, A. Kleinhammes, Y. Jia, Y. Wu, S. T. Nguyen and R. S. Ruoff, *Carbon*, 2007, **45**, 1558-1565.
178. D. W. Boukhvalov and M. I. Katsnelson, *J. Am. Chem. Soc.*, 2008, **130**, 10697-10701.
179. Q. Yu, J. Lian, S. Siriponglert, H. Li, Y. P. Chen and S.-S. Pei, *Appl. Phys. Lett.*, 2008, **93**, 113103.
180. K. S. Kim, Y. Zhao, H. Jang, S. Y. Lee, J. M. Kim, K. S. Kim, J.-H. Ahn, P. Kim, J.-Y. Choi and B. H. Hong, *Nature*, 2009, **457**, 706-710.
181. A. Reina, X. Jia, J. Ho, D. Nezich, H. Son, V. Bulovic, M. S. Dresselhaus and J. Kong, *Nano Lett.*, 2008, **9**, 30-35.
182. L. Colombo, R. M. Wallace and R. S. Ruoff, *P. Inst. Electr. Elect.*, 2013, **101**, 1536-1556.
183. X. Li, W. Cai, J. An, S. Kim, J. Nah, D. Yang, R. Piner, A. Velamakanni, I. Jung, E. Tutuc, S. K. Banerjee, L. Colombo and R. S. Ruoff, *Science*, 2009, **324**, 1312-1314.
184. M. P. Levendorf, C. S. Ruiz-Vargas, S. Garg and J. Park, *Nano Lett.*, 2009, **9**, 4479-4483.
185. Y. Lee, S. Bae, H. Jang, S. Jang, S.-E. Zhu, S. H. Sim, Y. I. Song, B. H. Hong and J.-H. Ahn, *Nano Lett.*, 2010, **10**, 490-493.
186. S. Bae, H. Kim, Y. Lee, X. Xu, J.-S. Park, Y. Zheng, J. Balakrishnan, T. Lei, H. Ri Kim, Y. I. Song, Y.-J. Kim, K. S. Kim, B. Ozyilmaz, J.-H. Ahn, B. H. Hong and S. Iijima, *Nat. Nano*, 2010, **5**, 574-578.
187. X. Li, Y. Zhu, W. Cai, M. Borysiak, B. Han, D. Chen, R. D. Piner, L. Colombo and R. S. Ruoff, *Nano Lett.*, 2009, **9**, 4359-4363.
188. D.-Y. Wang, I. S. Huang, P.-H. Ho, S.-S. Li, Y.-C. Yeh, D.-W. Wang, W.-L. Chen, Y.-Y. Lee, Y.-M. Chang, C.-C. Chen, C.-T. Liang and C.-W. Chen, *Adv. Mater.*, 2013, **25**, 4521-4526.
189. J. Kang, D. Shin, S. Bae and B. H. Hong, *Nanoscale*, 2012, **4**, 5527-5537.
190. Y.-C. Lin, C. Jin, J.-C. Lee, S.-F. Jen, K. Suenaga and P.-W. Chiu, *ACS Nano*, 2011, **5**, 2362-2368.
191. P. Chen and R. L. McCreery, *Anal. Chem.*, 1996, **68**, 3958-3965.
192. A. N. Obraztsov, E. A. Obraztsova, A. V. Tyurnina and A. A. Zolotukhin, *Carbon*, 2007, **45**, 2017-2021.
193. N. Liu, Z. Pan, L. Fu, C. Zhang, B. Dai and Z. Liu, *Nano Res.*, 2011, **4**, 996-1004.
194. K. Xu, P. Cao and J. R. Heath, *Nano Lett.*, 2009, **9**, 4446-4451.
195. J. Kang, S. Hwang, J. H. Kim, M. H. Kim, J. Ryu, S. J. Seo, B. H. Hong, M. K. Kim and J.-B. Choi, *ACS Nano*, 2012, **6**, 5360-5365.
196. P. Blake, E. W. Hill, A. H. C. Neto, K. S. Novoselov, D. Jiang, R. Yang, T. J. Booth and A. K. Geim, *Appl. Phys. Lett.*, 2007, **91**, 063124-063123.
197. Z. Ni, Y. Wang, T. Yu and Z. Shen, *Nano Res.*, 2008, **1**, 273-291.
198. A. C. Ferrari, J. C. Meyer, V. Scardaci, C. Casiraghi, M. Lazzeri, F. Mauri, S. Piscanec, D. Jiang, K. S. Novoselov, S. Roth and A. K. Geim, *Phys. Rev. Lett.*, 2006, **97**, 187401.
199. W. Li, C. Tan, M. A. Lowe, H. D. Abruña and D. C. Ralph, *ACS Nano*, 2011, **5**, 2264-2270.
200. A. T. Valota, I. A. Kinloch, K. S. Novoselov, C. Casiraghi, A. Eckmann, E. W. Hill and R. A. W. Dryfe, *ACS Nano*, 2011, **5**, 8809-8815.

- 201. D. A. C. Brownson and C. E. Banks, *Phys. Chem. Chem. Phys.*, 2011, **13**, 15825-15828.
- 202. A. Ambrosi and M. Pumera, *J. Phys. Chem. C*, 2013, **117**, 2053-2058.
- 203. A. G. Güell, N. Ebejer, M. E. Snowden, J. V. Macpherson and P. R. Unwin, *J. Am. Chem. Soc.*, 2012, **134**, 7258-7261.

2

Experimental

In this chapter the methodologies, experimental procedures and instrumentation used throughout this thesis are detailed. This includes the synthesis, characterisation and electrode fabrication of SWNT and graphene.

2.1 SWNT catalyst preparation

2.1.1 2D SWNT networks

Si/SiO₂ was cleaved into ca. 1 × 1 cm squares from a 4” diameter wafer (IDB Technologies Ltd, n-type, 525 mm thick with 300 nm of thermally grown oxide) by scratching (polished face) with a diamond scribe at the wafer edge and applying a small force to the reverse, causing breakage along defined crystallographic directions. These substrates were cleaned to remove contaminants by washing with acetone (99%, Fisher Scientific), and then immediately rinsing with propan-2-ol (99.99%, Fisher Scientific) before the acetone evaporated, to prevent visible drying marks. The propan-2-ol was blown from the surface with N₂ before it dried, again stopping drying marks. The Si/SiO₂ was placed (polished oxidised face upwards) on top of a flat Teflon block, in preparation for catalyst deposition.

Ferritin (Sigma-aldrich, 125 mg_{ferritin} ml⁻¹ in saline solution), a naturally occurring Fe storage protein,¹ was diluted with 18.2 MΩ cm at 25 °C Milli-Q (Millipore Corporation) water (all DI water conforms to these specifications) to a number of different concentrations as this dictated SWNT network density. Common dilution factors were 1 part ferritin solution to 150 or 500 parts DI water. The catalyst was thoroughly mixed by sonication before the solution was pipetted on top of the Si/SiO₂ until it covered the whole surface, right to the edge of the substrate. This was then left for 30 mins to allow the ferritin to disperse on the surface. The underlying hydrophobic Teflon acts to stabilise the droplet by stopping it leaking from the Si/SiO₂ substrate. After this time had elapsed a steady and gentle flow of N₂ was used to blow the solution droplet from the

surface. The Si/SiO₂/ferritin was then exposed to an oxygen plasma (K1050X plasma asher, Emitech, UK; O₂ pressure 6×10^{-1} mbar, 100 W) for 2 mins to remove the protein shell from the ferritin NPs, leaving discrete Fe NPs on the surface.²⁻⁴

2.1.2 Very high density (VHD) SWNT networks

Si/SiO₂ was prepared and cleaned as discussed above, but then placed in a table top sputtering system (1 kV, 10 mA; Quorum Technologies SC7640 sputter coater) fitted with a Co target (99.95%, Testbourne Ltd. UK). NP density was varied by varying sputtering time. For very high density (VHD) networks (complete 'mats' of SWNT on the Si/SiO₂ surface) Co was deposited for 30 seconds.

2.1.3 3D SWNT forests

A polished silicon wafer with a natural oxide (n-type, 525 µm thick, IDB Technologies Ltd, UK) was deposited with a 10 nm thick layer of aluminium by sputtering (Plassys, MP 900S) by Dr David Burt at the University of Glasgow, Dept. of Engineering. This substrate was cleaved and cleaned with acetone/propan-2-ol post Al deposition and exposed to an oxygen plasma for 2 mins to both remove adsorbed surface contamination and to fully oxidise the Al surface. Co was deposited for 180 s using the table top sputtering system.

2.2 SWNT Growth by cCVD

2.2.1 CVD systems

Two CVD systems were utilised to grow SWNT, namely the ‘hot wall’ and ‘cold wall’; schematics of which are shown in 2.2.1. The hot wall CVD consisted of a programmable split tube furnace (Lindberg/Blue M, Thermo scientific) fitted with a quartz tube (25 mm O.D, 50 cm length, 1.5 mm thick walls, Enterprise Q Ltd., UK) into the centre of which growth substrates were inserted by removing the cover on the exhaust end of the tube and pushing in on top of a ‘boat’ consisting of a 3 mm thick quartz plate. Process gases entered at one end of the tube and were vented to a fume hood from the other. Gas flow was controlled using mass flow controllers (MFCs)(MKS instruments Ltd., UK, 1179A) attached to an analogue control system (MKS instruments Ltd., UK, Type 247).

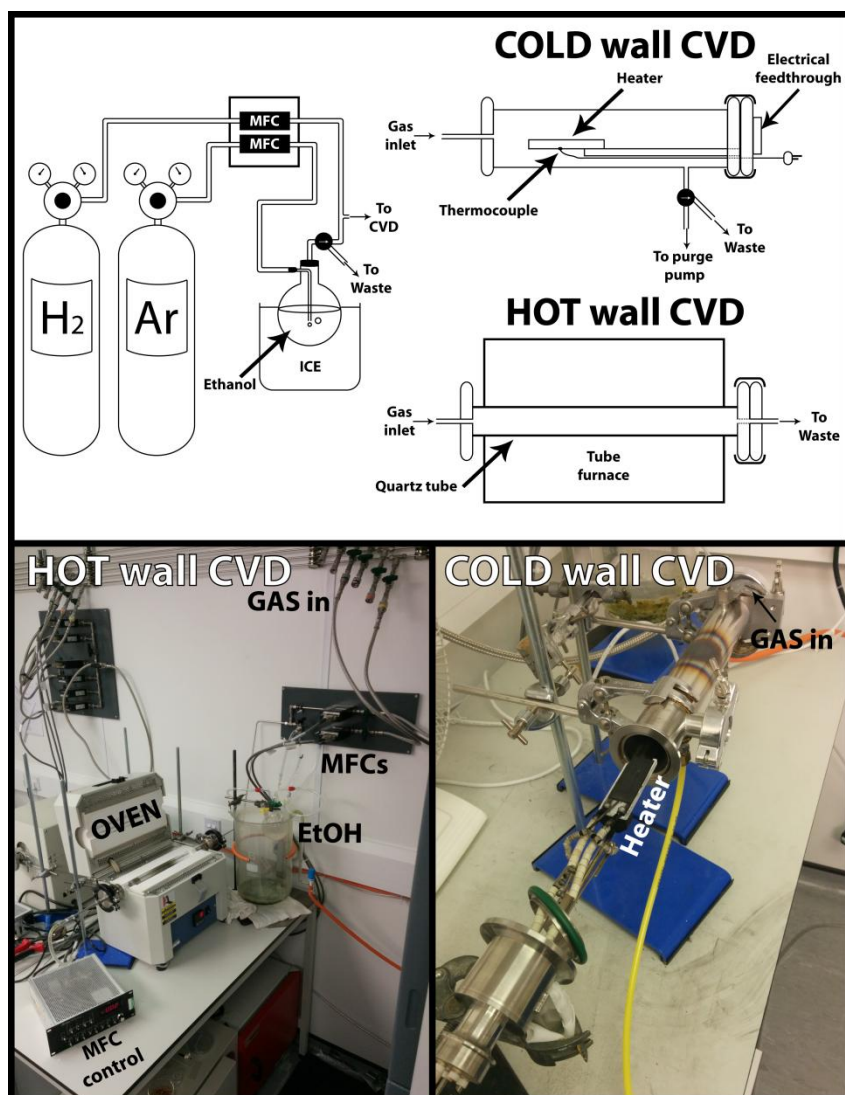


Figure 2.1 - Schematic and pictures of the cCVD systems used to grow SWNT (not to scale).

The cold wall CVD system was designed in collaboration with and custom built by Moorfield Associates and consisted of a heater element supported in a ceramic surround which was also fitted with a thermocouple. The heater was inserted into a metallic tube into which the process gases were fed at one end and the other had a feedthrough for electrical supply (for the heater) and the thermocouple. Process gasses exit from a vent on the side of the tube, this exit was also fitted with a diaphragm pump (KNF Neuberger Ltd., UK, PME6634) which was used to purge the chamber (pump, backfill with Ar, pump)

before growth. Gas flow was controlled with MFCs connected to a digital control system (MKS instruments ltd., UK, Type 647C). The heater temperature was controlled (by PID control loop) by an external controller (Moorfield Associates). Both of the above systems utilised ethanol (EtOH, 99.99%, Fisher Scientific) vapour as a carbon source, which was created by bubbling Ar through a flask of EtOH which was maintained at 0 °C by insertion in an ice bath.

2.2.2 Generalised cCVD growth procedure

The first step to any growth procedure was to insert the growth substrate into the CVD chamber after which a purge procedure was performed. For the hot walled CVD system this purge consisted of flowing 1000 standard cubic centimetres per minute (sccm, i.e. flow rate in cubic centimetres at standard temperature/pressure) H₂ (99.995%, BOC) for 5 mins at room temperature. The cold wall CVD system was purged by pumping the chamber for 2 mins, turning off pump, flowing Ar (99.9995%, BOC) 1000 sccm for 2 min, stopping Ar flow, and then repeating twice more.

Figure 2.2 shows a graphical representation of a generic cCVD growth scheme which follows a purge routine. T_1 and 2 are process temperatures, t_1 to 4 are process times and G_1 to 5 are process gas mixtures, values for different growth procedures can be found in Table 2.1.

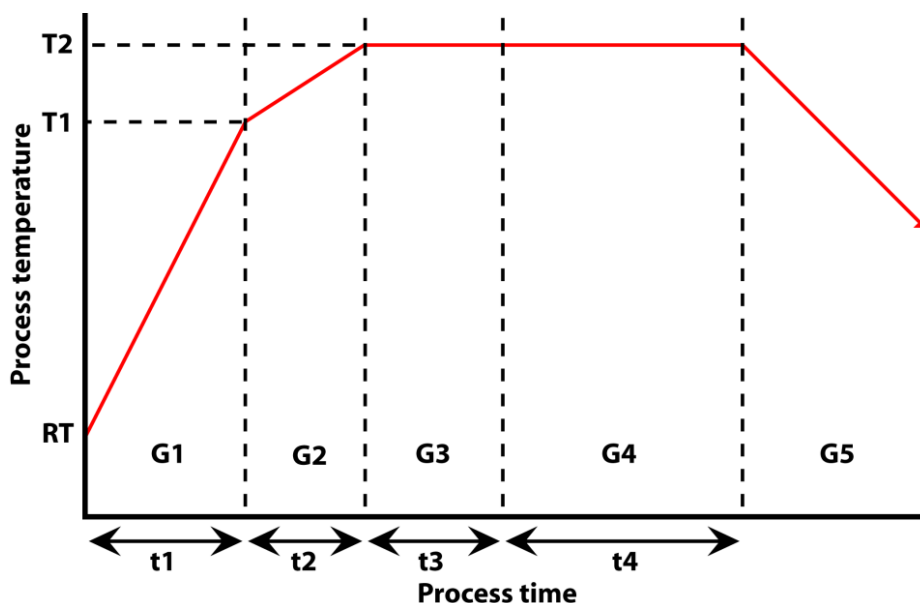


Figure 2.2 - Graphical representation of a generic cCVD growth scheme, $t1-4$ represent process times, $G1-5$ represent process gas mixtures, $T1$ and 2 represent process temperatures (not to scale). See Table 2.1 for T , t and G values.

In a generalised cCVD growth the substrate first is heated from room temperature (RT) to $T1$ under a gas flow defined by $G1$ in time $t1$. The oven is then heated to the growth temperature ($T2$) more slowly ($t2$) and held there ($t3$) to allow catalyst stabilisation. The scheme then entered the ‘growth stage’ where the carbon containing feedstock (Ar/EtOH, $G4$) was introduced for a set period of time ($t4$). After the growth time had elapsed the flow of Ar/EtOH was stopped ($G5$) and the chamber was allowed to cool to 200 °C under gas flow ($G5$). Substrates were then removed from the chamber.

	Hot wall CVD 2D network growth	Cold wall CVD 2D network growth	Hot wall CVD VHD network growth	Hot wall CVD forest growth	
t1/min	10	ASAP	8	10	Process time (min)
t2/min	10	ASAP	5	10	
t3/min	5	1	2	0	
t4/min	10	5	20	40	
T1/°C	700	700	700	700	Temp (°C)
T2/°C	850	795	850	850	
G1/sccm	150 H ₂	150 H ₂ & 850 Ar	150 H ₂	50 H ₂	Process Gases (sccm)
G2/sccm	150 H ₂	150 H ₂ & 850 Ar	150 H ₂	50 H ₂	
G3/sccm	150 H ₂	150 H ₂ & 850 Ar	150 H ₂	-	
G4/sccm	150 H ₂ & 850 Ar/EtOH	150 H ₂ & 850 Ar/EtOH	150 H ₂ & 850 Ar/EtOH	150 Ar/EtOH	
G5/sccm	150 H ₂	150 H ₂ & 850 Ar	150 H ₂	50 H ₂	

Table 2.1 – CVD growth conditions for different SWNT structures

2.3 Graphene growth by cCVD

2.3.1 CVD system

Graphene was grown using a commercial cCVD system (NanoCVD 8G) which was developed during this project in collaboration with Moorfield Associates (MA) and Dr Jon Edgeworth (University of Warwick and MA). The CVD system was developed from the cold wall system discussed in section 2.2.1. The apparatus was modified for reduced pressure (2 mTorr) growth by attaching a pump and pressure control system. Figure 2.3 shows the two systems.

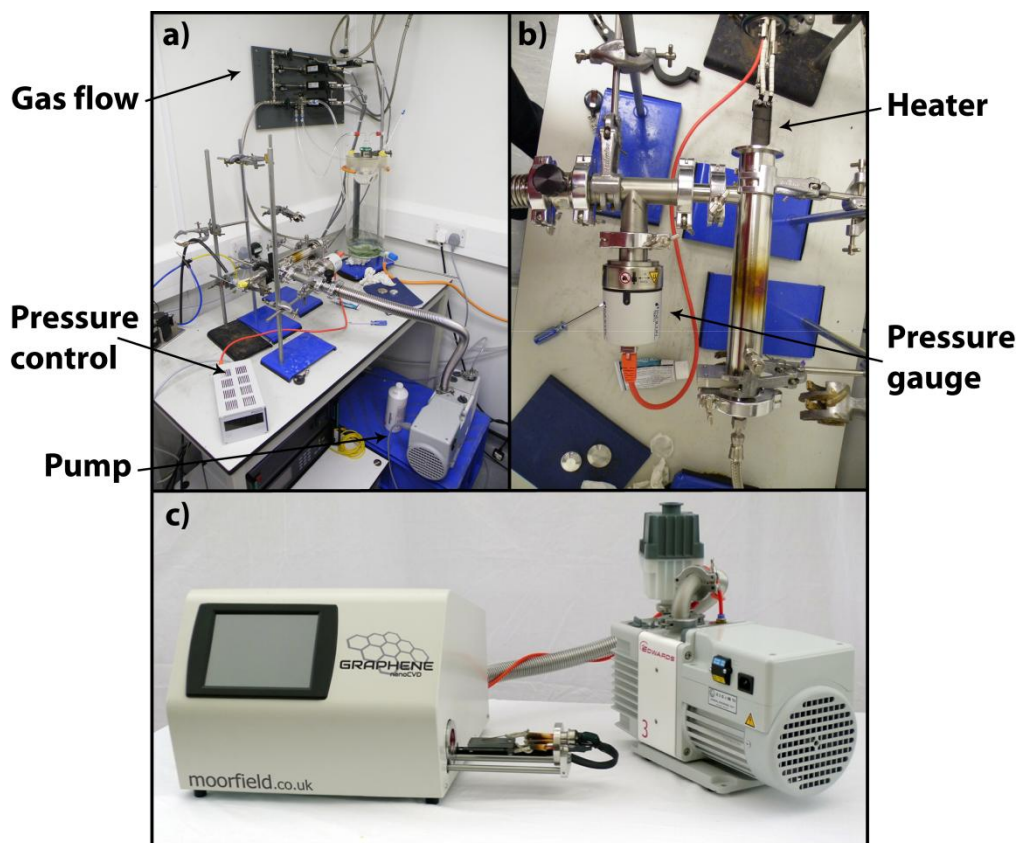


Figure 2.3 – a) & b) low pressure cold wall CVD system, c) NanoCVD 8G commercial CVD system.

The commercial low pressure CVD system has a hot plate capable of reaching 1100 °C and automatically adjusts the temperature, gas flows and pressure automatically from a user defined program. It utilises Ar, H₂ and CH₄ gases. A standard graphene growth using this system is discussed in section 2.3.3.

2.3.2 Substrate preparation

Cu foils were cut into 1 by 1 cm squares from a larger foil (0.025 mm thick, 99.8 %, Alfa Aesar) using scissors. These foils were placed in acetone before sonication for 5 mins to remove any surface residues or contamination from manufacture. The foils were then removed from solution, rinsed with

acetone, then rinsed with propan-2-ol and dried with a flow of N₂. Once fully dry the foil was submerged in a solution of HCl:water (1:4) at 50 °C for 30 seconds, which acts to further remove surface contaminants, oxides and layers added during manufacture to prevent oxidation (e.g. chromium⁵). The foils are then submerged in and then rinsed with water and again dried with N₂ flow. Prior to growth the Cu foils are flattened by placing them between glass slides (cleaned with acetone/IPA) and squeezing them in a vice, which removes macro scale roughness.

2.3.3 Graphene growth by cCVD

Unlike the atmospheric cCVD process described in section 2.2.2 the pressure is also controlled in the graphene growth regime. Controlling the system pressure was performed using two distinct modes, namely pressure control or flow control. With pressure control the user defines a pressure (up to 20 Torr) and the proportion (%) of Ar, H₂ and CH₄ flowing. The system then adjusts the total gas flow (keeping the proportions as defined) to maintain the required pressure. Using flow control the user defines the gas flow (sccm) and the pressure is allowed to change accordingly. A graphical schematic describing a standard cCVD growth procedure using copper foil as a catalyst material is shown in Figure 2.4.

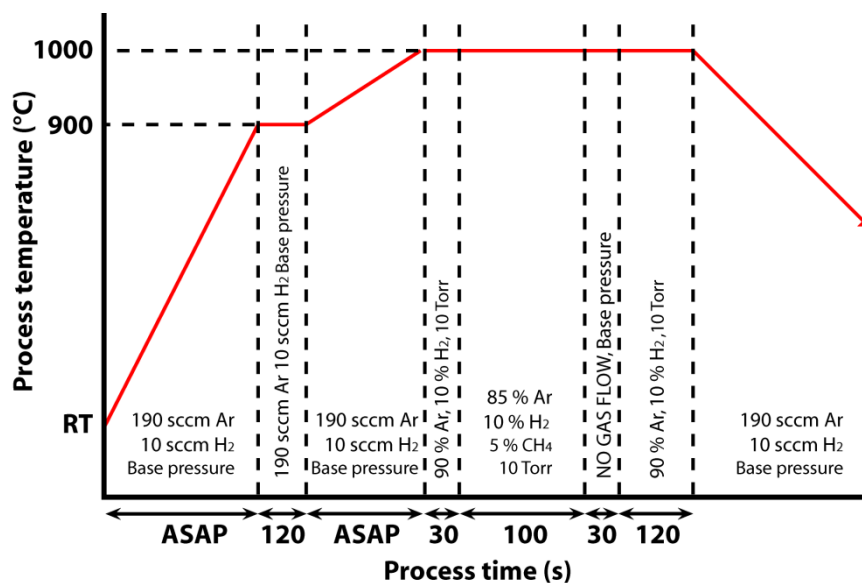


Figure 2.4 – cCVD growth regime for graphene growth on Cu foil.

After a Cu foil has been placed into the growth chamber a purge regime was performed, where the system was pumped and then back filled with Ar, five times. When the purge was complete the growth program was started, beginning by heating to 900 °C under flow controlled Ar and H₂ as quickly as possible before maintaining the temperature for 2 mins to stabilise the catalyst. The temperature was then increased to 1000 °C as quickly as possible under the same gas flow. The pressure regime was changed to pressure control, maintaining the system at 10 Torr, which was allowed to stabilise for 30 s, before 5 % (of total gas flow) CH₄ was introduced for 100 s promoting graphene growth. After the growth time had elapsed all gas flow was halted (temperature maintained at 1000 °C) and the pressure allowed to return to its base value to facilitate the quick removal of carbon containing gas, halting growth. Before the chamber was cooled the system was returned to pressure control and Ar and H₂ were reintroduced for 2 mins to allow time for surface reorganisation, facilitating the

production of higher quality graphene. The system was then cooled under Ar and H₂ until 200 °C, when samples were removed.

2.3.4 Graphene transfer

The transfer of graphene to an insulating substrate (Si/SiO₂ or quartz) was a prolonged, multi-stage process based on the procedure used by *Ruoff et al*⁶ and adapted with reference to other reports.⁷ The copper foil with graphene was stuck (graphene face up) onto a square of glass with Gel-Pak (Gel-Pak, California) before poly(methyl methacrylate) (PMMA, 1 g PMMA Mw ~ 996 000, Sigma Aldrich Co. in 10 ml chlorobenzene) was spin-coated onto the surface (2000 rpm, 45 s). The coated foil was then placed into a desiccator and dried under vacuum for 1 hour. When dry, the reverse side of the copper (side which was face down on heater) was gently polished with sand paper (Struers waterproof silicon carbide paper #4000) to break any graphitic coverage from cCVD and then floated onto ammonium persulphate (0.1 M) with the bare copper facing the solution and the graphene/PMMA facing upwards. This was left overnight, by which time the copper had dissolved leaving the graphene/PMMA floating on the surface of the solution. The graphene/PMMA was cleaned by repeatedly moving it to fresh water (six times). This was performed using ‘the spoon technique’ where a plastic spoon was used to scoop the sample from the solution surface, leaving it floating on a small volume solution and then carefully floating it onto clean water. The graphene/PMMA was then ‘scooped’ from the water surface using a clean (acetone, IPA, N₂) insulating substrate and allowed to dry in air on a non-absorbent surface. When dry the graphene/PMMA was heated to 180 °C for 1 hour, which flattened the graphene, which was then allowed to cool.

PMMA was then removed from the surface in acetone at 50 °C. A schematic of the graphene transfer process is shown in Figure 2.5.

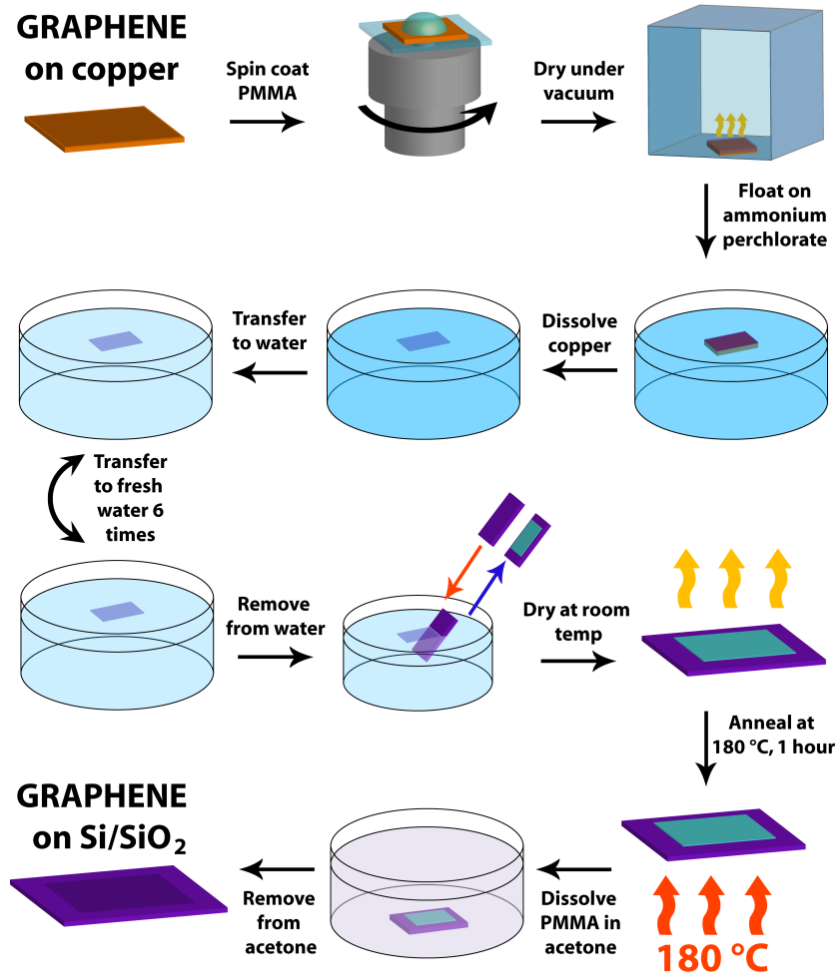


Figure 2.5 – A schematic of the processes required to transfer graphene.

2.4 Characterisation techniques

The following section details techniques that were used to characterise SWNTs and graphene post cCVD growth.

2.4.1 Optical microscopy

Optical microscopy was performed using an Olympus BH2 optical microscope fitted with lenses allowing $\times 50$ to $\times 1000$ magnification.

2.4.2 Field-emission scanning electron microscopy (FE-SEM)

FE-SEM images were acquired using a Zeiss SUPRA 55 VP FE-SEM using a 1 kV accelerating voltage (5 kV was used for VHD SWNTs). The tilted stage was utilised to take images of SWNT forests. As FE-SEM is known to contaminate surfaces images were routinely taken post electrochemical measurements.

2.4.3 Transmission electron microscopy (TEM)

TEM images were taken using a Jeol 2000FX TEM with a 90 kV acceleration voltage. Images were captured using a Gatan ORIUS 11 megapixel digital camera. SWNTs were deposited onto lacey carbon film coated TEM grids (Agar Scientific).

2.4.4 Atomic force microscopy (AFM)

AFM images were recorded using a Bruker AXS Enviroscope with Nanoscope IV electronics, in tapping mode. Bruker MPP-21100-10 AFM tips were used. Resolution in AFM images of SWNT is significantly higher in the z -plane as tip convolution broadens the image in the x - and y - planes. Hence SWNT diameters were always measured via SWNT height.

2.4.5 Micro-Raman microscopy

Micro-Raman spectra were collected using a Renishaw inVia Raman microscope fitted with a CCD detector and either a 633 nm HeNe or a 514 nm Ar⁺ laser (10 mW power) with a spot size of 3 μm . Before measurements the spectrometer was calibrated using the Si peak at 521 cm^{-1} .

2.4.6 X-ray photoelectron microscopy

XPS spectra were taken using a Scienta ESCA300 photoelectron spectrometer, with a monochromated rotating anode Al K α X-ray source at the National Centre for Electron Spectroscopy and Surface analysis, Daresbury Laboratory, UK.

2.4.7 SWNT network density calculation

SWNT network density was calculated from FE-SEM images taken at a minimum of 3 areas of a SWNT network ($10000 \times$ magnification). These images were cropped to leave just the image area and the colour of the images was inverted using the freeware software ImageJ. The images of SWNT networks were analysed using in-house written software (Anthony Holmes) which used the contrast of the images to estimate the length of SWNT in the image, outputting a total length in pixels. By measuring the length of the scale bar provided on the FE-SEM images in pixels, using ImageJ, the length of the SWNT was converted into μm , which can be divided by the image area to give a $\mu\text{m}_{\text{SWNT}} \mu\text{m}^{-2}$ value. A mean value from all images was then calculated. This is summarised in Figure 2.6.

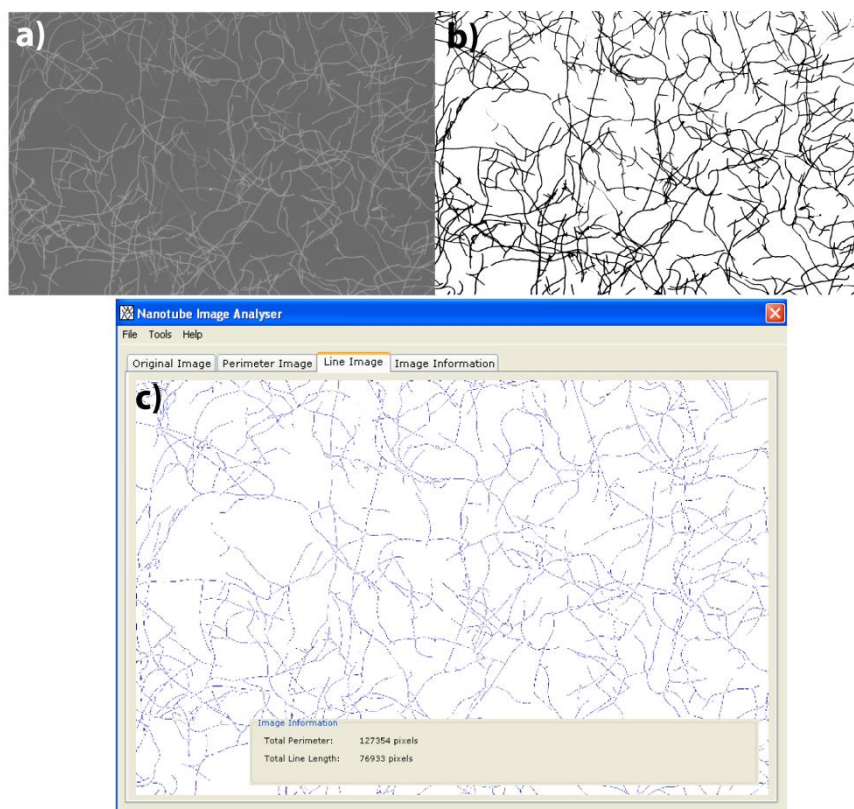


Figure 2.6 – Summary of the SWNT network density calculation process, from a) FE-SEM image, b) colour inversion and c) density calculation.

2.5 Substrate preparation

2.5.1 Evaporation of gold contacts

An electrical connection to SWNT networks and forests was achieved through a gold band, prepared by the evaporation (Moorfields MiniLab 060, Moorfield Associates) of a band of 2 nm Cr (to aid adhesion) followed by 60 nm (2D networks) or 200 nm (3D forests) of Au. The bulk of the SWNTs were protected during evaporation by a mask created by supporting a piece of Si just above the substrate surface with a Si/SiO₂ stack (Figure 2.7) which stopped any Au from coating the area covered.

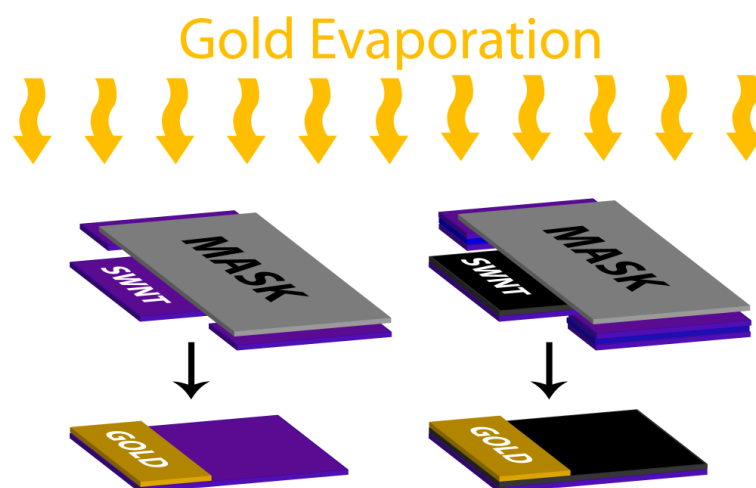


Figure 2.7 – Schematic of masking and evaporation of gold onto SWNT networks and forests.

2.6 Electrochemical measurements

The vast majority of the electrochemical measurements featured in this thesis were performed using capillary based electrochemical methods.⁸⁻¹⁰ These were utilised as they allowed many microelectrode experiments to be performed on the same surface without the need for lithographic processing.

2.6.1 Microcapillary electrochemical method (MCEM)

Electrochemical measurements were performed using the microcapillary electrochemical method.^{8, 11} A glass capillary (Harvard Apparatus, borosilicate glass, 1.2 mm O.D., 0.69 mm I.D.) was pulled to a sharp tip (Sutter instruments P2000 laser puller), polished on a wheel with 0.5 μm diamond lapping disk (Buehler UltraPrep) to reveal an aperture of 40 - 100 μm , characterised using optical microscopy and thoroughly cleaned with ultra-pure water. The outer walls of the capillary were rendered hydrophobic by immersion in dichlorodimethylsilane (Fisher Scientific) for 2 mins with high-purity Ar flowing through the capillary to prevent internal coating. The capillary was filled with the redox mediator of interest (in excess supporting electrolyte), and a quasi-

reference/counter electrode (QRCE) (Pd-H_2 ¹² or Ag/AgCl). Different QRCEs are used as the Ag/AgCl QRCE is unstable in acidic conditions and the same applies for the Pd-H_2 QRCE in neutral conditions.

The substrate being investigated was connected as the working electrode and placed within a humidified glass cell. This cell consisted of a glass body which had a flat viewing window, fitted onto a Teflon base which had a raised central sample platform which allowed a moat below the sample for humidification. The capillary was lowered towards the substrate using an *x-y-z* micropositioner (Newport 433 series) while being monitored by a camera (PixeLINK PL-B776U). Once the capillary was approximately one radius above the surface, a quick tap on the micropositioner caused the electrolyte meniscus at the end of the capillary to ‘snap to contact’ with the surface, with no physical contact between the capillary and the substrate. Once contact had been made a CV was performed using a CHI instruments, model CHI730A, potentiostat. After the measurement was complete the capillary was withdrawn, moved to a new location and the process was repeated. All measurements were made at ambient temperature (23 ± 2 °C). Measurements could be performed under either aerated or deaerated conditions, by flowing hydrated (bubbled through H_2O) N_2 into the cell for 15 mins.

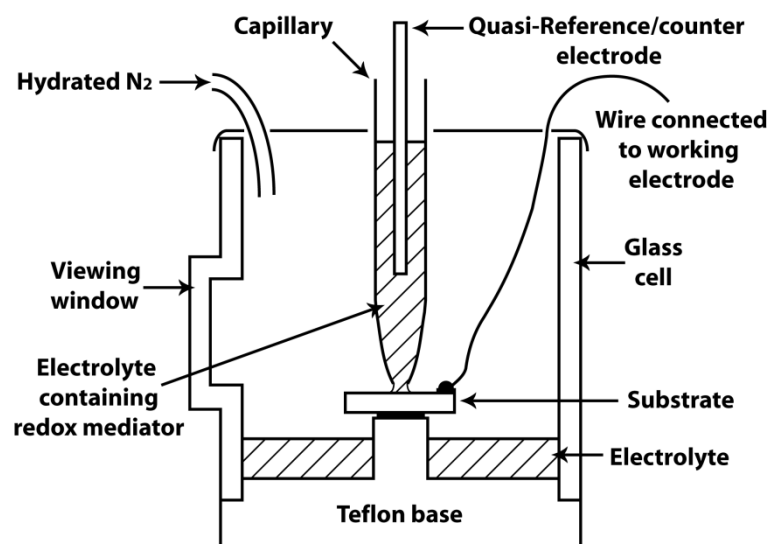


Figure 2.8 – Generalised schematic for a microcapillary electrochemical method (MCEM) measurement. Not to scale.

2.6.2 Nano-scale capillary measurements

The pipet tips were produced by pulling theta glass borosilicate pipets (Harvard Apparatus) using a Sutter instruments P2000 laser puller. Pipets were filled with the solution of interest and Ag/AgCl quasi-reference electrodes were placed in each barrel. Pipets of inner diameter ~400 nm were routinely employed herein and were accurately characterised using FE-SEM.

The pipet was translated towards the surface using a piezoelectric actuator (Physik Instrumente (PI) Nanocube), in conjunction with in-house written software (labview). During approach, a potential bias, corresponding to the diffusion-limited oxidation/reduction potential of the mediator of interest was applied to one barrel of the capillary, whilst the substrate was held at ground. A current was sensed as soon as the meniscus at the end of the capillary established contact with the SWNT forest substrate; at this point the approach was automatically stopped and a CV was run. Both during approach and while on

surface the conductance current between the two barrels of the theta-pipet was used to monitor the state and stability of the meniscus. Changes in the size of the meniscus resulted in a change in the effective resistance between barrels and therefore the current measured. After the measurement was made the pipet was withdrawn, moved to another location and the process was repeated.

2.7 Carbon fibre ultramicroelectrodes (UMEs) for generation/collection

2.7.1 Fabrication

The fabrication method used to produce polymer coated, high aspect ratio carbon fibre UMEs has been reported previously.¹³ A ca. 2 cm length of 8 μm diameter carbon fibre (Goodfellow Cambridge Ltd.) was electrically connected to a copper wire using conductive silver paint (RS) leaving half of the fibre protruding from the end of the wire. This was fitted into a glass capillary (Harvard Apparatus, borosilicate glass, 1.2 mm O.D., 0.69 mm I.D.), leaving the fibre protruding from one end and the Cu wire from the other and the Cu end was sealed using epoxy resin (Araldite) and dried. The end of the capillary with the protruding carbon fibre was sealed using insulating paint, ensuring any metal (Cu or Ag paint) was covered. The carbon fibre was coated in polyoxyphenylene via electropolymerisation by submerging it into a 1:1, methanol (99.5%, Fisher scientific):water solution containing phenol (60 mM, 99.0%, BDH laboratory supplies), 2-allyl phenol (90 mM, 98%, Aldrich), 2-butoxyethanol (156 mM, 99%, Lancaster) and Triton X-405 (0.3 mM, 70%, Acros organics) and applying 4 V vs. Ag/AgCl quasi reference for 30 mins.¹³ The electrode was then annealed

at 150 °C for 30 mins. The UME surface was exposed by removing the end of the fibre with a scalpel.

The carbon fibre UME was modified with Pt NPs by submersion in 0.5 M K_2PtCl_6 (99.99%, Aldrich) in 0.5 M HClO_4 (70%, Acros organics) and cycling between 1.3 V and -0.05 V (vs. Pd- H_2 quasi reference) to drive Pt nucleation for 10 cycles.

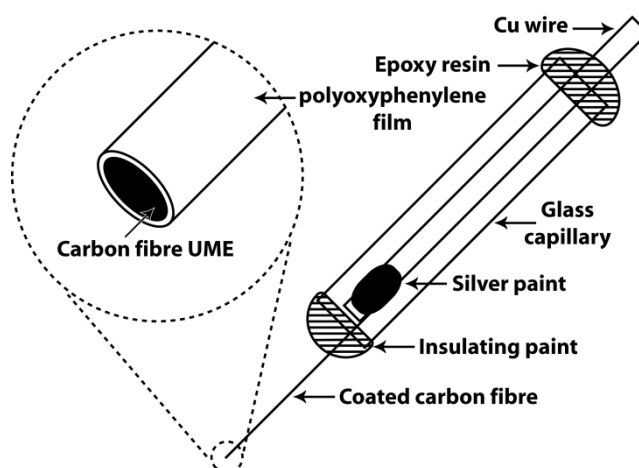


Figure 2.9 – Schematic of a carbon fibre UME. Not to scale.

2.7.2 MCEM generation/collection experiments

To perform generation/collection (G/C) measurements in the meniscus of a microcapillary, the carbon fibre UME was mounted on a second x - y - z micropositioner using a custom capillary holder, positioning it at a 45° angle to the surface. Once the meniscus from the microcapillary had formed on the surface (see section 2.6.1), the carbon fibre UME was carefully inserted from the side (Figure 2.10) with the aid of a high resolution camera. The UME cannot be in contact with the surface as this causes a current overflow on the potentiostat.

Electrochemical measurements were made by scanning the potential of the surface (working electrode 1, generation) while the UME (working electrode

2, collection) was held at a second potential. Measurements were made with a CHI instruments, model CHI730A, bi-potentiostat.

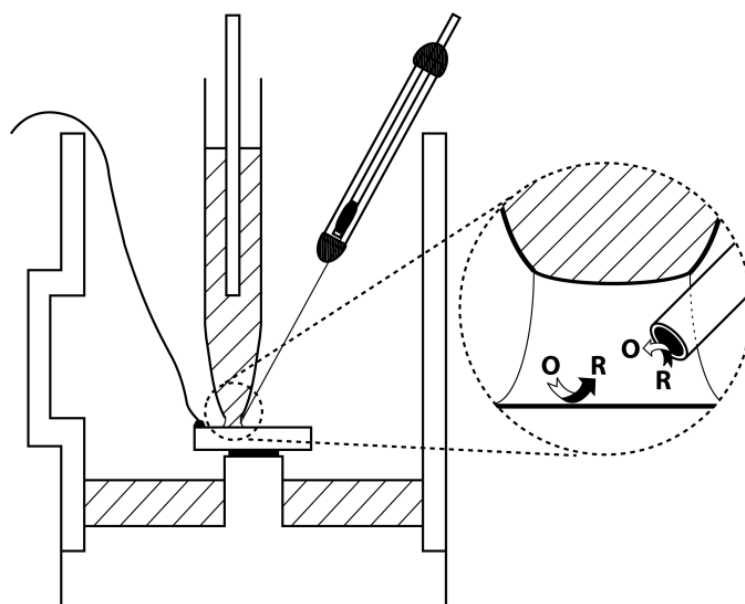


Figure 2.10 – Schematic of the microcapillary based generation/collection set up. Not to scale.

2.8 Chemicals, reagents and materials

Material	Supplier/Details
<i>Substrates</i>	-
Silicon wafer	4", 525 μm thick, <100>, 0.001 – 0.002 $\Omega\text{ cm}$ resistivity, n-type, single-side polished, IDB Technologies Ltd., U.K.
Oxidised silicon wafer	4", 525 μm thick, <100>, 1 – 10 $\Omega\text{ cm}$ resistivity, n-type, single-side polished, 300 nm thermally grown oxide, IDB Technologies Ltd., U.K.
Copper foil	0.025 mm thick, 99.8 %, Alfa Aesar
<i>Solvents</i>	
Acetone	99%, Fisher Scientific
Propan-2-ol	99.99%, Fisher Scientific
Ethanol	99.99%, Fisher Scientific
Methanol	99.5%, Fisher Scientific
Chlorobenzene	$\geq 99.5\%$ Sigma Aldrich Co
<i>Gases</i>	-
Argon	99.9995%, BOC Gases

Hydrogen	99.95%, BOC Gases
Methane	99.995%, BOC Gases
Oxygen	99.5%, BOC Gases
<i>Catalyst deposition from solution</i>	-
Ferritin	Sigma Aldrich Co, 125 mg ferritin (from horse spleen) per ml saline solution
<i>Graphene transfer</i>	-
polymethyl methacrylate (PMMA)	Mw ~ 996 000, Sigma Aldrich Co.
Ammonium persulphate	≥98 % Sigma Aldrich Co.
<i>Catalyst deposition by sputtering</i>	-
Co target	0.5 mm, 99.95%, Testbourne Ltd., U.K.
<i>Evaporation sources</i>	-
Gold wire	99.99%, Goodfellow Cambridge Ltd.
Chromium coated tungsten rod	99.9%, Goodfellow Cambridge Ltd.
<i>Capillaries</i>	-
Borosilicate glass capillaries	1.2 mm outer diameter, 0.69 mm internal diameter, Harvard Apparatus Ltd. USA
Borosilicate theta glass capillaries	1.5 mm outer diameter, 0.13 mm wall thickness, 0.17 mm septum thickness, Harvard Apparatus Ltd. USA
<i>Chemicals for electrochemistry</i>	-
(Ferrocenyl-methyl) trimethylammonium hexafluorophosphate (FcTMA ⁺)PF ₆ ⁻	Prepared via metathesis of FcTMA ⁺ I ⁻ (99%, Stern Chemicals Ltd., UK) with Ag ⁺ PF ₆ ⁻ (99.5%, Stem Chemicals Ltd., UK)
Ruthenium (III) hexaamine (Ru(NH ₃) ₆) ³⁺ Cl ⁻	99%, Stern Chemicals Ltd., UK
Potassium Ferrocyanide K ₄ Fe(CN) ₆ ·3H ₂ O	≥99.99% Sigma-Aldrich Co.
Iron (II) sulphate heptahydarte FeSO ₄ ·7H ₂ O	>99.0% Sigma Aldrich Co.
Sodium Chloride (KCl)	99% Fisher Scientific
<i>Chemicals for metal deposition</i>	-
Potassium Hexachloroplatinate(IV) K ₂ PtCl ₆	99.99%, Sigma Aldrich Co.
<i>Acids</i>	-
Nitric acid	70 %, Fisher Scientific

Hydrochloric acid	37 %, Fisher Scientific
Sulphuric acid	96%, Sigma Aldrich Co.
Perchloric acid	70%, Acros organics
<i>Quasi-reference/counter electrodes</i>	-
Silver wire	99.99%, 0.25 mm diameter, Goodfellow, Cambridge, UK
Palladium wire	99.99%, 0.25 mm diameter, Goodfellow, Cambridge, UK
<i>Electropolymerisation solution</i>	-
Phenol	99.0%, BDH laboratory supplies
2-allyl phenol	98%, Sigma Aldrich Co.
2-butoxyethanol	99%, Lancaster
Triton X-405	70%, Acros organics
<i>Miscellaneous</i>	-
Water	<18 M Ω cm at 25°C Milli-Q, Millipore Corporation

Table 2.2 – List of materials and chemicals used in this work.

2.9 References

1. G. A. Clegg, J. E. Fitton, P. M. Harrison and A. Treffry, *Prog. Biophys. Mol. Biol.*, 1981, **36**, 53-86.
2. Y. Li, W. Kim, Y. Zhang, M. Rolandi, D. Wang and H. Dai, *J. Phys. Chem. B*, 2001, **105**, 11424-11431.
3. C. Kocabas, M. Shim and J. A. Rogers, *J. Am. Chem. Soc.*, 2006, **128**, 4540-4541.
4. J. P. Edgeworth, N. R. Wilson and J. V. Macpherson, *Small*, 2007, **3**, 860-870.
5. B. Zhang, W. H. Lee, R. Piner, I. Kholmanov, Y. Wu, H. Li, H. Ji and R. S. Ruoff, *ACS Nano*, 2012, **6**, 2471-2476.
6. X. Li, Y. Zhu, W. Cai, M. Borysiak, B. Han, D. Chen, R. D. Piner, L. Colombo and R. S. Ruoff, *Nano Lett.*, 2009, **9**, 4359-4363.
7. J. Kang, D. Shin, S. Bae and B. H. Hong, *Nanoscale*, 2012, **4**, 5527-5537.
8. T. M. Day, P. R. Unwin and J. V. Macpherson, *Nano Lett.*, 2007, **7**, 51-57.
9. P. V. Dudin, P. R. Unwin and J. V. Macpherson, *J. Phys. Chem. C*, 2010, **114**, 13241-13248.
10. N. Ebejer, M. Schnippering, A. W. Colburn, M. A. Edwards and P. R. Unwin, *Anal. Chem.*, 2010, **82**, 9141-9145.
11. P. V. Dudin, M. E. Snowden, J. V. Macpherson and P. R. Unwin, *ACS Nano*, 2011, **5**, 10017-10025.
12. M. J. Vasile and C. G. Enke, *J. Electrochem. Soc.*, 1965, **112**, 865-870.
13. D. P. Burt and P. R. Unwin, *Electrochem. Commun.*, 2008, **10**, 934-937.

3

Single walled carbon nanotubes and graphene:

Growth and characterisation

In this chapter the growth of SWNTs in both 2D network and 3D forest formats is investigated, as well as the growth of graphene on copper foil and its subsequent transfer to insulating substrates; all for use in electrochemical applications. These materials are thoroughly characterised by AFM, FE-SEM, micro-Raman spectroscopy as well as other techniques where appropriate, including optical microscopy.

3.1 Introduction

3.1.1 Carbon nanotubes

As discussed in section 1.2.3 cCVD can be optimised to grow pristine (i.e. low defect density) CNTs directly onto insulating substrates (Si/SiO₂, quartz) with minimal contamination from amorphous carbon.^{1, 2} As only a single catalytic NP is required per growing CNT, the total NP density can be kept very low; with the majority of any excess NP remaining electrochemically isolated from the insulating surface.¹ This negates the need for any post-growth cleaning procedures, ensuring the CNTs remain unfunctionalised, unshortened and with their end caps closed.³ A further benefit of cCVD is that if the density of CNTs is above a certain threshold, the resultant ‘network’ will become metal-like, meaning it can be utilised as an electrode in the as-grown format.^{1, 4-6} In this electrode geometry only the electrochemical signal from the CNTs is observed *i.e.* no component from the support substrate making this an ideal substrate for the investigation of the intrinsic electrochemical properties of CNTs.^{7, 8}

As only 1 in 3 SWNT display metal-like behaviour^{9, 10} (the others being semiconductors) the electronic properties of a 2D-SWNT network are heavily dependent on network density.¹ A semiconducting network is created at low densities by ensuring there is no continuous ‘metallic’ to ‘metallic’ SWNT conducting pathways through the network. By increasing the density of SWNT to the point where there is a continuous ‘metallic’ to ‘metallic’ SWNT pathway, the network then takes on metallic conduction properties,¹ and increasing density even further increases the number of these pathways. The threshold between these two distinct points can be predicted through the theory of percolation.^{11, 12}

3D forests are grown by cCVD when the growing SWNT density is so high that the tubes can no longer lie flat onto the surface, but are forced vertically upwards, perpendicular to the substrate.^{13, 14} In this case the density of SWNT is significantly above the density required for metallic network behaviour. However, reports utilising CNT forests as electrodes often use samples with high levels of amorphous carbon or defects^{15, 16} and post process the CNT to form the electrode,^{15, 17} rather than utilising them in the pristine state.

In the first part of this chapter the controlled growth of different density 2D SWNT networks and 3D SWNT forests by cCVD is described. The catalysts systems used in each synthesis are investigated and the resultant SWNT are characterised by FE-SEM, AFM, micro-Raman spectroscopy and XPS.

3.1.2 Graphene

As with CNTs, SLG can be isolated by a variety of techniques, each with its associated issues,¹⁸ as discussed in section 1.7.2. Isolation by chemical exfoliation is capable of producing bulk quantities of SLG, but creates a far from pristine material which is often functionalised with oxygen containing groups.^{19, 20} Conversely, mechanical exfoliation produces a very high quality material, but in small quantities.^{21, 22} However, synthesis by cCVD has been shown to both produce high quality^{23, 24} and large area²⁵ SLG, making this method an excellent synthetic route. Unfortunately, as SLG is usually grown in cCVD using metal catalysts¹⁸ (either foils or layers deposited by evaporation or sputtering) the SLG must usually be transferred to an insulating substrate before it can be utilised to avoid contribution from the underlying material.

Graphene transfer usually involves the coating of the as grown SLG with a polymeric support, commonly PMMA²⁶ polycarbonate (PC)²⁷ or polydimethylsiloxane (PDMS)²⁸, etching the metal catalyst away, transferral to an insulating support and dissolving the polymer coating. During this process the SLG is very prone to damage^{27, 29} and contamination,^{26, 29} which can severely reduce the quality of the as grown SLG. This problem is especially significant for CVD grown SLG graphene samples intended for electrochemical applications as the remaining polymer can impede ET and it is well known that inner sphere ET can be strongly affected by the chemical state of the surface.^{30, 31}

3.2 2D SWNT networks results and discussion

3.2.1 Catalyst nanoparticle deposition

To grow SWNT by cCVD it is (in the vast majority of cases) necessary to utilise metal NP as a catalyst for carbon decomposition.³² The most commonly used metals are iron,³³⁻³⁶ nickel^{37, 38} and cobalt,^{33, 39, 40} although there have been reports using many others e.g. molybdenum⁴¹ and palladium.⁴² In this work SWNT were grown from both Fe and Co NPs, deposited onto Si/SiO₂ by two different methods. Detailed descriptions of the catalyst deposition are given in section 2.1, but briefly, Fe NPs were deposited by a solution based method utilising the iron storage protein ferritin.^{43, 44} This covered the surface in pre-formed Fe NPs, which were surrounded by a shell of protein, which was then removed by exposure to an oxygen plasma. Co catalyst was deposited through the sputtering of a sub-monolayer of Co onto Si/SiO₂. Unlike ferritin deposition, with this method NPs were not formed until the sample was heated (Figure 3.1 a,

b). Because of this, sputtered catalyst deposition has advantages for the patterned growth of SWNT networks as thin films can be easily patterned via masking, although this is not demonstrated here. Figure 3.1 shows the different catalytic NP systems used for 2D network growth.

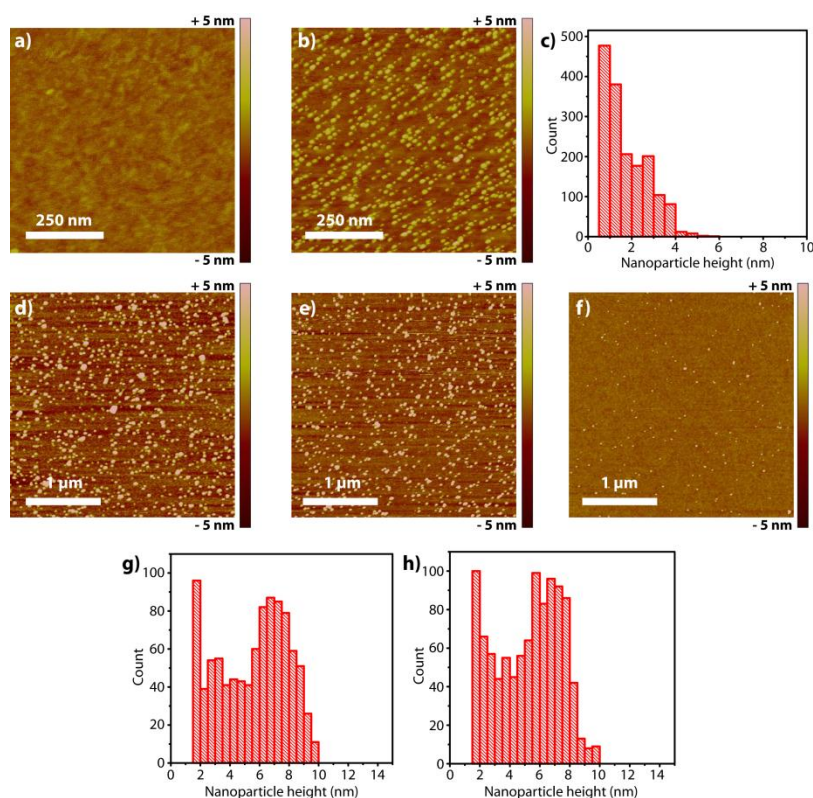


Figure 3.1 – Different catalytic NP systems used for 2D network growth of SWNT (all on Si/SiO₂). a) as deposited sputtered Co, b) Co NP formed by heating (a) to 850 °C under H₂ flow, c) histogram showing the height distribution of Co NPs, d) as deposited ferritin (1:150, ferritin:water), e) resultant Fe NPs after exposing (d) to an oxygen plasma, f) resultant Fe NPs after deposition and exposure to an oxygen plasma of 1:500 (ferritin:water) g) histogram showing the height distribution of ferritin particles (as deposited), h) histogram showing the height distribution of Fe NPs (after oxygen plasma).

Figure 3.1 (a) shows an AFM image of a Si/SiO₂ surface after it has been sputtered with a sub-monolayer of Co. It can be seen that this results in a flat, smooth surface, which is largely indistinguishable from uncoated Si/SiO₂.

However, once this substrate is heated to 850 °C for 10 minutes in a H₂ atmosphere (to keep the Co in a reduced state), a surface rearrangement occurs allowing Co to diffuse across the surface and form particles, resulting in a relatively uniform coverage of Co NPs (Figure 3.1 (b)). From histogram analysis of these NPs (Figure 3.1 (c)) it is apparent that there is a relatively tight distribution in particle size, with the vast majority < 4 nm in height and the mean height being 2.1 nm. Co sputtering is ineffective at producing low densities of catalyst as the deposition of very thin films introduces significant error, reducing reproducibility.

In contrast to the as deposited Co, the as-deposited ferritin with its protein shell still intact (1:150, ferritin:water) is easily distinguishable from the Si/SiO₂ substrate (Figure 3.1 (d)). There is a wide particle size distribution, the majority between 2 and 10 nm, as seen in the histogram analysis (Figure 3.1 (g)). After this substrate has been exposed to an oxygen plasma the density of particles on the surface looks relatively unchanged (Figure 3.1 (e)), however from the histogram in Figure 3.1 (h) it is apparent that there is a slight reduction in the mean particle height from 6.6 to 5.4 nm, indicating that the protein shell has been removed leaving only the Fe core. This NP size correlates with the literature values for the size of the cavity in ferritin (5 – 8 nm),^{43, 44} particles seemingly larger than 8 nm in Figure 3.1 (f) are due to agglomerates. Literature also suggests that ferritin is rarely at its maximum iron storage capacity,⁴³ which may go some way to explain the breadth of the particle height distribution. Fe NPs deposited from ferritin at a lower concentration (1:500, ferritin:water) are shown in Figure 3.1(f), demonstrating how the NP density can be controlled simply through ferritin concentration.

One advantage of sputtered Co deposition over Fe deposition from ferritin is that it allows for the deposition of very high densities of NPs (Figure 3.1 b), for growth of very high densities of SWNTs, which is not possible with ferritin deposition highly concentrated solutions tend to form NP agglomerates on the surface.

3.2.2 2D SWNT network growth and network density evaluation

2D SWNT networks were routinely grown on Si/SiO₂, with the catalyst systems described above, using two different cCVD systems, namely, hot walled cCVD and cold walled cCVD. Details of these systems (including detailed growth schemes) are given in section 2.2, however as both systems produce equally high quality SWNT and there is little discernible difference in the networks produced, the term cCVD will be used interchangeably. A representative cCVD growth scheme is as follows. The substrate (with catalyst) is heated to 850 °C under H₂ flow. Once this temperature has been achieved, argon which has been bubbled through a flask of ethanol (held at 0 °C to maintain a constant vapour pressure) is introduced for 10 mins, which acts as a carbon feedstock. After this time the argon flow is halted and the oven is cooled under H₂ flow until it reaches 200 °C, when the samples can be removed (full growth schemes for all cCVD processes can be found in section 2.2.2).

By tuning cCVD parameters including growth time, growth temperature, ratio of H₂:carbon feedstock and total gas flow rates, it is possible to tune the network density of SWNT; factors which were investigated previously.¹ Here the effect of catalytic NP density on the SWNT density is examined using fixed

growth conditions (section 2.2.2). Figure 3.2 shows AFM and FE-SEM images of SWNT grown from Fe NPs at two distinct densities.

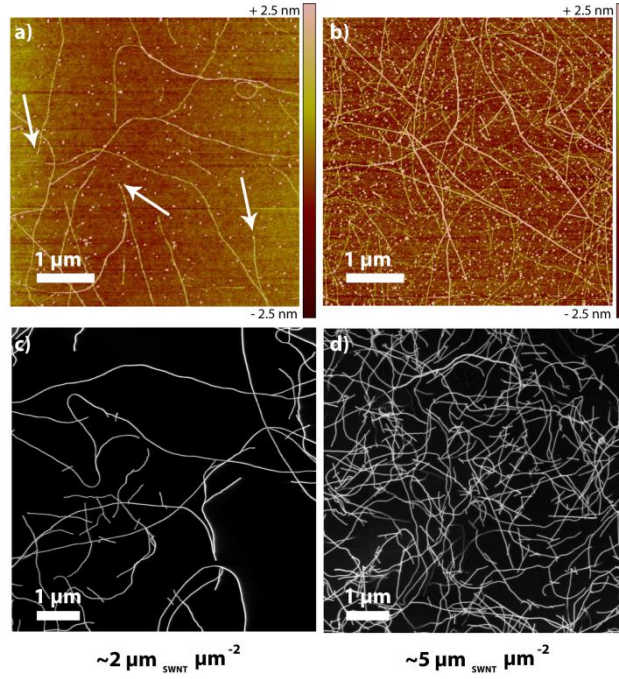


Figure 3.2 – 2D SWNT networks: AFM (a) and FE-SEM (c) of low density ($2 \mu\text{m}_{\text{SWNT}} \mu\text{m}^{-2}$) SWNT network grown using catalyst deposited from 1:500 ferritin:water. AFM (b) and FE-SEM (d) of high density ($5 \mu\text{m}_{\text{SWNT}} \mu\text{m}^{-2}$) SWNT network grown using catalyst deposited from 1:150 ferritin:water.

In the AFM images of the different density networks, shown in Figure 3.2 (a) and (b), we see the catalytic NPs on the surface (as in Figure 3.1), however, it is apparent that the surface is also covered in randomly oriented SWNT. The arrows indicate instances where it is possible to observe a catalytic NP with a SWNT emerging from it, confirming SWNT growth by cCVD is catalysed by NPs.

Depositing different densities of Fe NPs on the Si/SiO₂ surface, by changing the concentration of ferritin in the deposition solution, is shown to grow SWNT networks of different densities. Here for ferritin concentrations of

1:150 and 1:500 (ferritin:water), SWNT network densities of $5 \mu\text{m}_{\text{SWNT}} \mu\text{m}^{-2}$ and $2 \mu\text{m}_{\text{SWNT}} \mu\text{m}^{-2}$ result. These densities were calculated from FE-SEM images (Figure 3.2 c, d) taken at a minimum of three random locations on the network using the method described in section 2.4.7. Although SWNT have diameters on a scale that would usually be difficult to observe using FE-SEM, we are able to use this technique to image SWNT due to charging of the network,⁴⁵ Although SWNT growth is reproducible with cCVD, there is usually some network density variation between samples, meaning each sample must be individually characterised. Network density can be measured from AFM images by measuring the total length of SWNT (in μm) and dividing by the total area (in μm^2). However, as AFM images are often on a small scale (and are relatively slow to capture), this method does not often give the best estimate of the density of the network.

Although calculating the density of SWNT networks is a convenient way to monitor the effect of growth conditions, it is important to link this quantitative value to the electrical characteristics of the network. Based on the theory of percolation, which describes the connectivity of randomly oriented ‘sticks’ on a 2D surface,¹¹ equation (3.1)¹¹ describes the percolation threshold (ρ_{th}) at which a network of randomly oriented ‘sticks’, of a given length, will become connected,

$$\rho_{th} = \frac{17.944}{l\pi} \quad (3.1)$$

where l is the length of a ‘stick’ (i.e. the length of a SWNT). This equation has been adapted to output in the units of $\mu\text{m}_{\text{SWNT}} \mu\text{m}^{-2}$ rather than a number density.

Equation (3.1) assumes all ‘sticks’ are straight, which is not the case for SWNT, however, it does allow for a good approximation of the density required

for a network to form. Unfortunately, it also assumes all ‘sticks’ are of a known and uniform length, which again, is not the case for SWNTs. From FE-SEM analysis an estimate of the mean length of SWNT is $\sim 10 \mu\text{m}$. This was estimated from measurement multiple SWNT (> 100) over multiple (> 5) SWNT networks and is the length used in all further calculations. However, when calculating ρ_{th} one must be aware that this is a potential source of error. The ρ_{th} predicted by equation (3.1) is $\sim 0.55 \mu\text{m}_{\text{SWNT}} \mu\text{m}^{-2}$, meaning this is the density necessary for having a connected network, however, as it is known that only 1 in 3 SWNTs exhibit metallic behaviour,^{9, 10} this density would only be high enough to create a semiconducting network, i.e. $\rho_{th}^{\text{semiconducting}} \approx 0.55 \mu\text{m}_{\text{SWNT}} \mu\text{m}^{-2}$. To create a metallic network the density must be high enough that each SWNT is contacted by 3 others to ensure a metallic_{SWNT} to metallic_{SWNT} contact, therefore $\rho_{th}^{\text{metallic}} \approx 1.65 \mu\text{m}_{\text{SWNT}} \mu\text{m}^{-2}$. It is apparent, therefore, that although the SWNT networks in Figure 3.2 are different densities, both are above $\rho_{th}^{\text{metallic}}$.

To grow SWNTs of a density where they transition from a 2D network to a ‘mat’ of SWNT that cover the bulk of the surface and pile on top of one another (known as very high density, VHD), a higher density of NPs was essential. Agglomeration of ferritin renders high density NP deposition from solution problematic, therefore Co sputtering is used to form NPs. The AFM image in Figure 3.1 (b) shows this method produces a uniform, high density of NPs.

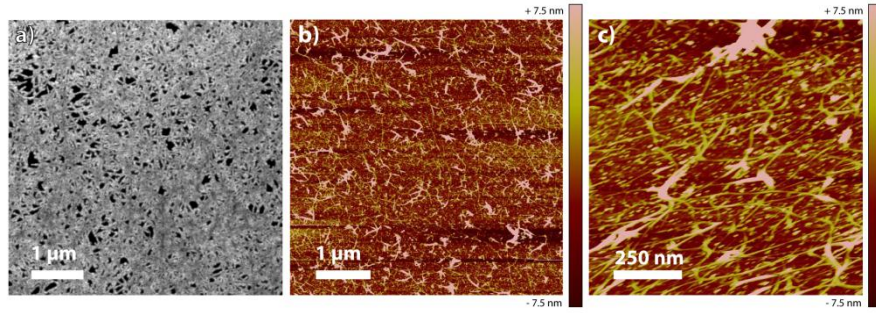


Figure 3.3 - 2D VHD SWNT networks: FE-SEM (a) and AFM (b & c) of a very high density SWNT network.

SWNT networks with VHDs were grown in the hot walled cCVD system from Co NP catalysts (as discussed in 3.2.1) with a growth scheme discussed in section 2.2.2. Figure 3.3 (a) and (b) show FE-SEM and AFM images respectively of a VHD SWNTs network on the same magnification scale as the images shown in Figure 3.2. On this scale it is difficult to discern individual SWNT as the network density is so high, in areas forming layers multiple SWNT thick. In Figure 3.3 (c) a $1 \times 1 \mu\text{m}$ AFM image of this network is shown and on this smaller scale it is easier to resolve SWNT network density. It is obvious that the density here is significantly above $\rho_{th}^{metallic}$, although calculation of the actual density is not trivial due to difficulty in resolving SWNTs in FE-SEM images, meaning density cannot be calculated as described in section 2.4.7. However, by measuring the SWNT length in Figure 3.3 (c), it is estimated that the network density is $> 20 \mu\text{m}_{\text{SWNT}} \mu\text{m}^{-2}$.

3.2.3 Micro-Raman spectroscopy

Micro-Raman spectroscopy was routinely used to characterise SWNT networks, including the $5 \mu\text{m}_{\text{SWNT}} \mu\text{m}^{-2}$ and VHD SWNT networks discussed in section 3.2.2 (shown in Figure 3.4). This technique can be performed on the CNT

on the Si/SiO₂ surface, meaning it is ideal for routine characterisation. SWNTs and MWNTs display micro-Raman spectra with different characteristic peak shapes^{46, 47} which means they can be distinguished from each other. There are two major features of a SWNT micro-Raman spectrum that differentiates it from that of a MWNT. The presence of radial breathing modes (RBM) between 100 and 350 cm⁻¹ caused by the vibration of carbon in the radial direction of the SWNT, not possible in a MWNT due to concentric layers, is one of these. The other is a shoulder on the G band at 1585 cm⁻¹, a peak which is indicative of sp² carbon. In the spectrum for a MWNT this peak would have a single Lorentzian lineshape, however the spectrum of a SWNT network has two peaks due to the presence of both semiconducting and metallic SWNTs.

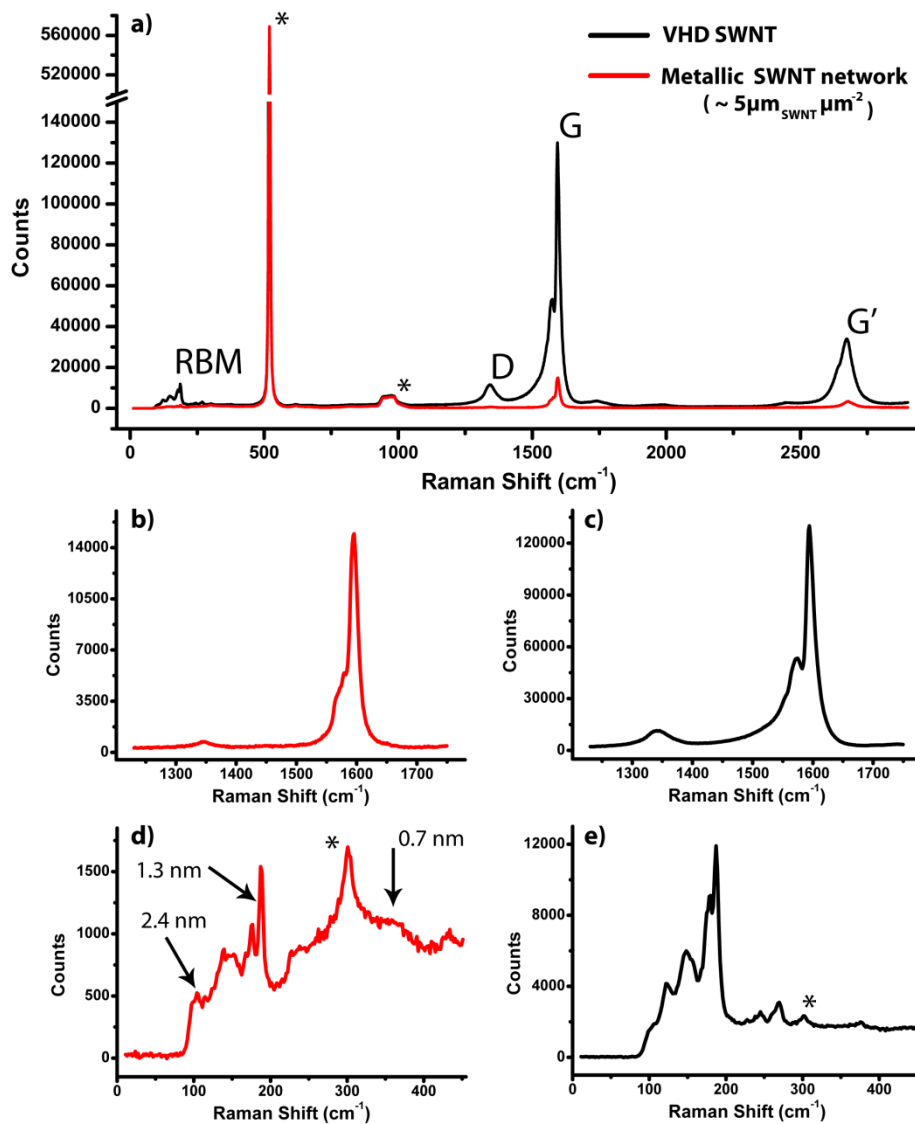


Figure 3.4 – Typical Micro-Raman spectroscopy (laser wavelength 514 nm) of metallic (all red lines) and VHD (all black lines) SWNT networks. a) Full range survey with the RBM, G, D and G' peaks labelled. b) and c) magnification of the D and G peaks. d) and e) magnification of the RBM region.

Figure 3.4 (a) shows the micro-Raman spectra of a metallic SWNT network ($5 \mu\text{m}_{\text{SWNT}} \mu\text{m}^{-2}$) grown from Fe NPs (red line) and a VHD SWNT network grown from Co NP (black line). The peaks marked with an (*) at 303 cm^{-1} , 521 cm^{-1} and 963 cm^{-1} originate from the Si/SiO₂ substrate and not from the SWNT, however, they do act as a useful reference against which other peak

intensities can be measured. In both sets of spectra it is clear that the G peak has a shoulder and there are RBM, confirming that the networks consist of SWNTs, however further analysis allows more information about the networks to be found.

It is apparent that the magnitude of the signal from the two different samples is quite different, with the signal from the VHD sample approximately 1 order of magnitude larger. Both spectra were captured using the same exposure parameters, resulting in the Si/SiO₂ peaks at 521 cm⁻¹ being of comparable heights (565000 and 569000), demonstrating that exposure effects are not the cause of this apparent difference. Normalised peak height has been demonstrated previously as a method for characterisation of SWNT network density,¹ but the data here cannot be directly correlated to this work. However, this work did show that the normalised peak height scales linearly with network density. As the metallic network density was calculated as 5 μm_{SWNT} μm⁻² and the normalised peak height for the VHD sample is ca. 1 order of magnitude larger, the VHD network density could reasonably be estimated to be up to 50 μm_{SWNT} μm⁻².

Micro-Raman spectroscopy can also be used to assess how ‘pristine’ the SWNT networks were, using the ‘D band’ at 1350 cm⁻¹, which originates from sp³ carbon found at defects or in amorphous carbon deposits.^{46, 47} A magnification of this peak can be seen in Figure 3.4 (c) and (d). The higher the ratio of the magnitude of G peak to the magnitude of this peak, the cleaner SWNT network is. This ratio is 12:1 for the VHD SWNT, and 20:1 for the metallic density network, showing that in both cases the SWNT are very clean and have low defect densities.

A magnification of the RBM can be seen in Figure 3.4 (d) and (e) and the presence of many overlapping peaks is apparent. From analysis of the RBM it is possible to calculate the diameters of the SWNTs being analysed. In a single-SWNT micro-Raman spectrum, a single peak would occur in the RBM region as this peak is due to a vibration of the SWNT in the radial direction,^{46, 47} making the SWNT expand and contract as if it were ‘breathing’. Different diameter tubes require different excitation energies to cause this effect, resulting in a Raman shift dependence on SWNT diameter. The SWNT diameter (d_{SWNT}) can be calculated using equation (3.2)^{46, 47}

$$d_{SWNT} = \frac{\alpha}{\omega_{RBM}} \quad (3.2)$$

where α is a proportionality constant experimentally found to be $248 \text{ cm}^{-1} \text{ nm}$ ^{46,}
⁴⁷ and ω_{RBM} is the RBM wavenumber (cm^{-1}).

As shown in Figure 3.4 (d) the RBM appear as a broad peak between 100 and 350 cm^{-1} , which indicates d_{SWNT} ranges from 0.7 nm to 2.4 nm, however, there are clear peaks within this range, the largest of which corresponds to a d_{SWNT} of 1.3 nm, suggesting SWNT of this diameter, and those close to it, occur most frequently. To confirm this analysis, AFM was used to measure the height (in the z -direction) of more than 200 SWNT(across 5 SWNT networks) grown by cCVD from Fe NPs on Si/SiO₂. A histogram of these data is shown in Figure 3.5 (a).

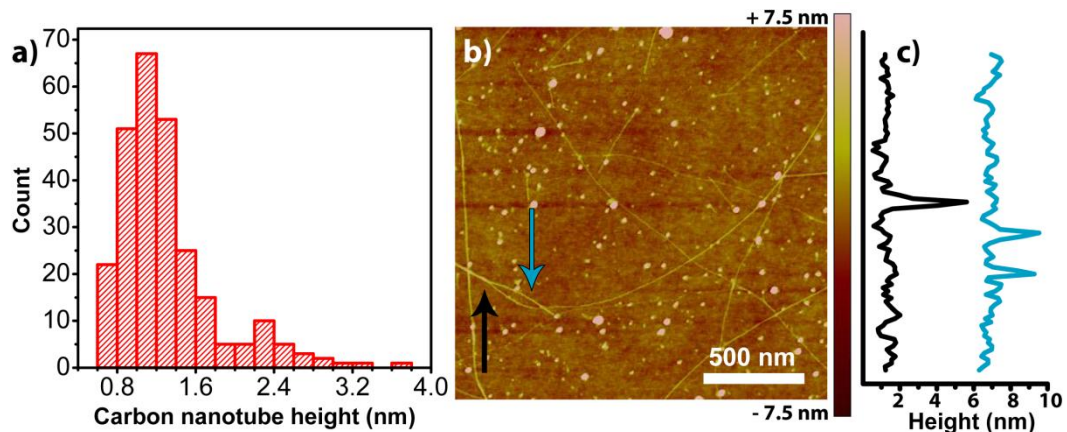


Figure 3.5 – a) Histogram showing the distribution in diameter of SWNT grown from Fe NPs by *c*CVD. b) AFM image of SWNT network, black arrow indicates SWNT bundle, blue arrow indicates the SWNT bundle splitting into individual SWNT, height scale ± 7.5 nm. c) Line trace showing SWNT bundle (black line) and individual SWNT (blue line).

The histogram in Figure 3.5 (a) shows that the significant majority of SWNT measured fit within the range of 0.7 to 2 nm, with the mean d_{SWNT} being 1.3 nm. The modal d_{SWNT} is between 1 and 1.2 nm, which correlates precisely with the analysis from micro-Raman spectroscopy. It is also apparent from the histogram that CNT have been measured up to 4 nm, which could be interpreted as there being a small proportion of MWNT in the network. However, the AFM image in Figure 3.5 (b) demonstrates that these instances of high d_{SWNT} are in fact due to SWNTs bundling, which can appear as a single CNT. The black arrow (and the black line segment shown in Figure 3.5 (c)) show a SWNT bundle which has a $d_{SWNT \text{ bundle}}$ of ~ 4 nm, but as indicated by the blue arrow (and blue line segment) this bundle splits into 2 SWNT with d_{SWNT} of 1.7 nm and 1.9 nm, further demonstrating that the whole network is made of SWNT.

Interestingly, although the Co and Fe NP have a significantly different average particle sizes (2.1 and 5.4 nm respectively) the SWNT that are grown from them have a very similar d_{SWNT} (both ~ 1.3 nm from micro-Raman

spectroscopy in Figure 3.4) suggesting that in this case there is not a precise correlation between catalyst and SWNT diameter, which has been observed previously.¹

3.3 3D SWNT forests results and discussion

3.3.1 Catalyst system

The growth of SWNT forests, where the SWNT density is so high that the SWNT are forced to grow vertically upwards, perpendicular to the substrate due to crowding effects, typically requires the use of a catalyst support material.⁴⁸⁻⁵⁰ The role of this support material, most commonly oxidised aluminium (Al/Al₂O₃),^{13, 51} is to promote catalytic NP activity (and consequently CNT growth).⁴⁹⁻⁵² The roughness of the Al₂O₃ has been shown to mediate the size of the catalytic NPs by reducing surface diffusion, stopping them from agglomerating therefore keeping them at an active size in a high density.⁵¹ In this work we did not aim to investigate the mechanism by which Al/Al₂O₃ promotes CNT growth, but undertook thorough characterisation of the catalyst and support surface to ensure optimum substrates could be replicated.

Details regarding the preparation of the SWNT forest catalyst system can be found in section 2.1.3, however, in all cases the catalyst was prepared by sputtering 10 nm of Al onto Si (with a native oxide layer), which was then oxidised in an oxygen plasma for 2 mins to fully oxidise the surface and remove adsorbed contamination. This substrate was then sputtered with Co for 180 s (6 times the sputtering time used for the VHD samples) which formed into NPs on

heating in the cCVD growth chamber. AFM images of the catalyst system after each of the aforementioned stages can be seen in Figure 3.6.

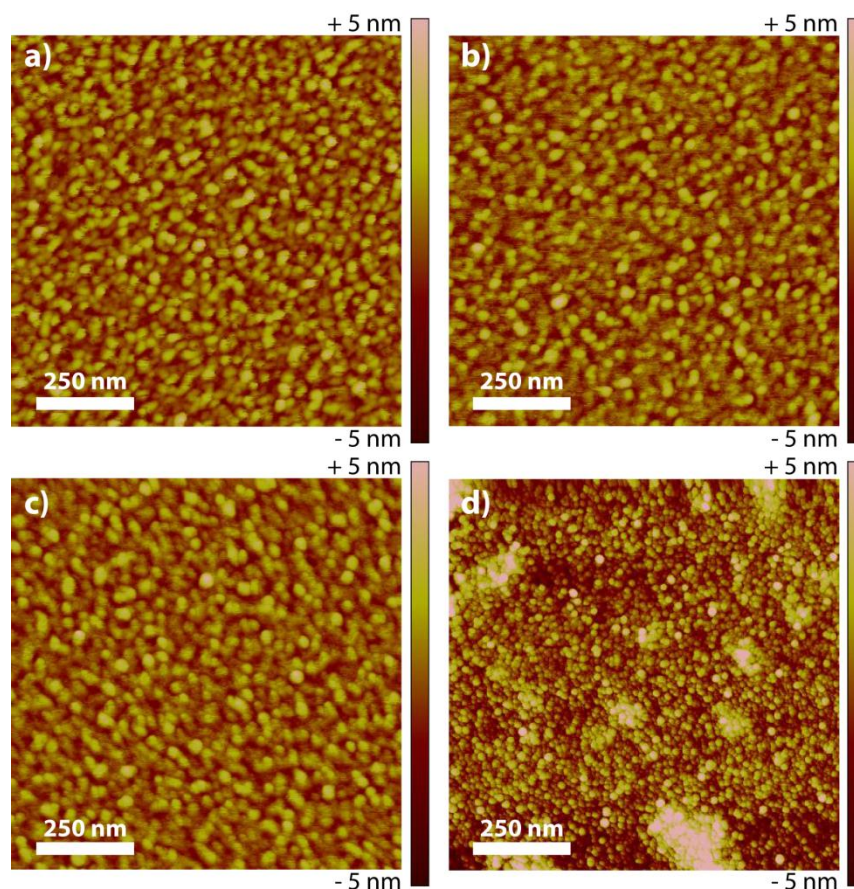


Figure 3.6 – SWNT forest catalyst system a) as deposited Al b) Al after exposure to oxygen plasma 2 mins c) Al/Al₂O₃ with sputtered Co d) Forest catalyst after heating (with no source of carbon).

The as-sputtered Al, shown in Figure 3.6 (a), shows the characteristically large grains found with this material, with a surface roughness of ca. 5 nm. Figure 3.6 (b) and (c) show that exposure to an oxygen plasma and deposition of Co by sputtering have little effect on the resulting surface, including roughness. However, Figure 3.6 (d) shows that heating the catalyst to 850 °C (with no source of carbon) has a significant effect on surface structure and the presence of a very high density of ~ 3 nm NPs (estimated by AFM height analysis) is clear

across the whole of the surface. The high density of stabilised and active NPs means that during growth the density of growing SWNTs is too high to allow them to ‘fall’ onto the surface and form a network, they are instead forced upwards.

To further understand the nature of the different components of the catalyst X-ray photoelectron spectroscopy (XPS) (details found in section 2.4.6) was performed on the substrate in the state shown in Figure 3.6 (d) (heated to 850 °C under H₂ flow). The resultant spectra can be seen in Figure 3.7.

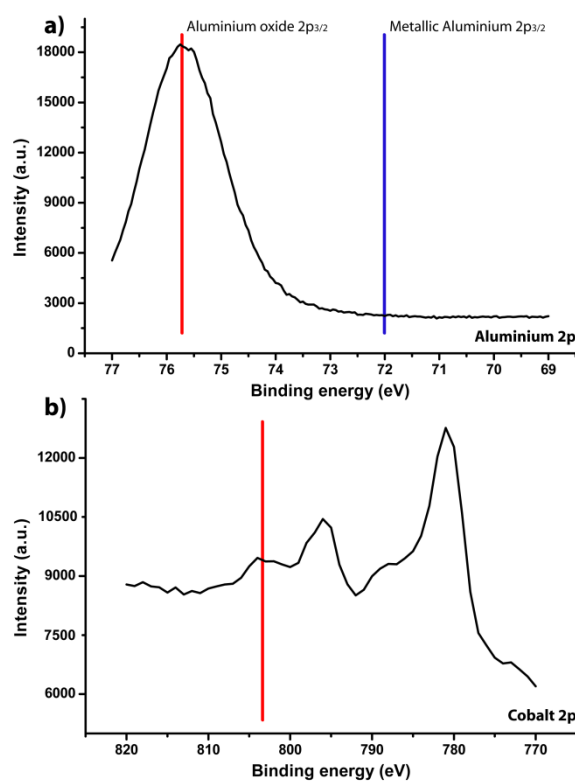


Figure 3.7 – XPS spectra of the SWNT growth catalyst system. a) Al 2p region b) Co 2p region.

The blue line in Figure 3.7 (a) indicates the region in which the Al 2p_{3/2} peak of metallic Al would occur, with the location of the Al 2p_{3/2} for oxidised Al being indicated by the red line. Partially oxidised Al would have peak components in each location, from which the degree of oxidation can be

calculated.⁵³ It is clear from the XPS spectrum of the Al catalyst component that the Al is fully oxidised to Al_2O_3 , with no metallic component remaining.

Characterisation of the XPS spectra of the Co catalyst component is less trivial than for Al as there are multiple forms of oxidised Co, each with its own characteristic Co 2p spectrum.⁵⁴ However, the XPS spectrum for oxidised Co (any form of oxide, CoO , $\text{Co}(\text{OH})_2$ and Co_3O_4)⁵⁴ has a peak at 803 eV (as shown by the red line in Figure 3.7 (b)), which is not present in the metallic form.⁵⁴ It is therefore possible to say that XPS analysis of Co post heating (Figure 3.7 (b)) suggests the Co is, at least to some degree, oxidised, although not necessarily during the growth process.

3.3.2 3D SWNT forest growth and characterisation

SWNT forests were grown using the catalyst system described in section 3.3.1, in the hot-walled cCVD system with growth parameters as detailed in section 2.1.3). Figure 3.8 (a) and (b) show a photograph and an FE-SEM image, respectively, of a typical SWNT forest. For the FE-SEM the forest was scratched with a razor blade to allow both the top and side surfaces to be seen. In the photograph two gold bands have been evaporated onto the forest surface to allow it to be connected as an electrode, which is discussed further in section 2.5.1.

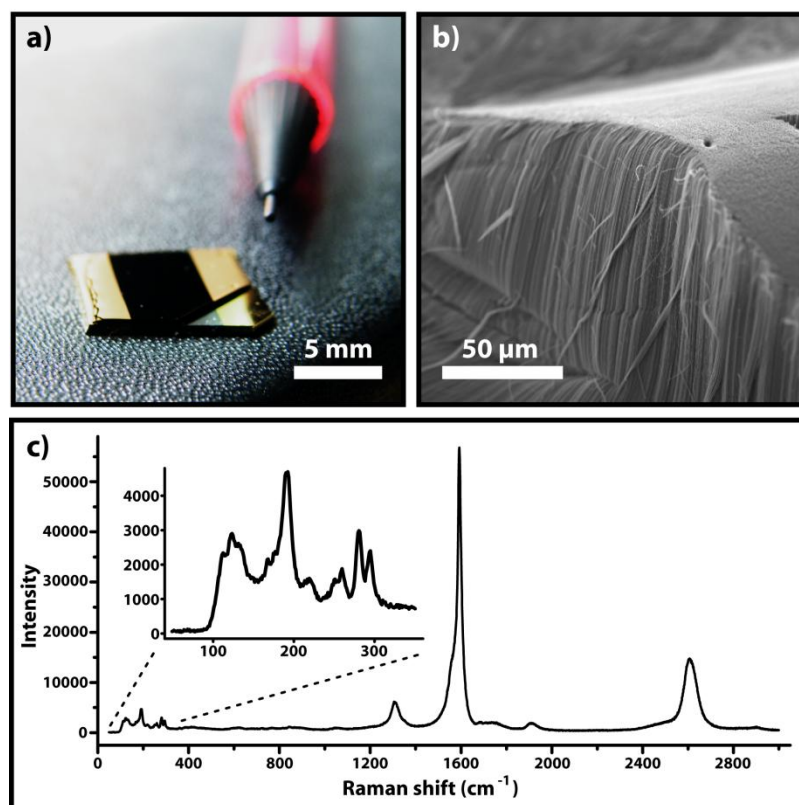


Figure 3.8 – a) photograph of SWNT forest with two gold bands evaporated onto the surface b) FE-SEM image of SWNT forest c) micro-Raman spectrum (laser wavelength 514 nm) of SWNT forest, inset shows the RBM region in more detail.

The photograph in Figure 3.8 (a) clearly shows the millimetre-scale height of this structure as one corner of the forest has been removed, which allows the substrate and the forest edge to be seen. It is also apparent that the forest is very uniform in height and consistent across the surface. The FE-SEM image (Figure 3.8 b) shows both the top surface and the sidewalls of the SWNT forest, where the vertical alignment can be seen. It is also clear that the density of SWNTs is incredibly high, significantly more so than even VHD SWNT networks. Micro-Raman spectroscopy (Figure 3.8 (c)) of the forest confirms, through the shape and position of the G band (1585 cm⁻¹) and presence of RBM (as discussed in section 3.2.3) both that the structure is indeed formed from

CNTs and that they are single-walled. The G:D ratio in this case is 11:1 which, as with the SWNT networks, indicates that the forest is of high quality with little amorphous carbon and few defects and it should be noted that this is significantly higher than other examples of CNT forests in the literature.^{15, 51}

Analysis of the RBM indicates that there is a large range in d_{SWNT} in the forest, from 0.85 nm (290 cm^{-1}) to 2.4 nm (100 cm^{-1}), but the largest peak (at 190 cm^{-1}) once again correlates to a d_{SWNT} of 1.3 nm, which is the same as was found in the SWNT networks and indicates that although the SWNT density is significantly higher in the forest format, the SWNT produced are actually very similar. The spectral features observed at 1750 cm^{-1} and 1950 cm^{-1} are known as the M-band and the iTOLA feature, respectively, and represent double resonance processes. The nature of these features has been shown to depend on SWNT diameter and chirality,⁵⁵ however it is only possible to extract this data from measurements of single SWNTs. Due to the significant height of the SWNT forest it is also notable that there are no peaks present for Si/SiO₂, meaning all features are due to SWNTs.

3.4 Graphene results and discussion

3.4.1 Growth and characterisation of SLG on Cu foils

As with the growth of the SWNT structures discussed above, the first step in the synthesis of SLG is the preparation of the catalyst structures. In the case of SLG growth the catalyst simply consisted of a 0.025 mm thick Cu foil cut into squares $\sim 1 \times 1\text{ cm}^2$, which is a common catalyst system for graphene growth.²³ The use of thin Cu films $\sim 500\text{ nm}$ thick was initially considered, however it was

found that at the temperature required for SLG growth (1000 °C) the thin films became unstable, partially melting and therefore providing a less than ideal catalyst.

Cu foils were prepared for growth by first sonicating in acetone, to remove any residues from the manufacturing process and subsequent handling. Surface oxide contamination was removed using HCl (2 M at 50 °C, 30 s). Once prepared for growth the substrate was inserted into the cCVD system and graphene was grown according to the scheme in section 2.3.3.

Figure 3.9 shows an AFM image of a Cu foil that has been exposed to graphene growth conditions, showing the intersection between three Cu grains. Although it is not possible to see the graphene on the surface, this image does show that despite the high temperature of growth, the Cu foil retains its roughness, which is significant later during transfer. The image also shows that despite the thorough substrate preparation and the use of optimised cCVD parameters the Cu surface is not homogeneous.

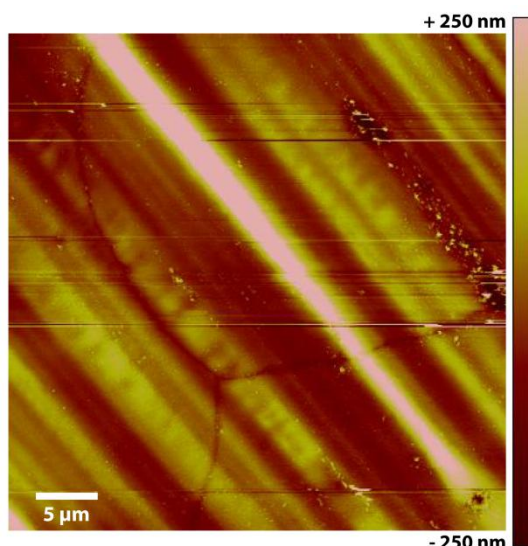


Figure 3.9 – AFM image of a Cu foil post graphene growth according to scheme described in section 2.3.3.

The cCVD growth conditions for the system being utilised in this work needed to be optimised for the growth of SLG. This was achieved by performing micro-Raman spectroscopy on the as grown graphene while it was still on the Cu catalyst surface. This route was taken due to a combination of the risk of damage to as grown graphene grown during any attempt at transfer and due to the large amounts of time that full graphene transfer to Si/SiO₂ takes (~ 2 days between start and end).

Figure 3.10 (d) shows a representative micro-Raman spectrum of a bare Cu surface which had been cleaned, but not exposed to graphene growth conditions. It is clear from this spectrum that the bare Cu surface contributes a significant background to the micro-Raman spectrum, however, there are no peaks in the regions commonly associated with sp² carbon. Micro-Raman spectroscopy performed on copper foils exposed to graphene growth (Figure 3.10 a,b,c), produces spectra with notable peaks above the Cu background, namely the G and 2D (G') peaks usually associated with graphene.^{56, 57} The presence of these peaks was, in the first instance, used as confirmation that the cCVD process was indeed growing a graphitic material. The relative shape and intensity of these peaks was also used to gain further information on the number of graphene layers.

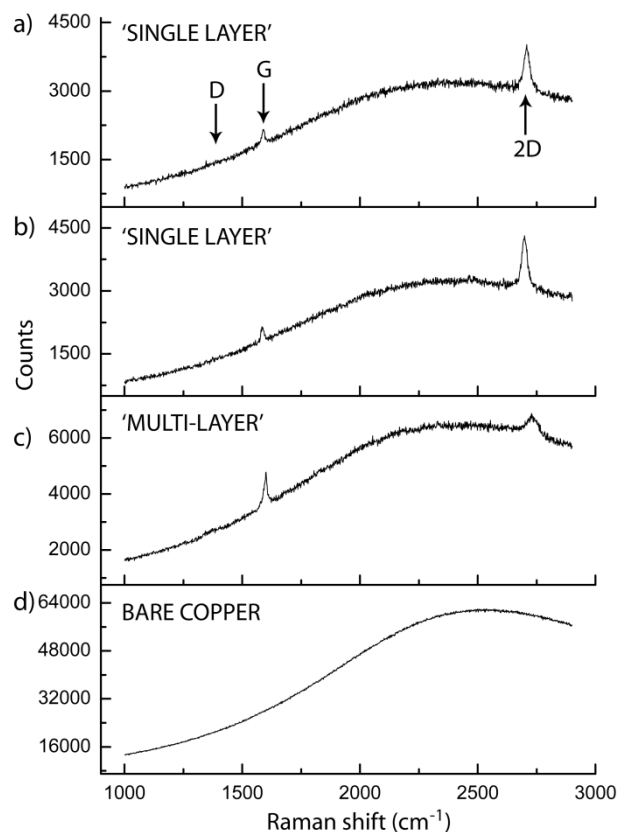


Figure 3.10 – Micro-Raman spectra (laser wavelength 514 nm) on copper: a) and b) single layer graphene, c) multi-layer graphene and d) bare copper. The bare copper sample was exposed for an increased number of cycles to demonstrate that no weak sp^2 carbon peaks were present.

In Figure 3.10 (c) the intensity of the 2D peak can be seen to be of an almost equal magnitude to that of the G peak and is broad, appearing to have at least two components. These features are indicative of graphene with more than two layers,⁵⁶ although due to the background it is difficult to assign any numerical value to the thickness. However, the spectra in both Figure 3.10 (a) and (b) have a 2D peak which is very sharp and appears to be a single Lorentzian feature. This feature also has a relative intensity approximately four times greater than that of their respective G peaks, which is indicative of SLG.^{56, 57} One further notable feature of these spectra is that there is no discernible D peak, the presence of which is indicative of defects in the graphene lattice, or sp^3

contamination. If this peak was small or nonexistent (low defect density) it was obscured by the Cu background, however if sample had a high defect the D peak became visible. This indicates that post-growth the SLG is of high quality.

By using this method of testing, and changing growth parameters such as proportion of CH_4 during growth and growth time, to ensure that each Cu sample displayed SLG characteristics across its entire surface (i.e. micro-Raman spectra appear as those shown in Figure 3.10 (a) and (b)), the cCVD conditions were optimised (details of the optimum parameters can be found in section 2.3.3).

3.4.2 Characterisation of graphene post-transfer to Si/SiO₂.

After growth by cCVD, the Cu catalysts that were confirmed to be covered with SLG were transferred to insulating substrates (Si/SiO₂ or quartz) using the method discussed in section 2.3.4. After this micro-Raman spectroscopy was routinely used to characterise the SLG samples, a representative example of which can be seen in Figure 3.11.

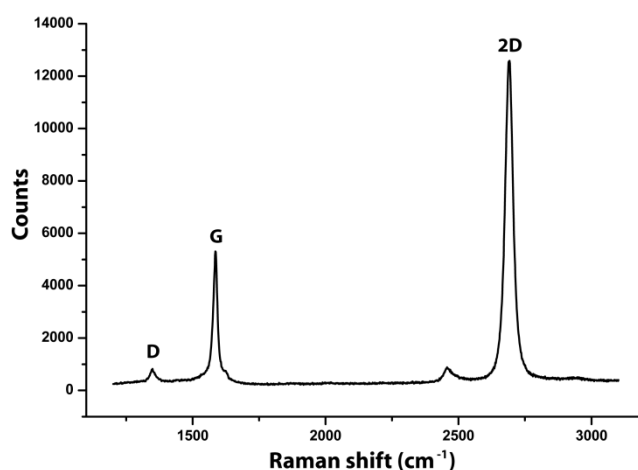


Figure 3.11 – Typical micro-Raman spectra (laser wavelength 514 nm) of SLG on Si/SiO₂

As was seen when graphene was investigated on the Cu, the micro-Raman spectrum shows the characteristic peaks of an sp^2 carbon surface.

However, now the graphene is on a Si/SiO₂ surface, which exhibits a small background, it is possible to analyse the spectrum to glean information on the quality of graphene produced. The micro-Raman spectrum of graphene on Si/SiO₂ does display the characteristics one would expect for SLG, namely the 2D peak is more than twice the height of the G peak and has a full width at half maximum (FWHM) of 31 cm⁻¹, close to the value of ~ 25 cm⁻¹ expected for ideal SLG. This firstly confirms that our cCVD system is capable of growing SLG and also confirms that the use of micro-Raman spectroscopy of graphene on Cu is a valid method of optimisation.

It is, however, also now possible to resolve a small D peak at 1350 cm⁻¹, which is indicative of defects in the graphene structure.⁵⁷ This peak is 6.5 times smaller than the G peak at 1585 cm⁻¹, the ratio of which is indicative of relative defect density, showing that post-transfer the graphene is not perfect. It is difficult to know if these defects are a consequence of growth or if they are introduced during transfer, as a peak only one sixth the size of the G peak would not be discernible in the micro-Raman spectra of SLG on Cu due to background noise.

To further investigate the quality of the SLG, it was investigated using optical microscopy, FE-SEM and AFM. From the optical images shown in Figure 3.12 (a) and (b) it is possible to make a range of conclusions. First, it is clear to see that the graphene is of a uniform colour across the majority of the surface. This indicates that the SLG grows in a uniform manner across the Cu surface, not appearing to form 'islands' of multi-layer structures, which would be seen as darker areas.^{58, 59} Second, the SLG does not appear, on this scale, to be heavily contaminated with residues of polymer that are associated with graphene

transfer. However, the optical images also confirm the SLG is not continuous and contains a series of rips in the surface. As graphene transfer is not a trivial matter and involves multiple aggressive steps, including dissolution of the Cu substrate and later the dissolution of PMMA, there is a tendency for graphene to become damaged.^{27, 29} We have not yet found a satisfactory solution to this problem.

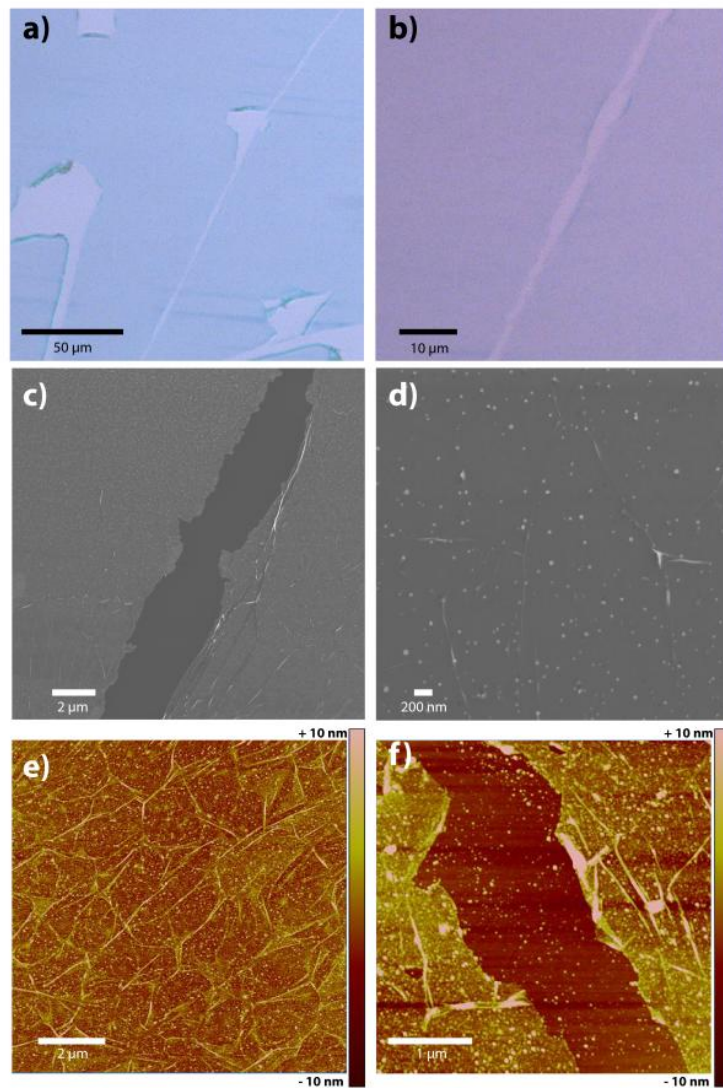


Figure 3.12 – Optical microscope images at a) 200 \times and b) 500 \times magnification, FE-SEM images (c and d) and AFM images (e and f) of SLG on Si with 300 nm SiO₂.

In Figure 3.12 (c) a rip in the SLG can be seen more closely through the use of FE-SEM. It is clear from this image that the two edges of this tear were initially joined and, at some point, were forcefully torn apart, reinforcing the idea that the transfer process is aggressive. From this image and the one shown in Figure 3.12, it is also possible to resolve that the SLG surface is not as clean as it initially seemed. The SLG surface is, in fact, coated in particular contamination, again likely introduced during the transfer stage. Another interesting feature of the FE-SEM images is that it is possible to see that the graphene has ‘wrinkles’, i.e. areas where the SLG does not lie flat on the surface, but has become corrugated. These features are more clearly visible in the AFM images in Figure 3.12 (e) and (f). The wrinkles are considered to originate in part from the difference between the amount of thermal relaxation the metal growth substrates and graphene undergo on cooling post growth⁶⁰ and also from the level of surface roughness of the metal surface causing issues with transfer.⁶¹ Both of these factors cause the graphene to fold up on itself, increasing roughness. The AFM images also more clearly show that the SLG surface is quite contaminated. This contamination is likely to be due to PMMA residues, as PMMA forms a strong interaction with the graphene surface which is not easily broken, even with long exposure to solvents.²⁷ Measurement of graphene layer thickness using AFM proved ineffective as folding at edges and surface contamination made the results inaccurate.

3.4.3 Electrochemical measurements.

Although it has been shown that the SLG produced has surface contamination, it is still of interest to test this material as an electrode as

significant surface coverage (contamination) might negatively affect ET. Two CVs for the oxidation of FcTMA^+ at different areas of a SLG electrode are shown in Figure 3.13. These were performed with a capillary of 50 μm diameter using the microcapillary electrochemical method (MCEM) on SLG connected via the evaporation of a gold band.

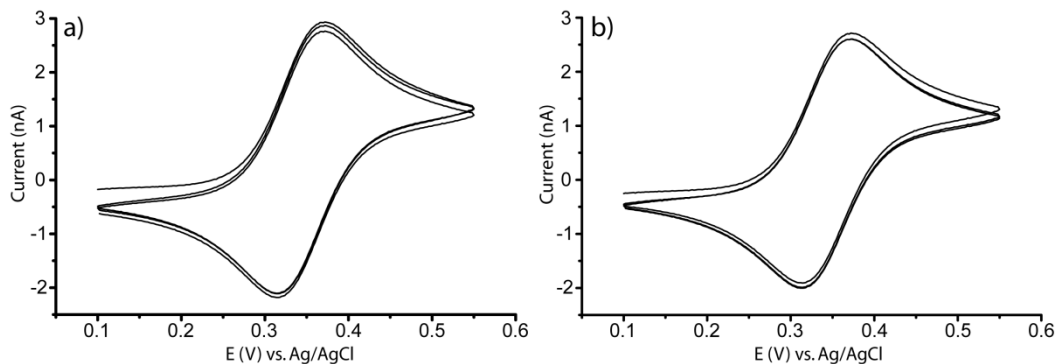


Figure 3.13 – CVs for the oxidation of 0.5 mM FcTMA^+ in 50 mM KCl, 50 mV s^{-1} performed at two different areas of a SLG connected as an electrode.

It can be seen from Figure 3.13 that the transferred SLG seems to perform as an effective electrode, giving CVs with the expected shape for an electrode with a linear diffusion profile. A theoretical value for the peak current (i_p) can be calculated from the Randles–Sevcik equation⁶² for a planar disk macroelectrode

$$i_p = 2.69 \times 10^5 n^{3/2} A D^{1/2} \nu^{1/2} C_{\text{bulk}} \quad (3.3)$$

where n is the number of electrons transferred, A is the electrode area, D is the diffusion coefficient ($6.3 \times 10^{-6} \text{ cm}^2 \text{ s}^{-1}$)⁶³, ν is the scan rate and C_{bulk} is the bulk concentration. Based on a meniscus radius of 65 μm (previously shown to be larger than the capillary radius^{64, 65} and also shown in section 6.3.2) i_p is expected to be 2.5 nA, which is comparable to the i_p for FcTMA^+ oxidation on SLG (2.4 – 2.7 nA). Also, for the oxidation of FcTMA^+ ΔE_p is found to be 58 mV (Figure

3.13 a) and 59 mV (Figure 3.13 b). This demonstrates that the outer sphere process $\text{FcTMA}^{+/2+}$ acts reversibly when SLG is utilised as an electrode.

Although this data demonstrates that the SLG being produced currently is capable of fast heterogeneous ET it would be erroneous to use this to draw any conclusions on the ET properties of pristine SLG, due to the presence of contaminants and wrinkles which may play a role in ET.

3.5 Conclusions

This work has demonstrated that cCVD is a powerful tool for the production of sp^2 carbon materials. Through the judicious choice of catalyst materials and growth parameters it is possible to grow structures ranging from 2D SWNT networks, 3D SWNT forests and SLG.

The SWNT produced have been thoroughly characterised both microscopically and spectroscopically and have been shown to be of high quality with a low density of defects and minimal amounts of amorphous carbon. This work has also demonstrated that we are capable of the reliable growth of SLG. This was achieved by optimising the cCVD growth conditions and routinely characterising the as grown material on the Cu growth substrate using micro-Raman spectroscopy. However, during transfer to insulating substrates the SLG is contaminated and torn, issues which have not yet been satisfactorily resolved. By working on the graphene transfer regime we aim in the future to produce SLG to a similar level of quality as we are currently capable of for SWNT which can then be used for electrochemical applications.

3.6 References

1. J. P. Edgeworth, N. R. Wilson and J. V. Macpherson, *Small*, 2007, **3**, 860-870.
2. H. Dai, A. G. Rinzier, P. Nikolaev, A. Thess, D. T. Colbert and R. E. Smalley, *Chem. Phys. Lett.*, 1996, **260**, 471-475.
3. I. Dumitrescu, N. R. Wilson and J. V. Macpherson, *J. Phys. Chem. C*, 2007, **111**, 12944-12953.
4. I. Dumitrescu, P. R. Unwin, N. R. Wilson and J. V. Macpherson, *Anal. Chem.*, 2008, **80**, 3598-3605.
5. I. Dumitrescu, P. R. Unwin and J. V. Macpherson, *Electrochem. Commun.*, 2009, **11**, 2081-2084.
6. I. Dumitrescu, P. V. Dudin, J. P. Edgeworth, J. V. Macpherson and P. R. Unwin, *J. Phys. Chem. C*, 2010, **114**, 2633-2639.
7. A. G. Güell, N. Ebejer, M. E. Snowden, K. McKelvey, J. V. Macpherson and P. R. Unwin, *Proceedings of the National Academy of Sciences*, 2012.
8. I. Heller, J. Kong, H. A. Heering, K. A. Williams, S. G. Lemay and C. Dekker, *Nano Lett.*, 2004, **5**, 137-142.
9. H. Dai, *Surf. Sci.*, 2002, **500**, 218-241.
10. R. Saito, M. Fujita, G. Dresselhaus and M. S. Dresselhaus, *Appl. Phys. Lett.*, 1992, **60**, 2204-2206.
11. L. Hu, D. S. Hecht and G. Grüner, *Nano Lett.*, 2004, **4**, 2513-2517.
12. G. E. Pike and C. H. Seager, *Phys. Rev. B*, 1974, **10**, 1421-1434.
13. K. Hata, D. N. Futaba, K. Mizuno, T. Namai, M. Yumura and S. Iijima, *Science*, 2004, **306**, 1362-1364.
14. H. Cui, G. Eres, J. Y. Howe, A. Puretzky, M. Varela, D. B. Geohegan and D. H. Lowndes, *Chem. Phys. Lett.*, 2003, **374**, 222-228.
15. K. Gong, S. Chakrabarti and L. Dai, *Angew. Chem. Int. Ed.*, 2008, **47**, 5446-5450.
16. J. Li, A. Cassell, L. Delzeit, J. Han and M. Meyyappan, *J. Phys. Chem. B*, 2002, **106**, 9299-9305.
17. D. J. Garrett, P. A. Brooksby, F. J. Rawson, K. H. R. Baronian and A. J. Downard, *Anal. Chem.*, 2011, **83**, 8347-8351.
18. Y. Zhu, S. Murali, W. Cai, X. Li, J. W. Suk, J. R. Potts and R. S. Ruoff, *Adv. Mater.*, 2010, **22**, 3906-3924.
19. S. Stankovich, D. A. Dikin, R. D. Piner, K. A. Kohlhaas, A. Kleinhammes, Y. Jia, Y. Wu, S. T. Nguyen and R. S. Ruoff, *Carbon*, 2007, **45**, 1558-1565.
20. D. W. Boukhvalov and M. I. Katsnelson, *J. Am. Chem. Soc.*, 2008, **130**, 10697-10701.
21. K. S. Novoselov, D. Jiang, F. Schedin, T. J. Booth, V. V. Khotkevich, S. V. Morozov and A. K. Geim, *Proc. Natl. Acad. Sci. U.S.A.*, 2005, **102**, 10451-10453.
22. A. K. Geim and K. S. Novoselov, *Nat. Mater.*, 2007, **6**, 183-191.
23. X. Li, W. Cai, J. An, S. Kim, J. Nah, D. Yang, R. Piner, A. Velamakanni, I. Jung, E. Tutuc, S. K. Banerjee, L. Colombo and R. S. Ruoff, *Science*, 2009, **324**, 1312-1314.

24. X. Li, Y. Zhu, W. Cai, M. Borysiak, B. Han, D. Chen, R. D. Piner, L. Colombo and R. S. Ruoff, *Nano Lett.*, 2009, **9**, 4359-4363.
25. Y. Lee, S. Bae, H. Jang, S. Jang, S.-E. Zhu, S. H. Sim, Y. I. Song, B. H. Hong and J.-H. Ahn, *Nano Lett.*, 2010, **10**, 490-493.
26. J. Kang, D. Shin, S. Bae and B. H. Hong, *Nanoscale*, 2012, **4**, 5527-5537.
27. Y.-C. Lin, C. Jin, J.-C. Lee, S.-F. Jen, K. Suenaga and P.-W. Chiu, *ACS Nano*, 2011, **5**, 2362-2368.
28. K. S. Kim, Y. Zhao, H. Jang, S. Y. Lee, J. M. Kim, K. S. Kim, J.-H. Ahn, P. Kim, J.-Y. Choi and B. H. Hong, *Nature*, 2009, **457**, 706-710.
29. D.-Y. Wang, I. S. Huang, P.-H. Ho, S.-S. Li, Y.-C. Yeh, D.-W. Wang, W.-L. Chen, Y.-Y. Lee, Y.-M. Chang, C.-C. Chen, C.-T. Liang and C.-W. Chen, *Adv. Mater.*, 2013, **25**, 4521-4526.
30. P. Chen and R. L. McCreery, *Anal. Chem.*, 1996, **68**, 3958-3965.
31. R. L. McCreery, *Chem. Rev.*, 2008, **108**, 2646-2687.
32. E. Mora, J. M. Pigós, F. Ding, B. I. Yakobson and A. R. Harutyunyan, *J. Am. Chem. Soc.*, 2008, **130**, 11840-11841.
33. V. Ivanov, J. B. Nagy, P. Lambin, A. Lucas, X. B. Zhang, X. F. Zhang, D. Bernaerts, G. Van Tendeloo, S. Amelinckx and J. Van Landuyt, *Chem. Phys. Lett.*, 1994, **223**, 329-335.
34. M. Jose-Yacamán, M. Miki-Yoshida, L. Rendon and J. G. Santiesteban, *Appl. Phys. Lett.*, 1993, **62**, 657-659.
35. S. Fan, M. G. Chapline, N. R. Franklin, T. W. Tombler, A. M. Cassell and H. Dai, *Science*, 1999, **283**, 512-514.
36. Q. Fu, S. Huang and J. Liu, *J. Phys. Chem. B*, 2004, **108**, 6124-6129.
37. M. L. Terranova, V. Sessa and M. Rossi, *Chem. Vap.*, 2006, **12**, 315-325.
38. P. M. Campbell, E. S. Snow and J. P. Novak, *Appl. Phys. Lett.*, 2002, **81**, 4586-4588.
39. Y. Murakami, Y. Miyauchi, S. Chiashi and S. Maruyama, *Chem. Phys. Lett.*, 2003, **377**, 49-54.
40. S. Amelinckx, X. B. Zhang, D. Bernaerts, X. F. Zhang, V. Ivanov and J. B. Nagy, *Science*, 1994, **265**, 635-639.
41. D. Yuan, L. Ding, H. Chu, Y. Feng, T. P. McNicholas and J. Liu, *Nano Lett.*, 2008, **8**, 2576-2579.
42. D. Takagi, Y. Homma, H. Hibino, S. Suzuki and Y. Kobayashi, *Nano Lett.*, 2006, **6**, 2642-2645.
43. G. A. Clegg, J. E. Fitton, P. M. Harrison and A. Treffry, *Prog. Biophys. Mol. Biol.*, 1981, **36**, 53-86.
44. X. Liu and E. C. Theil, *Acc. Chem. Res.*, 2005, **38**, 167-175.
45. T. Brintlinger, Y.-F. Chen, T. Durkop, E. Cobas, M. S. Fuhrer, J. D. Barry and J. Melngailis, *Appl. Phys. Lett.*, 2002, **81**, 2454-2456.
46. M. S. Dresselhaus, G. Dresselhaus, A. Jorio, A. G. Souza Filho, M. A. Pimenta and R. Saito, *Acc. Chem. Res.*, 2002, **35**, 1070-1078.
47. M. S. Dresselhaus, G. Dresselhaus, R. Saito and A. Jorio, *Phys. Rep.*, 2005, **409**, 47-99.
48. J.-h. Han, H. J. Kim, M.-H. Yang, C. W. Yang, J.-B. Yoo, C.-Y. Park, Y.-H. Song and K.-S. Nam, *Mater. Sci. Eng. C*, 2001, **16**, 65-68.
49. L. Delzeit, B. Chen, A. Cassell, R. Stevens, C. Nguyen and M. Meyyappan, *Chem. Phys. Lett.*, 2001, **348**, 368-374.

50. T. de los Arcos, M. Gunnar Garnier, P. Oelhafen, D. Mathys, J. Won Seo, C. Domingo, J. Vicente Garcia-Ramos and S. Sanchez-Cortes, *Carbon*, 2004, **42**, 187-190.
51. D. P. Burt, W. M. Whyte, J. M. R. Weaver, A. Glidle, J. P. Edgeworth, J. V. Macpherson and P. S. Dobson, *J. Phys. Chem. C*, 2009, **113**, 15133-15139.
52. H. Hongo, F. Nihey, T. Ichihashi, Y. Ochiai, M. Yudasaka and S. Iijima, *Chem. Phys. Lett.*, 2003, **380**, 158-164.
53. B. R. Strohmeier, *Surf. Interface Anal.*, 1990, **15**, 51-56.
54. M. C. Biesinger, B. P. Payne, A. P. Grosvenor, L. W. M. Lau, A. R. Gerson and R. S. C. Smart, *Appl. Surf. Sci.*, 2011, **257**, 2717-2730.
55. V. W. Brar, G. G. Samsonidze, M. S. Dresselhaus, G. Dresselhaus, R. Saito, A. K. Swan, M. S. Ünlü, B. B. Goldberg, A. G. Souza Filho and A. Jorio, *Phys. Rev. B*, 2002, **66**, 155418.
56. A. C. Ferrari, J. C. Meyer, V. Scardaci, C. Casiraghi, M. Lazzeri, F. Mauri, S. Piscanec, D. Jiang, K. S. Novoselov, S. Roth and A. K. Geim, *Phys. Rev. Lett.*, 2006, **97**, 187401.
57. L. M. Malard, M. A. Pimenta, G. Dresselhaus and M. S. Dresselhaus, *Phys. Rep.*, 2009, **473**, 51-87.
58. P. Blake, E. W. Hill, A. H. C. Neto, K. S. Novoselov, D. Jiang, R. Yang, T. J. Booth and A. K. Geim, *Appl. Phys. Lett.*, 2007, **91**, 063124-063123.
59. A. Reina, X. Jia, J. Ho, D. Nezich, H. Son, V. Bulovic, M. S. Dresselhaus and J. Kong, *Nano Lett.*, 2008, **9**, 30-35.
60. A. N. Obraztsov, E. A. Obraztsova, A. V. Tyurnina and A. A. Zolotukhin, *Carbon*, 2007, **45**, 2017-2021.
61. N. Liu, Z. Pan, L. Fu, C. Zhang, B. Dai and Z. Liu, *Nano Res.*, 2011, **4**, 996-1004.
62. A. J. Bard and L. R. Faulkner, *Electrochemical Methods: Fundamentals and Applications, 2nd Edition*, 2nd edn., John Wiley & Sons, Inc, 2001.
63. P. Bertoncello, I. Ciani, F. Li and P. R. Unwin, *Langmuir*, 2006, **22**, 10380-10388.
64. T. M. Day, P. R. Unwin, N. R. Wilson and J. V. Macpherson, *J. Am. Chem. Soc.*, 2005, **127**, 10639-10647.
65. P. V. Dudin, P. R. Unwin and J. V. Macpherson, *J. Phys. Chem. C*, 2010, **114**, 13241-13248.

4

Electrochemistry at single-walled carbon nanotube forests: sidewalls and closed ends allow fast electron transfer

In this chapter the intrinsic electrochemical properties of the closed ends and sidewalls of pristine SWNT forests are investigated directly using a nanopipet electrochemical cell. Both are shown to promote fast electron transfer, with no activation or processing of the CNT material required. This is in contrast to the current model in the literature which suggests that the sidewalls of CNT are inactive (except at defected sites) and the vast majority of electron transfer occurs at the open ends of CNT.

4.1 Introduction

CNTs are of considerable interest for a wide variety of applications including batteries,¹ sensors^{2,3} and electrocatalysts,^{4,5} to name but a few, and can be arranged in a multitude of different geometries, ranging from 1D isolated tubes to 2D planar arrays and random networks, and 3D forests. The forest is particularly interesting with wide ranging applications.⁶⁻⁸ In the electrochemical arena, forests have been proposed for sensing and energy applications,⁹ with the vast majority of studies focusing on forests with open ends. Open ends also provide sites for surface functionalisation.¹⁰ Furthermore, open-ended CNT forests have been proposed as the preferred arrangement for electrochemistry,¹¹ since some work has suggested that heterogeneous electron transfer occurs much more readily at open ends, rather than sidewalls, of CNTs in general, with sidewalls suggested as being electrochemically inert¹²⁻¹⁴, even to simple ‘outer sphere’ redox couples. This analysis stems, in part, from analogies drawn between the structure of MWNTs and HOPG,¹⁵⁻¹⁷ which comprises of sp^2 carbon basal planes interspersed with edge planes.^{13, 18, 19} The postulate that only the open ends of MWNTs are electrochemically active, has also been extended to SWNTs.^{13, 19} On the other hand, studies of isolated²⁰⁻²² and randomly arranged two-dimensional networks of SWNTs²³ have shown that the sidewalls of SWNTs promote facile electron transfer. This provides an impetus to determine whether similar activity is evident in SWNT forests.

Many of the standard methods for growing CNTs result in structures with closed tube ends.¹⁴ However, as clean-up procedures (often using harsh purification steps including boiling in concentrated acid, sonication and plasma treatments) are typically required to eliminate amorphous carbon and metal

NPs,²⁴ the ends are opened and sidewall defects are created.^{12, 25} Not only can functionalization of CNTs, from chemical clean-up, complicate electrochemical data interpretation, but a further issue with many previous studies of CNT electroactivity has been a reliance on a conducting support for the CNTs. This makes the unambiguous separation of CNT activity and support electrode effects very difficult.²⁴ In comparison, SWNTs produced by CVD can be grown directly onto an insulating substrate, (usually Si/SiO₂ or quartz) but surprisingly, have been less studied as an electrode material. Such material is also close to ideal for fundamental studies because it is grown with minimal levels of amorphous carbon, and thus requires no chemical clean up before use. Furthermore, each CNT contains only a single, encapsulated, catalytic nanoparticle, at one end²⁶ with the other end retaining a pristine closed structure.²⁷⁻²⁹

In this work we investigate SWNT forests grown by CVD providing electrodes, where the closed ends and sidewalls are intrinsically separated, but without the disadvantages associated with single CNT experiments. This method was chosen in preference to chemical processing and vertical alignment via chemical binding to a substrate, as CVD enables high density, pristine, closed-ended SWNTs to be grown directly. Chemical processing, results in cutting and shortening of the SWNTs and an incomplete coverage of the underlying conducting substrate.^{13, 30} These structures are tested using a new nanoscale electrochemical cell technique,^{31, 32} which allows us to examine electrochemistry at the characteristic closed ends and sidewall sites, in isolation. In essence, a nanopipet containing electrolyte solution and one or more reference/counter electrode(s) is used to make an electrochemical cell within a targeted region of a sample, which is connected as a working electrode. For the present application,

this is particularly powerful, as any type of post processing, lithography²⁰ or mechanical cutting of the SWNTs is avoided,³³ allowing the study of the true electrochemical activity of the forests in the native, pristine, unprocessed state.

4.2 Results and discussion

4.2.1 Preparation and characterisation of SWNT forest electrodes

Figure 4.1 shows a representative FE-SEM image of an as-grown (details given in sections 2.2.2 and 3.3) CVD SWNT forest (a) and a typical TEM image (b) of a SWNT extracted from the forest. In this case SWNTs were deposited onto lacey carbon film coated TEM grids by rubbing the grid onto the side of the forest, this was found to introduce less contamination and cause less damage to the SWNT than solution based methods (sonication).

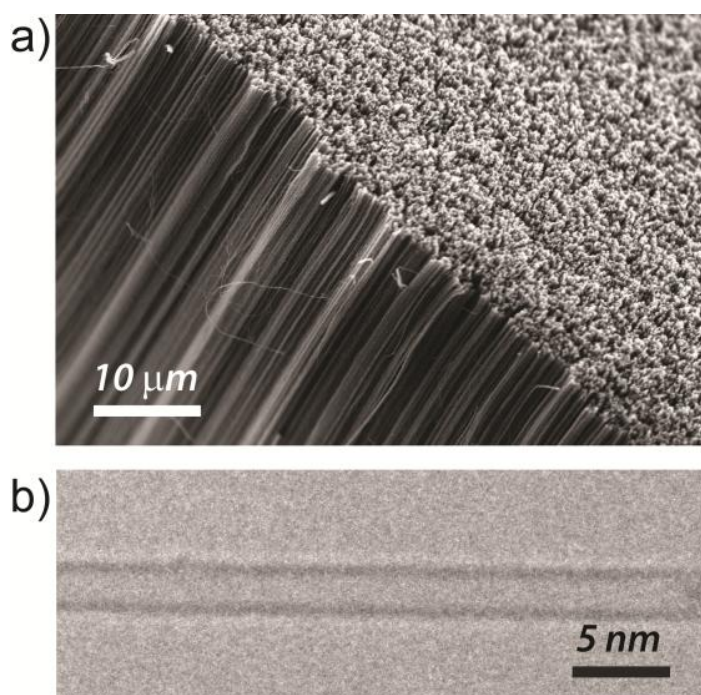


Figure 4.1 - (a) FE-SEM image of a SWNT forest. (b) Typical TEM image of a SWNT extracted from a forest.

The FE-SEM image in Figure 4.1(a) clearly shows the two unique surfaces of the SWNT forest. In the bottom left half of the image the surface consisting of a vast majority of SWNT sidewalls can be seen, showing the characteristic alignment and dense CNT packing of forest structures. The vertical height of the SWNT forests used in this investigation was ca. 0.5 mm when measured from the substrate. In the top right of the image the surface mainly consisting of closed SWNT ends is shown. TEM analysis of CNTs extracted from the forest confirmed that they were single-walled and the absence of any amorphous carbon on the SWNT sidewall is noteworthy. The high quality of the forests was further proven using micro-Raman spectroscopy on intact forests, with spectra recorded from both the SWNT ends and the sidewalls (Figure 4.2).

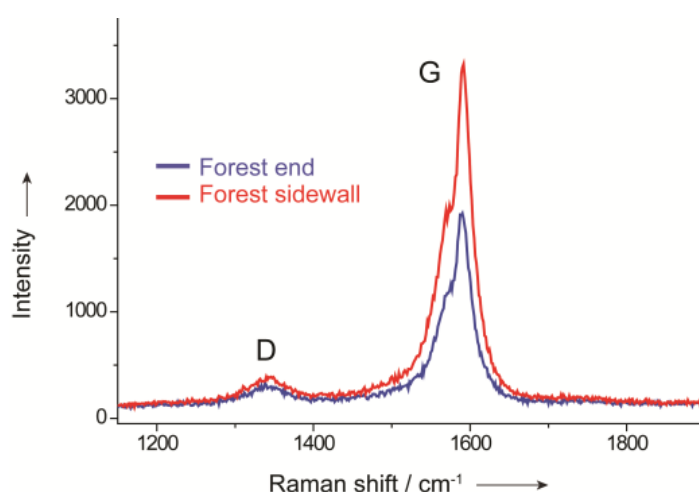


Figure 4.2 - Micro-Raman spectra of an intact SWNT forest focusing on the sidewalls and tube ends.

By tilting the sample the microscope was focused onto the forest sidewalls, allowing a Raman spectrum of this face to be obtained. The shape and location of the G band (sp^2) at 1589 cm^{-1} , in both spectra in Figure 4.2, is indicative of SWNTs.^{34, 35} Whilst small D peaks (sp^3 carbon) are visible in both spectra, the G / D ratios for the ends and the sidewalls, 7:1 and 9:1 respectively,

indicate significantly higher quality forests (i.e. cleaner, lower defect density) than those previously described in the literature.^{33, 35}

It was also particularly important to confirm that the ends of the forests were free from catalytic metal NPs, since these can impact significantly on the electrochemical response of SWNTs.³⁶⁻³⁹ The results of XPS are shown in Figure 4.3(a), for the top surface of the forest (black line), and the aluminium oxide on Si/SiO₂ substrate surface with the cobalt (Co) catalyst (red line) after subjecting it to ‘growth’ conditions (heating to 850 °C under H₂ flow) but without a carbon source (i.e. no actual growth).

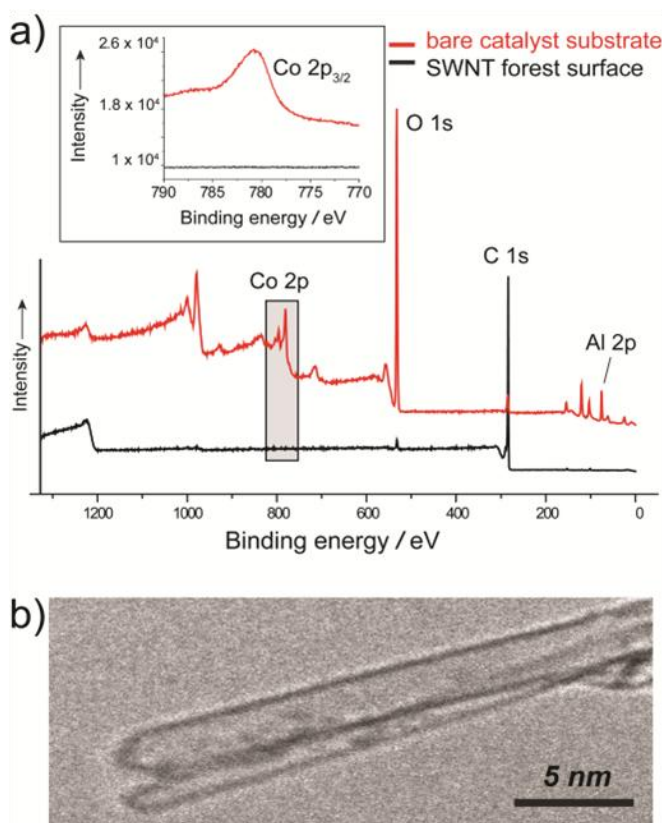


Figure 4.3 - a) XPS spectra of bare catalyst substrate (red line) and SWNT forest surface (black line). The inset shows the spectral range corresponding to Co 2p_{3/2} for both SWNT forest (black line) and catalyst (red line) surfaces. b) Typical TEM image of SWNT ends.

The catalyst sample shows a distinct cobalt 2p peak at 780 eV. The peaks at 75 eV and 530 eV are for aluminium (Al 2p) and oxygen (O 1s), respectively, originating from the aluminium oxide under-layer. In contrast, in the XPS spectrum for the SWNT forest the Co peak has disappeared and the spectrum is dominated by the carbon 1s peak at 290 eV. Since the penetration depth of XPS is ca. 10 nm and as the forest was ca. 500 μm thick, this analysis proves that these SWNT forests exhibit a root growth process,⁴⁰ where the catalytic NPs remain on the substrate, i.e. at the base of the forest, and the SWNT grow upwards from them. There is a very small oxygen 1s peak, relative to C 1s, originating from the top 10 nm of the SWNT forest. This, most likely, originates from a small degree of oxygenation of the SWNT forest under ambient conditions, but it is insignificant compared to the signals obtained when a SWNT end is deliberately opened.^{13, 33} Further evidence, from TEM images of the ends and end-caps of forest SWNTs, Figure 4.3(b), confirmed that they were both closed and free from catalyst NPs, which is in agreement with the XPS data.

4.2.2 Conductance and voltammetric analysis

Figure 4.4(a) shows a photograph and a schematic of the experimental arrangement for the voltammetric measurements. To produce an electrical contact to the SWNT forest, a 200 nm thick gold film was evaporated onto half of the sample, covering both the top and sides, by means of a shadow mask, leaving the rest of the sample intact and free from metal contamination for electrochemical analysis. The sample was then mounted to align either the top of the forest (ends) or the sidewalls, for electrochemical interrogation. Theta glass (double barrelled) pipet tips, of typical inner diameter ~ 400 nm (accurately

characterised using FE-SEM) were filled with the solution of interest, and Ag/AgCl quasi-reference-counter electrodes (QRCEs) were inserted into each of the barrels. With a bias applied between the two barrels the conductance current, which flows between barrels, via the meniscus at the end of the pipet tip, could be monitored. This enabled us to: (i) accurately position the tip, keeping the tip and meniscus in a fixed position during voltammetric measurements;^{31, 32} and (ii) assess the contact area of the meniscus with the area of interest on the SWNT forest.

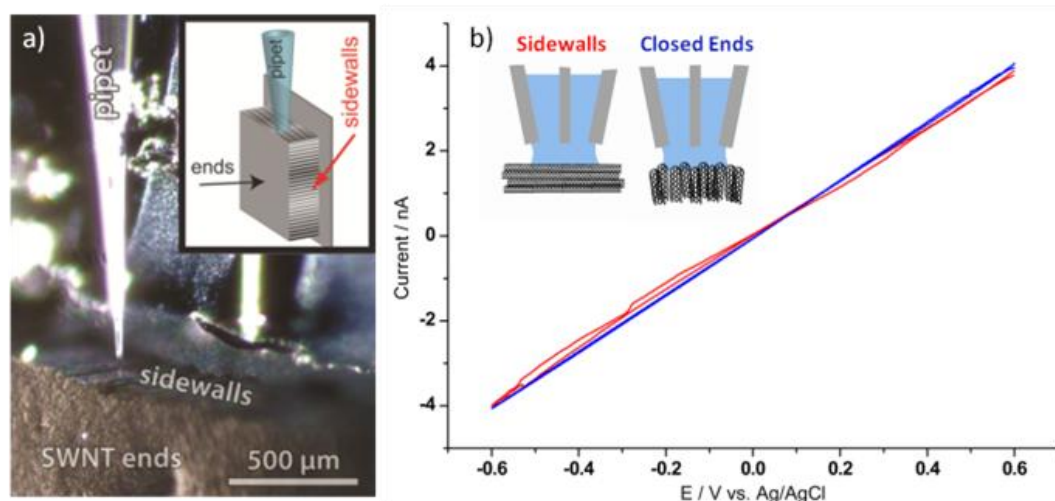


Figure 4.4 - a) Digital photograph and schematic (not to scale) of the pipet in contact with the forest sidewalls, for voltammetric and conductance analysis. b) Current-voltage curves (forward and reverse) recorded on the closed ends (blue) and sidewalls (red), with a pipet of inner diameter 400 nm, containing 50 mM KCl, at 100 mV s⁻¹.

Figure 4.4(b) shows typical conductance current – voltage curves, recorded by sweeping the potential of one QCRE with respect to the other (held at ground), with 50 mM potassium chloride solution in the pipet. The meniscus contact was maintained in a fixed position on the SWNT forest over the closed ends (blue line) or sidewalls (red line). A similar response is seen in both locations, which is close to that recorded for similar sized theta pipet tips on

hydrophobic impermeable substrates.⁴¹ This both indicates that the meniscus is stable (on both surfaces) and does not wet into the forest structure over the timescales used in the electrochemical experiments, as this would cause a reduction in the effective resistance, and that the meniscus height is similar in both cases. We thus conclude that the SNWT forest is not permeated to any significant extent by electrolyte from the pipet tip.

For redox measurements, the pipet was filled with solution containing both supporting electrolyte (KCl, 50 mM) and the redox species of interest. Once contact had been made between the pipet meniscus and forest (sidewall or ends), CV measurements were carried out, with the SWNT forest connected as the working electrode. These were repeated multiple times at different spots on several samples, at both the forest ends and the sidewalls. Two well-known outer sphere, redox couples, with very different formal potentials (E^0 values), (ferrocenylmethyl) trimethylammonium, $(\text{FcTMA}^{+/2+})^{20}$ and hexaammineruthenium ($\text{Ru}(\text{NH}_3)_6^{3+/2+}$), were used to probe the local electrochemical response. Figure 4.5 and Figure 4.6, show typical CVs recorded at the SWNT ends and sidewalls for these mediators. These data clearly show that, for both couples, the electrochemical response is comparable with a difference in the $1/4$ -wave and $3/4$ -wave potential, $E_{3/4} - E_{1/4}$, in the range 57 – 64 mV, indicating that the reactions are close to reversible in all locations. The slight difference in capacitive background between the sidewalls and ends is likely due to increased surface roughness on the top surface (ends), leading to slightly increased double-layer capacitance.

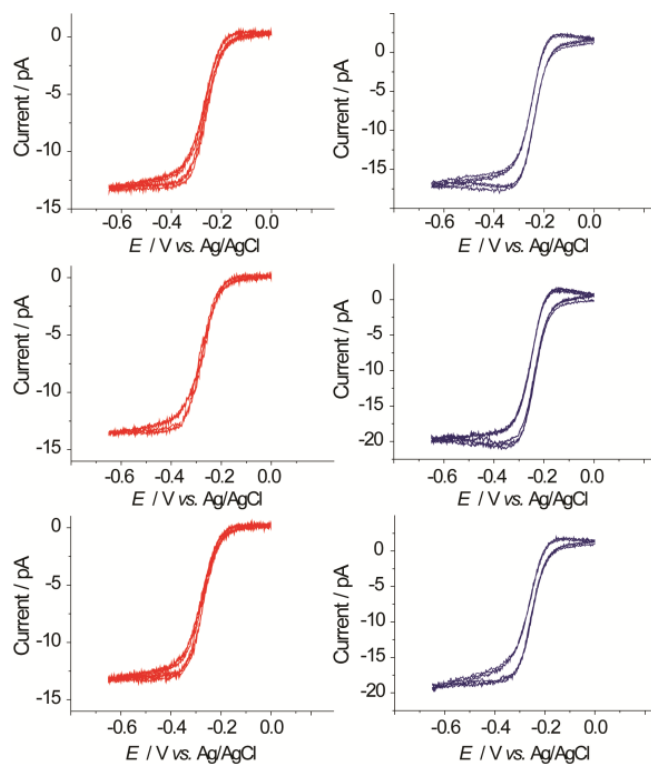


Figure 4.5 - Typical CVs of 5 mM $\text{Ru}(\text{NH}_3)_6^{3+}$ reduction in 50 mM KCl at a scan rate of 100 mV s^{-1} . Red lines indicate forest sidewalls, blue lines, forest closed ends.

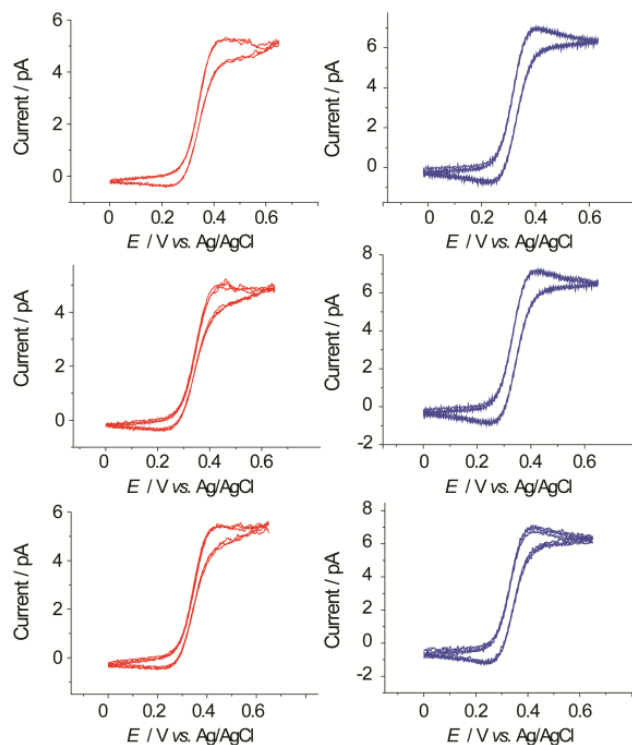


Figure 4.6 –Typical CVs of 2 mM FcTMA^{+2+} oxidation in 50 mM KCl at a scan rate of 100 mV s^{-1} . Red lines indicate forest sidewalls, blue lines, the forest closed ends.

The mass transfer rate coefficient (k_t) for this pipet electrode arrangement is estimated as $\sim 0.03 \text{ cm s}^{-1}$, from simple analysis of the limiting current using equation(4.1):

$$i_{\text{lim}} = nFAk_t C_{\text{bulk}} \quad (4.1)$$

where i_{lim} is the limiting current, n is the number of electrons transferred, F is the Faraday constant, A is the electrode area, k_t is the mass transfer rate coefficient and C_{bulk} is the bulk concentration. Hence, as the reaction is reversible, the effective standard heterogeneous electron transfer rate constant is significantly larger than this (0.03 cm s^{-1}) on both the ends and sidewalls of the SWNT forest. Since k_t is higher, in this arrangement, than that experienced in standard CV experiments, we deduce that SWNT forests should display essentially reversible behaviour for outer sphere redox couples using most common electrochemical techniques. Thus, both the closed ends and sidewalls of CVD grown SWNT forests should be considered highly electrochemically active, and capable of fast electron transfer. Furthermore, it should not be necessary, as has been suggested by others,^{14-16, 18, 42} to carry out any pretreatment or activation of CVD-grown SWNTs for electrochemical studies and measurements with redox couples of this type. Note that for some inner sphere processes which often need to bind directly with the electrode surface in order to undergo efficient electron transfer,⁴³ the chemical nature of the surface (and whether the end is open or closed) may be more important.

4.3 Conclusions

In conclusion, we have demonstrated a novel approach for interrogating the electrochemistry of different parts of SWNTs in a forest arrangement, using a

mobile nanoscopic electrochemical cell. In this way the electrochemical activity of the forest, or for that matter, any complex sample, can be studied in its native state, in any desired location, at high spatial resolution, without the need for sample processing. Using this arrangement, we have conclusively proved that a SWNT end does not need to be open for it to support fast electrochemistry with outer sphere redox couples. This overturns the present consensus that the electrochemistry of SWNTs is dominated by open ends^{13, 14, 19, 44} erroneously formulated from the results of CV measurements averaged over macro-sized areas of SWNTs assembled on conducting surfaces. Our results also now naturally bring into question the assumption that MWNT ends must be open in order for the CNT to exhibit efficient ET.¹⁵⁻¹⁷

The studies herein provide further convincing direct evidence for the considerable activity of SWNT sidewalls,²⁰⁻²² in contrast to various indirect studies which have suggested that such sites are electrochemically inert.^{14, 18, 42} More generally, direct nanoscopic studies such as those reported herein are providing a new consensus that the basal surface of various related sp^2 carbon materials promotes fast electron transfer.^{24, 32, 45}

4.4 References

1. C. Ban, Z. Wu, D. T. Gillaspie, L. Chen, Y. Yan, J. L. Blackburn and A. C. Dillon, *Adv. Mater.*, 2010, **22**, E145-E149.
2. J. Kong, N. R. Franklin, C. Zhou, M. G. Chapline, S. Peng, K. Cho and H. Dai, *Science*, 2000, **287**, 622-625.
3. R. H. Baughman, A. A. Zakhidov and W. A. de Heer, *Science*, 2002, **297**, 787-792.
4. D.-J. Guo and H.-L. Li, *J. Electroanal. Chem.*, 2004, **573**, 197-202.
5. H. Luo, Z. Shi, N. Li, Z. Gu and Q. Zhuang, *Anal. Chem.*, 2001, **73**, 915-920.
6. D. N. Futaba, K. Hata, T. Yamada, T. Hiraoka, Y. Hayamizu, Y. Kakudate, O. Tanaike, H. Hatori, M. Yumura and S. Iijima, *Nat. Mater.*, 2006, **5**, 987-994.
7. S. Fan, M. G. Chapline, N. R. Franklin, T. W. Tombler, A. M. Cassell and H. Dai, *Science*, 1999, **283**, 512-514.
8. H. Huang, C. H. Liu, Y. Wu and S. Fan, *Adv. Mater.*, 2005, **17**, 1652-1656.
9. J. Wang, *Electroanal*, 2005, **17**, 7-14.
10. X. Yu, B. Munge, V. Patel, G. Jensen, A. Bhirde, J. D. Gong, S. N. Kim, J. Gillespie, J. S. Gutkind, F. Papadimitrakopoulos and J. F. Rusling, *J. Am. Chem. Soc.*, 2006, **128**, 11199-11205.
11. D. J. Garrett, P. A. Brooksby, F. J. Rawson, K. H. R. Baronian and A. J. Downard, *Anal. Chem.*, 2011, **83**, 8347-8351.
12. J. Li, A. Cassell, L. Delzeit, J. Han and M. Meyyappan, *J. Phys. Chem. B*, 2002, **106**, 9299-9305.
13. A. Chou, T. Bocking, N. K. Singh and J. J. Gooding, *Chem. Commun.*, 2005, 842-844.
14. A. F. Holloway, K. Toghill, G. G. Wildgoose, R. G. Compton, M. A. H. Ward, G. Tobias, S. A. Llewellyn, B. n. Ballesteros, M. L. H. Green and A. Crossley, *J. Phys. Chem. C*, 2008, **112**, 10389-10397.
15. C. E. Banks, R. R. Moore, T. J. Davies and R. G. Compton, *Chem. Commun.*, 2004, 1804-1805.
16. C. E. Banks and R. G. Compton, *Analyst*, 2006, **131**, 15-21.
17. C. E. Banks, T. J. Davies, G. G. Wildgoose and R. G. Compton, *Chem. Commun.*, 2005, 829-841.
18. M. Pumera, *Chem. – Eur. J.*, 2009, **15**, 4970-4978.
19. J. J. Gooding, R. Wibowo, Liu, W. Yang, D. Losic, S. Orbons, F. J. Mearns, J. G. Shapter and D. B. Hibbert, *J. Am. Chem. Soc.*, 2003, **125**, 9006-9007.
20. I. Heller, J. Kong, H. A. Heering, K. A. Williams, S. G. Lemay and C. Dekker, *Nano Lett.*, 2004, **5**, 137-142.
21. J. Kim, H. Xiong, M. Hofmann, J. Kong and S. Amemiya, *Anal. Chem.*, 2010, **82**, 1605-1607.
22. P. V. Dudin, M. E. Snowden, J. V. Macpherson and P. R. Unwin, *ACS Nano*, 2011, **5**, 10017-10025.

23. I. Dumitrescu, P. V. Dudin, J. P. Edgeworth, J. V. Macpherson and P. R. Unwin, *J. Phys. Chem. C*, 2010, **114**, 2633-2639.
24. I. Dumitrescu, P. R. Unwin and J. V. Macpherson, *Chem. Commun.*, 2009, 6886-6901.
25. I. Dumitrescu, N. R. Wilson and J. V. Macpherson, *J. Phys. Chem. C*, 2007, **111**, 12944-12953.
26. J. F. Colomer, C. Stephan, S. Lefrant, G. Van Tendeloo, I. Willems, Z. Kónya, A. Fonseca, C. Laurent and J. B. Nagy, *Chem. Phys. Lett.*, 2000, **317**, 83-89.
27. M. Lin, J. P. Ying Tan, C. Boothroyd, K. P. Loh, E. S. Tok and Y.-L. Foo, *Nano Lett.*, 2006, **6**, 449-452.
28. H. Zhu, K. Suenaga, A. Hashimoto, K. Urita, K. Hata and S. Iijima, *Small*, 2005, **1**, 1180-1183.
29. S. Hofmann, R. Sharma, C. Ducati, G. Du, C. Mattevi, C. Cepek, M. Cantoro, S. Pisana, A. Parvez, F. Cervantes-Sodi, A. C. Ferrari, R. Dunin-Borkowski, S. Lizzit, L. Petaccia, A. Goldoni and J. Robertson, *Nano Lett.*, 2007, **7**, 602-608.
30. X.-J. Huang, H.-S. Im, O. Yarimaga, J.-H. Kim, D.-Y. Jang, D.-H. Lee, H.-S. Kim and Y.-K. Choi, *J. Electroanal. Chem.*, 2006, **594**, 27-34.
31. N. Ebejer, M. Schnippering, A. W. Colburn, M. A. Edwards and P. R. Unwin, *Anal. Chem.*, 2010, **82**, 9141-9145.
32. S. C. S. Lai, A. N. Patel, K. McKelvey and P. R. Unwin, *Angew. Chem. Int. Ed.*, 2012, **51**, 5405-5408.
33. K. Gong, S. Chakrabarti and L. Dai, *Angew. Chem. Int. Ed.*, 2008, **47**, 5446-5450.
34. M. S. Dresselhaus, G. Dresselhaus, R. Saito and A. Jorio, *Phys. Rep.*, 2005, **409**, 47-99.
35. D. P. Burt, W. M. Whyte, J. M. R. Weaver, A. Glidle, J. P. Edgeworth, J. V. Macpherson and P. S. Dobson, *J. Phys. Chem. C*, 2009, **113**, 15133-15139.
36. M. Pumera, *Langmuir*, 2007, **23**, 6453-6458.
37. J. Kruusma, N. Mould, K. Jurkschat, A. Crossley and C. E. Banks, *Electrochem. Commun.*, 2007, **9**, 2330-2333.
38. M. Pumera and H. Iwai, *J. Phys. Chem. C*, 2009, **113**, 4401-4405.
39. E. J. E. Stuart and M. Pumera, *J. Phys. Chem. C*, 2010, **114**, 21296-21298.
40. K. Hata, D. N. Futaba, K. Mizuno, T. Namai, M. Yumura and S. Iijima, *Science*, 2004, **306**, 1362-1364.
41. M. E. Snowden, A. G. Güell, S. C. S. Lai, K. McKelvey, N. Ebejer, M. A. O'Connell, A. W. Colburn and P. R. Unwin, *Anal. Chem.*, 2012, **84**, 2483-2491.
42. R. L. McCreery, *Chem. Rev.*, 2008, **108**, 2646-2687.
43. A. J. Bard, *J. Am. Chem. Soc.*, 2010, **132**, 7559-7567.
44. J. Liu, A. Chou, W. Rahmat, M. N. Paddon-Row and J. J. Gooding, *Electroanal.*, 2005, **17**, 38-46.
45. A. G. Güell, N. Ebejer, M. E. Snowden, J. V. Macpherson and P. R. Unwin, *J. Am. Chem. Soc.*, 2012, **134**, 7258-7261.

5

Electrochemical activation of pristine single walled carbon nanotubes: impact on oxygen reduction and other surface sensitive redox processes

In this chapter the effect of systematic anodic pre-treatments of SWNT forests on the electrochemical response towards a variety of redox processes is investigated. An experimental arrangement is adopted whereby a microcapillary containing the solution of interest and a quasi-reference electrode is brought into contact with a small portion of the forest to enable measurements on the surface before and after controlled anodic polarisation (AP). AP of the surface is found to both improve the voltammetric response (faster apparent heterogeneous electron transfer kinetics) of surface sensitive redox processes, such as $\text{Fe}^{2+/3+}$, and enhance the electrocatalytic response of the SWNTs towards oxygen reduction; the extent of which can be carefully controlled via the applied anodic potential. AP is expected to remove any trace organic (atmospheric) contaminants that may accumulate on the forest over extended periods as well as allowing the controlled introduction of defects, as confirmed by micro-Raman spectroscopy.

5.1 Introduction

CNTs have attracted considerable attention for a diverse range of electrochemical applications and technologies, ranging from batteries¹ to sensors.^{2, 3} They have been widely studied as electrode materials in electrochemistry,^{4, 5} in a variety of geometrical formats.⁶⁻⁸ There has, however, been significant debate over the fundamental electrochemical properties of CNT materials, for both SWNTs and MWNTs. Even for outer sphere redox processes it was believed that heterogeneous electron transfer (HET) only occurred at side-wall defects⁹, open ends^{10, 11} or residual catalytic NPs.¹² This position was largely based on experiments using aggressively cleaned¹³ and processed¹⁴ CNTs, often ultrasonically dispersed and drop-cast onto conductive substrates.^{4, 15, 16} However, there is now a sizeable body of evidence (including section 4.2.2) that fast HET is possible for *outer-sphere redox couples*, at both pristine sidewalls and the closed ends of clean, unprocessed SWNTs.^{6, 8, 16-20}

The role of defects and open ends may play a more important part when considering inner-sphere redox processes, which require favourable interactions between the redox active species and the surface. For example, acid and oxygen plasma treatment of pristine SWNT network electrodes,²¹ assisted the voltammetric oxidation of dopamine, compared to the untreated surface. The impact of electrochemical activation of CNT surfaces on HET has also been investigated, however most studies employed CNTs that have already been cleaned prior to use via strong acid treatments and ultrasound, and hence were already likely to contain significant defects, as a result of the CNT clean-up process. For example, Wang *et al*²² observed that the voltammetric response of a MWNT modified electrode could be improved towards a variety of inner sphere

mediators by anodically polarising the electrode. This was attributed to the creation of ‘edge plane’ sites in the CNTs. Li *et al*²³ found the electrochemical oxidation of SWNT-modified electrodes improved their performance towards both inner and outer sphere mediators.

The ORR is a highly surface sensitive²⁴ electrochemical process which is currently of much interest in fuel cells. One area of activity is concerned with replacement of precious-metal based fuel cell catalysts with more sustainable options. Carbon-based alternatives have been suggested,²⁵ with nitrogen doped CNTs showing particular promise.²⁶⁻²⁸ Electron withdrawing dopants, such as nitrogen, are thought to create active sites for ORR by increasing the positive charge density on surrounding carbon atoms. Adsorption of oxygen at these sites, weakens the O-O bond, facilitating ORR.²⁹ The use of a poly(di-allyldimethylammonium chloride) electrolyte also leads to a similar effect, due to the creation of net positive charge on the CNTs.³⁰ However, previous work has typically employed either CNTs which contain high levels of amorphous carbon and catalytic NPs,³¹ which can catalyse the ORR process, or CNTs that were already highly defected due to aggressive acid cleaning.^{21,25, 31-33} Moreover, the CNTs were typically dispersed on a support electrode, such as HOPG^{25, 33} or glassy carbon,^{31,32} which itself can contribute significantly to the electrochemical response.³⁴

In this work we focus on electrochemical oxidation as a means of introducing defects, as confirmed by micro-Raman spectroscopy, into SWNTs in a controlled manner and investigate how this influences the voltammetric response towards important and well-studied redox systems. Importantly, we start with CNT forest electrodes which are high quality (low defect density),

dopant free, have closed ends and contain low levels of amorphous carbon, so that the effect of a defined electrochemical treatment can be clearly understood. Specifically, we employ vertically aligned forests of SWNTs where the catalytic NPs are only encapsulated at the base of the structure.¹⁷ Micro-scale pipette techniques enable the investigation of the HET response of the pristine and electrochemically oxidised ‘forest’ in defined areas.³⁵ Herein, we investigate the uppermost (top) structure of the forest, far from the underlying catalytic NPs, with the meniscus of the pipette wetting an array of SWNT with closed ends.

5.2 Electrode preparation and Electrochemical measurements

SWNT forests (Figure 5.1 a) were grown as discussed in section 2.2 and were electrically contacted through evaporation of a 200 nm thick gold band on the top of the forest, defined using a shadow mask, leaving the bulk of the surface unmodified: see Figure 5.1.

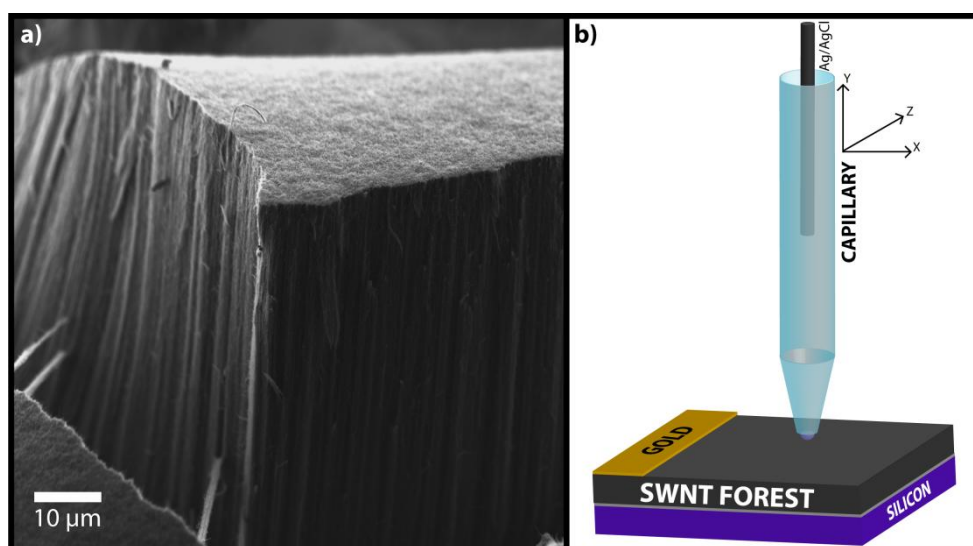


Figure 5.1 - (a) FE-SEM image of a typical SWNT forest. (b) Schematic of the micro-capillary set up used for voltammetric experiments.

Electrochemical measurements were undertaken using a micro-capillary technique, described previously^{17, 35, 36} and in more detail in section 2.6.1. This technique allowed multiple measurements to be made at fresh locations on the electrode surface (SWNT forest). A schematic of the setup is shown in Figure 5.1 (b). All electrochemical measurements were repeated a minimum of four times to ensure consistency.

5.3 Electrochemistry of surface sensitive redox couples and the effect of anodic oxidation of SWNTs

The $\text{Fe}^{2+/3+}$ redox process is perhaps the most studied ‘simple’ electrochemical reaction that is influenced significantly by the electrode surface structure, surface cleaning, supporting electrolyte and counter anion effects,³⁷⁻⁴² and so is often termed an ‘inner sphere’ redox system. Typical CVs for the one-electron oxidation of 1 mM Fe^{2+} (FeSO_4) in 50 mM HClO_4 on the SWNT forest surface, are shown in Figure 5.2, recorded over the potential range -0.2 V to +0.87 V (start -0.2 V) vs. Ag/AgCl QRCE (red dotted lines) and -0.2 V to +0.95 V vs. Ag/AgCl QRCE (blue lines) at a scan rate of 50 mV s⁻¹. When the anodic potential limit was +0.87 V, the $\text{Fe}^{2+/3+}$ oxidation/reduction peaks are separated by a ‘peak to peak’ potential (ΔE_p) of 718 mV for the first scan (oxidation peak position 0.792 V) which decreases slightly, to 626 mV on repeat scanning (oxidation peak position 0.748 V). This was typical of four repeat experiments with ΔE_p ranging between 706 and 718 mV (on the first scan) and between 607 and 626 mV (after 5 scans). In contrast, by scanning to +0.95 V on the first scan, the oxidation peak again occurs at 0.790 V (blue line), but, on the second voltammetric scan the peak potential has shifted to 0.628 V, with a significant

reduction in ΔE_p from 718 to 319 mV. ΔE_p ranged between 317 and 323 mV on the second scan (four repeats). After a total of five CVs the response stabilises with the oxidation peak shifting to 0.574 V, and ΔE_p decreasing to 226 mV. ΔE_p ranged between 226 and 260 mV after five CVs (four repeats).

Interestingly, the data show that a difference in the oxidation potential limit of less than 100 mV can have a significant effect on the resulting electrochemical response for this $\text{Fe}^{2+/3+}$ couple. It has been shown that the introduction of carbonyl groups, in particular quinones, on carbon surfaces facilitates oxidation of Fe^{2+} , enabling significantly faster HET compared to the pristine sp^2 structure.⁴³ Thus, scanning to anodic potentials may have the effect of introducing oxygen containing defects although it is also very possible anodic polarisation acts to clean the SWNT surface allowing faster HET to the tube ends.

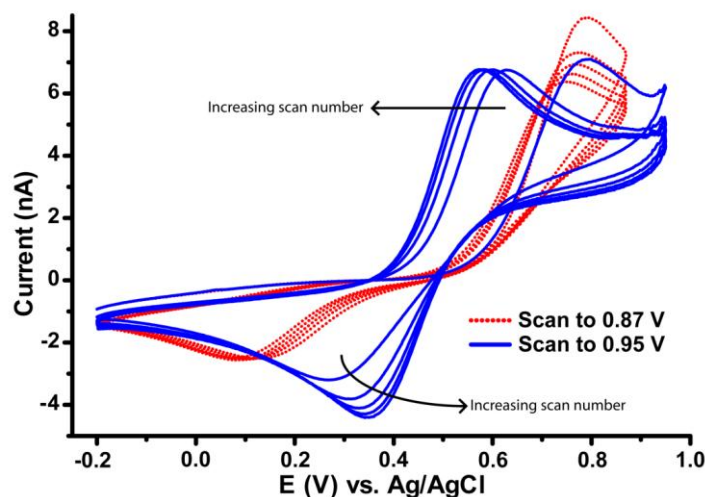


Figure 5.2 - Typical CVs for the oxidation of 1 mM Fe^{2+} (50 mV s^{-1}) in 50 mM HClO_4 performed on the top surface of an SWNT forest. Capillary inner diameter was 50 μm . The CVs were scanned from -0.2 V to +0.87 V (red dotted line) and -0.2 V to +0.95 V (blue line).

For CV responses with significant interfacial kinetic effects, it is also important to consider whether there is any change in the surface area of the

SWNT forest wetted by the meniscus. From the data in Figure 5.2, we do not see any appreciable change in the background capacitance current, and this is a feature that we explore and confirm later in the chapter. The reasonably close similarity of the forward peak currents also indicated that the lateral dimension of the meniscus contact is approximately similar. There appears to be a small decrease in the peak current magnitude from the first sweep to subsequent sweeps, even though the first sweep is most affected by kinetics. This suggests a small decrease in the lateral area wetted with time. Although the final voltammogram, in a series of five scans to 0.95 V, is not strictly reversible (ΔE_p 226 to 260 mV), we can use the peak current magnitude to reasonably estimate the area of the meniscus contact via the Randles-Sevcik equation. Although this equation is strictly only applicable to reversible electrochemistry, it is sufficient to give an estimate of the electrode area in this case. Using the Randles-Sevcik equation and assuming a planar disk electrode (diffusion coefficient, $D_{\text{Fe}^{2+/3+}} = 9 \times 10^{-6} \text{ cm}^2 \text{ s}^{-1}$)⁴¹ we estimate an electrode radius of 35 μm , which compares favourably with the capillary radius used (25 μm); as found previously⁴⁴⁻⁴⁸ for a range of capillary sizes, the meniscus contact area is of the order of (or slightly larger than) the pipet dimensions.¹⁷

The commonly used redox couple $\text{Fe}(\text{CN})_6^{4-/3-}$ has been used for the investigation of HET kinetics on carbon materials,^{9, 44, 49} although there is now significant evidence that the voltammetric response of this couple is surface sensitive and the redox process itself can cause blockage, or fouling, of carbon surfaces.^{40, 44} Given these complications, and perhaps because of them, this is a rather interesting candidate to investigate the effect of AP of SWNTs on HET (Figure 5.3 a). AP was performed by holding the electrode at an oxidising

potential of +1 V versus Ag/AgCl QRCE for 2 s prior to running the CV from -0.1 V to 0.4 V and back to -0.1 V (50 mV s⁻¹). A constant potential, applied for a short time period, was used to modify the surface, rather than scanning the potential between extended limits, in order to minimise possible fouling effects associated with Fe(CN)₆⁴⁻ oxidation at the electrode.⁴⁴ The potential for AP was selected in light of the data presented in Figure 5.2 which showed that potentials $\geq +0.95$ versus Ag/AgCl QRCE were effective in improving HET.

For the pristine forest (black dotted line), $\Delta E_p = 130$ mV for Fe(CN)₆⁴⁻ oxidation and this was typical of five measurements (ΔE_p ranged between 127 mV and 146 mV). ΔE_p increased slightly with repeat scans in the same area, possibly due to some surface fouling with Fe(CN)₆^{4-/3-}, which has been reported for HOPG⁴⁴ and was typical of all measurements, while the peak current decreased slightly. However, after AP (in a different location), $\Delta E_p = 78$ mV (ΔE_p ranged between 75 mV and 82 mV over five measurements) close to the value expected for a reversible process.

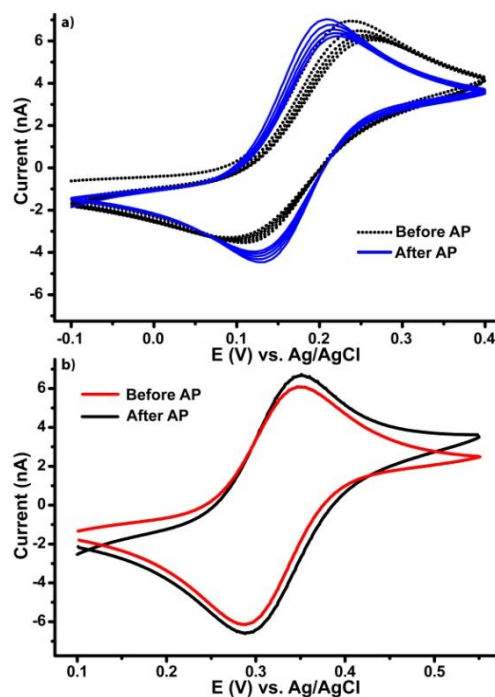


Figure 5.3 - a) CVs for the oxidation of 1 mM $\text{Fe}(\text{CN})_6^{4-}$ in 50 mM KCl (50 mV s^{-1}) on SWNT forests: black dotted line shows the response with no AP; blue line after AP at +1 V for 2 s. b) CVs for the oxidation of 1 mM FcTMA^+ in 50 mM KCl (50 mV s^{-1}) on SWNT forests: red line shows response before AP; black line after AP at 1 V for 2 s.

To examine further whether AP had a significant effect on the lateral wettability of the SWNT, the effect of AP on the outer sphere redox mediator, $\text{FcTMA}^{+/2+}$ was investigated. CVs for the one-electron oxidation of 1 mM FcTMA^+ in 50 mM KCl can be seen in Figure 5.3 (b). On the pristine forest (red line) $\Delta E_p = 61 \text{ mV}$ (ΔE_p ranged between 58 mV and 61 mV over five measurements), indicating fast, reversible HET, as seen previously on a range of pristine SWNT with ferrocene derivatives^{6, 8, 16, 20, 46} with a peak current, i_p of 6 nA. After AP, of 1 V for 2 s, on an adjacent spot on the forest surface (black line), the ΔE_p value is unchanged, as expected for a reversible process (ΔE_p ranged between 56 mV and 61 mV over five measurements), and i_p increased by only 10 %. Coupled with the data for $\text{Fe}^{2+/3+}$ and $\text{Fe}(\text{CN})_6^{4-/3-}$ this indicates that

AP leads to minimal change in lateral wettability with the droplet configuration employed.

5.4 Effect of anodic pre-treatments on oxygen reduction at SWNTs

The effect of AP on the ORR at a SWNT forest electrode can be seen in Figure 5.4 CVs were recorded in 0.1 M KCl at a scan rate of 0.1 V s^{-1} . In Figure 5.4 (a), the CV cycle commenced at 0 V, with a negative going scan to -1.3 V and then positive to 1.5 V, before returning to -1.3 V and the cycle repeated. In the first cycle (red line), a minimal ORR current signal was observed (38 nA at -0.6 V versus Ag/AgCl) characteristic of pristine sp^2 carbon electrodes.⁵⁰ However, in the second cycle (black line), a significant ORR current (514 nA at -0.6 V) becomes evident, but only after AP of the SWNT forest. This significant change in the voltammetric characteristics was found in >20 measurements on several different SWNT forest samples. A similar observation towards the electrocatalysis of oxygen reduction was made by Yano *et al.* at polycrystalline boron-doped diamond electrodes pre-treated at oxidising potentials greater than 1.4 V versus Ag/AgCl (in 0.5 M H_2SO_4). The effect was attributed to oxidation of sp^2 impurities in the diamond surface introducing quinone groups which were considered responsible for promoting the ORR.⁵¹

Comparison of CVs recorded in both aerated and de-aerated (N_2 saturated) KCl solutions are shown in Figure 5.4 (b). Here, and in all subsequent CVs, the electrode potential was first scanned anodically (from 0 V to 1.3 V) before reversing the potential and scanning cathodically (to -1 V). In de-aerated solutions, the absence of a noticeable current in the potential region -0.4 to -1.0

V, confirms that the current in this region is due to the ORR. It has been demonstrated both theoretically⁵² and experimentally⁵³ that oxygen containing groups on functionalized SWNTs withdraw electron density. Thus, it is entirely possible that favourable sites for ORR are introduced when the SWNTs pristine structure is perturbed.

It is worth commenting on the magnitude of the ORR current compared to the limiting current seen with the three redox couples considered above. Although ORR can involve up to 4 electrons (if reduction proceeds all the way to water) and the D of O_2 is relatively high ($2.1 \times 10^{-5} \text{ cm}^2 \text{ s}^{-1}$),²⁵ the concentration of O_2 in aerated water at ambient temperatures (25 °C) is only ca. 0.25 mM.²⁵ Yet, the limiting current values for the ORR in Figure 5.4 are two orders of magnitude higher than seen for the other redox couples. This is due to the three-phase meniscus contact arrangement, which mimics that of the oxygen reduction electrode in low temperature proton exchange membrane fuel cells. With the meniscus arrangement there is a large area of air/aqueous/carbon electrode contact, allowing fast transport of the oxygen across the water/air interface leading to the high ORR currents.⁵⁴

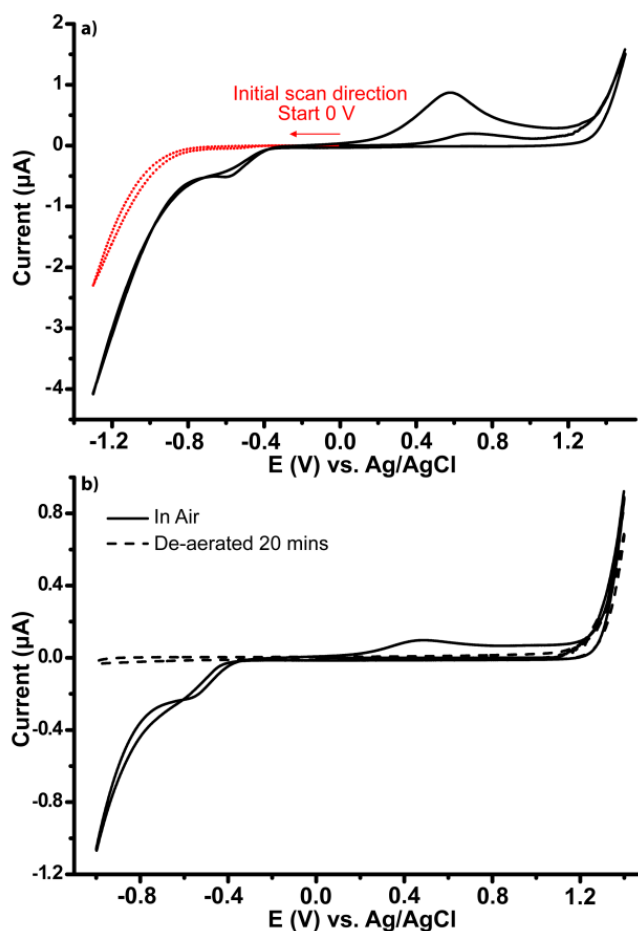


Figure 5.4 - a) CV showing the response of a SWNT forest electrode to ORR in 100 mM KCl. CV is scanned from 0 V to -1.3 V and then back to +1.5 V. Cathodic segment of first scan (red line), anodic segment of first scan and full second scan (black line). b) CV response of the SWNT forest electrode in 100 mM KCl, starting at 0 V to +1.4 V then to -1 V (100 mV s⁻¹). Dashed line (de-aerated solution), solid line (aerated).

To determine the effect of electrochemical oxidation on the SWNT forest surface, micro-Raman spectroscopy (Figure 5.5) was performed on the pristine surface and in an area where repeat CVs between +1.3 (sufficient to promote ORR) and -1.0 V (starting at 0 V) in 50 mM KCl (100 mV s⁻¹) were recorded ($n = 10$). The spectrum, representative of many recorded for the pristine surface, shows the characteristic ‘shoulder’ on the G band (1590 cm⁻¹), indicative of SWNTs⁵⁵ and a small D band, indicating low sp³ content. However, after anodic

treatment there is a notable reduction in the G:D peak ratio, from 12:1 to 5:1, suggesting a disturbance in the pristine SWNT structure, consistent with defect creation by oxidative treatment.

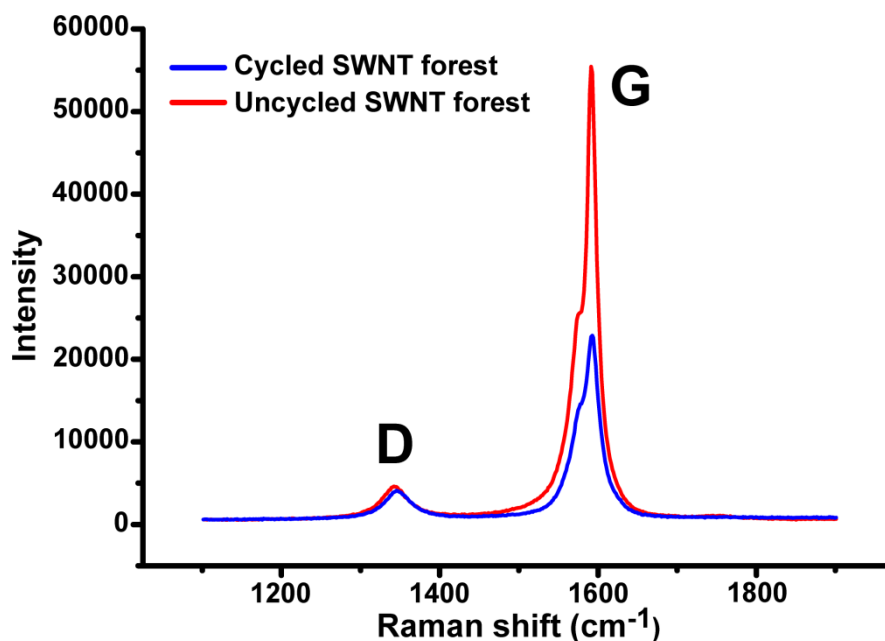


Figure 5.5 - Micro-Raman spectra of adjacent spots on a SWNT forest. Red line as grown forest, blue line, electrochemically cycled forest; the electrode potential was scanned 10 times from 0 V to +1.3 V, and then back to -1.0 V (100 mV s^{-1}).

To determine the potential threshold for ORR activation, CVs were also performed by changing the positive potential limit (from 1.1 V to 1.35 V). In all cases the same capillary, scan rate (0.1 V s^{-1}), starting potential (0 V) and end potential (-0.6 V), were employed (Figure 5.6) with the initial scan direction always anodic. For each different measurement the capillary was moved to a different location on the SWNT forest and the effective electrode area was also monitored using capacitance, by running a CV at 1 V s^{-1} (to enhance the current signal), over the potential range -0.1V to +0.1 V, immediately prior to each measurement (Figure 5.6 f). For the two lowest oxidative potential limits (+1.1

V and +1.2 V) the currents at -0.6 V, attributed to ORR (Figure 5.4), are minimal (Figure 5.6 a, b). However, by applying just 50 mV more positive potential in the anodic scan (+1.25 V (Figure 5.6 c)) the ORR current response at -0.6 V increases by 100 nA, even though capacitative measurements suggest a slightly smaller electrolyte contact area. The ORR current increases further as the anodic potential limit is made even more positive (Figure 5.6 d,e); this highlights the ability to control the level of surface activation with the procedures described herein, and the extent to which ORR occurs. At potentials greater than +1.4 V we occasionally observed droplet instability and thus for these multiple measurement experiments chose not to use potentials more positive than 1.4 V.

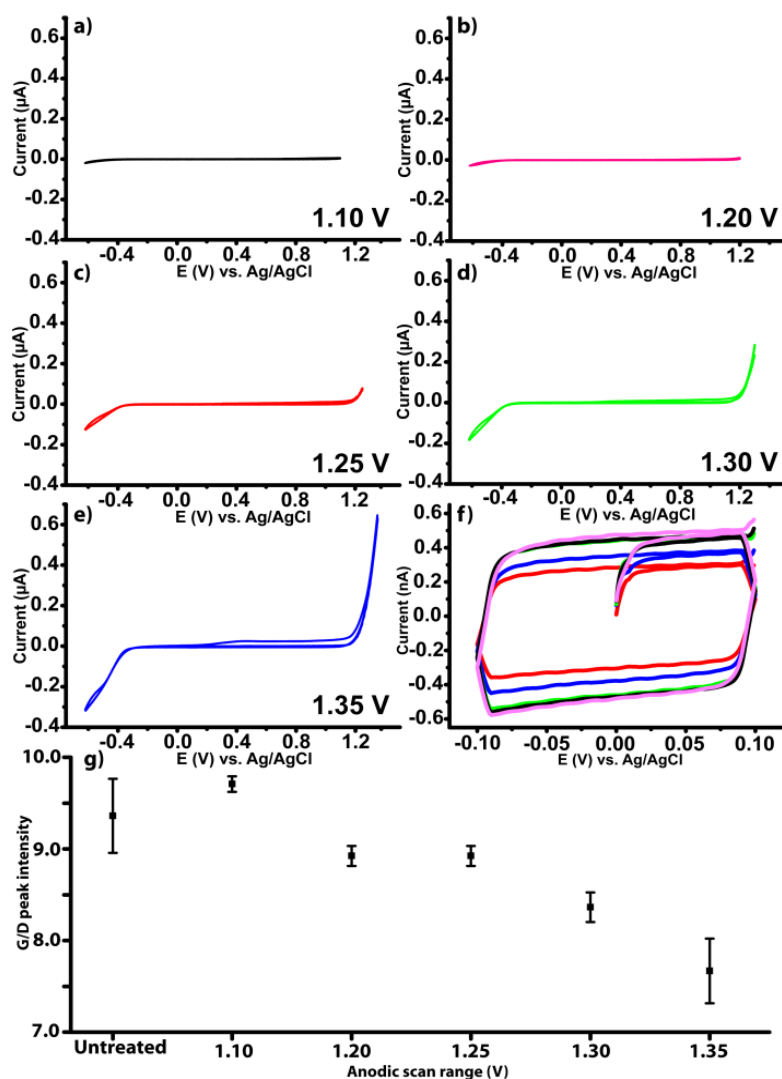


Figure 5.6 - CVs showing the ORR response on the SWNT forest in 100 mM KCl (0.1 V s^{-1}) scanned first from 0 V to different positive potentials: a) + 1.1 V (black); b) +1.2V (pink); c) +1.25 V (red); d) +1.3 V (green); e) +1.35 V (blue) and then to -0.6 V. f) The capacitive current measured prior to each CV, used to assess the wetted electrode area (1 V s^{-1}), colour coded to the CVs in a-e. g) Comparison of mean G/D values measured from micro-Raman spectra taken at an untreated SWNT forest (5 areas) and at areas anodically pre-treated at different scan ranges. Error bars show plus/minus one standard deviation.

Figure 5.6 (g) shows a comparison between the mean G/D ratio measured from micro-Raman spectra recorded in five different areas of a SWNT forest, exposed to increasingly positive potential scans from 0 V to +1.1 V, +1.2 V, +1.25 V, +1.3 V and +1.35 V, at 100 mV s^{-1} using the microcapillary set-up. The

plot clearly shows that as the potential scan increases in anodic potential, the mean $G(sp^2)/D(sp^3)$ ratio decreases indicating an increasing contribution from the D peak. Significant differences in ratio (taking account of errors) are seen for potentials > 1.25 V, consistent with the experimental observations which show the surface becomes significantly activated towards ORR when the potential ≥ 1.25 V. This suggests that sufficiently positive potentials are capable of perturbing the SWNT sp^2 structure. The data also indicate that at the anodic potential limit of the Fe^{2+}/Fe^{3+} experiment (Figure 5.2) surface cleaning rather than defect creation may be a more likely explanation for the effect seen.

From the data in Figure 5.6 (f) we are able to calculate an approximate capacitance due to the area of SWNT forest exposed to the meniscus, allowing us to assess the extent of the wetting into the structure. This was done using equation (4.2)

$$C = \frac{i_{cap}}{2\nu A} \quad (4.2)$$

where i_{cap} is the total capacitative current, ν is the scan rate and A is the electrode area. Using the meniscus contact radius calculated from the peak current of the $Fe^{2+/3+}$ couple (35 μm), the calculated capacitance is ca. 10 $\mu F\ cm^{-2}$ (based on the projected area), which compares favourably when compared to values from literature (ca. 10 $\mu F\ cm^{-2}$ for a SWNT bundle⁵⁶, 2 $\mu F\ cm^{-2}$ on basal plane HOPG⁵⁷). As the capacitance values are in broad agreement with those for planar carbon electrodes it can be reasoned that the meniscus does not wet significantly into the forest structure.

5.5 Macroscopic SWNT forest electrodes

To allow us to investigate the extent to which ORR can be catalysed, it was desirable to investigate if electrochemically activated SWNTs could act effectively as electrodes on the macroscale. SWNT forest macroelectrodes were prepared (Figure 5.7, inset) by carefully removing the forest from the underlying silicon support and attaching a copper wire using a silver based adhesive. The electrode was then scanned from 0 V to +1.3 V (AP) and then to -1.0 V then back to 0 V, multiple times in 0.1 M KCl at 0.1 V s^{-1} in order to establish the most efficient number of cycles required for electrochemical optimisation of the ORR current signal (Figure 5.7).

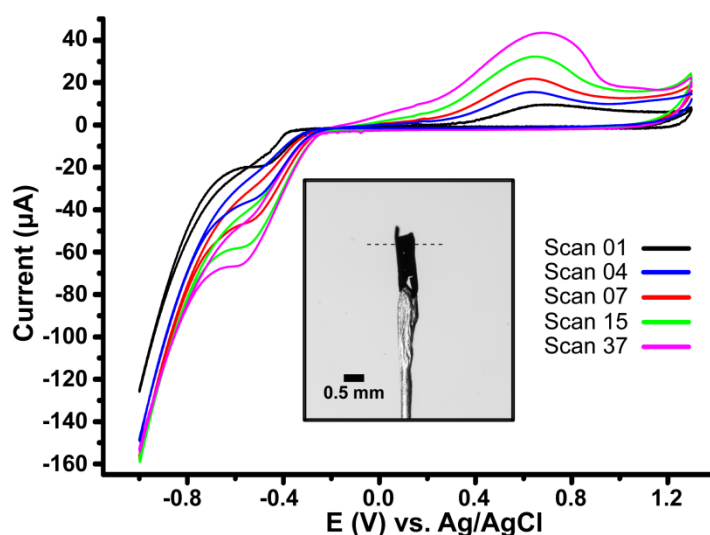


Figure 5.7 - a) ORR CV response of a SWNT forest macroelectrode in 100 mM KCl cycled from 0 V to +1.3 V and back to -1.0 V at 0.1 V s^{-1} . Inset shows an optical photograph of the SWNT forest macroelectrode, dashed line indicates proportion of submerged electrode.

The CVs present interesting findings. After $n = 7$, i_p for ORR ($46 \mu\text{A}$) is more than twice the value for $n = 1$ ($19 \mu\text{A}$), increasing further, although more gradually after $n = 15$ ($57 \mu\text{A}$) and reaching a maximum after $n = 37$ ($66 \mu\text{A}$); further 10 cycles show the same behaviour (not shown). With each cycle more

sites become active for ORR, most likely through the introduction of oxidised defects (section 5.4)

5.6 Conclusions

We have demonstrated that it is possible to improve the electrocatalytic activity of high quality pristine SWNTs, in a forest format, by the judicious use of an AP procedure. Studies mainly employed a microcapillary configuration (typical inner diameter 50 μm) where the solution of interest was brought into contact with the top surface of the SWNT forest. In this way it was possible to make many measurements simply and rapidly by moving the capillary from one location to the next. For the $\text{Fe}^{2+/3+}$ couple we show that subjecting the SWNTs to anodic potentials $\geq +0.95$ V versus Ag/AgCl (QRCE), in a solution containing 50 mM HClO_4 significantly affects ΔE_p for this process, making the HET reaction much faster. AP also slightly improved (decreased) the ΔE_p value for $\text{Fe}(\text{CN})_6^{4-/3-}$. Importantly AP did not appreciably change wetting by the meniscus (laterally) or into the SWNT forest. For ORR, potentials $\geq +1.25$ V versus Ag/AgCl (QRCE) in 50 mM KCl were needed to noticeably activate the SWNTs; the extent of which could be carefully controlled via the applied anodic potential. At these oxidising potentials, the G/D ratios in the micro-Raman spectra were significantly reduced indicating an increase in defect density and a perturbation of the pristine sp^2 structure. Moving away from a microcapillary format to macroelectrodes, we demonstrated it was possible to activate large area forests of SWNTs towards ORR.

5.7 References

1. C. Ban, Z. Wu, D. T. Gillaspie, L. Chen, Y. Yan, J. L. Blackburn and A. C. Dillon, *Adv. Mater.*, 2010, **22**, E145-E149.
2. J. Kong, N. R. Franklin, C. Zhou, M. G. Chapline, S. Peng, K. Cho and H. Dai, *Science*, 2000, **287**, 622-625.
3. R. H. Baughman, A. A. Zakhidov and W. A. de Heer, *Science*, 2002, **297**, 787-792.
4. I. Dumitrescu, P. R. Unwin and J. V. Macpherson, *Chem. Commun.*, 2009, 6886-6901.
5. C. E. Banks and R. G. Compton, *Analyst*, 2006, **131**, 15-21.
6. I. Dumitrescu, P. R. Unwin, N. R. Wilson and J. V. Macpherson, *Anal. Chem.*, 2008, **80**, 3598-3605.
7. K. Gong, S. Chakrabarti and L. Dai, *Angew. Chem. Int. Ed.*, 2008, **47**, 5446-5450.
8. I. Heller, J. Kong, H. A. Heering, K. A. Williams, S. G. Lemay and C. Dekker, *Nano Lett.*, 2004, **5**, 137-142.
9. C. E. Banks, T. J. Davies, G. G. Wildgoose and R. G. Compton, *Chem. Commun.*, 2005, 829-841.
10. A. F. Holloway, K. Toghill, G. G. Wildgoose, R. G. Compton, M. A. H. Ward, G. Tobias, S. A. Llewellyn, B. n. Ballesteros, M. L. H. Green and A. Crossley, *J. Phys. Chem. C*, 2008, **112**, 10389-10397.
11. A. Chou, T. Bocking, N. K. Singh and J. J. Gooding, *Chem. Commun.*, 2005, 842-844.
12. K. Jurkschat, X. Ji, A. Crossley, R. G. Compton and C. E. Banks, *Analyst*, 2007, **132**, 21-23.
13. M. Pumera, *Langmuir*, 2007, **23**, 6453-6458.
14. C. E. Banks, R. R. Moore, T. J. Davies and R. G. Compton, *Chem. Commun.*, 2004, 1804-1805.
15. R. R. Moore, C. E. Banks and R. G. Compton, *Anal. Chem.*, 2004, **76**, 2677-2682.
16. I. Dumitrescu, P. V. Dudin, J. P. Edgeworth, J. V. Macpherson and P. R. Unwin, *J. Phys. Chem. C*, 2010, **114**, 2633-2639.
17. P. V. Dudin, M. E. Snowden, J. V. Macpherson and P. R. Unwin, *ACS Nano*, 2011, **5**, 10017-10025.
18. I. Dumitrescu, P. R. Unwin and J. V. Macpherson, *Electrochem. Commun.*, 2009, **11**, 2081-2084.
19. P. Bertoncello, J. P. Edgeworth, J. V. Macpherson and P. R. Unwin, *J. Am. Chem. Soc.*, 2007, **129**, 10982-10983.
20. J. Kim, H. Xiong, M. Hofmann, J. Kong and S. Amemiya, *Anal. Chem.*, 2010, **82**, 1605-1607.
21. I. Dumitrescu, N. R. Wilson and J. V. Macpherson, *J. Phys. Chem. C*, 2007, **111**, 12944-12953.
22. M. Musameh, N. S. Lawrence and J. Wang, *Electrochem. Commun.*, 2005, **7**, 14-18.
23. S. Alwarappan, S. Prabhulkar, A. Durygin and C.-Z. Li, *Journal of Nanoscience and Nanotechnology*, **9**, 2991-2996.
24. R. L. McCreery, *Chem. Rev.*, 2008, **108**, 2646-2687.
25. M. Gara and R. G. Compton, *New J. Chem.*, 2011, **35**, 2647-2652.

26. Y. Li, W. Zhou, H. Wang, L. Xie, Y. Liang, F. Wei, J.-C. Idrobo, S. J. Pennycook and H. Dai, *Nat. Nano*, 2012, **7**, 394-400.
27. D. Yu, Y. Xue and L. Dai, *J. Phys. Chem. Lett.*, 2012, **3**, 2863-2870.
28. T. C. Nagaiah, S. Kundu, M. Bron, M. Muhler and W. Schuhmann, *Electrochem. Commun.*, 2010, **12**, 338-341.
29. K. Gong, F. Du, Z. Xia, M. Durstock and L. Dai, *Science*, 2009, **323**, 760-764.
30. S. Wang, D. Yu and L. Dai, *J. Am. Chem. Soc.*, 2011, **133**, 5182-5185.
31. I. Kruusenberg, N. Alexeyeva, K. Tammeveski, J. Kozlova, L. Matisen, V. Sammelselg, J. Solla-Gullón and J. M. Feliu, *Carbon*, 2011, **49**, 4031-4039.
32. N. Alexeyeva and K. Tammeveski, *Electrochem. Solid St.*, 2007, **10**, F18-F21.
33. G. Jürmann and K. Tammeveski, *J. Electroanal. Chem.*, 2006, **597**, 119-126.
34. S. C. S. Lai, A. N. Patel, K. McKelvey and P. R. Unwin, *Angew. Chem. Int. Ed.*, 2012, **51**, 5405-5408.
35. P. V. Dudin, P. R. Unwin and J. V. Macpherson, *J. Phys. Chem. C*, 2010, **114**, 13241-13248.
36. T. M. Day, P. R. Unwin and J. V. Macpherson, *Nano Lett.*, 2007, **7**, 51-57.
37. L. A. Hutton, J. G. Iacobini, E. Bitziou, R. B. Channon, M. E. Newton and J. V. Macpherson, *Anal. Chem.*, 2013, **85**, 7230-7240.
38. H. V. Patten, S. C. S. Lai, J. V. Macpherson and P. R. Unwin, *Anal. Chem.*, 2012, **84**, 5427-5432.
39. B. D. B. Aaronson, C.-H. Chen, H. Li, M. T. M. Koper, S. C. S. Lai and P. R. Unwin, *J. Am. Chem. Soc.*, 2013, **135**, 3873-3880.
40. P. Chen and R. L. McCreery, *Anal. Chem.*, 1996, **68**, 3958-3965.
41. A. E. Fischer, Y. Show and G. M. Swain, *Anal. Chem.*, 2004, **76**, 2553-2560.
42. H. G. Bochmann and W. Vielstich, *Electrochim. Acta*, 1988, **33**, 805-809.
43. P. Chen, M. A. Fryling and R. L. McCreery, *Anal. Chem.*, 1995, **67**, 3115-3122.
44. A. N. Patel, M. Guille Collignon, M. A. O'Connell, W. O. Y. Hung, K. McKelvey, J. V. Macpherson and P. R. Unwin, *Journal of the American Chemical Society*, 2012.
45. M. E. Snowden, A. G. Güell, S. C. S. Lai, K. McKelvey, N. Ebejer, M. A. O'Connell, A. W. Colburn and P. R. Unwin, *Anal. Chem.*, 2012, **84**, 2483-2491.
46. A. G. Güell, N. Ebejer, M. E. Snowden, K. McKelvey, J. V. Macpherson and P. R. Unwin, *Proceedings of the National Academy of Sciences*, 2012.
47. A. G. Güell, N. Ebejer, M. E. Snowden, J. V. Macpherson and P. R. Unwin, *J. Am. Chem. Soc.*, 2012, **134**, 7258-7261.
48. A. N. Patel, K. McKelvey and P. R. Unwin, *J. Am. Chem. Soc.*, 2012, **134**, 20246-20249.
49. K. R. Kneten and R. L. McCreery, *Anal. Chem.*, 1992, **64**, 2518-2524.
50. I. Morcos and E. Yeager, *Electrochim. Acta*, 1970, **15**, 953-975.

51. T. Yano, E. Popa, D. A. Tryk, K. Hashimoto and A. Fujishima, *J. Electrochem. Soc.*, 1999, **146**, 1081-1087.
52. J. Zhao, H. Park, J. Han and J. P. Lu, *J. Phys. Chem. B*, 2004, **108**, 4227-4230.
53. C. I. Bergeret, J. Cousseau, V. Fernandez, J.-Y. Mevellec and S. Lefrant, *J. Phys. Chem. C*, 2008, **112**, 16411-16416.
54. C. J. Slevin, S. Ryley, D. J. Walton and P. R. Unwin, *Langmuir*, 1998, **14**, 5331-5334.
55. M. S. Dresselhaus, G. Dresselhaus, A. Jorio, A. G. Souza Filho, M. A. Pimenta and R. Saito, *Acc. Chem. Res.*, 2002, **35**, 1070-1078.
56. S. Shiraishi, H. Kurihara, K. Okabe, D. Hulicova and A. Oya, *Electrochem. Commun.*, 2002, **4**, 593-598.
57. R. J. Rice and R. L. McCreery, *Anal. Chem.*, 1989, **61**, 1637-1641.

6

Pt Nanoparticle Modified Single walled carbon nanotube network electrodes for electrocatalysis: control of the specific surface area of Pt-modified electrodes over three orders of magnitude.

In this chapter the deposition of Pt NPs on SWNT networks for use as ORR and MOR electrocatalysts investigated. Both Pt NP deposition and investigation of electrocatalysis are undertaken using the microcapillary electrochemical method, meaning multiple measurements can be performed on a surface. This ability allows Pt catalysts, with surface areas over 3 orders of magnitude, to be optimised for the ORR and MOR.

6.1 Introduction

The electrochemical ORR and MOR have become fields of intense research, particularly as a consequence of the development of direct methanol fuel cells (DMFCs)¹. Much of this research is targeted towards the use of precious metal catalysts, most commonly Pt^{2, 3}, which has high electrocatalytic activity towards both the ORR and MOR. However, with limited global availability and the high price of Pt, there is a drive to maximise the catalytic performance for the DMFC reactions with the minimal amount of precious metals, especially through the use of Pt NPs, which present a high surface to volume ratio, supported on various types of carbon materials.^{4, 5} The properties of this support material have been shown to significantly affect the stability and electrochemical properties of catalytic Pt NPs.⁶⁻⁸

CNTs have long been considered as a support for metal catalysts in fuel cells⁹⁻¹¹ and more generally in electrochemistry,¹² due to their large surface area to volume ratio, excellent electrical conductivity^{13, 14} and low capacitance in the pristine form.¹⁴ NPs have been deposited on CNTs using methods including metal vapour deposition,¹⁵ the chemical reduction of metal salts,^{15, 16} and electrodeposition.^{12, 17, 18} Electrodeposition is particularly attractive, as it circumvents the need for stabilising ligands, which may both hinder the catalytic properties of the metal and introduce impurities into the catalytic system.¹⁸ Through the careful control of deposition parameters, electrodeposition allows the direct growth of NPs on CNTs with control over density and size,^{17, 19} without the need for any further functionalization.

Previous studies investigating the electrodeposition of Pt on CNTs for electrocatalytic studies have employed nanotube electrodes prepared by dropcasting onto glassy carbon^{20, 21} or other conducting substrates,^{22, 23} which can complicate the electrochemical analysis due to the rather large background currents at the support electrode. In contrast, pristine SWNTs grown on an insulating support using CVD have been shown to be an excellent support for the deposition of Ag, Au, Pd and Pt NPs^{12, 19, 24, 25} and have also been utilised to examine ORR at the single NP scale.²⁶

In this study we demonstrate how the size and density of Pt NPs on two dimensional, single layer SWNT networks, grown on an insulating surface can be manipulated through control of the electrodeposition parameters. In all cases we use network densities above the metallic percolation threshold.²⁷ The resulting Pt/SWNT composite structures are thoroughly characterised and their efficiency towards the ORR and MOR is investigated.

6.2 Electrodeposition of Pt NPs on SWNT networks

Electrochemical measurements were performed using the microcapillary electrochemical method^{19, 25} as described in section 2.6.1. For the electrodeposition of Pt on the SWNT network, the capillary was filled with a de-aerated (purged with N₂ for at least 20 mins) solution of K₂PtCl₆ (0.5 mM for low density NP studies and 5 mM for higher density studies) in 0.5 M HClO₄, and a Pd-H₂ quasi-reference electrode.²⁸ Electrodeposition from a microcapillary allows small scale patterning of a variety of substrate electrodes, without the need for time-consuming lithographic processing (which can also lead to surface contamination).²⁵ A schematic of this process is shown in Figure 6.1 (c).

Furthermore, it allows many electrodeposition experiments to be performed on a single sample by simply moving the microcapillary to a new location.

Pt NPs were electrodeposited on the SWNT network ($> 5 \mu\text{m}_{\text{SWNT}} \mu\text{m}^{-2}$, grown from Fe NPs, Figure 6.1 a, b) using cyclic voltammetry by scanning between 1.3 V and -0.05 V and back to 1.3 V at 50 mV s^{-1} . Deposition by cycling was used rather than constant potential methods as it allowed the progress of the deposition to be monitored (via the hydrogen adsorption/desorption peaks) meaning data corresponding to the relative increase in Pt surface area over each cycle could be collected. The amount of NPs deposited can be controlled by varying the number of voltammetric cycles (section 6.3.2). After each deposition the droplet was moved to a fresh adjacent area of the SWNT network allowing multiple measurements on the same sample.

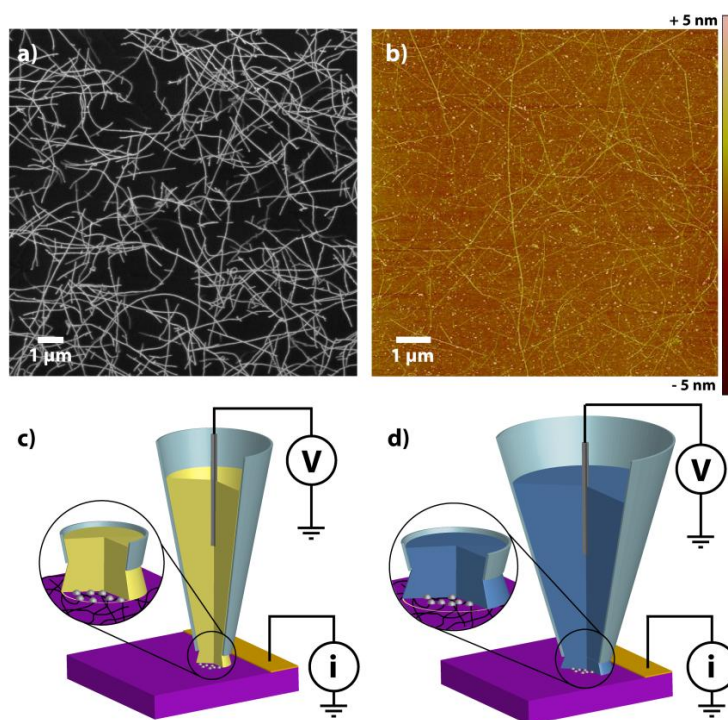


Figure 6.1 - a) FE-SEM image of a typical SWNT network above the metallic percolation threshold. b) AFM image of a typical SWNT network c) Schematic of Pt NP electrodeposition using the microcapillary. d) Schematic of the set up used to measure ORR and MOR.

6.3 Pt deposition and NP characterisation

6.3.1 Deposition procedure

All measurements to study the electrocatalytic properties of the electrodeposited NPs were made using the capillary technique, described above. However, the capillaries employed for the electrocatalytic investigations were larger than those employed for electrodeposition (100 μm vs. 60 μm diameter), so that the resulting droplet fully encapsulated the deposited Pt NP-SWNT microdisk (Figure 6.1 d). As the SWNT network itself showed minimal electrocatalytic activity towards both the MOR and ORR, there was an insignificant catalytic contribution from the extra electrode area exposed.

Electrocatalytic measurements were made in the following order. First, the specific surface area was measured. The humidity cell was thoroughly de-oxygenated and the capillary was filled with a de-oxygenated solution of 0.5 M H_2SO_4 . CVs were performed at 100 mV s^{-1} between 1.3 V and -0.05 V. The specific surface area (also known as electrochemically active surface area) of the Pt NPs was calculated by integration of the hydrogen desorption peak (210 $\mu\text{C cm}^{-2}$).²⁹ Second, the humidity cell was opened and left to aerate, and the ORR was measured using the same 0.5 M H_2SO_4 solution, but now in equilibrium with air (giving rise to an oxygen concentration ≈ 0.25 mM) under the same scan conditions as above. The MOR was investigated last on the NP assemblies, as the intermediates of this process are known to contaminate the Pt surface. Under de-aerated conditions 0.5 M methanol was oxidised for ten voltammetric cycles in 0.5 M H_2SO_4 over the potential scan range defined above.

6.3.2 Pt deposition and NP characterisation

Figure 6.2 (a) shows representative CVs for the decoration of SWNT networks with Pt NPs by potential cycling between +1.3 V and -0.05 V (5 mM K_2PtCl_6). The first and last cycles are highlighted in red and green and shown separately in an inset. On the first deposition cycle, the reduction of Pt(IV) to Pt(0) takes place at potentials cathodic of +0.3 V. No indication of Pt dissolution is observed in the anodic sweep as this process is irreversible over this potential range. In subsequent voltammetric cycles, the classic voltammetric profile of polycrystalline platinum starts to develop in tandem with the Pt deposition: the oxidation and reduction of the Pt surface can be observed above +0.9 V in the anodic sweep and centred around +0.8 V in the cathodic sweep, respectively, while the features in the potential region between +0.2 to -0.05 V can be assigned to the adsorption and desorption of hydrogen (H_{UPD}). By following the development of the magnitude of these peaks it is possible to monitor the deposition process in some detail.

By measuring the charge transferred during hydrogen desorption from the Pt surface it was possible to estimate the rate of increase of electroactive Pt surface area at different stages of deposition (Figure 6.2 b), using $210 \mu\text{C cm}^{-2}$ for monolayer hydrogen adsorption.²⁹ Note in this case the charge cannot be directly converted to the total Pt surface area as Pt deposition also occurs in the same potential range. Nevertheless it provides a semi-quantitative way to monitor electrodeposition in situ.

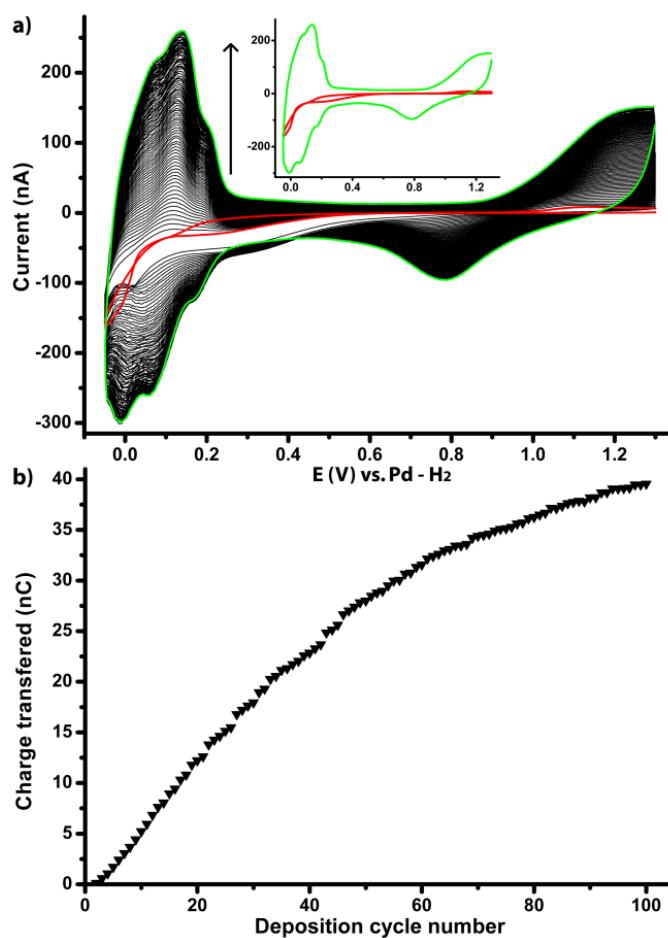


Figure 6.2 - a) CVs for the deposition of Pt NPs, 5 mM K_2PtCl_6 , one hundred voltammetric cycles at 50 mV s^{-1} . The first and the last voltammetric cycles are shown in red and green and shown in an inset for clarity. b) Plot of charge transferred during hydrogen desorption vs. deposition cycle number.

From the first to the eighteenth deposition cycle the charge transferred (and therefore active surface area) is seen to increase in an almost linear fashion. However, after this point the rate of change begins to decrease, until for the last ten deposition cycles the charge transferred vs. cycle number gradient is less than one quarter of that for the first ten. This means the active surface area increases much more slowly for longer deposition procedures and is due to mass transport to individual NPs decreasing as NPs grow in size and diffusion fields at neighbouring NPs begin to overlap. Agglomeration of NPs also acts to lower the

surface area and increase particle volume as this is more energetically favourable. Information presented in Figure 6.2 (b) allows the electrodeposited Pt surface area to be fine-tuned.

To gain further insight into the nucleation and initial NP growth, low density Pt NP deposits were studied (deposited from 0.5 mM K_2PtCl_6). Figure 6.3 shows representative FE-SEM and AFM images of Pt NPs deposited from 1, 10 and 25 deposition cycles (5, 15 and 20 cycles were also investigated). Histograms of NP size distribution, from AFM analysis, are also shown.

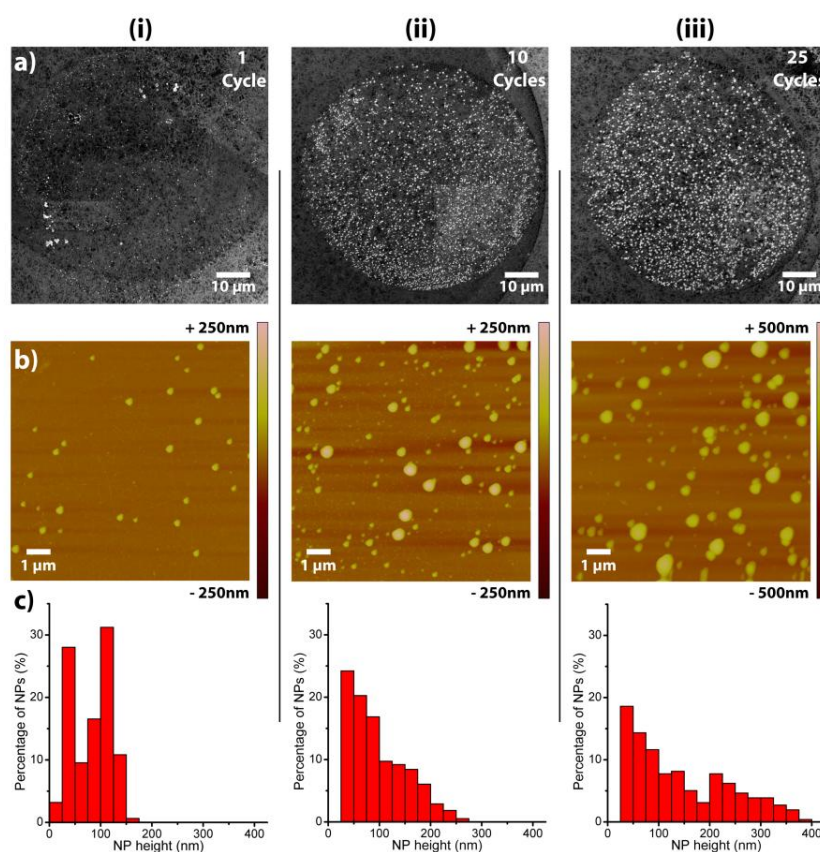


Figure 6.3 - (a) FE-SEM and (b) AFM images of electrodeposited NPs and (c) Histogram analysis of Pt NP heights extracted from AFM images of three repeats of each of Pt deposition regime: (i) 1 deposition cycle; (ii) 10 deposition cycles and (iii) 25 deposition cycles.

Both FE-SEM and AFM images clearly show the formation of Pt NPs on the SWNT networks and confirm that by increasing the number of deposition

cycles both the density and the size of deposited NP increases. The NP densities were ca. 0.45 NPs μm^{-2} (1 cycle); 0.80 NPs μm^{-2} (15 cycles) and 0.85 NPs μm^{-2} (25 cycles), when averaged over three repeats of each Pt NP deposition regime on SWNTs. Furthermore, a closer look at the histograms as a function of deposition cycles shows that the size distribution broadens with increasing deposition cycles (after one cycle there is a particle height range of 175 nm, after 25 cycles this range is 375 nm) suggesting that NP nucleation not only takes place during the first cycles, but also during subsequent cycles, which show both the nucleation of new NPs as well as growth of existing NPs. This suggests that the Pt NPs form progressively,³⁰ agreeing with a previous study.³¹

A significant advantage to using SWNT networks as support material for electrocatalytically active (Pt) NPs is the low surface coverage of the network, which is ca. 1%.²⁷ The network density is high enough to allow the SWNT to behave as a contiguous electrode under typical electrochemical mass transport conditions,^{14, 32} but 99% of the surface is insulating (inert). This means that Pt electrodeposition does not occur on the vast majority of the surface (AFM Figure 6.3), and the Pt NPs are thus less likely to form agglomerates. This is important as agglomeration reduces the electroactive surface area, leading to sub-optimal metal utilisation.

To investigate the surface coverage more precisely, we carried out electrodeposition as above, stopping after a defined number of cycles and analysed the amount of Pt that had been electrodeposited by running CVs in de-aerated 0.5 M H_2SO_4 (50 mVs^{-1}). Figure 6.4 a,b,c shows that with an increasing number of deposition cycles, the overall magnitude of the current in the CVs increases due to the increasing surface area, as described above. The increase in

the integrated charge of the H_{UPD} can be used to calculate the specific Pt surface area ($210 \mu\text{C cm}^{-2}$).

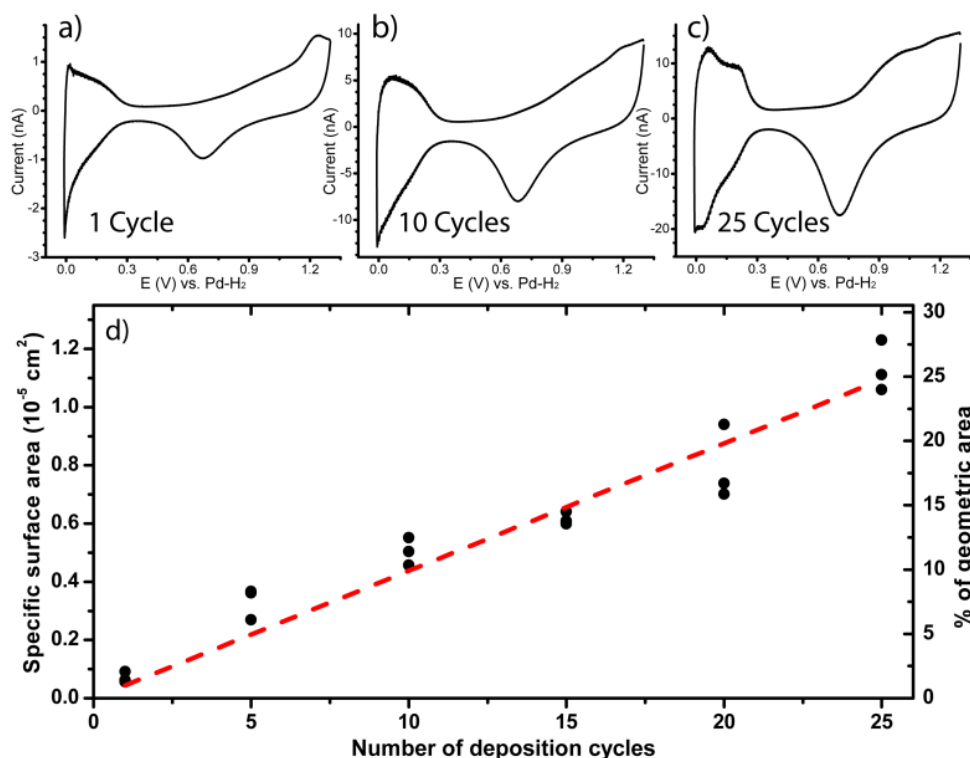


Figure 6.4 - CVs of electrodeposited Pt NPs in de-aerated 0.5 M H_2SO_4 , (50 mV s^{-1}) prepared by: a) 1 deposition cycle; b) 10 deposition cycles; c) 25 deposition cycles. d) Plot of specific surface area as a function of the number of deposition cycles, calculated from the charge passed in the H_{UPD} region (left axis) and the percentage of the geometric surface area with respect to the area of the droplet on the SWNT network during electrodeposition (right axis).

Figure 6.4 (d) summarises the change in specific Pt surface area with increasing numbers of deposition cycles, up to 25 cycles, measured in 0.5 M H_2SO_4 with no K_2PtCl_6 . Each point on the graph represents a separate Pt deposit experiment on the same SWNT network reaffirming the multi-measurement advantage of the microcapillary electrochemical method. The plot shows that over this range the increase in specific surface area is reasonably linear with respect to the number of deposition cycles, consistent with the data in Figure 6.2

(b). Each deposition adds ca. $45 \mu\text{m}^2$ to the specific surface area, which corresponds to ca. 1 % of the geometric area of the electrode (meniscus footprint). This demonstrates that great control of the Pt NP density that can be gained using the CV deposition process and suggests that Pt loading can be tuned. The trend also confirms that the deposition proceeds consistently across different areas of the SWNT network, further confirming its reasonable uniformity both physically (SWNT coverage) and electrochemically.

6.4 ORR and MOR on low density SWNT/Pt composites.

6.4.1 ORR on low density SWNT/Pt composites

The ORR response of the electrodeposited Pt NPs was investigated in aerated 0.5 M H_2SO_4 ($\sim 0.25 \text{ mM O}_2$ at 298 K).³³ Typical linear sweep voltammograms (LSVs) starting at 1.3 V for ORR on Pt deposited with 1, 10 and 25 deposition cycles are shown in Figure 6.5 (a).

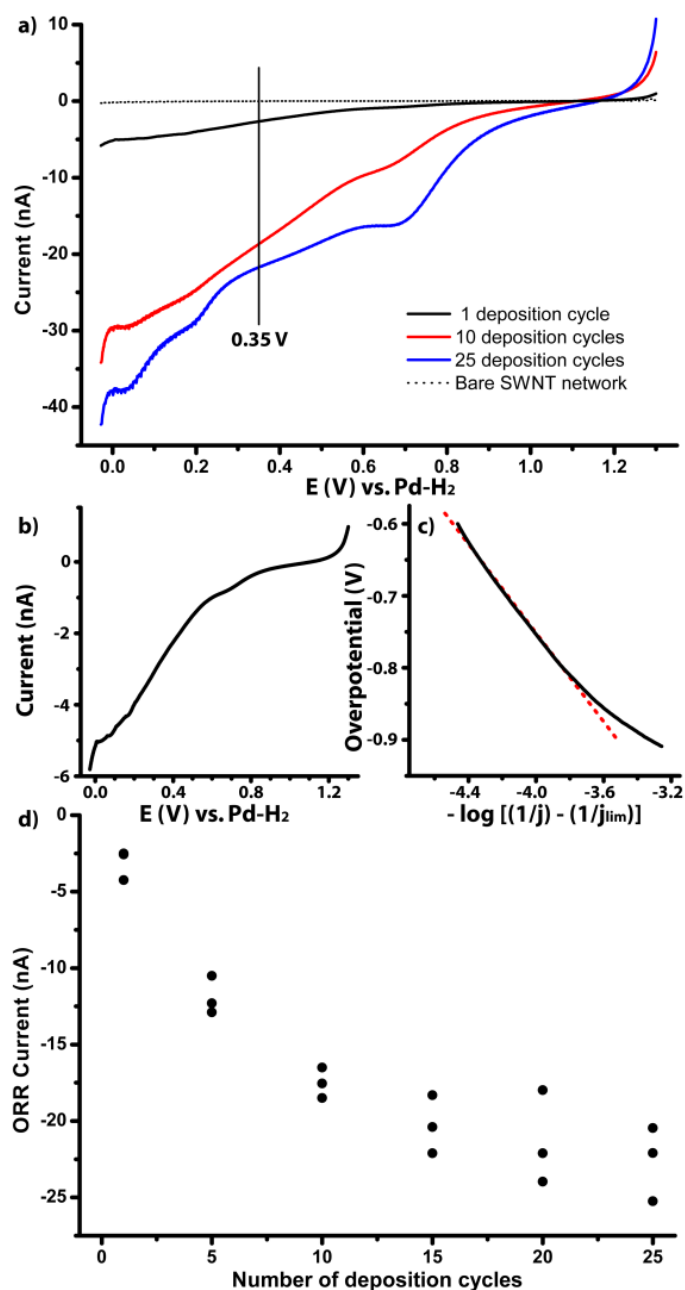


Figure 6.5 - a) Linear sweep voltammograms for ORR (0.5 M H_2SO_4 , 100 $mV s^{-1}$) on Pt NP deposited with 1, 10 and 25 cycles. b) Magnification of the LSV for the ORR on Pt NP deposited with 1 cycle. c) Mass-transport corrected Tafel plot for the high overpotential region of the ORR LSV on Pt NP deposited with 1 cycle, red dotted line has a slope of $-275 mV dec^{-1}$. d) Plot of ORR current measured at 0.35 V (chosen as it was close to limiting but before there was a contribution from hydrogen adsorption) vs. number of Pt deposition cycles.

The electrocatalytic activity of Pt NP on SWNT towards the ORR can be clearly observed even after 1 deposition cycle. A pristine bare SWNT network exhibits minimal ORR catalysis without a high overpotential, and so the response for the unfunctionalised SWNT is negligible (Figure 6.5 a). The ORR begins with a peak at 0.7 V attributed to the onset of reduction of oxides on the Pt surface, which leads into the diffusion limited ORR at higher overpotentials. The slight slope of the limiting ORR current is attributed to the increased O₂ flux from the edges of the meniscus from air. This acts to replenish the depleted O₂ at the electrode surface. Below 0.25 V, the peaks due to the adsorption of hydrogen begin to appear and when scanning cathodic of 0 V, the hydrogen evolution reaction (HER) becomes significant. As the number of deposition cycles is increased from 1 to 10 there is a slight positive shift (ca. 5 mV) in the ORR onset potential, but significantly there is a seven-fold increase in the ORR current. With 25 deposition cycles there is a further positive shift (ca. 50 mV) in onset potential, but the ORR current only increases an additional 3 nA (25%) due to increased diffusional overlap between the NPs.

Figure 6.5 (b) shows a magnification of the ORR LSV on the 1 cycle Pt NP electrodeposit. As shown in Figure 6.3 (i) this electrodeposit is made up of Pt NPs with a diameter ca. 100 nm, which on average are spaced many microns apart. It has been suggested that the separation of Pt particles plays an important role in ORR catalysis,⁵ as with increased overlap of diffusion fields there is reduced probability of intermediates (H₂O₂) desorbing and diffusing from the electrode surface before they are fully converted (to H₂O).³⁴ This effect is enhanced at NPs due to the increased rates of mass transport at small electrodes, which means diffusion of intermediates from the electrode is fast. It is estimated,

from the limiting ORR current, that the rate of mass transport for the electrodeposit of 100 nm Pt particles (1 deposition cycle) is ca. 0.1 cm s^{-1} , a rate that would be difficult to achieve using traditional hydrodynamic techniques such as rotating disk.³⁵ These effects have led to the use of arrays of small electrodes or NPs for the investigation of the kinetics of electrocatalysts.³⁶⁻³⁸

Figure 6.5 (c) shows a mass transport corrected Tafel plot³⁹ of the high overpotential region of the LSV shown in Figure 6.5 (b). Due to the presence of the oxide stripping peak it was not possible to perform Tafel analysis at lower overpotentials. The slope of this plot is 275 mV dec^{-1} , which is comparable to that found in a similar overpotential region for the ORR on single Pt particles³⁵, from this slope the apparent symmetry factor (α) is calculated as 0.22, according to equation 6.1,³⁹

$$-\log j_k(E) = -\log \left[\frac{1}{j} - \frac{1}{j_{lim}} \right] = -\frac{2.303\alpha nF}{RT} \eta + \log k_0 + \log(nF[O]_{\infty}) \quad (6.1)$$

where, j_k is the kinetic current density, *i.e.* current density in the absence of mass transport limitations, j is current density, j_{lim} is mass transport limited current density, n is the number of electrons transferred, F is the Faraday constant, R is the universal gas constant, T is temperature, k_0 is the standard rate constant and $[O]_{\infty}$ is the bulk concentration of oxygen. The low α for the ORR in this overpotential region is similar to a previously reported value³⁵ and has been attributed to a change in the rate determining step from electron transfer to oxygen adsorption or adsorption affecting the potential profile in the double layer, which is important for inner sphere reactions.³⁵ This analysis demonstrates that the electrodeposition of NPs on a supporting SWNT network, using the microcapillary electrochemical method is potentially an effective method for

creation of NP arrays for kinetic analysis, without the need for complex lithographic procedures.

Figure 6.5 (d), which shows the ORR current at 0.35 V (corrected for capacitance) as a function of the number of Pt deposition cycles, highlights the effects of increased diffusional overlap which acts to reduce the loss of intermediates. The potential at which the limiting current was measured was chosen as it was very close to mass transport limitations, but with no contribution from hydrogen adsorption. The oxygen reduction current increases quickly for depositions up to 10 cycles, but after this the increase in ORR with more deposition becomes much more gradual and tends towards a plateau. At very low Pt densities there may be an increased contribution from the 2 electron pathway, yielding H_2O_2 , however, in this case it is difficult to tell if the limitations from the particle density or mechanistic changes dominate.

As the density of Pt NPs increases their diffusion fields overlap to a greater extent, meaning it is less likely for intermediates to diffuse into the bulk solution and the electrode increasingly acts like a planar disk. Consequently, the reaction switched from being limited by Pt density towards being limited by the diffusion towards the (geometric) disk electrode. From Figure 6.5 (d) it is apparent that diffusion towards the Pt becomes dominant at around 15 deposition cycles, stabilising at $\sim 20 - 25$ nA. This value is comparable (albeit slightly lower) to that calculated for an inlaid disk UME of the same dimensions (29 nA for a 4-electron process, $D = 2 \times 10^{-5} \text{ cm s}^{-1}$ ⁴⁰), although note the geometry is different in the current experimental setup. An inlaid disk electrode of this size in bulk solution (infinite diffusion) displays a hemispherical diffusion regime whereas with the microcapillary electrochemical method diffusion from the sides

of the electrode is limited, due to the relatively small size of the droplet covering the Pt NPs. These data suggest that for the ORR the optimum Pt NP density can be achieved by around 15 deposition cycles. This results in a Pt surface with only a specific surface area ca. 15 % of the geometric surface area that behaves similarly to a bulk Pt surface, due to the diffusion dependence of the ORR.

6.4.2 MOR on low density SWNT/Pt composites

Typical CVs for the oxidation of methanol on the Pt NP-SWNT networks, deposited for 1, 10 and 25 cycles are shown in Figure 6.6 (a), which show the characteristic features for the oxidation of small organic molecules at platinum surfaces. In the anodic sweep, the currents in the H_{UPD} region are somewhat suppressed due to surface blocking by decomposition products (mainly adsorbed CO). Starting at a potential between 0.4 V - 0.5 V, the decomposition products are oxidized, freeing up surface sites for continuous oxidation, leading to an anodic peak at ca. 0.7 V (with a shoulder at 0.5 V). At higher potentials, the surface is blocked by the formation of irreversible oxides. In the cathodic sweep, the surface oxides are reduced, reactivating the oxidation of methanol until the overpotential is too low to oxidize methanol (or its decomposition products).

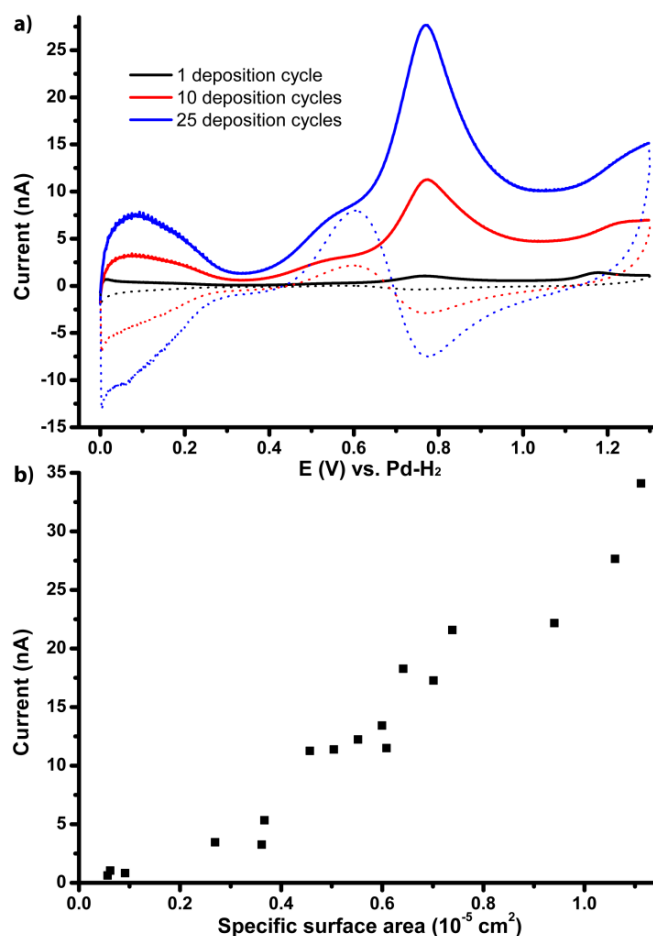


Figure 6.6 - a) CVs for the MOR (0.5 M methanol in 0.5 M H₂SO₄, 100 mV s⁻¹) on Pt NP deposited for 1, 10 and 25 cycles. The anodic sweep is shown with a solid line; the cathodic sweep is shown by dotted line. b) Plot of MOR peak current vs. specific Pt surface area.

As with the ORR, a single Pt deposition cycle is enough to give rise to a noticeable peak for the MOR (1.1 nA). However, unlike the ORR, subsequent deposition cycles continue to increase the MOR peak current (10 cycles 11.2 nA, 25 cycles 27.7 nA), as the MOR is a sluggish, surface-limited process. The peak current density based on the specific Pt surface area is ca. 2 – 3 mA cm⁻², consistent to values reported literature on macroscale polycrystalline Pt electrodes.^{41, 42} Figure 6.6 (b) shows the dependence of MOR peak current on Pt specific surface area, in this case surface area is more relevant than for ORR.

Over this range, it can be seen that the MOR peak current does not plateau, but increases linearly with surface area.

6.5 ORR and MOR on high density SWNT/Pt composites.

6.5.1 ORR on high density SWNT/Pt composites

High density Pt was deposited using the same method as discussed previously (same voltammetric scan range and rate), but with 5 mM K_2PtCl_6 (rather than 0.5 mM) and electrodeposition on SWNTs networks for 50, 75 and 100 cycles. Typical resulting structures can be seen in Figure 6.7.

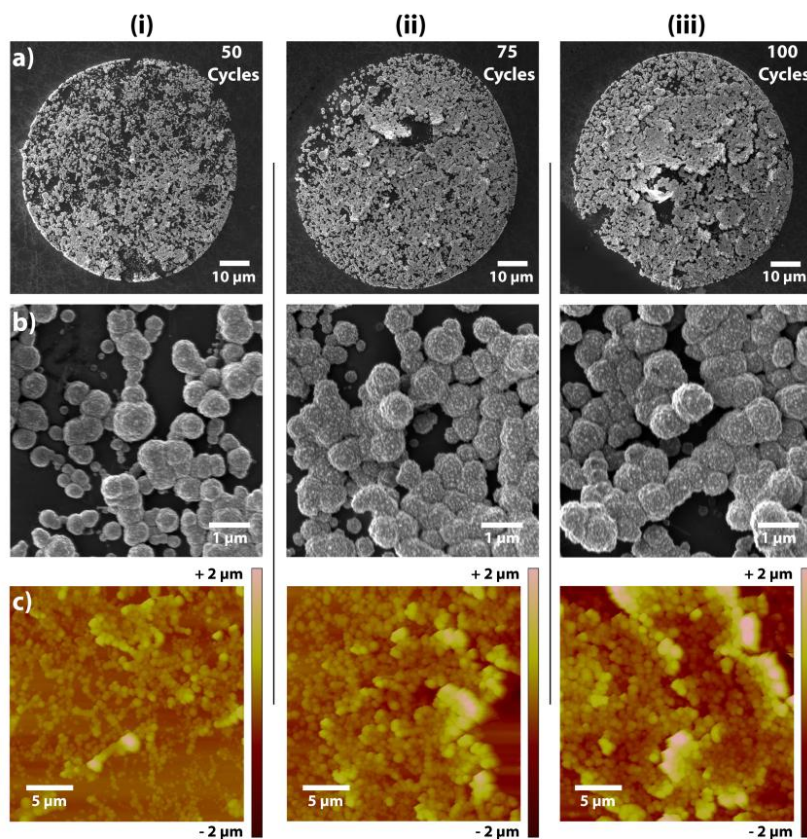


Figure 6.7 - FE-SEM (a and b) and AFM (c) images of electrodeposited NPs (from 5 mM K_2PtCl_6) after: (i) 50 deposition cycle; (ii) 75 deposition cycles and (iii) 100 deposition cycles.

It can be seen that after 50 deposition cycles at the higher concentration of PtCl_6^{2-} , the Pt electrodeposit has the form of large high surface area agglomerates, although individual NPs can still be resolved. After 100 cycles, a Pt surface with significant texture on the micro and nanoscale has formed. At these high Pt densities Pt structures are formed with a specific surface area ~ 4 (50 cycles), ~ 7 (75 cycles) and ~ 9 (100 cycles) times that of the geometric electrode area. This represents a very large increase in the surface area of the electrode with no increase in electrode geometry; there is also minimal wasted Pt volume. However, at these relatively high surface densities the stability of the Pt on the SWNT becomes somewhat compromised as they are only attached by their interaction with the SWNT. This means the structures can be mechanically detached unless handled very carefully.

Figure 6.8 (a) shows the response of the high density Pt/SWNT composites for the ORR. The same characteristic wave shape can be seen here as with the low density deposits (Figure 6.5), but the Pt oxide stripping peak (at 0.7 V) and hydrogen adsorption peaks (at 0.15 V and -0.05 V) are much more pronounced due to the large specific surface area of the electrodeposits. However, the response for the ORR has changed little with increased Pt density; when measured at 0.35 V, and corrected for capacitive current, the reduction current for all Pt densities is ca. 60 nA. This is above the theoretical limiting current for an inlaid disk electrode of this size, part attributed to Pt protruding from the electrode surface increasing effective area and the difficulty of accounting for the capacitive current. Importantly, this finding demonstrated that there is little benefit to significantly increasing the amount of Pt used.

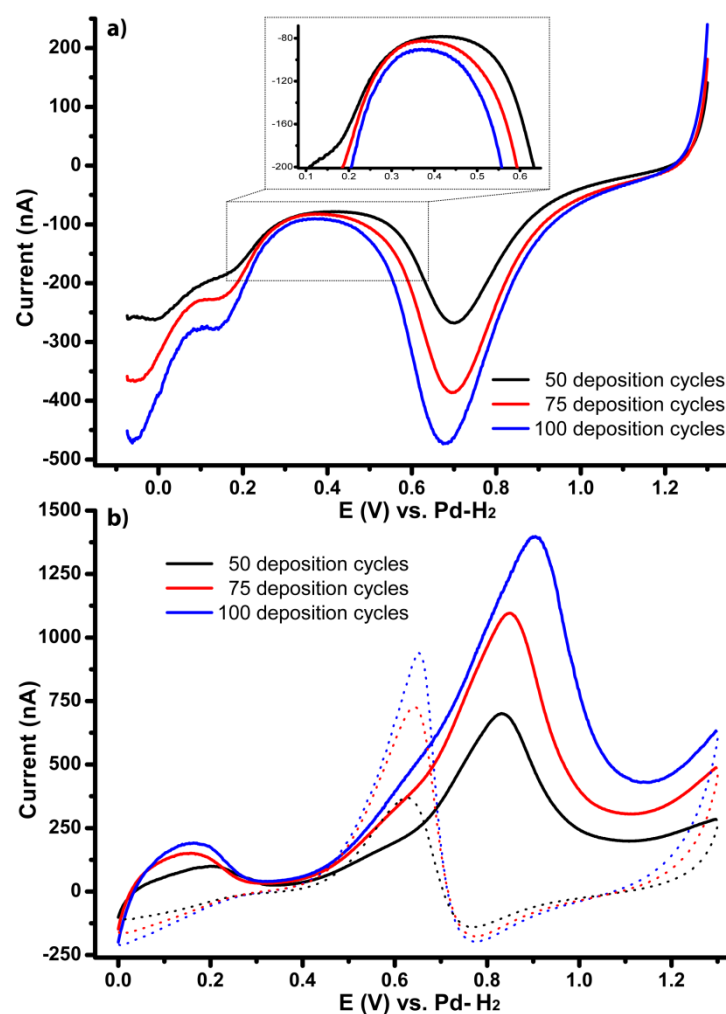


Figure 6.8 - a) LSVs starting at 1.3 V and extending to -0.1 V (aerated 0.5 M H₂SO₄, 100 mV s⁻¹) at Pt electrodeposits (from 5 mM PtCl₆²⁻) for different numbers of deposition cycles, b) CVs for the MOR (0.5 M methanol in 0.5 M H₂SO₄, 100 mV s⁻¹) performed on Pt NP deposited from 5 mM PtCl₆²⁻ for different numbers of cycles (start and end potential 0 V, scanning to 1.3 V).

6.5.2 MOR on high density SWNT/Pt composites

Finally, the MOR response for the high density Pt nanostructures is shown in Figure 6.8 (b) where the MOR response increases with Pt specific surface area. The peak current for MOR at Pt deposited for 100 cycles at 5 mM K₂PtCl₆ is 50 times greater than that for 25 cycles at 0.5 mM K₂PtCl₆ (Figure 6.5 a). The peak current densities based on geometric electrode area are 18, 28 and 36 mA

cm^{-2} respectively for 50, 75 and 100 cycles, while the peak current density based on specific surface area for all high density samples is ca. 4 mA cm^{-2} , which again (as for the lower density deposits, Figure 6.6) is comparable to literature values based on macro scale electrodes ($1\text{-}3 \text{ mA cm}^{-2}$).^{43, 44}

6.6 Conclusions

In this study we have demonstrated that the coverage of Pt NPs supported on SWNT network electrodes can be controlled with very high precision over three orders of magnitude specific surface area, between $0.057 \times 10^{-5} \text{ cm}^2$ for 1 deposition cycle using $0.5 \text{ mM K}_2\text{PtCl}_6$ and $33.4 \times 10^{-5} \text{ cm}^2$ for 100 deposition cycles using $5 \text{ mM K}_2\text{PtCl}_6$. This work also serves to demonstrate the versatility of the microcapillary electrochemical method as a deposition technique, allowing a wide range of composite materials to be created and analysed from low loaded, well separated Pt NP catalysts suitable for the ORR to highly loaded Pt structures more useful for the MOR which requires very high surface area catalysts as this process is surface limited. By simply altering the number of deposition cycles it is easy to control the NP density, allowing optimisation of the Pt density to a particular reaction, and providing a versatile approach for elucidating the impact of specific surface area of an electrocatalyst on the activity.

Due to the ability to carefully control Pt NP surface coverage, for the ORR it was found that once the specific Pt surface area was $\geq 15\%$ of the geometric electrode area, it was possible to create a catalyst that acts comparably to a bulk electrode. In contrast the best catalyst for the MOR utilised in this work was found to have a very high specific surface area ($>850\%$ geometric area) with a very fine nanostructured surface. A highly favourable current density of

36 mA cm⁻² was achieved. Finally, it has been demonstrated that SWNTs provide an excellent support for catalytic materials, allowing nucleation and growth of well separated particles, which with further deposition allows the production of very high surface area structures.

6.7 References

1. A. S. Aricò, S. Srinivasan and V. Antonucci, *Fuel Cells*, 2001, **1**, 133-161.
2. B. D. McNicol, D. A. J. Rand and K. R. Williams, *J. Power Sources*, 1999, **83**, 15-31.
3. S. Wasmus and A. Küver, *J. Electroanal. Chem.*, 1999, **461**, 14-31.
4. K.-Y. Chan, J. Ding, J. Ren, S. Cheng and K. Y. Tsang, *J. Mater. Chem.*, 2004, **14**, 505-516.
5. M. Watanabe, H. Sei and P. Stonehart, *J. Electroanal. Chem.*, 1989, **261**, 375-387.
6. J.-S. Yu, S. Kang, S. B. Yoon and G. Chai, *J. Am. Chem. Soc.*, 2002, **124**, 9382-9383.
7. K.-W. Park, Y.-E. Sung, S. Han, Y. Yun and T. Hyeon, *J. Phys. Chem. B*, 2003, **108**, 939-944.
8. Y. Takasu, T. Kawaguchi, W. Sugimoto and Y. Murakami, *Electrochim. Acta*, 2003, **48**, 3861-3868.
9. B. Coq, J. Marc Planeix and V. Brotons, *Appl. Catal., A*, 1998, **173**, 175-183.
10. T. W. Ebbesen, H. Hiura, M. E. Bisher, M. M. J. Treacy, J. L. Shreeve-Keyer and R. C. Haushalter, *Adv. Mater.*, 1996, **8**, 155-157.
11. Y. Mu, H. Liang, J. Hu, L. Jiang and L. Wan, *J. Phys. Chem. B*, 2005, **109**, 22212-22216.
12. T. M. Day, P. R. Unwin, N. R. Wilson and J. V. Macpherson, *J. Am. Chem. Soc.*, 2005, **127**, 10639-10647.
13. R. Saito, M. Fujita, G. Dresselhaus and M. S. Dresselhaus, *Applied Physics Letters*, 1992, **60**, 2204-2206.
14. P. Bertoncello, J. P. Edgeworth, J. V. Macpherson and P. R. Unwin, *J. Am. Chem. Soc.*, 2007, **129**, 10982-10983.
15. D. Bera, S. C. Kuiry, M. McCutchen, S. Seal, H. Heinrich and G. C. Slane, *J. Appl. Phys.*, 2004, **96**, 5152-5157.
16. Y. Xing, *J. Phys. Chem. B*, 2004, **108**, 19255-19259.
17. B. M. Quinn, C. Dekker and S. G. Lemay, *J. Am. Chem. Soc.*, 2005, **127**, 6146-6147.
18. Z. He, J. Chen, D. Liu, H. Zhou and Y. Kuang, *Diam. Relat. Mater.*, 2004, **13**, 1764-1770.
19. T. M. Day, P. R. Unwin and J. V. Macpherson, *Nano Lett.*, 2007, **7**, 51-57.
20. Y. Xu and X. Lin, *Electrochim. Acta*, 2007, **52**, 5140-5149.
21. A. N. Golikand and L. Irannejad, *Electroanal.*, 2008, **20**, 1121-1127.
22. H.-F. Cui, J.-S. Ye, W.-D. Zhang, J. Wang and F.-S. Sheu, *J. Electroanal. Chem.*, 2005, **577**, 295-302.
23. Z. F. Ren, Z. P. Huang, J. W. Xu, J. H. Wang, P. Bush, M. P. Siegal and P. N. Provencio, *Science*, 1998, **282**, 1105-1107.
24. P. V. Dudin, P. R. Unwin and J. V. Macpherson, *J. Phys. Chem. C*, 2010, **114**, 13241-13248.
25. P. V. Dudin, M. E. Snowden, J. V. Macpherson and P. R. Unwin, *ACS Nano*, 2011, **5**, 10017-10025.

26. S. C. S. Lai, P. V. Dudin, J. V. Macpherson and P. R. Unwin, *J. Am. Chem. Soc.*, 2011, **133**, 10744-10747.
27. J. P. Edgeworth, N. R. Wilson and J. V. Macpherson, *Small*, 2007, **3**, 860-870.
28. M. J. Vasile and C. G. Enke, *J. Electrochem. Soc.*, 1965, **112**, 865-870.
29. S. Trasatti and O. A. Petrii, *J. Electroanal. Chem.*, 1992, **327**, 353-376.
30. R. M. Penner, *J. Phys. Chem. B*, 2002, **106**, 3339-3353.
31. T. M. Day, P. R. Unwin and J. V. Macpherson, *Nano Lett.*, 2006, **7**, 51-57.
32. M. E. Snowden, P. R. Unwin and J. V. Macpherson, *Electrochem. Commun.*, 2011, **13**, 186-189.
33. T. N. Das, *Ind. Eng. Chem. Res.*, 2005, **44**, 1660-1664.
34. Y. E. Seidel, A. Schneider, Z. Jusys, B. Wickman, B. Kasemo and R. J. Behm, *Faraday Discuss.*, 2009, **140**, 167-184.
35. S. Chen and A. Kucernak, *J. Phys. Chem. B*, 2004, **108**, 3262-3276.
36. M. Gustavsson, H. Fredriksson, B. Kasemo, Z. Jusys, J. Kaiser, C. Jun and R. J. Behm, *J. Electroanal. Chem.*, 2004, **568**, 371-377.
37. I. Dumitrescu, D. F. Yancey and R. M. Crooks, *Lab Chip*, 2012, **12**, 986-993.
38. I. Dumitrescu and R. M. Crooks, *Proc. Natl. Acad. Sci. U.S.A.*, 2012, **109**, 11493-11497.
39. C. M. A. Brett and A. M. O. Brett, *ELECTROCHEMISTRY Principles, Methods, and Applications*, Oxford University Press, UK, 1993.
40. M. Gara and R. G. Compton, *New J. Chem.*, 2011, **35**, 2647-2652.
41. R. G. Freitas, M. C. Santos, R. T. S. Oliveira, L. O. S. Bulhões and E. C. Pereira, *J. Power Sources*, 2006, **158**, 164-168.
42. J. L. Cohen, D. J. Volpe and H. D. Abruna, *Phys. Chem. Chem. Phys.*, 2007, **9**, 49-77.
43. H. Wang, C. Xu, F. Cheng, M. Zhang, S. Wang and S. P. Jiang, *Electrochem. Commun.*, 2008, **10**, 1575-1578.
44. K. Yahikozawa, Y. Fujii, Y. Matsuda, K. Nishimura and Y. Takasu, *Electrochim. Acta*, 1991, **36**, 973-978.

7

Generation – collection measurements within the meniscus of a microcapillary electrochemical cell using a carbon fibre ultramicroelectrode.

In this work microcapillary based electrochemical methodology is combined with the generation/collection electrode format utilising very high aspect ratio carbon fibre ultramicroelectrodes. First, the concept is demonstrated with a common outer sphere redox mediator, showing that the generator electrode is capable of influencing the response at the collector. It is then utilised, first to investigate a reaction on a complex electrode geometry, i.e. a single walled carbon nanotube forest, which is not easily investigated using traditional techniques which require the electrode material to be physically encapsulated. The technique is then used to probe the different mechanistic pathways of the oxygen reduction reaction by detecting any H_2O_2 generated in the electrode process.

7.1 Introduction

In a generator-collector (G/C) electrochemical system, a chemical species is produced at one working electrode (generator) by a redox reaction (e.g. $A + e^- \rightarrow B$). A proportion of this species (B) undergoes a second electrochemical process, which may be reformation of the initial species ($B \rightarrow A + e^-$) or the formation of a third ($B \pm e^- \rightarrow C$), at a second working electrode (collector), coupled by diffusion or convection/diffusion to the generator electrode.¹ This approach has been used to probe reactions as varied as the ORR,² the oxidation of ascorbic acid via a catalytic EC' mechanism³ and trace level analyte detection,⁴ among many possible examples, allowing greater understanding of kinetic and mechanistic aspects of these processes. Traditionally, G/C often involves the use of complicated experimental set ups e.g. flow cells,⁵ the rotating-disk electrode (RDE)⁶ or specialised electrodes,⁷ meaning its use becomes prohibitive, especially for electrode materials that cannot be encapsulated in these formats.

Microcapillary-based electrochemical techniques expand the range of electrode formats that can be studied without the need for electrode material encapsulation. Measurements are made by landing the meniscus of a solution-filled capillary, with a micrometer-scale aperture, on an electrode surface.⁸⁻¹⁰ As the electrochemical cell is limited to the meniscus footprint, these methods have proven useful in areas where multiple measurements are to be made on a single surface, for example in localised corrosion studies¹¹ or the electrodeposition of metal nanoparticles (NPs).^{8, 10} It also allows the user to make electrochemical measurements at targeted areas of a surface.⁹ Importantly, this method negates

the need for post-processing electrode surfaces, e.g. through the use of lithography, saving time and ensuring the surface is free from leftover residues which may hinder electrode processes.⁹

In this work we demonstrate a simple method to combine the benefits of the microcapillary electrochemical method (MCEM) (described in section 2.6.1) with the analytical power of G/C studies, through the use of very high aspect ratio carbon fibre ultramicroelectrodes (UMEs). These can be readily inserted into the meniscus and used as a means of monitoring the electrode process.

7.2 Microcapillary generation-collection (G/C)

Details regarding the production of carbon fibre UMEs, the MCEM and a detailed description of the microcapillary generation/collection (MCEM G/C) experimental set up can be found in section 2.7. Briefly, to perform G/C measurements in the meniscus of the microcapillary, the carbon fibre UME was mounted on a secondary *x-y-z* micropositioner using a custom capillary holder to enable it to be positioned at a 45° angle with respect to the electrode surface. Once the meniscus from the microcapillary had formed on the surface, the carbon fibre UME was carefully inserted from the side (Figure 7.1 c). The capillary radius (R_c) has been found to be a good approximation for the height of the meniscus from the surface both in this investigation and previously.⁹ This means that the maximum possible height of the UME from the surface was R_c (i.e. between 25 and 50 μm), in reality it was likely to be much closer. Electrochemical measurements were made by scanning the potential of the surface (working electrode 1) while the UME (working electrode 2) was held at a constant potential to act as a collector.

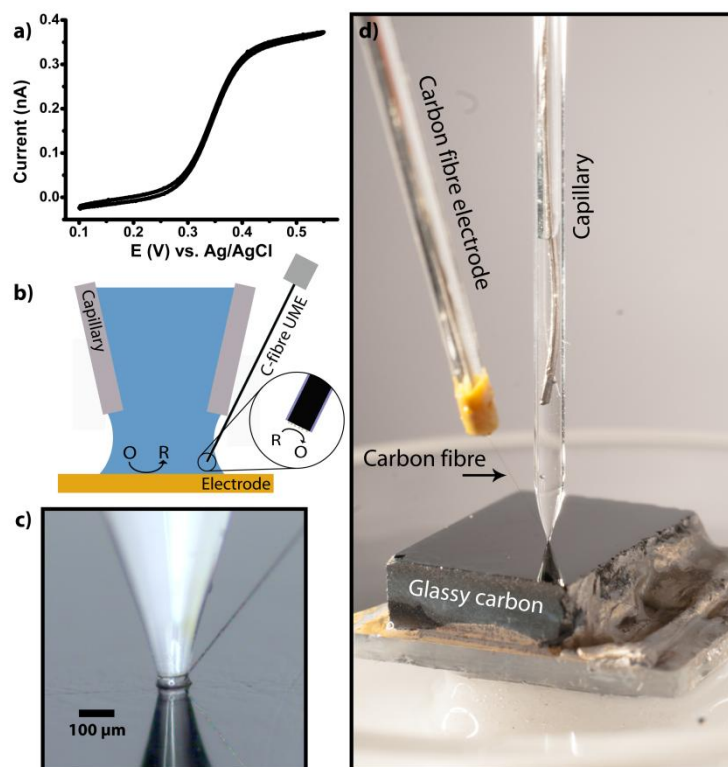


Figure 7.1 - a) CV for the oxidation of 0.25 mM $\text{FcTMA}^{+/2+}$ in 50 mM KCl (25 mV s^{-1}) at a carbon fibre UME. b) Schematic of the MCEM G/C set up. c) Optical photograph of carbon fibre UME in the capillary meniscus. d) Large scale view of MCEM G/C on a glassy carbon electrode.

7.3 Proof of concept

Figure 7.1(a) shows a typical cyclic voltammogram (CV) for the oxidation of FcTMA^+ recorded at a carbon fibre UME with a carbon fibre diameter of $8 \mu\text{m}$ (Figure 7.2). This CV shows the typical wave shape for fast ET at a UME i.e. it shows steady-state behaviour and exhibits reversible ET ($\Delta E_{3/2} - E_{1/4} = 59 \text{ mV}$). The limiting current (i_{lim}) in electrodes with small RGs (RG=electrode surround radius/electrode radius) can be estimated using equation 1.1¹²

$$i_{lim} = 4nFDaC^* \beta \quad (7.1)$$

where n is the number of electrons transferred, F is the Faraday constant, D is the diffusion coefficient ($D \text{ FcTMA}^+ = 6.3 \times 10^{-6} \text{ cm}^2 \text{ s}^{-1}$)¹³, a is the electrode radius, C^* is bulk concentration and β is a correction factor related to RG which takes into account back diffusion.¹⁴ The RG for this electrode is close to 1, as only a monolayer film of polyoxyphenylene is formed during electrodeposition, meaning $\beta = 1.43$ as calculated by *Girault et al.*¹⁴ This indicates that diffusion from the back of the electrode has a significant effect on the mass transport to an electrode of this geometry, increasing the limiting current by ca. 40%. The theoretical limiting current is therefore calculated to be 0.345 nA, which is in close agreement to the experimental value ($i_{\text{lim}} = 0.36 \text{ nA}$). This is slightly higher due to the probable exposure of slightly more carbon fibre during the cutting step by, for example, cutting on a slight angle. This can be seen in Figure 7.2.

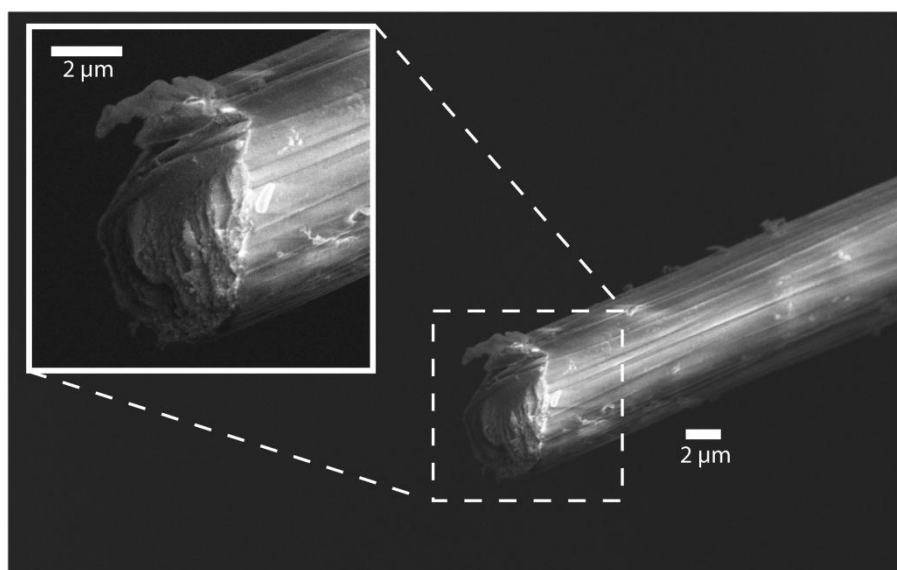


Figure 7.2 - FE-SEM images of a polyoxyphenylene coated carbon fibre which has been cut to form a UME.

Figure 7.3 shows CVs for the one electron oxidation of 0.5 mM FcTMA⁺ on a SWNT network, a process which has previously been shown to be

reversible.¹⁵ This experiment was performed with a capillary of R_c 45 μm and in this case a bare carbon fibre UME was inserted into the capillary meniscus. This was held at either 0 V, a potential where FcTMA^+ oxidation did not readily occur on the UME, but the reduction of any FcTMA^{2+} that reached the electrode would be strongly driven, or 0.4 V where the oxidation of FcTMA^+ was driven at the carbon fibre electrode.

Figure 7.3 a/b demonstrates the MCEM G/C in operation in a traditional G/C arrangement, whereby a collector electrode is used to perform the reverse process to that occurring at the generator. As FcTMA^{2+} is generated at the SWNT surface, it diffuses towards the collector UME where a proportion of it is reduced back to FcTMA^+ , in principle this process could also increase flux towards the generator electrode. The CV in Figure 7.3 (a) displays the characteristic shape of a reversible redox process at an electrode with a linear diffusion profile (this is the case with the capillary arrangement as there is minimal diffusion from the electrode edge). The wave in Figure 7.3 (b) shows the corresponding current at the collector electrode plotted against the potential of the generator electrode. This shows the characteristic shape of a process at an electrode with a high flux, reaching a plateau limited by the electrode size. However as this electrode is held at a constant potential (0 V) the increase in current is not driven by increased driving potential, but by the increase in the concentration of FcTMA^{2+} in the solution as it is generated at the SWNT surface. As the electrode is very close to the SWNT surface, the collector (UME) current reaches a limiting value which is equivalent to that of the diffusion limited current in a bulk concentration of FcTMA^{2+} , i.e. 0.5 mM. The hysteresis in this

wave is caused by the time required for species to diffuse between the two electrodes.

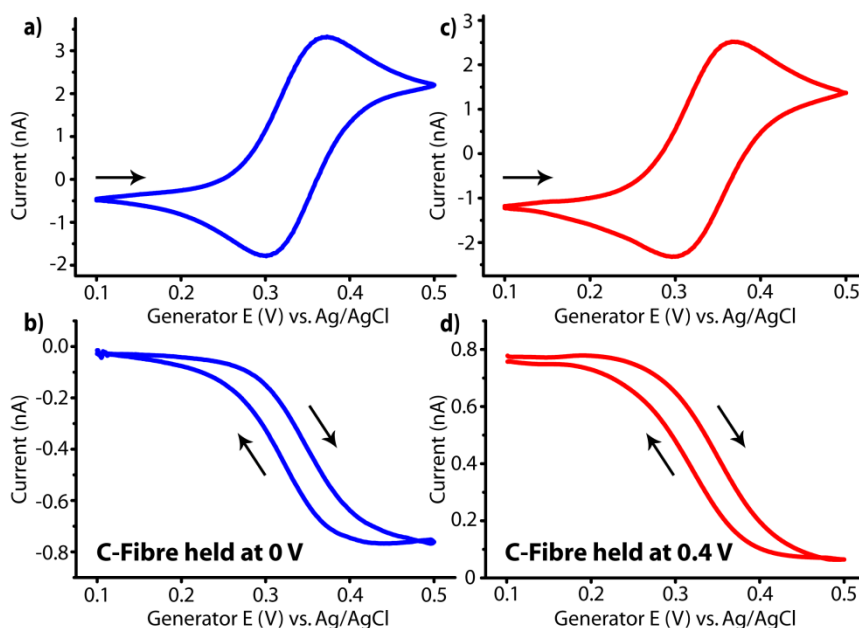


Figure 7.3 - G/C CVs of 0.5 mM $\text{FcTMA}^{+/2+}$ in 50 mM KCl, 25 mVs^{-1} , performed on a SWNT network: a) generation; b) collection with UME held at 0 V. c) generation; d) collection with UME held at 0.4 V.

In Figure 7.3 c/d a G/C CV is shown for the system discussed above, but in this case the collector UME was held at a 0.4 V, meaning the oxidation of FcTMA^+ was driven at both the SWNT and carbon fibre electrodes, meaning they were in direct competition. Initially the collector electrode drives FcTMA^+ oxidation at a diffusion limited rate, however as the significantly larger generator electrode (~ 65 times larger geometric area) begins to drive the same process a drop in the current at the collector electrode is observed because the concentration of FcTMA^+ at the surface becomes depleted. The current magnitude at the collector electrode does not fall to zero, but reaches a second plateau controlled by the rate of diffusion towards the electrode when in direct competition with the generator electrode. From this limiting current the FcTMA^+

concentration at the UME surface is calculated to be 0.035 mM. The current once again increases towards its initial value when the generator electrode begins the reverse reaction.

7.4 Applications

7.4.1 SWNT forest

To further demonstrate the versatility of the carbon fibre UME for G/C experiments, the oxidation of 0.5 mM FcTMA^+ was performed on the top surface of a SWNT forest (discussed in section 3.3.2). This substrate consists of super high density SWNTs which are vertically aligned and rise ~ 0.5 mm above the surface and which have been shown (section 4.2.2) to possess impressive electrochemical properties.¹⁶ This is an example of an electrode format that is not easily investigated using traditional techniques (e.g. RDE) as it is non-reflecting, rough and easy to penetrate.

Figure 7.4 shows the reversible oxidation of the FcTMA^+ on the SWNT forest surface (R_c 50 μm). The carbon fibre UME was again held at 0 V to drive the reduction of FcTMA^{2+} . Like the example shown in Figure 7.3 a/b, the oxidation of FcTMA^+ at the forest surface caused an increase in current at the UME, which was within the FcTMA^{2+} diffusion field. The current at the UME decreased back to its initial value as the FcTMA^{2+} became depleted as the forest electrode was scanned back to its starting potential, with hysteresis due to diffusional lag.

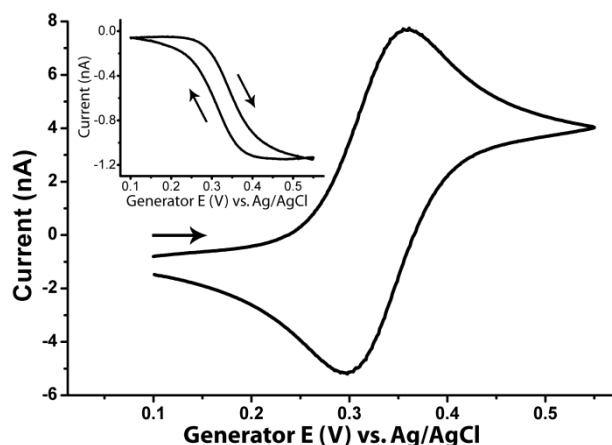


Figure 7.4 - G/C CVs of 0.5 mM $\text{FcTMA}^{+/2+}$ in 50 mM KCl, 50 mVs^{-1} , performed on a SWNT forest. Generation is shown in the main figure body, collection inset, with UME held at 0 V.

7.4.2 Oxygen reduction reaction mechanism

The ORR, which is of great importance in fuel cell research,¹⁷ is known to proceed via different mechanisms depending on the electrode surface. In acid solutions it can proceed either by a direct 4-electron reduction or by two separate 2-electron reduction processes with hydrogen peroxide as an intermediate.¹⁸ The direct pathway is known to dominate on clean platinum surfaces,¹⁷ whereas on most carbons the peroxide pathway is predominant.¹⁹

To investigate the different mechanisms of the ORR, MCEM G/C measurements were performed on Pt NP decorated SWNT electrodes (as discussed in section 6.3.2) and a bare glassy carbon electrode. The Pt NPs were deposited by cycling the surface between 1.3 V and -0.05 V in K_2PtCl_6 using the MCEM (R_c 25 μm). To enhance the detection of intermediates in the ORR process, the carbon fibre UME was also decorated with Pt as described above.

Figure 7.5 a/b shows the G/C response for a CV performed on Pt decorated SWNT in 0.5 M H_2SO_4 . The generator electrode shows the characteristic background response for Pt, with ORR beginning at ~ 1 V, the

hydrogen adsorption/desorption region $\sim 0.35 - 0$ V and the H_2 evolution region < 0 V. In this case the Pt-coated collector electrode was held at 0.9 V (vs. a Pd- H_2 quasi-reference/counter electrode²⁰), a potential capable of oxidising H_2O_2 ,²¹ but where no background processes occur. The response at the collector electrode Figure 7.5 (b) is featureless until the generator electrode reaches ~ 50 mV, where it begins to oxidise the generated H_2 . As an undetectable amount of H_2O_2 is oxidised at the Pt coated carbon fibre UME this demonstrates that the ORR on Pt proceeds mainly via the H_2O_2 free 4-electron reduction.

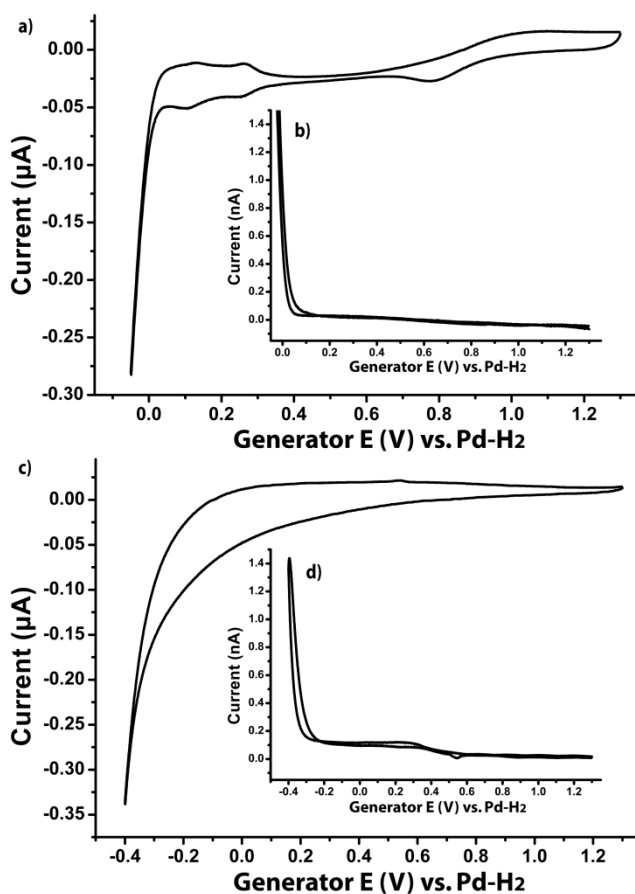


Figure 7.5 - a) CV in 0.5 M H_2SO_4 , 25 mVs^{-1} , on a Pt NP decorated SWNT network. b) Collector response at Pt coated UME held at 0.9 V. c) CV in 0.5 M H_2SO_4 , 25 mVs^{-1} , on a glassy carbon electrode. d) Collector response at Pt coated UME held at 0.9 V.

The ORR response of a glassy carbon electrode in aerated 0.5 M H₂SO₄, investigated using the MCEM-G/C technique, is shown in Figure 7.5 c/d. At the glassy carbon generator electrode the ORR current begins at ~ 0.5 V, gradually increasing until the current becomes dominated by H₂ evolution at potentials < -0.3 V. Unlike when ORR was performed on Pt NPs, the onset of the ORR on the glassy carbon electrode caused a current response at the collector electrode Figure 7.5 (d), which was again held at 0.9 V. This current is attributed to the oxidation of H₂O₂ produced during the first step of the two electron ORR on the Pt NPs on the carbon fibre UME. This confirms that the ORR proceeds by the peroxide pathway on glassy carbon.

Although it has been extensively reported the ORR proceeds via these two distinct pathways on Pt and carbon electrodes,^{18, 22} this investigation has shown that the MCEM-G/C methodology is capable of investigating mechanistic aspects of complex reactions, meaning it could be utilised to probe other, less well understood, reactions.

7.5 Conclusions

In conclusion, we have developed a simple, yet versatile, method of performing G/C measurements in tandem with the conventional MCEM. We have demonstrated that the method is applicable to a varied range of surfaces and processes and that through the modification of the carbon fibre UME it is capable of detecting mechanistic changes of reactions. The technique allows the investigation of systems where traditional techniques, such as RDE measurements, are not possible and may prove powerful as a tool to analyse the

feasibility of more complex techniques involving feedback e.g. scanning electrochemical microscopy.

7.6 References

1. E. O. Barnes, G. E. M. Lewis, S. E. C. Dale, F. Marken and R. G. Compton, *Analyst*, 2012, **137**, 1068-1081.
2. A. Damjanovic, M. A. Genshaw and J. O. M. Bockris, *J. Electrochem. Soc.*, 1967, **114**, 1107-1112.
3. E. Bitziou, M. E. Snowden, M. B. Joseph, S. J. Leigh, J. A. Covington, J. V. Macpherson and P. R. Unwin, *J. Electroanal. Chem.*, 2013, **692**, 72-79.
4. S. E. C. Dale, A. Vuorema, E. M. Y. Ashmore, B. Kasprzyk-Horden, M. Sillanpää, G. Denuault and F. Marken, *Chem. Rec.*, 2012, **12**, 143-148.
5. A. C. Fisher and R. G. Compton, *J. Appl. Electrochem.*, 1991, **21**, 208-212.
6. N. A. Anastasijević, V. Vesović and R. R. Adžić, *J. Electroanal. Chem.*, 1987, **229**, 305-316.
7. P. Tomčík, S. Jursa, Š. Mesároš and D. Bustin, *J. Electroanal. Chem.*, 1997, **423**, 115-118.
8. P. V. Dudin, P. R. Unwin and J. V. Macpherson, *J. Phys. Chem. C*, 2010, **114**, 13241-13248.
9. P. V. Dudin, M. E. Snowden, J. V. Macpherson and P. R. Unwin, *ACS Nano*, 2011, **5**, 10017-10025.
10. T. M. Day, P. R. Unwin and J. V. Macpherson, *Nano Lett.*, 2006, **7**, 51-57.
11. T. Suter and H. Böhni, *Electrochim. Acta*, 1997, **42**, 3275-3280.
12. C. Lefrou and R. Cornut, *ChemPhysChem*, 2010, **11**, 547-556.
13. P. Bertoncello, I. Ciani, F. Li and P. R. Unwin, *Langmuir*, 2006, **22**, 10380-10388.
14. F. Cortés-Salazar, H. Deng, P. Peljo, C. M. Pereira, K. Kontturi and H. H. Girault, *Electrochim. Acta*, 2013, **110**, 22-29.
15. I. Dumitrescu, P. R. Unwin, N. R. Wilson and J. V. Macpherson, *Anal. Chem.*, 2008, **80**, 3598-3605.
16. K. Gong, S. Chakrabarti and L. Dai, *Angew. Chem. Int. Ed.*, 2008, **47**, 5446-5450.
17. E. Yeager, *Electrochim. Acta*, 1984, **29**, 1527-1537.
18. E. Yeager, *J. Mol. Catal.*, 1986, **38**, 5-25.
19. M. Gara and R. G. Compton, *New J. Chem.*, 2011, **35**, 2647-2652.
20. M. J. Vasile and C. G. Enke, *J. Electrochem. Soc.*, 1965, **112**, 865-870.
21. S. B. Hall, E. A. Khudaish and A. L. Hart, *Electrochim. Acta*, 1998, **43**, 2015-2024.
22. I. Morcos and E. Yeager, *Electrochim. Acta*, 1970, **15**, 953-975.

8

Conclusions

In this thesis the synthesis of 2D SWNT networks, 3D SWNT forests and graphene by cCVD has been investigated. These structures were utilised in studies ranging from investigation of fundamental electrochemical properties to electrocatalysis. The implementation of a novel electrochemical method integrating generation/collection measurements with pre-existing microcapillary electrochemical methodology was also demonstrated.

In Chapter 3, atmospheric pressure thermal cCVD was utilised to grow SWNT in 3 distinct geometries, namely 2D networks, very high density networks and 3D forests. These materials were thoroughly characterised using AFM, FE-SEM, micro-Raman spectroscopy and XPS which showed that in all cases the tubes produced were single walled and of very high quality with a low density of defects and little amorphous carbon. Each of these structures also required a unique catalyst system, which were themselves developed and thoroughly characterised in this work. In this chapter the synthesis and subsequent transfer of SLG, using low pressure cCVD, was also discussed. By performing thorough characterisation of the SLG on the Cu substrate the cCVD process was optimised to grow uniform large areas ($\sim 1 \text{ cm}^2$) SLG. It was also shown that the SLG

became damaged and contaminated during transfer to Si/SiO₂, however this information can be used to improve this process in the future.

In Chapter 4, SWNT forests were investigated with an electrochemical cell consisting of a nanopipet, meaning electrochemical measurements were confined to either closed SWNT ends or SWNT sidewalls. This methodology allowed the forest structure to be probed in its pristine state, negating the need for sample processing, meaning the electrochemical activity originated from the undamaged sp² surfaces. Using two common outer sphere redox mediators it was shown that ET was fast, and near identical, on both closed ends and sidewalls, overturning the consensus that ET at SWNTs is driven by defects and open ends.

In Chapter 5 it was demonstrated that the simple application of anodic potentials to SWNT forests resulted in an enhancement of their ET response to a range of complex reactions, including the catalysis of the ORR. This work utilised a capillary based electrochemical technique which allowed many measurements to be performed on the SWNT surface meaning the effect of anodic potentials on pristine SWNTs could be reliably investigated. It was shown that the application of anodic potentials of ~1 V improved the response of both the Fe^{2+/3+} and Fe(CN)₆^{4-/3-} couples while having little effect on the outer sphere oxidation of FcTMA⁺. Potentials greater than 1.25 V were shown to activate the SWNT towards ORR catalysis, which was correlated with the introduction of defects into the SWNT structure using micro-Raman spectroscopy.

In Chapter 6, SWNTs networks were shown to be effective supports for Pt ORR and MOR catalysts. Pt NPs were formed on the SWNT networks by electrodeposition using a capillary with an opening of ~ 50 µm, meaning multiple

deposits could be made on a single surface which allowed the effect of NP density on catalytic behaviour to be investigated. It was found that it was only necessary to deposit Pt NPs with a surface area equivalent to 15 % of that of an equivalent disk electrode to provide a comparable level of catalysis, due to diffusion limitations. Conversely, for the surface-limited MOR the best Pt loading was found to be significantly higher. Deposition on SWNT networks was shown to be capable of creating MOR catalyst structures with a surface area equivalent to 850 % of the geometric area, demonstrating that SWNT networks can be a diverse support for catalyst materials, the density of which can be fine tuned to the application.

In Chapter 7 a method of performing generation/collection type measurements within the confines of a meniscus formed by a microcapillary was demonstrated. This work utilised carbon fibre electrodes which were fabricated with an electrode diameter of $\sim 8\ \mu\text{m}$, which allowed them to be into the meniscus formed by the capillary with relative ease. The performance of this methodology was initially assessed using the oxidation of outer sphere FcTMA^+ , after which it was demonstrated to be effective when used on complex substrates (SWNT forests) and could be utilised to understand mechanistic aspects of complex reactions (the ORR).

This thesis has shown that in their pristine state SWNT act as an excellent electrode material in a variety of formats. These not only act as a fascinating platform for research into the fundamental understanding of sp^2 materials, but also display properties that are more widely useful in industrially relevant processes. This work has challenged the widely accepted consensus that the ET

at SWNTs is driven by open ends and defect sites without having to resort to the use of single isolated tubes. This was achieved using the often ignored principle that careful synthesis and characterisation are essential before electrochemical studies are undertaken. By knowing that the SWNTs being produced were of very high quality and with a low defect density, we were more able to investigate effect of introduction of defects or catalytic sites.

It is essential that principles similar to those utilised in this work are taken forward when work on improving the transfer of SLG is undertaken. Only when it can be shown that the SLG produced by cCVD and transferred to Si/SiO₂ is of a low defect density and has little contamination should it be used for to investigate the fundamental ET properties of graphene.